Advances in Polymer Science 278

Klaus Müllen
Xinliang Feng *Editors*

From Polyphenylenes to Nanographenes and Graphene Nanoribbons

Springer

278
Advances in Polymer Science

Aims and Scope

The series Advances in Polymer Science presents critical reviews of the present and future trends in polymer and biopolymer science. It covers all areas of research in polymer and biopolymer science including chemistry, physical chemistry, physics, material science.

The thematic volumes are addressed to scientists, whether at universities or in industry, who wish to keep abreast of the important advances in the covered topics.

Advances in Polymer Science enjoys a longstanding tradition and good reputation in its community. Each volume is dedicated to a current topic, and each review critically surveys one aspect of that topic, to place it within the context of the volume. The volumes typically summarize the significant developments of the last 5 to 10 years and discuss them critically, presenting selected examples, explaining and illustrating the important principles, and bringing together many important references of primary literature. On that basis, future research directions in the area can be discussed. Advances in Polymer Science volumes thus are important references for every polymer scientist, as well as for other scientists interested in polymer science - as an introduction to a neighboring field, or as a compilation of detailed information for the specialist.

Review articles for the individual volumes are invited by the volume editors. Single contributions can be specially commissioned.

Readership: Polymer scientists, or scientists in related fields interested in polymer and biopolymer science, at universities or in industry, graduate students.

Special offer:
For all clients with a standing order we offer the electronic form of Advances in Polymer Science free of charge.

More information about this series at http://www.springer.com/series/12

Klaus Müllen • Xinliang Feng
Editors

From Polyphenylenes to Nanographenes and Graphene Nanoribbons

With contributions by

K. Amsharov · R. Berger · S. Chen · L. Chi · X. Feng ·
F.R. Fischer · L. Grill · S. Hecht · A. Hu · M. Koch · J. Liu ·
K. Müllen · H. Wang · Y. Wang · H. Zhang

Springer

Editors
Klaus Müllen
Max Planck Institute for Polymer Research
Mainz, Germany

Xinliang Feng
Center for Advancing Electronics Dresden (cfaed) & Department of Chemistry and Food Chemistry
Technische Universitaet Dresden
Dresden, Germany

ISSN 0065-3195 ISSN 1436-5030 (electronic)
Advances in Polymer Science
ISBN 978-3-319-64169-0 ISBN 978-3-319-64170-6 (eBook)
DOI 10.1007/978-3-319-64170-6

Library of Congress Control Number: 2017948408

© Springer International Publishing AG 2017
This work is subject to copyright. All rights are reserved by the Publisher, whether the whole or part of the material is concerned, specifically the rights of translation, reprinting, reuse of illustrations, recitation, broadcasting, reproduction on microfilms or in any other physical way, and transmission or information storage and retrieval, electronic adaptation, computer software, or by similar or dissimilar methodology now known or hereafter developed.
The use of general descriptive names, registered names, trademarks, service marks, etc. in this publication does not imply, even in the absence of a specific statement, that such names are exempt from the relevant protective laws and regulations and therefore free for general use.
The publisher, the authors and the editors are safe to assume that the advice and information in this book are believed to be true and accurate at the date of publication. Neither the publisher nor the authors or the editors give a warranty, express or implied, with respect to the material contained herein or for any errors or omissions that may have been made. The publisher remains neutral with regard to jurisdictional claims in published maps and institutional affiliations.

Printed on acid-free paper

This Springer imprint is published by Springer Nature
The registered company is Springer International Publishing AG
The registered company address is: Gewerbestrasse 11, 6330 Cham, Switzerland

Preface

Polyphenylenes have been a key object of chemical synthesis, partly because of their role as a prototype of linear conjugated polymers. There have, however, always been highly substituted polyphenylenes (e.g., with additional phenyl groups), which have been looked at as "carbon-rich" polymers. In addition, polyphenylenes have been extended to ladder polymers with or without conjugated bridging groups. Polyphenylenes have more recently served as essential precursors for synthesis of graphene nanoribbons (GNRs), either in solution or on a surface. That opens an entry to a whole new family of conjugated polymers, which allow one to combine high charge carrier mobility with processibility and appropriate on/off behavior in field effect transistors. Accordingly, one key question is how GNRs can be tackled as a challenge of polymer synthesis. Large polycyclic aromatic hydrocarbons (PAHs), which are also classified as nanographenes (NGs), can be regarded as finite graphene "cut-outs" composed of all sp^2 carbons. NGs are one of the classical structure types of organic chemistry, which have had an enormous impact on the development of molecular orbital theory and spectroscopy. NGs can be accessed via the so-called planarization and graphitization of dendritic polyphenylenes or oligophenylenes and related methods. Making NGs larger and larger provides an entry into bottom-up synthesis of graphenes. There, again, arises the interesting question of whether such molecules can be made by a controlled bottom-up approach.

This volume, "From Polyphenylenes to Nanographenes and Graphene Nanoribbons," covers the state-of-the-art knowledge about synthesis and chemical reactions of molecularly defined graphene nanostructures (NGs and GNRs) with high structural precision. The first chapter is devoted to recent advancements in synthesis and characterization of zigzag-edged NGs and GNRs. Compared with armchair-edged NGs and GNRs, graphene nanostructures with zigzag edge peripheries display unique electronic, magnetic, and photophysical properties resulting from the spin-polarized state at the zigzag edges. In the past decade, fabrication of covalently bonded molecular/polymer structures on metal surfaces has attracted increased attention because such powerful synthetic strategies provide direct access to novel materials with potential applications in nanoelectronics. In contrast to traditional solution-based synthetic protocols, surface-assisted reactions have advantages in structural control of the produced NGs, GNRs, and other 1D or 2D covalently bonded nanostructures. Moreover, an understanding of reaction mechanisms after surface immobilization can be achieved at the atomic or molecular level. Along these lines, the chapters "Bottom-Up Synthesis of Graphene Nanoribbons on Surfaces," "Surface-Assisted Reaction Under Ultrahigh Vacuum Conditions," and "On-Surface Polymerization: From Polyarylenes to Graphene Nanoribbons and Two-Dimensional Networks" are dedicated to bottom-up on-surface synthesis of carbon-rich materials, ranging from small molecules to 1D polymer chains, as well as 2D sheets and networks. Compared with planar π-conjugated carbon skeletons, which have been synthesized on metal surfaces, the surface-assisted strategy has proven to also be prolific for synthesis of nonplanar sp^2-based carbon nanostructures. Therefore, in the chapter "Rational Synthesis of Fullerenes, Buckybowls, and Single-Walled Carbon Nanotubes by a Surface-Assisted Approach," the possibility of fabricating carbon nanostructures, such as higher fullerenes and single-walled carbon nanotubes, in a fully controllable manner, by surface-mediated synthesis, is demonstrated. Besides synthesis of atomically precise graphene-based nanostructures, other approaches to synthetic carbon nanostructures and their applications in nanodevices are discussed in the chapter "Chemical Synthesis of Carbon Nanomaterials Through Bergman Cyclization." Therein, novel synthetic strategies toward structurally unique carbon-rich materials by Bergman cyclization are described, which include formation of nanoparticles by intramolecular collapse of single polymer chains, fabrication of conjugated microporous polymers, and construction of carbon nanomembranes. This special volume, "From Polyphenylenes to Nanographenes and Graphene Nanoribbons," would not have been possible without the excellent contributions of many scientists. We want to express our sincere gratitude to them for sharing their scientific points of view on different aspects of polyphenylene and graphene chemistry.

We hope this volume will contribute to further development not only of synthesis and characterization of NGs and GNRs, but also of their applications, which can help to bridge borders between the different disciplines in the future.

Dresden, Germany — Xinliang Feng
Mainz, Germany — Klaus Müllen

Contents

Adv Polym Sci (2017) 278: 1–32
DOI: 10.1007/12_2017_1

Nanographenes and Graphene Nanoribbons with Zigzag-Edged Structures

Junzhi Liu, Reinhard Berger, Klaus Müllen, and Xinliang Feng

Abstract Compared with armchair-edged nanographenes (NGs) and graphene nanoribbons (GNRs), graphene nanostructures with zigzag edge peripheries display unique electronic, magnetic, and photophysical properties resulting from the spin-polarized state at the zigzag edges. More interestingly, some possess prominent biradical/polyradical character in the ground state. Thanks to the development of chemistry in recent decades, such NGs and GNRs with unique zigzag peripheries are now synthetically accessible. This chapter discusses several strategies for the synthesis of zigzag-edged NGs and GNRs, their structural characterization, physical properties, and potential applications.

Keywords Graphene Nanoribbons • Hetroartoms • Nanographenes • Radicals • Zigzag-Edge

Contents

J. Liu, R. Berger, and X. Feng (✉)
Center for Advancing Electronics Dresden (CFAED), Department of Chemistry and Food Chemistry, Technische Universität Dresden, 01062 Dresden, Germany
e-mail: xinliang.feng@tu-dresden.de

K. Müllen
Max-Planck Institut für Polymerforschung, Ackermannweg 10, 55128 Mainz, Germany
e-mail: muellen@mpip-mainz.mpg.de

1 Introduction

Graphene is a two-dimensional (2D), atomically thick sheet composed of a hexagonal network of sp^2-hybridized carbon atoms. It has been intensively investigated since its first isolation in 2004, when Geim, Novoselov and colleagues reported a micromechanical cleavage method for the exfoliation of graphite, based on repeated peeling of highly oriented pyrolyzed graphite [1]. For their pioneering work revealing the exceptional physical properties of graphene, they were awarded the 2010 Nobel Prize in physics. The extraordinary electronic, thermal, and mechanical properties of graphene make it a promising candidate for various future applications [2] in electronics, sensing, catalysis, energy storage and conversion, as well as biological labelling. Nevertheless, the implementation of graphene in electronics still remains challenging [3]. One of the greatest challenges at present is the lack of an efficient way to produce graphene both in large quantities and with high quality. Another difficulty is the lack of a controllable synthetic method for producing graphene with defined size, shape, and edge structures. Graphene is semimetallic in nature with zero band gap [4–7]. However, when graphene is cut into narrow strips, the generated graphene nanoribbons (GNRs) exhibit a band gap, rendering them potentially applicable in electronics [8–12]. Depending on their edge structures, three different types of GNRs can be classified: armchair-edged GNRs (AGNRs), zigzag-edged GNRs (ZGNRs), and cove-edged GNRs (CGNRs) (Fig. 1).

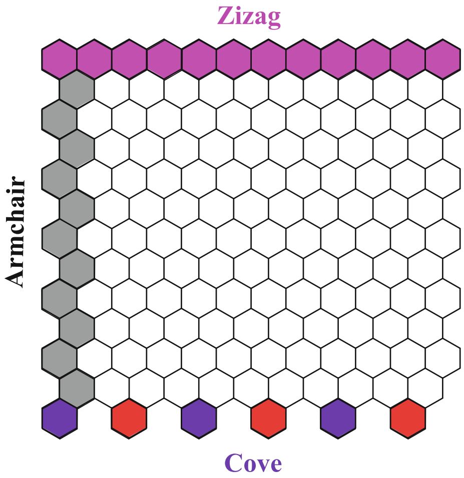

Fig. 1 Edge structures of graphene

GNRs have been of theoretical interest for many decades, particularly regarding prediction of their intriguing physical properties. In the last decade, great efforts have been made to fabricate high quality GNRs with narrow widths and smooth edges. Two main strategies have been established for preparation of GNRs, namely “top-down” and “bottom-up” approaches. Top-down approaches [13–16], such as the cutting of graphene, sonochemical extraction from expanded graphite, and unzipping of carbon nanotubes, have produced GNRs with widths of less than 10 nm, revealing their semiconducting nature and excellent charge transport properties. However, these top-down methods generally suffer from low yields and nonuniform widths, as well as ill-defined edge structures, which essentially sacrifice their electronic properties. Thereby, it is highly desirable to produce GNRs with precise structures and controllable widths. To this end, bottom-up chemical synthesis provides a marvelous strategy for preparation of structurally well-defined GNRs [17–21]. Synthesis is typically based on solution-mediated or surface-assisted cyclodehydrogenation and “planarization” of three-dimensional (3D) polyphenylene precursors. The polyphenylene precursors are designed and synthesized from small organic monomers, providing access to GNRs of different widths and edge structures. Compared with AGNRs, theoretical studies predict that ZGNRs can exhibit amazing physical properties; however, so far these properties have been barely observed experimentally [22]. In order to explore the fundamental electronic and magnetic properties related to zigzag edges and to realize specific graphene nanostructures with properties such as spin confinement or spin filtering, fabrication of ZGNRs with atomically precise edge structures is urgently needed.

Large polycyclic aromatic hydrocarbons (PAHs), which are also classified as nanographenes (NGs), can be regarded as finite graphene segments composed of only sp^2 carbons. NGs have attracted enormous interest because of their intriguing electronic and optoelectronic properties as well as for their possible application in organic electronics [23]. Bottom-up organic synthesis has been developed, which could serve as an indispensable tool for creating structurally defined NGs [24]. Fundamental contributions to the bottom-up synthesis and characterization of NGs were made early in the twentieth century by R. Scholl and E. Clar, who achieved the synthesis of numerous NGs under drastic conditions, such as at high temperatures and using strong oxidants [25]. A remarkable synthetic breakthrough was achieved with a help of progress in analytical techniques, which made it possible to selectively synthesize various NGs under mild conditions. The systematic study of NGs and their application as materials have stimulated scientists for several decades. Typical synthesis of extended NGs is based on intramolecular cyclodehydrogenation (planarization of 3D dendritic or hyperbranched polyphenylene precursors) [26]. By employing this synthetic strategy, various kinds of large NGs with different molecular sizes, shapes, symmetries, and edge peripheries have been successfully obtained. Among them, hexa-*peri*-hexabenzocoronene (HBC) [27], with 42 sp^2 carbons, is one of the most extensively studied NGs.

At first sight, one may think that NGs constitute a single class of very similar molecules, all built up solely of sp^2 carbons. However, the optical properties, chemical activity, and aromaticity of the NGs are totally different depending on their size, shape, edge structure, and periphery substitutions [28]. Certainly, electronic properties such as the corresponding energy gaps of NGs are very important for potential applications [29] (e.g., as organic semiconductors or in graphene electronics). Similar to the classification of graphene, three different classes of NGs can be defined according to their edge structures: armchair-edged nanographenes (A-NGs), cove-edged nanographenes (C-NGs), and zigzag-edged nanographenes (Z-NGs) [30]. NGs with only zigzag edges can be seen as cut out of graphene with a zigzag motif, or series of benzene rings fused in a triangular manner [31]. Because of the special shape and edge structure, this type of NG is usually claimed to have a non-Kekulé or open-shell structure, which inevitably results in one or more unpaired electrons within the molecule. Thus, Z-NGs offer promising potential in electronics and for spintronic devices [32]. However, synthesis of NGs with only zigzag edges is highly challenging because the intrinsic properties of such open-shell systems, such as low stability or high chemical reactivity, obstructs their synthesis, isolation, and application. Generally, the decomposition of these systems under ambient condition is ascribed to the side reactions of generated radical species, including dimerization, hydrogen abstraction, and oxidation [33]. Thanks to a deeper understanding of the decomposition mechanism and the development of modern organic chemistry, many strategies have been conceived for stabilization of these systems under ambient conditions, such as protection with steric bulky groups, employment of heteroatoms doped in the aromatic frameworks, or fusion with other aromatic skeletons.

This chapter summarizes recent progress in the study of NGs and GNRs with zigzag edge peripheries by addressing the relationship between their structure and optoelectronic properties. The chapter consists of five sections that discuss (1) HBC-derived NGs with rich zigzag-edge structures, (2) *peri*-acene-derived NGs, (3) phenalenyl-derived NGs, (4) doped NGs possessing zigzag-edge structures, and (5) GNRs with zigzag-edge structures. The discussion covers their synthetic strategies, structural characterization, physical properties, and potential material applications.

2 HBC-Derived NGs with Rich Zigzag-Edge Structures

Compared with fully benzenoid A-NGs, Z-NGs are annulated with another ring in a bay region, where the two added π-electrons cannot be included in a sextet. For instance, if fully benzenoid HBC **1** (Fig. 2) is annulated with one, two, or three additional benzene rings at the bay regions, HBCs with partial zigzag-edge or “reactive” double bonds can be obtained, providing mono-zigzag HBC **2** [34], bis-zigzag HBC **3** [35], and tri-zigzag HBC **4** [36] (Fig. 2), respectively. The integration of zigzag edges on HBC dramatically influences not only its electronic and optoelectronic properties but also its chemical reactivity and potential two- and three-dimensional self-assembly behavior.

Synthetic routes for obtaining mono-zigzag HBC **2**, bis-zigzag HBC **3**, and tri-zigzag HBC **4** are described in Fig. 3. The Diels–Alder conversion of compound

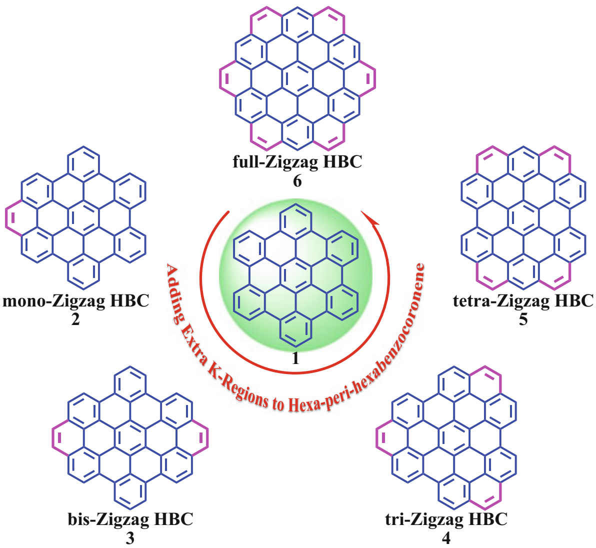

Fig. 2 Various NGs with zigzag-edged structures based on HBC core

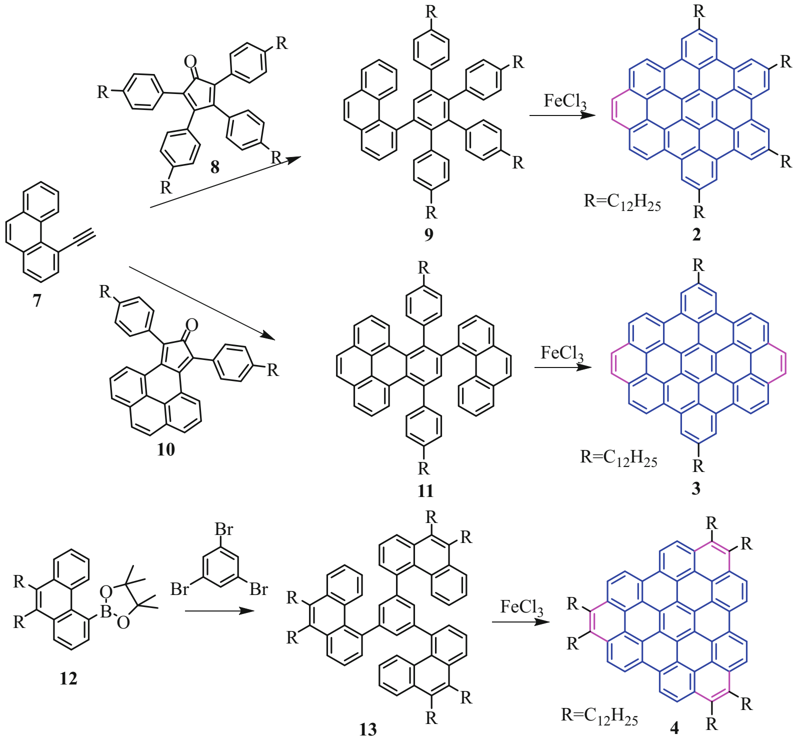

Fig. 3 Synthetic routes toward mono-zigzag HBC **2**, bis-zigzag HBC **3**, and tri-zigzag HBC **4**

7 with **8** and **10** affords the polyphenylene precursors **9** and **11**, respectively. The Suzuki cross-coupling reaction with pinacol boronic ester **12** and 1,3,5-tribromobenzene requires a strong base to yield the sterically crowded precursor molecule **13**. Finally, precursors **9**, **11**, and **13** are oxidatively planarized with iron (III) chloride to afford the mono-zigzag HBC **2**, bis-zigzag HBC **3**, and tri-zigzag HBC **4** in good yields. The structural differences between these three molecules have a strong effect on the absorption spectra. The α-bands and β-bands follow a linear trend with the number of carbon atoms in the zigzag edges. The α-bands of **2** are at 484 nm and those of **4** at 530 nm. The β-bands go from 380 nm for **2** to 400 nm for **4**. The p-bands, however, show a different trend. Bis-zigzag HBC **3** shows p-bands at longer wavelengths (473 nm) than **4** (425 nm) as a result of the differing symmetries. Tri-zigzag HBC **4** shows a D_{3h} symmetry and, as a consequence, the highest occupied molecular orbit (HOMO)/HOMO-1 and the lowest occupied molecular orbit (LUMO)/LUMO-1 are degenerate, leading to a transition at shorter wavelengths. The symmetry also exerts an influence on the fine structure of the absorption spectrum. The higher the symmetry, the more symmetry-forbidden transitions exist, leading to a high degree of fine structure. Lower symmetry, as for mono-zigzag HBC **2** and bis-zigzag HBC **3** (D_{2h}), broadens the peaks in the absorption spectrum. The intensity of the α-bands in this series also depends on the symmetry: the higher the symmetry, the lower the intensity.

Very recently, the synthesis of a new stable non-fully benzenoid HBC derivative with four additional K-regions (A K-region is defined to be an exposed outer corner on a phenanthrene segment in the molecule [37]), namely tetra-zigzag HBC **5** was achieved [38]. The synthesis was based on a key precursor **16** with two pre-fused benzotetraphene units (Fig. 4), which could be prepared through fourfold cycloaromatization of **15**, forming the zigzag edges prior to planarization. To

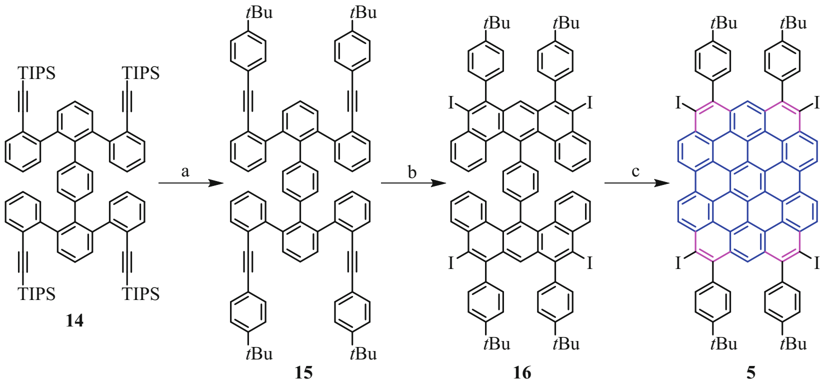

Fig. 4 Synthetic route toward tetra-zigzag HBC **5**: (a) (1) TBAF, DCM, r.t., 2 h, (2) 1-*tert*-butyl-4-iodobenzene, piperidine, CuI, Pd(PPh$_3$)$_4$, 60°C, 4 h; (b) bis(pyridine)iodonium-tetrafluoroborate, TFMSA, DCM, −40°C, 6 h; (c) DDQ, TFMSA, DCM, r.t., 16 h. *TBAF* tetrabutylammoium fluoride, *DCM* dichloromethane, *TFMSA* trifluoromethanesulfonic acid, *DDQ* 2,3-dichloro-5,6-dicyano-*p*-benzoquinone, *r.t.* room temperature

stabilize the zigzag edges of **5**, additional phenyl rings were introduced. UV/vis absorption analysis of **5** demonstrated a significant red shift of the maximum absorption peak and lowering of the HOMO–LUMO gap compared with HBC (**1**) and its derivatives with one (**2**) or three (**4**) K-regions. The UV/vis absorption of **5** disclosed three optically allowed vertical transitions with large oscillator strengths at 562 nm (*p*-band), 421 nm (β-band), and 394 nm (β'-band). Here, *p*-, β-, and β'-bands are based on Clar's notation and mainly correspond to HOMO → LUMO, HOMO → LUMO+1, and HOMO−1 → LUMO+1 transitions, respectively. Compared with the parent HBC (**1**) and the D_{2h} symmetrical bis-zigzag HBC (**3**), the *p*-band of **5** is red-shifted by 128 nm and 64 nm, respectively, which is in line with the trend observed for the HOMO–LUMO gaps.

3 *Peri*-Acene-Derived NGs

Another group of Z-NGs, built up by *peri*-annulation of naphthalene, is the rylene series. In naphthalene, one ring can be formed as an electron Clar sextet, and the other ring remains with four π-electrons. The partial olefinic character of the π-electrons leads to increased reactivity, especially for Diels–Alder reactions at the bay position of higher rylenes [39], and lower optical energy gap than for fully benzenoid NGs. For example, perylene (**17**) shows absorption wavelengths up to 440 nm [40], having only two more π-electrons than triphenylene, which does not absorb at wavelengths longer than 300 nm [41–44]. Bisanthene (**18**), which can also be viewed as laterally expanded perylene (Fig. 5), has been known for many years [45–48]. More interestingly, compared with the A-NGs, some of Z-NGs possess a prominent biradical character in the ground state. Recently, larger NGs with zigzag peripheries (e.g., teranthene (**19**) [49] and quateranthene (**20**) [50]) have been obtained by extending the bisanthene structure along the longitudinal direction (Fig. 5).

For bisanthene (**18**), the destabilization energy of the π-bond cleavage is not compensated by the formation of additional Clar sextets. Thus, the Kekulé form has a dominant contribution to the ground state in **18** (Fig. 5) [51]. For larger anthenes, such as teranthene (**19**) and quateranthene (**20**), the difference in the number of Clar sextets between the biradical and the Kekulé forms increases with increasing molecular size, that is, three for teranthene and four for quateranthene (**19–1** and **20–1**, respectively). More Clar sextets in the biradical forms result in the gain of more aromatic stabilization energy and thus more dominant contribution of the biradical form to the ground state (Fig. 5) [52].

Figure 6 presents three synthetic routes for preparation of derivatives of teranthene (**19**) and quateranthene (**20**). The key steps for the preparations are partial cyclization with KOH/quinoline and full cyclization mediated with 2,3-dichloro-5,6-dicyano-*p*-benzoquinone (DDQ)/Sc(OTf)$_3$. Compound **19** was obtained as dark green plates by recrystallization from a CH_2Cl_2/hexane solution under argon flow. A toluene solution of **19** showed gradual decomposition with a half-life period of 3 days at room temperature when exposed to air under sunlight.

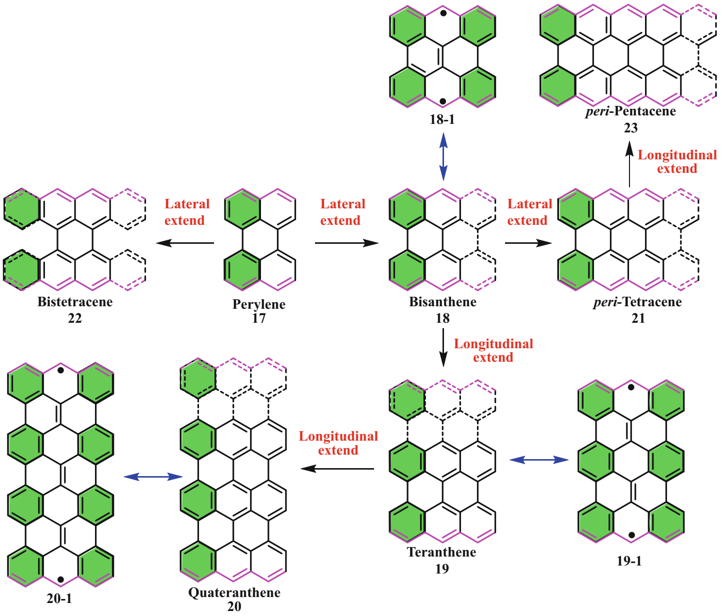

Fig. 5 Chemical structure of *peri*-acene obtained by extending the perylene along the lateral and longitudinal direction

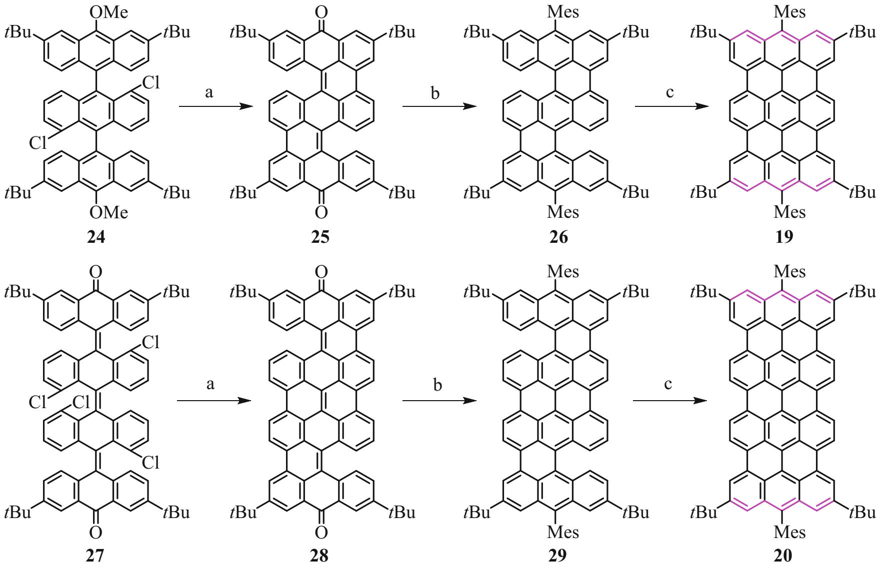

Fig. 6 Synthetic routes toward teranthene **19** and quateranthene **20**: (a) KOH, quinolone, 190°C; (b) (1) ArMgBr, $CeCl_3$,THF, (2) $SnCl_2$, AcOH; (c) DDQ, $Sc(OTf)_3$, toluene, reflux

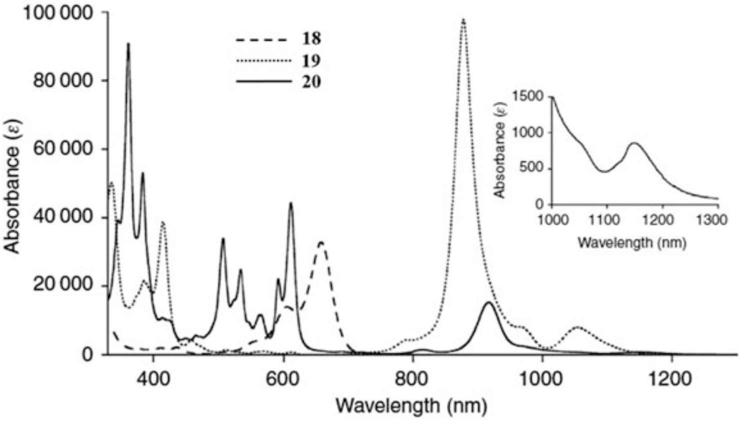

Fig. 7 UV/vis absorption spectra of **18** (*hashed line*), **19** (*dotted line*), and **20** (*solid line*). The *inset* indicates the weak band of **20** [51]

The half-life of **20** under such conditions was only 15 h. The edge-localized electrons of **19** and **20** also give rise to their unique optical properties. One signature of the biradicaloid character is the presence of a low-lying excited singlet state dominated by the doubly excited configuration [53]. Both compounds show a weak low-energy band, centered at 1,054 nm (**19**) and 1,147 nm (**20**), respectively (Fig. 7). Compared with bisanthene (**18**), however, antiferromagnetic NGs **19** and **20** give totally different band shapes and feature very weak low-energy bands, where the low-energy band absorption indicates a small HOMO–LUMO gap. Based on theoretical (NEVPT2) calculations, the weak band of **20** at around 1,150 nm is associated with simultaneous excitation of the two edge-localized electrons.

However, attempts to synthesize the next generation of *peri*-fused acenes, such as *peri*-tetracene, by expanding the bisanthene along the lateral direction have not been successful so far, most probably because of the extremely high reactivity as well as the lack of proper synthetic protocols [48, 54–56]. Theoretical calculations predict that the energy gap drastically decreases upon increasing the length of *peri*-fused acenes [57, 58]. Recently, a novel tetrabenzo[*a*,*f*,*j*,*o*]perylene (**22**) [59], "bistetracene," in which two tetracenes are connected side by side with two bonds, was synthesized and characterized (Fig. 8). The key intermediate compound **30** was prepared in eight steps and was subjected to Grignard treatment followed by ring fusion and oxidative dehydrogenation to afford **22** as a green powder. An optical energy gap of about 1.56 eV was derived from the UV/vis absorption spectrum, showing the low optical gap feature of Z-NGs. Interestingly, such NGs possess a prominent biradical character in the ground state. The biradical contribution to the ground state arises from the five Clar sextets in open-shell form, compared with the two Clar sextets in closed-shell form (Fig. 9a). By calculation, **22** has a moderate singlet biradical character index ($y = 0.615$), and a large singlet–triplet energy gap of -6.7 kcal mol^{-1} is derived. Furthermore, the biradical

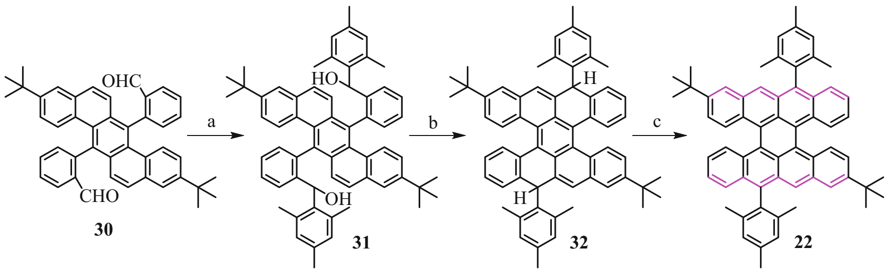

Fig. 8 Synthetic route toward bistetracene **22**: (a) mesitylmagnesium bromide, THF, r.t, 2 h; (b) $BF_3 \cdot OEt_2$, DCM, r.t, 30 min; (c) *p*-chloranil, toluene, r.t, 12 h

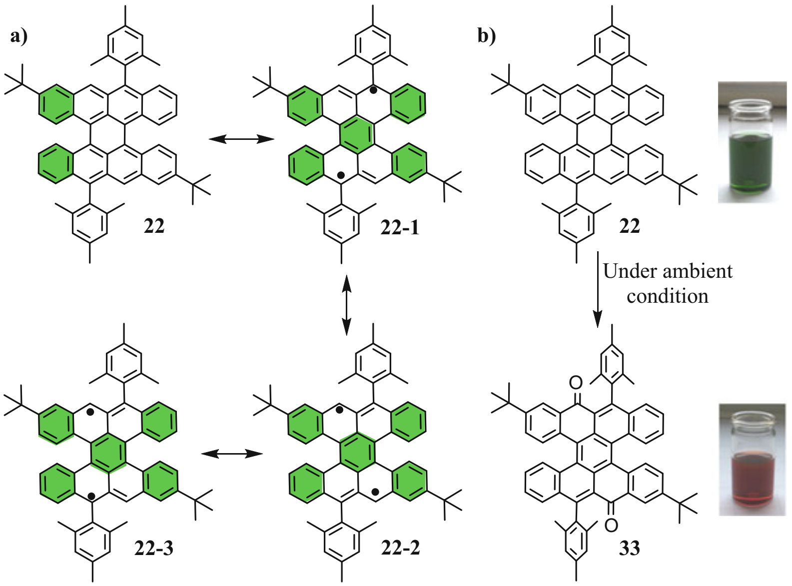

Fig. 9 (**a**) Resonance structures of **22**. (**b**) Oxidation of compound **22** to compound **33**

structure of **22** can be described by the presence of three resonance forms, namely **22–1**, **22–2**, and **22–3** (Fig. 9a). In **22–1**, the two radical centers are protected by bulky mesityl groups but these two sites are unprotected in **22–2**. Thus, compound **22** was found to be unstable under ambient conditions. Time-dependent electron paramagnetic resonance (EPR) measurement in toluene solution at room temperature indicated that the peak intensity decreased with time, and that the signal almost disappeared after 72 h. Notably, the color of **22** changed quickly when exposed to air (Fig. 9b), suggesting that the oxidation took place at the zigzag edge of **22** as the reactive site. Time-dependent UV/vis spectra indicated that when the intensity of the absorption maximum in the NIR region (727 nm) decreased, the absorption peak at high energy (295 nm) increased with time as a result of the oxidation

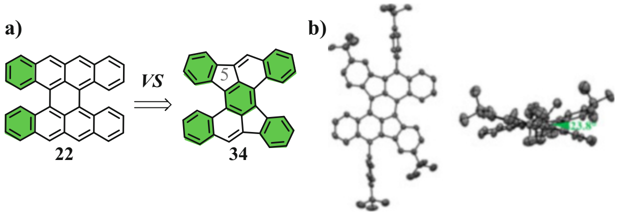

Fig. 10 (**a**) Chemical structures of bistatracene and its analogues with embedded five-membered rings. (**b**) Crystal structure of **34** (*top* and *side views* of enantiomer pair)

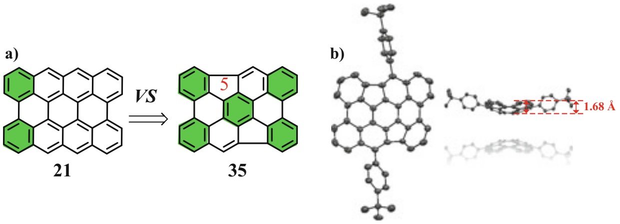

Fig. 11 (**a**) Chemical structures of *peri*-tetracene and its analogues with embedded five-membered rings. (**b**) Crystal structure of **35** (*top* and *side views*)

process. Finally, a red color was obtained for the oxidized product, which was identified as tetrabenzo[*a*,*f*,*j*,*o*]perylene-9,19-dione (**33**) (Fig. 9b).

To circumvent the stability issue in bistetracene, one strategy is the exploration of NGs containing five-membered rings in acene-like structures, rather than traditional acenes solely consisting of six-membered rings [60, 61]. Inspired by this strategy, a bistetracene analogue (**34**) containing two five-membered rings, namely dibenzo[*a*,*m*]rubicene (Fig. 10a) [62], was synthesized recently. Compound **34** displayed excellent stability, enabling full structural characterization; for example, reddish-brown prism-shaped crystals of **34** were obtained that were suitable for single-crystal X-ray analysis (Fig. 10b). Notably, internal C–H steric repulsions cause the nonplanarity of the skeleton of **34**, with a mean torsional angle of 23.8°. Furthermore, it was found that silylethynylated derivatives of **34** functioned as *p*-type organic semiconductors in solution-processed organic field effect transistors, with mobility of up to 1.0 $\mathrm{cm}^2\ \mathrm{V}^{-1}\ \mathrm{s}^{-1}$ [63]. These results suggest that the incorporation of five-membered rings in *peri*-acene analogues is a promising way to develop novel materials by avoiding the instability issue.

Very recently, *peri*-tetracene analogue **35** [64] with two embedded five-membered rings was prepared by the palladium-catalyzed intramolecular cyclization of pre-fused dibenzo[*a*,*m*]rubicene **34** (Fig. 11a). Importantly, there are five aromatic sextets in **35** in the ground state, whereas *peri*-tetracene **21** has only two (Fig. 11a). According to Clar's sextet rule, the compound with more aromatic sextets is more stable as a result of gaining aromatic stabilization energies, which suggests that the pentagon-embedding *peri*-tetracene **35** has enhanced stability with respect to the *peri*-tetracene **21**. On the other hand, compound **35** represents a

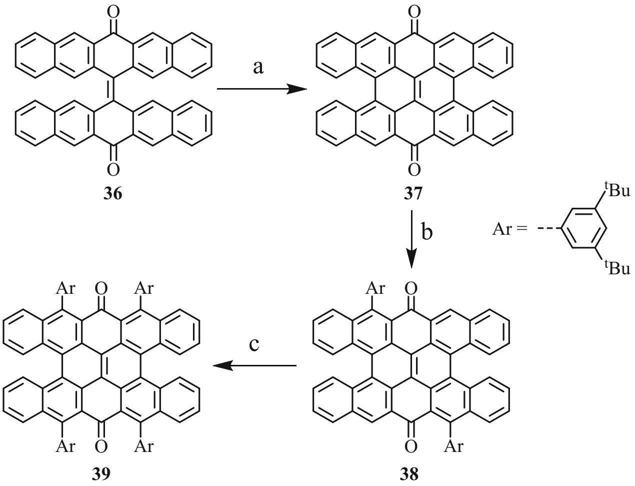

Fig. 12 Synthetic route toward bispentacenequinone **40**: (a) (1) I_2, benzene, *hv*, propylene oxide; (b) (1) Ar-MgBr, (2) H_3O^+, (3) air; (c) (1) Ar-MgBr, (2) H_3O^+, (3) air

subunit for C_{70} and other higher fullerenes. The crystal structure of **35** unambiguously discloses a bowl-shaped π-conjugated carbon skeleton (Fig. 11b). Notably, a bowl-to-bowl inversion for compound **35** in solution was investigated by dynamic NMR analysis, showing a bowl-to-bowl inversion energy ($\Delta G^{\ddagger}$) of 16.7 kcal mol^{-1}, which was further corroborated by density functional theory (DFT) calculations.

Scientists did not give up pursuit of even higher *peri*-fused acenes, although their synthesis remains a great challenge because of the extremely high reactivity of such molecules. To date, there have been two synthetic approaches proposed for production of *peri*-pentacene (**25**) in solution; however, both were unsuccessful. One work was attempted in 2010 (Fig. 12) [65] and first involved the oxidative photocyclization of **36** to obtain partially fused bis-pentacenequinone **37**. However, the subsequent nucleophilic reaction did not generate the desired 1,2-addition adduct. Instead, an unexpected 1,4-Michael addition product **38** was obtained when compound **37** was treated with excess Grignard reagent of 1-bromo-3,5-di-*tert*-butylbenzene in anhydrous THF followed by acidification in air. Further treatment of **38** with excess Grignard reagent followed by acidification in air gave the tetraaryl-substituted fused bispentacenequinone **39**.

Another synthetic approach was proposed in 2013 (Fig. 13) [66]. Starting with chlorination of 4,5,9,10-tetrakis[4-(*tert*-butyl)phenyl]pyrene (**40**) with sulfuryl chloride at room temperature gave **41**. Fourfold substitution of chlorine with copper(I) cyanide at elevated temperature in *N*-methyl-2-pyrrolidon (NMP) gave **43**. The cyclization of tetracyano pyrene derivative **43** afforded the tetraketone **44**, which unfortunately did not undergo further photocyclization. Adopting an alternative path of oxidative cyclodehydrogenation of **43** in the presence of phenyliodine bis(trifluoroacetate (PIFA)/$BF_3.Et_2O$ afforded **45**. Subsequent acid-

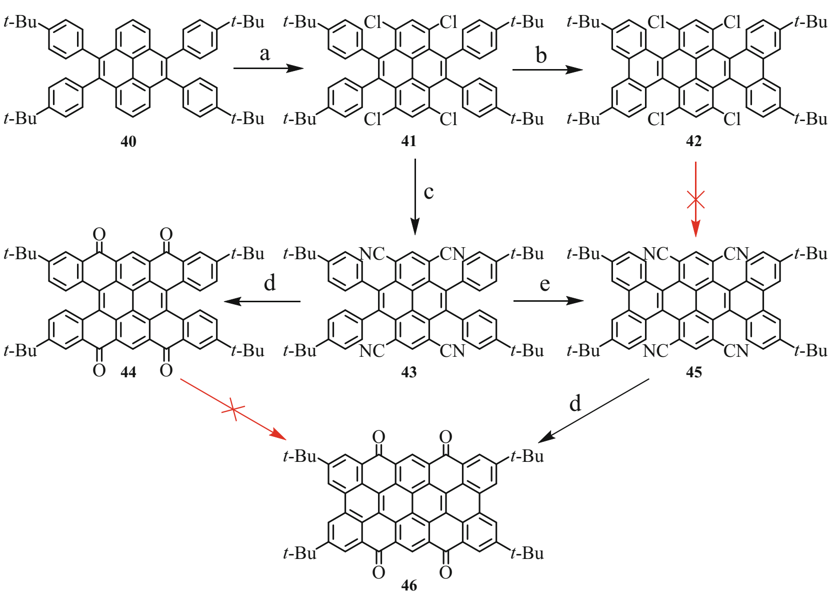

Fig. 13 Synthetic route toward *peri*-pentacenetetraketone **46**: (a) SO_2Cl_2, $CHCl_3$, r.t.; (b) $FeCl_3$ in $MeNO_2$, CH_2Cl_2, 50 min; (c) CuCN, NMP, 180°C, 3 days; (d) H_2SO_4 (60% v/v), 160°C, 65% for **44**, traces for **46**; (e) PIFA/$BF_3.Et_2O$, CH_2Cl_2, −60°C to r.t., overnight

promoted acylation provided the peripentacenetetraketone **46** in trace amounts with very poor solubility and no further reactions were conducted.

Very recently, the desired *peri*-pentacene (**25**) was obtained under ultrahigh-vacuum (UHV) conditions on an Au(111) surface by thermally induced cyclodehydrogenation of the precursor 6,6′-bipentacene (**47**) (Fig. 14) [67]. Scanning tunneling microscope (STM) imaging revealed that as-deposited **47** assembled into islands of highly ordered linear chains on the Au surface (Fig. 14b). The fully cyclized *peri*-pentacene (**25**) was produced by annealing **47** at 200°C for 30 min. STM images of **25** revealed a submonolayer coverage of the surface with uniform discrete rectangular structures (Fig. 14c). The structure of cyclized product **25** was unambiguously proved using subnanometer-resolved noncontact atomic force microscopy (nc-AFM) employing a CO-functionalized tip (Fig. 14e). Unlike the diffuse STM topographic image (Fig. 14d), which reflects frontier orbital local density of states, the nc-AFM image (Fig. 14e) demonstrated not only the exact position of carbon atoms but also the intramolecular bonds forming the aromatic carbon skeleton of **25**. The interaction of *peri*-pentacene with the free valences of the Au surface stabilizes this highly reactive molecule and prevents undesired radical side reactions.

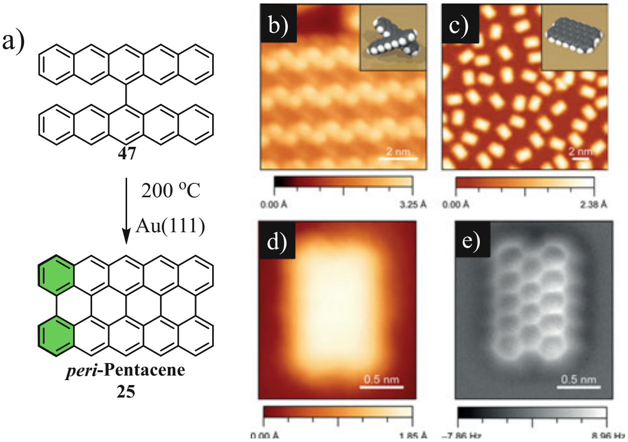

Fig. 14 (**a**) Synthetic route toward *peri*-pentacene (**25**) on an Au(111) surface. (**b**) STM image of **47** as deposited on Au(111). (**c**) STM image of **25** on Au(111) after annealing at 473 K. Molecular models are shown in *insets*. (**d**) STM images of a single *peri*-pentacene **25** on Au(111). (**e**) nc-AFM image of **25**

4 Phenalenyl-Derived NGs

Phenalenyl **48** [31, 68] is a representative of full Z-NGs and has long attracted the attention of experimental and theoretical organic chemists because of its delocalized spin structure (Fig. 15). The first studies of **48** in the 1950s found that it was reactive and could only survive in solution [69, 70]. Later, by introducing three bulky *tert*-butyl groups, the phenalenyl radical could be sufficiently stabilized to allow its isolation and characterization in the crystalline state [71, 72]. Since then, phenalenyl-based radicals have become useful and widely explored building blocks for preparation of biradical molecules [73–75]. For instance, in 2005 a phenyl-bridged biphenalenyl **49** was reported (Fig. 16) [76, 77] that consisted of *p*-quinodimethane and two phenalenyl units. The resonance structure indicated that its spins are delocalized over the whole phenalenyl moieties, as a result of the highly symmetric structure. The resonance form **49–2** leads to the conclusion that the molecule should be a stabilized singlet biradical molecule as a result of gaining the aromatization energy of the central six-membered ring.

Following the above strategy, naphthalene- and anthracene-bridged biphenalenyls **50** and **51** (Fig. 17), were also synthesized through replacement of the central benzene ring [78–80]. Biphenalenyls **50** and **51** showed larger biradical characters (**51** $y = 0.68$; **50** $y = 0.50$; **49** $y = 0.30$), most probably because naphthalene and anthracene have much larger aromatic stabilization energies than benzene. Single-crystal X-ray analysis revealed that **50** and **51** formed one-dimensional (1D) chains in a slipped stacking arrangement with the superimposed phenalenyl moieties overlapping, a structure identical to that of **49** (Fig. 18a). Biphenalenyl **50** packed more tightly in the 1D chain, with a π–π

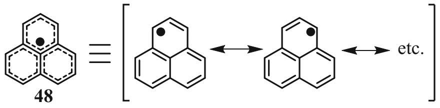

Fig. 15 Phenalenyl radical **48** and its resonance forms

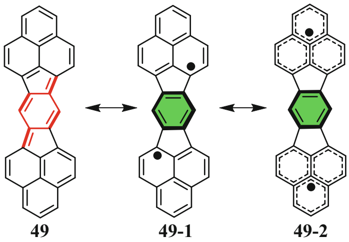

Fig. 16 Resonance forms of **49**

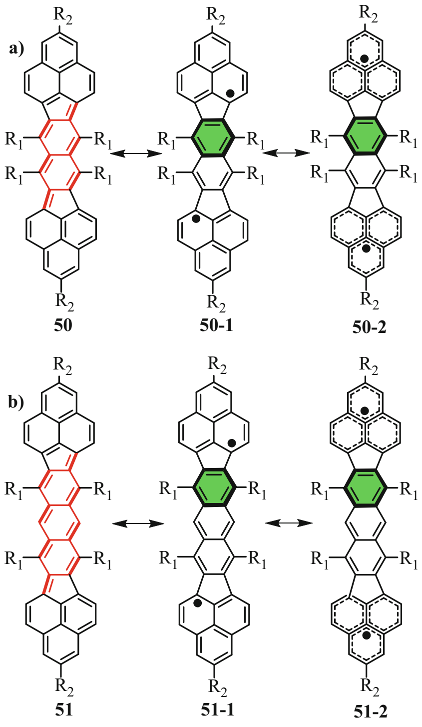

50a: R_1=R_2=H
50b: R_1=Ph, R_2=*tert*-Bu
50c: R_1=Ph, R_2=H

51a: R_1=R_2=H
51b: R_1=Ph, R_2=*tert*-Bu
51c: R_1=Ph, R_2=H

Fig. 17 Resonance forms of (**a**) **50** and (**b**) **51**

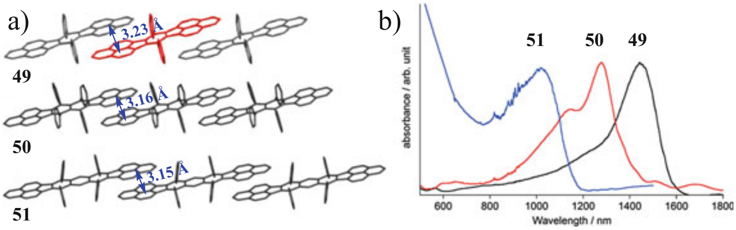

Fig. 18 (**a**) One-dimensional stack of **49**, **50**, and **51** in the crystals. (**b**) The lowest-energy absorption bands of solid **49** (*black line*), **50** (*red line*), and **51** (*blue line*) [81]

distance of 3.16 Å, than benzene-linked **49** (π–π distance of 3.23 Å). The very short π–π contacts suggest prominent noncovalent bonding interactions between the molecules [81]. Thin-film UV/vis absorption of **50** and **51** showed absorption bands in the near-infrared (NIR) region, which were shifted to a lower energy region relative to the solution absorption bands as a result of the coexistence of intra- and intermolecular interactions in the 1D stacks. However, the NIR bands observed in the solid state shifted to a higher energy region with increasing singlet biradical character, such as 1,440 nm for **49**, 1,280 nm for **50**, and 1,025 nm for **51** (Fig. 18b) [81]. This higher energy shift can be explained in terms of the intra- and intermolecular interactions, which become more unbalanced for larger singlet biradical systems [82].

Another outstanding NG with rich zigzag edge structure is zethrene **52**, which can be viewed as a “head-to-head” fusion of two phenalenyl moieties (Fig. 19) [83–86]. One characteristic feature of this molecule is the existence of two distinct resonance structures: a closed-shell quinoidal form and an open-shell biradical form. The biradical contribution to the ground-state electronic configuration is significant. It is predicted that zethrene **52** has interesting physical properties and potential applications as an optical, electronic, and spintronic material [87–90].

When the zethrene is longitudinally extended by introducing benzene or naphthalene between the two phenalenyl units, the higher analogues heptazethrene **53** and octazethrene **54** (Fig. 19), respectively, can be obtained [54, 55, 91, 92]. Efficient synthetic routes toward kinetically stabilized heptazethrene **53** and octazethrene **54** derivatives have been reported (Fig. 20a), starting from the corresponding diketones **56** and **57**, respectively, in which the most reactive sites are protected by triisopropylsilyl-acetylene groups [93]. The biradical character (y) of zethrene **52**, heptazethrene **53**, and octazethrene **54** were calculated to be 0.407, 0.537, and 0.628, respectively [94]. The higher biradical character of heptazethrene **53** and octazethrene **54** can be explained by the larger aromatic stabilization energies through the recovery of aromatic benzene and naphthalene rings, respectively, in their biradical resonance forms (Fig. 19). Interestingly, experimental results showed that heptazethrene **53** featured a closed-shell ground state whereas octazethrene **54** exhibited a singlet biradical ground state. This can be explained by the relatively larger energy gap of heptazethrene **53.** In the UV/vis absorption spectrum, heptazethrene **53** showed a well-resolved absorption peak at 634 nm,

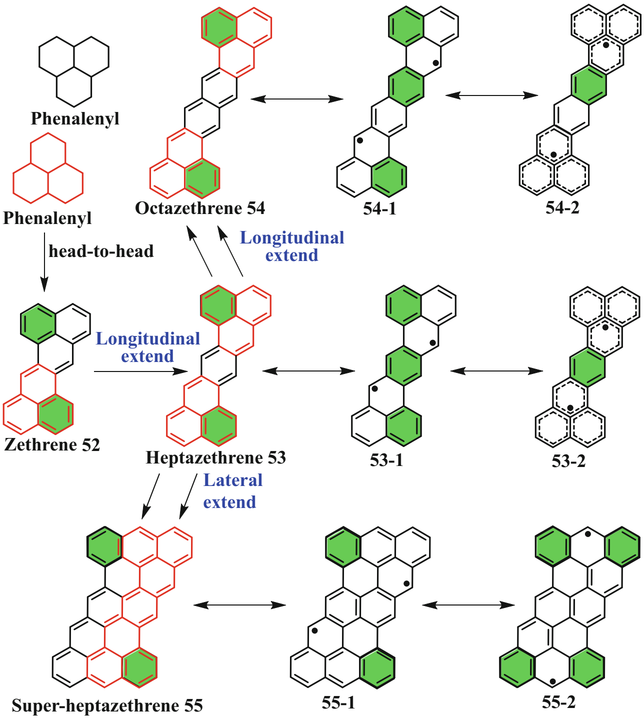

Fig. 19 Chemical structure of zethrene derivatives obtained by extending zethrene along the lateral and longitudinal directions

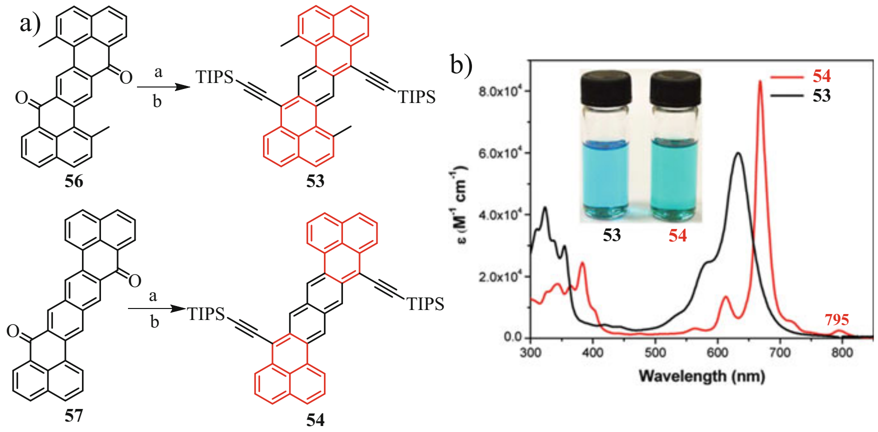

Fig. 20 (**a**) Synthetic routes toward heptazethrene **53** and octazethrene **54**: (*a*) i-Pr$_3$SiC $\equiv$ CMgCl, THF, r.t..; (*b*) SnCl$_2$, r.t.., 2 h. (**b**) UV/vis absorption spectra of **53** and **54**

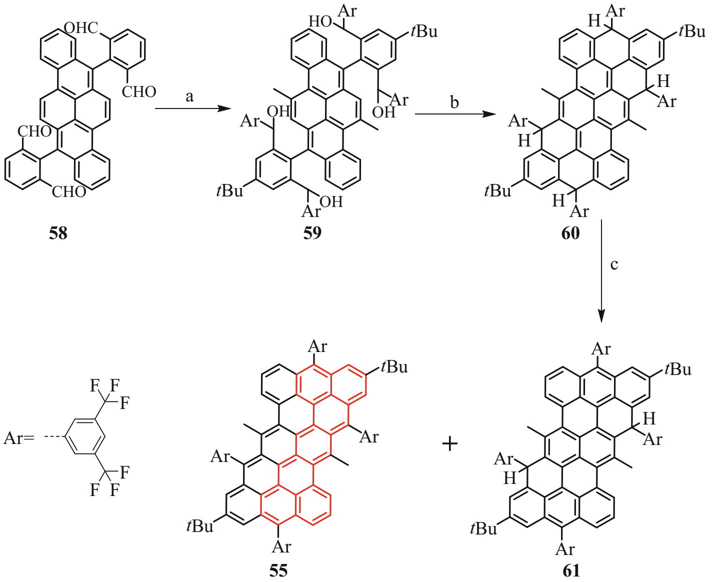

Fig. 21 Synthetic route toward super-heptazethrene **55**: (a) [3,5-bis(trifluoromethyl)phenyl] magnesium bromide, THF, r.t., 24 h; (b) excess $BF_3{\cdot}OEt_2$:TFA = 1:1, DCM, 30 min; (c) *p*-chloranil, DCM

which is typical for many closed-shell NGs (Fig. 20b) [95, 96]. In contrast, the absorption spectrum of octazethrene **54** displayed well-resolved absorption peaks in the NIR region, with maxima at 795, 719, 668, and 613 nm. Moreover, octazethrene **54** exhibited a weak peak at 795 nm that was not observed for heptazethrene **53**, which is a characteristic feature of singlet biradical molecules.

Recently, synthesis of a laterally extended heptazethrene molecule, "super-heptazethrene" (**55**), was reported (Fig. 21) [97]. The key intermediate compound is **58**, which rendered the synthesis of **60** through a fourfold Friedel–Crafts alkylation. Oxidative dehydrogenation of **60** with one equivalent of *p*-chloranil generated primarily the partially dehydrogenated dibenzo-terrylene compound **61**; using five equivalents of *p*-chloranil afforded primarily the target super-heptazethrene derivative **55**. Compound **61** was highly stable, but the solution of **55** was sensitive to air and light (Fig. 22) with a half-life of 4.34 h. Following Clar's sextet rule, compound **55** can gain a maximum of two additional aromatic sextets in the biradical form (**55–2** in Fig. 19). However, there is only one more Clar sextet (**53–1**) in the biradical form of heptazethrene **53** (Fig. 19). Thus, compound **55** was believed to have larger biradical character than **53**. Indeed, in contrast to the heptazethrene **53** ($y_0 = 17\%$), a large biradical character ($y_0 = 71\%$) was calculated for **55**. In the UV/vis absorption spectrum, compound **55** displayed a maximum absorption at 825 nm, together with two weak shoulder bands at 908 nm and 1,038 nm (Fig. 22). The long-wavelength absorption spectrum of **55** is similar to other singlet biradicaloids, such as octazethrene derivatives **54** (Fig. 20b), which

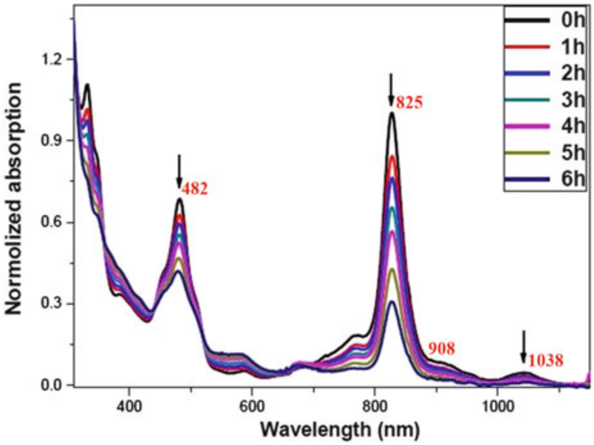

Fig. 22 Absorption spectra of **55** in DCM recorded at different times of exposure to ambient air and light [97]

originates from a low-lying singlet excited state dominated by a doubly excited electronic configuration ($H,H \rightarrow L,L$) [53].

5 Doped Nanographenes with Zigzag-Edge Structures

Doping of carbon materials with heteroatoms such as boron, nitrogen, oxygen, phosphorus, and sulfur has been extensively investigated for tuning the optoelectronic properties of materials [98]. By modifying the topology and heteroatom content of the π-conjugated carbon skeleton, such as in NGs, it is possible to control key features of the electronic structure, including the band gap, absorption spectra, and redox behavior.

The implementation of combinations of heteroatoms such as nitrogen and boron, for example substituting a C=C unit in aromatic molecules with an isoelectronic B–N moiety, could significantly affect the electronic structure while leaving the conjugated skeleton unchanged [99–102]. In addition, the B–N bond could also be considered as a zwitterionic double bond in the neutral state, and the oxidation process of the B–N bond has recently received growing interest [103–105]. Usually, only two carbon atoms are substituted by heteroatoms, but replacement of a full C_3-unit on the zigzag edge with heteroatoms has recently raised interest and allowed the synthesis of stable NGs with extended zigzag-edges. For example, oxygen-boron-oxygen (OBO)-doped *peri*-tetracene (**64**) (Fig. 23), obtained via the cyclodehydrogenation of OBO-doped double [5]helicenes [106, 107], offers the possibility for the construction of novel zigzag-edged NGs, in particular higher *peri*-acenes and ZGNRs.

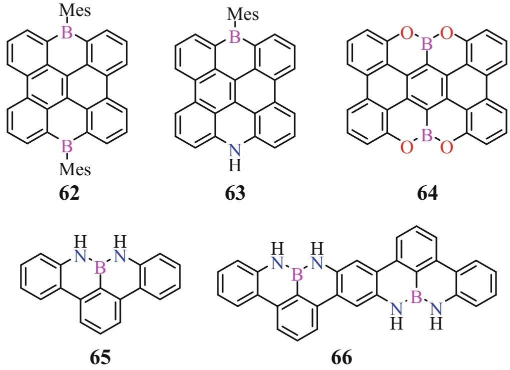

Fig. 23 Chemical structures of zigzag-edged NGs doped with boron (**62**), boron-nitrogen (**63**), boron-oxygen (**64**) and nitrogen-boron-nitrogen (**65**, **66**)

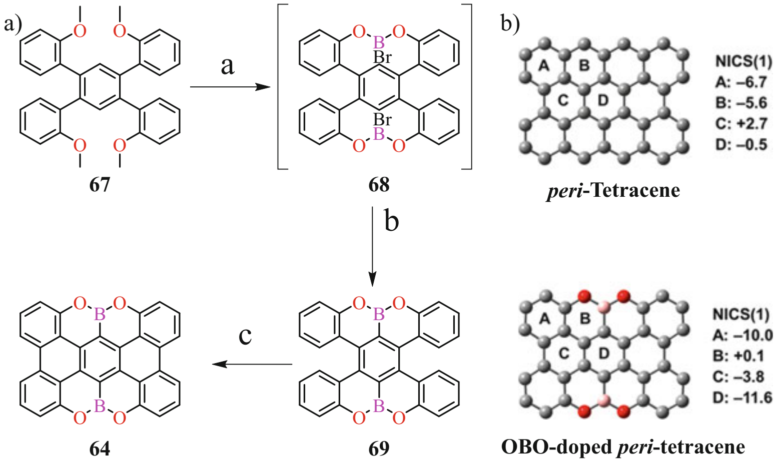

Fig. 24 (**a**) Synthesis of OBO-doped *peri*-tetracene **64**: (*a*) BBr3, ODCB, r.t.; (*b*) r.t. to 150°C, 12 h, 92%; (*c*) DDQ, TfOH, DCM, 0°C to r. t., 94%. (**b**) DFT-calculated NICS(1) values of *peri*-tetracene (*top*) and OBO-doped *peri*-tetracene (*bottom*)

The synthesis of **64** is illustrated in Fig. 24 [107]. Treatment of hexabromobenzene with (2-methoxyphenyl) magnesium bromide in THF provided **67** after quenching the mixture with dilute hydrochloric acid. Simply heating a solution of compound **67** in *o*-dichlorobenzene (ODCB) at 150°C in the presence of BBr_3 gave OBO-doped bistetracene **69** in 92% yield. The reaction presumably involved a demethylation process to form intermediate **68** with four new B–O bonds, followed by electrophilic borylation on the central benzene to establish two extra C–B bonds. The cyclodehydrogenation of **69** in the presence of DDQ/TfOH turned the twisted bistetracene analogue into the planar **64** in excellent yield (94%). This result also proved the good stability of the OBO zigzag-edged

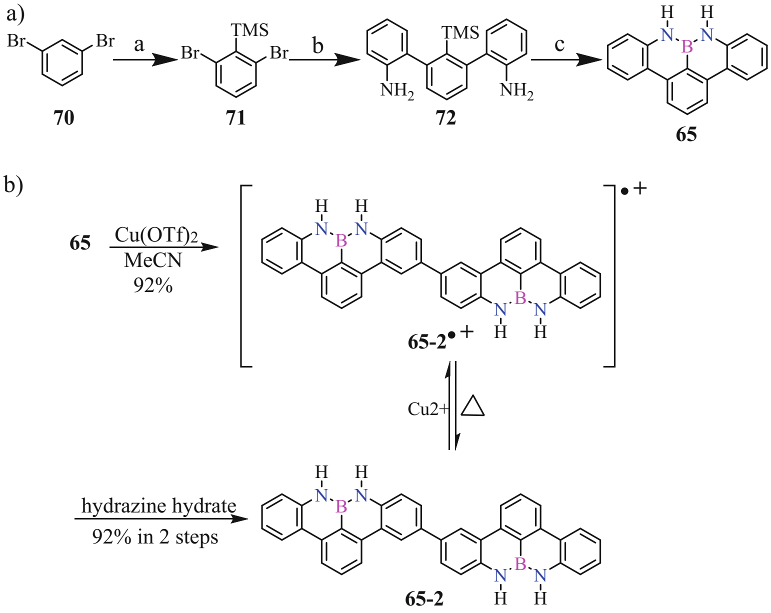

Fig. 25 (**a**) Synthesis of NBN-doped NG **65**: (*a*) LDA, TMSCl, THF, −78°C, 90%; (*b*) $Pd(PPh_3)_4$, $NaHCO_3$, DME, 90°C, 87%; (*c*) BCl_3, Et_3N, *o*-DBC, 180°C, 90%. (**b**) Plausible process for oxidation of **65**

peri-tetracene under acidic and oxidative conditions. Well-resolved vibronic structures were recorded for both the absorption and fluorescence spectra of **69** and **64**, respectively. Moreover, DFT-based nucleus-independent chemical shift (NICS) calculations were performed to compare the aromaticity of pristine *peri*-tetracene and the OBO-doped analogue (Fig. 24b). For instance, the benzene rings C and D in *peri*-tetracene are weakly antiaromatic and nonaromatic, respectively. By contrast, the rings A and D in OBO-doped *peri*-tetracene are both highly aromatic, whereas ring B is nonaromatic and ring C exhibits low aromaticity. These results indicate that the OBO unit cannot be simply viewed as a structural linkage, but has a significant impact on the electronic properties.

In addition to the incorporation of OBO-doped zigzag-edged structure, NGs such as **65** that contain nitrogen-boron-nitrogen (NBN) have also raised substantial interest as a new type of molecular optoelectronic material [108]. In particular, the NBN fragment in **65** can be selectively oxidized to the radical cation, the isoelectronic structure of which is analogous to that of pristine carbon.

The synthesis of compound **65** is based on a three-step protocol, as depicted in Fig. 25a. A trimethylsilyl (TMS) group was introduced as a directing group during facile twofold electrophilic aromatic borylation, which was used to fuse the NBN unit at the perimeter of the NG in high yield. First, 1,3-dibromobenzene (**70**) was selectively lithiated at the 2-position using lithium diisopropylamide (LDA), and the reaction quenched with trimethylsilyl chloride (TMSCl) to provide **71** in 90% yield. In the second step, palladium-catalyzed Suzuki coupling of **71** with the

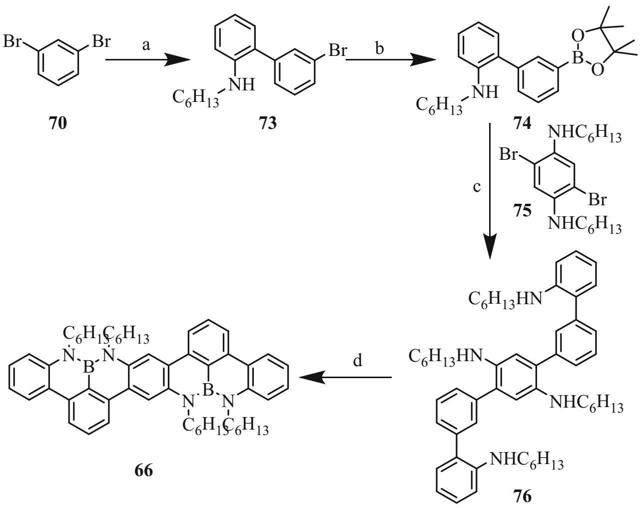

Fig. 26 Synthesis of NBN-doped NG **66**: (a) $Pd(PPh_3)_4$, $CsCO_3$, toluene/ethanol, 90°C, 68%; (b) $(Bpin)_2$, KOAc, DMSO, 100°C, 70%; (c) $Pd(PPh_3)_4$, $CsCO_3$, toluene/ethanol, 90°C, 73%; (d) BCl_3, Et_3N, *o*-DBC, 180°C, 35%

2-aminoarylboronic acid esters afforded **72** in 87% yield. In the final cyclization step, compound **72** was treated with BCl_3 and excess triethylamine at 180°C to furnish the targeted NBN-edged NG **65** via electrophilic borylation, which was directed by the central TMS group. The good stability of the NBN-doped **65** allowed further modifications of the skeleton to extend the π-conjugation and tune the optoelectronic properties of the resulting heteroatom-doped NG. Following a similar efficient synthetic strategy, compound **66** was obtained as a yellow solid from the same starting material 1,3-dibromobenzene (Fig. 26), which is the next homologue and a diazabora derivative of dibenzoheptazethrene (denoted as NBN-DBHZ). This efficient method highlights the scope of solution-based approaches for preparation of elongated NBN-zigzag-edged NGs or GNRs.

Interestingly, upon chemical oxidation of NBN-edged **65** by treatment with Cu $(OTf)_2$ under nitrogen atmosphere, compound **65** was nearly quantitatively converted to the σ-dimer through an open-shell intermediate (Fig. 25b). The UV/vis absorption spectra of **65** showed two main absorption bands in the wavelength regions of 250–300 and 300–400 nm, with an absorption maxima peak at 351 nm. For NBN-edged **66**, the absorption maximum peak is shifted further to 435 nm compared with monomer **65**. This bathochromic shift is consistent with the extended conjugation in the higher homologue of **66** with its repeated structural motif. Notably, compound **66** exhibited split emission bands at longer wavelengths, and had a much higher fluorescence quantum yield (Φ_{PL}) (0.83) than the smaller homologue **65**.

Titration of **65** with $Cu(OTf)_2$ resulted in formation of radical cation species, which can be monitored by UV/vis/NIR absorption spectra measurements (Fig. 27a) [109–111]. With the progressive addition of $Cu(OTf)_2$, a set of new

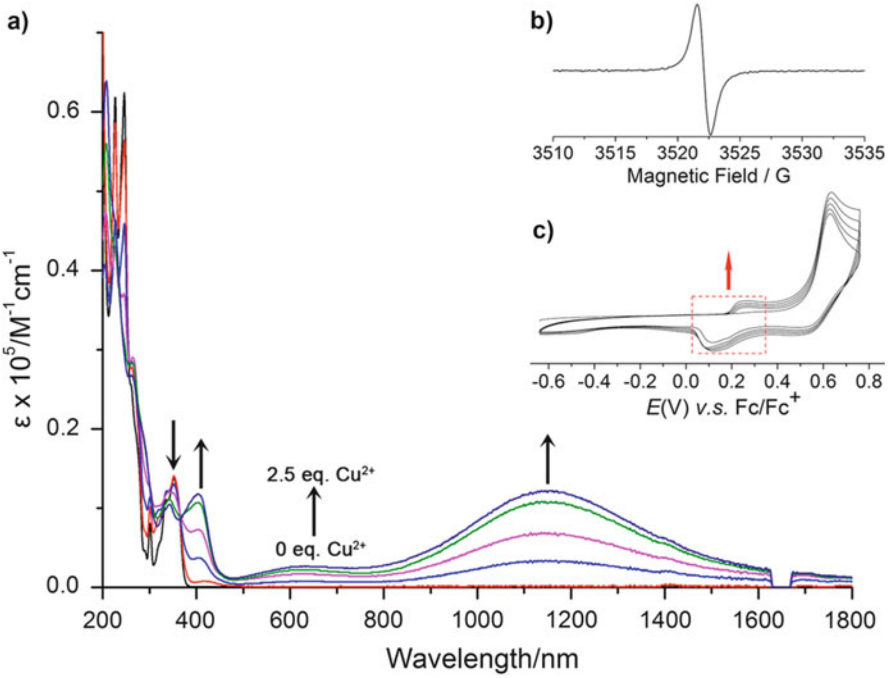

Fig. 27 (**a**) UV/vis/NIR absorption spectra of **65** titrated with Cu(OTf)$_2$ (0, 0.5, 1.0, 1.5, 2.0, and 2.5 equiv.) in acetonitrile (10^{-5} M). (**b**) EPR spectrum of the reaction solution of **65** + Cu(OTf)$_2$ at 10^{-3} M in acetonitrile.(**c**) Cyclic voltammograms of **65** measured in acetonitrile (0.1 mol/L *n*-Bu$_4$NPF$_6$) at a scan rate of 100 mV/s

absorption bands in the visible and NIR regions of **65** gradually evolved at 404, 620, and 1,150 nm, with a concomitant decrease in the $\pi - \pi^*$ transition peaks at 336 and 352 nm. Moreover, upon addition of Cu(OTf)$_2$ in acetonitrile solution of **65** at 10^{-3} M, the EPR spectrum revealed a strong signal at $g = 2.0033$ with a peak-to-peak width of 1 G (Fig. 27b), without any hyperfine coupling observed. This result clearly demonstrates the highly regioselective activity of such types of NBN-edged NGs [112].

6 Graphene Nanoribbons with Zigzag-Edge Structures

To date, a number of structurally defined GNRs with armchair edges (AGNR) have been successfully synthesized using solution-mediated methods [20, 21, 113–115]. However, microscopic visualization with atomic resolution and in-depth physical characterizations of such AGNRs have remained a challenge because of their strong aggregation and the difficulty of placing such AGNRs on a surface

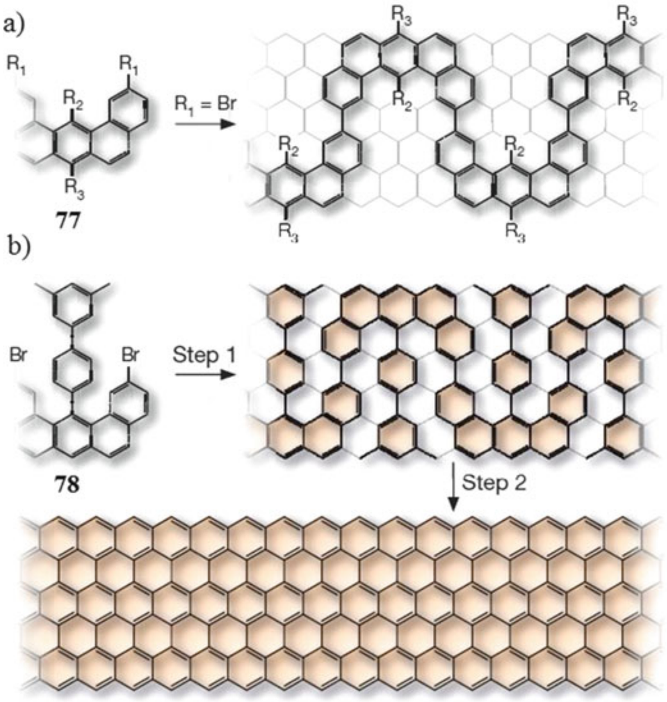

Fig. 28 (**a**) U-shaped **77** with halogen functions $R_1 = Br$ designed to enable surface-assisted aryl–aryl coupling into a snake-like polymer along the zigzag direction. (**b**) Monomer **78**, with an additional dimethyl-biphenyl group in the interior of the U-shape (R_2 position), which is designed to afford an $N = 6$ ZGNR (6-ZGNR; where N is the number of carbon zig-zag chains counted across the width of the ribbon)

without any contamination. In 2010, a complementary approach to solution synthesis, direct growth of AGNRs on metal surfaces under UHV conditions, was developed [116]. Using the surface-assisted method, atomically precise structures of the resulting AGNRs can be clearly observed using in situ high-resolution STM. In contrast to AGNRs showing semiconducting behavior with a direct energy gap, GNRs with zigzag-edge structures (ZGNR) show unique electronic properties that include profound lowering of the band gap and the presence of localized edge states that can be spin-polarized [117, 118]. In addition to computational calculations of ZGNR, its physical properties such as edge states and magneticity have been experimentally investigated in GNR systems with less-defined zigzag edge structures. For instance, it was possible to observe localized states at the zigzag edges of on-surface-synthesized finite 7-AGNRs [119–121].

Recently, a successful surface-assisted protocol was established to allow the bottom-up synthesis of ZGNRs with control over both ribbon width and edge morphology [122]. This approach depends on the choice of unique U-shaped monomer (**77**), shown in Fig. 28a. With two halogen functions for thermally

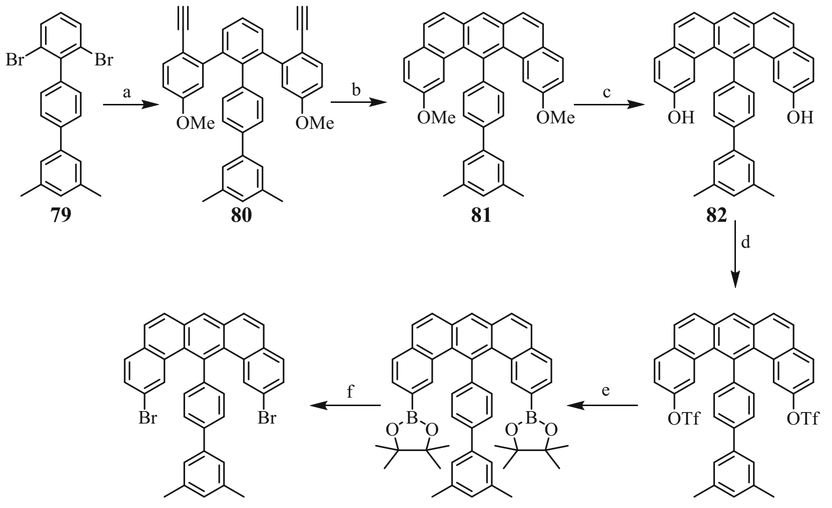

Fig. 29 Synthetic route toward U-shaped monomer **78**: (a) (1) $Pd(PPh_3)_4$, K_2CO_3, toluene/ ethanol, 90°C, 81%; (2) TBAF, THF, r.t., 99%; (b) $PtCl_2$, toluene, 80°C, 63%; (c) BBr_3, −78°C to r.t., 82%; (d) Tf_2O, Et_3N, DCM, 0°C to r.t., 78%; (e) $PdCl_2$(dppf), pinacolborane, dioxane, Et_3N, 71%; (f) $CuBr_2$, THF/methanol/H_2O, sealtube, 120°C, 60%

induced aryl–aryl coupling at the R_1 positions, this monomer allows surface-assisted polymerization into a snake-like polyphenylene polymer. Furthermore, this monomer can be extended by adding additional phenyl groups at the R_2 position pointing into the backbone of the GNR. The crucial precursor is monomer **78** (Fig. 28b), with two additional methyl groups at the periphery, which leads to formation of the full zigzag-edged GNRs by oxidative ring closure of the methyl groups.

Synthesis of the key building block **78** is illustrated in Fig. 29. The intermediate compound **79** was prepared in four steps, subjected to twofold Suzuki coupling, and subsequently treated with tetrabutylammoium fluoride (TBAF) solution to remove the triisopropyl (Tips) group to afford **80**. Compound **81** was then prepared after a catalytic cyclization reaction by treating **80** with platinum(II) chloride. Triflate **83** was obtained after demethylation by treating **81** with BBr_3 and subsequent treatment with trifluoromethanesulfonic anhydride (Tf_2O). Then, compound **84** was synthesized through borylation of **83** with pinacolborane. In the last step, the target “U-shaped” monomer **78** was achieved after treatment of **84** with copper (II) bromide in a sealed tube at 120°C.

Monomer **78** was deposited at 150°C and post-annealed at 200°C for 20 min. The STM images (Fig. 30a) show the formation of individual polymers and no cross-coupling between polymer strips at this temperature. Further annealing the substrate at 350°C resulted in complete planarization of the linear structures, consistent with the formation of the fully conjugated 6-ZGNR structure (Fig. 30b). The small-scale STM images (inset of Fig. 30b) demonstrate the

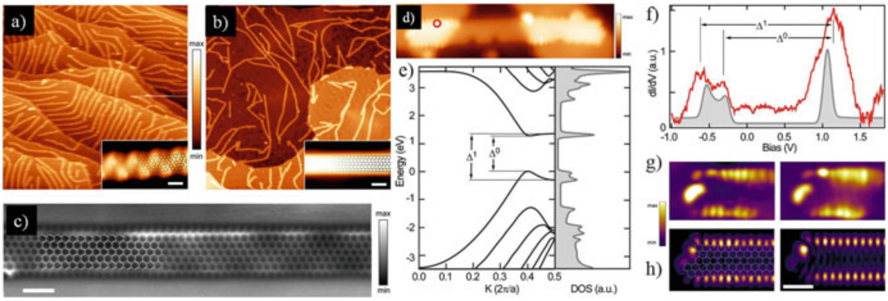

Fig. 30 Synthesis and characterization of atomically precise 6-ZGNRs: (**a**) STM image (200 nm × 200 nm) after deposition of monomer **67** on the surface. (**b**) STM image (200 nm × 200 nm) after annealing at 625 K. (**c**) nc-AFM image taken using a CO-functionalized tip. (**d**) STM image of a 6-ZGNR bridging between two NaCl monolayer islands. (**e**) Differential conductance (dI/dV) spectrum taken at the zigzag edge marked by the *red dot* in **d**. (**f**) GW band structure and density of states. (**g**) Differential conductance maps of filled (*left*) and empty (*right*) edge states taken at a sample bias of −0.3 V and 1.0 V, respectively; (**h**) DFT-based local density of states at 4 Å tip–sample distance

completely smooth and flat edge areas. Further structural details could be revealed by nc-AFM imaging with a CO-functionalized tip (Fig. 30c), which allowed direct confirmation that the width and edge morphology corresponded to the expected 6-ZGNR [123, 124].

Fort the first time, spin-polarized edge states of the perfect 6-ZGNRs could be confirmed and compared with their computational simulation. A strong electronic coupling between the ribbons and the metal surface obscures detection of the electronic edge states. However, clear evidence for the sought-after edge states could be obtained for 6-ZGNRs manipulated with the STM tip onto post-deposited insulating NaCl islands, where they are electronically decoupled from the underlying metal substrate (Fig. 30d) [125]. Although edge states have been observed in previous systems with less-defined zigzag edges [126–128], such as zigzag-edge graphene quantum dots (GQDs) with 7–8 nm average dimensions [7], their reported energy splitting varied greatly and was significantly smaller than for the present case. These results indicate that the electronic structure of zigzag edges is extremely sensitive to the edge roughness and interactions with the supporting substrate.

Moreover, a similar ZGNR (edge-modified 6-ZGNR) bearing additional fluoranthrene subunits was also synthesized on an Au surface. The key precursor monomer was an analogous compound, **85**, which is similar to **78** except that it bears an additional phenyl group (Fig. 31a). The ribbons were more efficiently decoupled from the surface and potentially also better shielded from neighboring GNRs as a result of steric hindrance brought about by the fluoranthrene units (Fig. 31b, c). More importantly, the edge modification reduced the ZGNR–substrate interaction sufficiently to allow STM to map the typical features of the edge state (Fig. 31d–g).

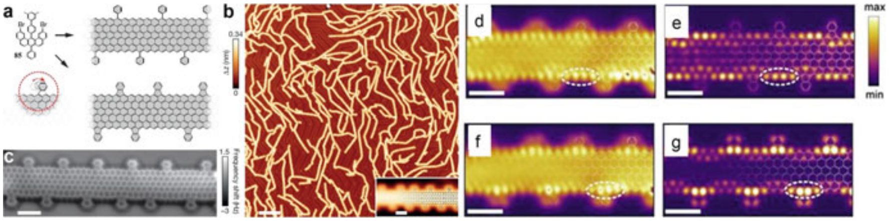

Fig. 31 Synthesis, characterization, and edge state of edge-modified 6-ZGNRs using monomer **85**: (**a**) Monomer **85** (*top left*) with an additional phenyl group at the R_3 position of monomer **77**, which is designed to afford an edge-modified 6-ZGNR upon polymerization and subsequent cyclization. (**b**) STM image of edge-modified 6-ZGNRs fabricated on an Au(111) surface. (**c**) Constant-height nc-AFM frequency-shift image of edge-modified 6-ZGNR. (**d**) Constant height dI/dV map of the occupied states. (**e**) DFT-based density of states of the highest occupied state. (**f**) Constant height dI/dV map of the unoccupied states. (**g**) DFT-based density of states of lowest unoccupied level. *Scale bars*: 1 nm

7 Conclusion

In the past two decades, the synthesis of NGs with rich zigzag edge peripheries has shown significant achievements, such as HBCs with one to four extra "double bonds," demonstrating varying symmetry and modulated optoelectronic properties. However, it still remains a great challenge to access the full zigzag-edged HBC (Fig. 2, compound **6**), namely "circumcoronene," which is fully surrounded by zigzag edges. On the other hand, synthesis is challenging because of the poor stability of such Z-NGs, as a result of oxidation under ambient conditions and photolytic degradation, leading to difficulties in handling in solution. For instance, the smaller analogues, perylene and bisanthene, have been known for a long time but attempts to synthesize the next generation of *peri*-fused acenes, such as *peri*-tetracene, by expanding bisanthene along the lateral direction have not yet been successful. To obtain stable and soluble materials in solution, reactive sites at the zigzag edges first need to be kinetically blocked with bulky groups. For example, by introducing three bulky *tert*-butyl groups, the phenalenyl radical could be sufficiently stabilized to allow isolation and characterization. Another attractive strategy is thermodynamic stabilization, for instance to delocalize the electrons over the whole π-conjugated framework or fuse with other aromatic skeletons. A third option is the introduction of heteroatoms, such as sulfur, nitrogen, boron, and oxygen, into the zigzag-edged frameworks to form stable heterostructures. By following this concept, a tandem demethylation/electrophilic borylation method was developed to synthesize new OBO-doped *peri*-tetracenes, which exhibit good stability. This work offers new possibilities for the construction of planar Z-NGs, in particular higher *peri*-acenes and eventually ZGNRs, with reasonable stability. In contrast to solution synthesis, ambient conditions can be avoided by using on-surface synthesis under UHV conditions, which is also a promising way to produce Z-NGs. For example, the thermally induced cyclodehydrogenation reaction of 6,6′-bipentacene precursors on Au(111) yields *peri*-pentacene under UHV conditions. The resultant Z-NG can be stabilized by surface interactions with the underlying metallic substrate. However solution synthesis is still elusive for *peri*-acenes beyond bisanthene.

Solution-mediated fabrication of ZGNRs is still highly challenging because of the relatively unstable nature of zigzag-edged structures, especially in an oxidative environment. Recently, the first example of a GNR with full zigzag edge, namely 6-ZGNR, was obtained using surface-assisted synthesis on Au(111) under UHV conditions. Here, a dihalogenated precursor with additional methyl groups at the periphery is crucial for building up the full zigzag edge by surface-assisted coupling of monomer and graphitization of the corresponding polyphenylene precursors. Successful bottom-up synthesis of atomically precise ZGNRs opens tremendous opportunities and challenges, not only for analysis of the electronic band structure but also for magnetic measurements, including the use of spin-polarized STM and the creation of spin valves. Nevertheless, optoelectronic and spintronic studies are required for the future use of such ZGNRs for device applications. This work is believed to be a milestone case in surface chemistry and was only possible through a combination of creative chemical design, in-situ STM, and state-of-the-art nc-AFM monitoring of surface-bound reactions. Moreover, GNRs with a hybrid of zigzag edge and other types of edge structures such as cove edges (see Fig. 1), are also promising targets, because they can have low band gaps and possess edge states at localized zigzag domains. Therefore, clear understanding and investigation of the stabilization issues of such systems at the molecular level are important for paving the way to their promising applications, such as field-effect transistors, electroconductors, and the next generation of spintronic materials.

Acknowledgements This work was financially supported by ERC grants on NANOGRAPH and 2DMATER, the EC under Graphene Flagship (No. CNECT-ICT-604391), Center for Advancing Electronics Dresden (CFAED), European Social Fund, and the Federal State of Saxony (ESF-Project “GRAPHD,” TU Dresden).

References

1. Novoselov KS, Geim AK, Morozov SV, Jiang D, Zhang Y, Dubonos SV, Grigorieva IV, Firsov AA (2004) Science 306:666–669
2. Novoselov KS, Geim AK, Morozov SV, Jiang D, Katsnelson MI, Grigorieva IV, Dubonos SV, Firsov AA (2005) Nature 438:197–200
3. Novoselov KS, Fal’ko VI, Colombo L, Gellert PR, Schwab MG, Kim K (2012) Nature 490:192–200
4. Castro-Neto AH, Guinea F, Peres NMR, Novoselov KS, Geim AK (2009) Rev Mod Phys 81:109–162
5. Gemayel ME, Narita A, Dössel LF, Sundaram RS, Kiersnowski A, Pisula W, Hansen MR, Ferrari AC, Orgiu E, Feng X, Müllen K, Samori P (2014) Nanoscale 6:6301–6314
6. Wang X, Ouyang Y, Li X, Wang H, Guo J, Dai H (2008) Phys Rew Lett 100:206803
7. Ritter KA, Lyding JW (2009) Nat Mater 8:235–242

8. Han M, Özyilmaz B, Zhang Y, Kim P (2007) Phys Rev Lett 98:206805
9. Yazyev O (2013) Acc Chem Res 46:2319–2328
10. Datta SS, Strachan DR, Khamis SM, Johnson ATC (2008) Nano Lett 8:1912–1915
11. Campos-Delgado J, Romo-Herrera J, Jia X, Cullen D, Muramatsu H, Kim Y, Hayashi T, Ren Z, Smith D, Okuno Y, Ohba T, Kanoh H, Kaneko K, Endo M, Terrones H, Dresselhaus M, Terrones M (2008) Nano Lett 8:2773–2778
12. Chen ZH, Lin YM, Rooks MJ, Avouris P (2007) Phys E 40:228–232
13. Elías A, Botello-Méndez A, Meneses-Rodríguez D, González V, Ramírez-González D, Ci L, Muñoz-Sandoval E, Ajayan M, Terrones H, Terrones M (2010) Nano Lett 10:366–372
14. Jiao L, Wang X, Diankov G, Wang H, Dai H (2010) Nat Nano 5:321–325
15. Pan Z, Liu N, Fu L, Liu Z (2011) J Am Chem Soc 133:17578–17581
16. Sakaguchi H, Kawagoe Y, Hirano Y, Iruka T, Yano M, Nakae T (2014) Adv Mater 26:4134–4138
17. Wu J, Gherghel L, Watson M, Li J, Wang Z, Simpson C, Kolb U, Müllen K (2003) Macromolecules 36:7082–7089
18. Yang X, Dou X, Rouhanipour A, Zhi L, Räder H, Müllen K (2008) J Am Chem Soc 130:4216–4217
19. Fogel Y, Zhi L, Rouhanipour A, Andrienko D, Räder H, Müllen K (2009) Macromolecule 42:6878–6884
20. Schwab MG, Narita N, Hernandez Y, Balandina Y, Mali KS, Feyter SD, Feng X, Müllen K (2012) J Am Chem Soc 134:18169–18172
21. Dössel L, Gherghel L, Feng X, Müllen K (2011) Angew Chem Int Ed 50:2540–2543
22. Son YW, Cohen ML, Louie SG (2006) Nature 444:347–349
23. Wu J, Pisula W, Müllen K (2007) Chem Rev 107:718–747
24. Chen L, Hernandez Y, Feng X, Müllen K (2012) Angew Chem Int Ed 51:7640–7654
25. Clar E (1972) The aromatic sextet. London, Wiley
26. Feng X, Pisula W, Müllen K (2009) Pure Appl Chem 81:2203–2224
27. Stabel A, Herwig P, Müllen K, Rabe JP (1995) Angew Chem Int Ed 34:1609–1611
28. Rieger R, Müllen K (2010) J Phys Org Chem 23:315–325
29. Pisula W, Feng X, Müllen K (2011) Chem Mater 23:554–567
30. Liu J, Li BW, Tan YZ, Giannakopoulos A, Sanchez-Sanchez C, Ruffieux P, Beljonne D, Fasel R, Feng X, Müllen K (2015) J Am Chem Soc 137:6097–6103
31. Reid DH (1958) Tetrahedron 3:339–352
32. Morita Y, Suzuki S, Sato K, Takui T (2011) Nat Chem 3:197–204
33. Purushothaman B, Bruzek M, Parkin SR, Miller AF, Anthony JE (2011) Angew Chem Int Ed 50:7013–7017
34. Stein SE, Brown RL (1987) J Am Chem Soc 109:3721–3729
35. Wang Z, Tomović Ź, Kastler M, Pretsch R, Negri F, Enkelmann V, Müllen K (2004) J Am Chem Soc 126:7794–7795
36. Kastler M, Schmidt J, Pisula W, Sebastiani D, Müllen K (2006) J Am Chem Soc 128:9526–9534
37. Lowe JP (1982) Int J Quantum Chem Quantum Biol Symp 9:5–13
38. Dumslaff T, Yang B, Maghsoumi A, Velpula G, Mali KS, Castiglioni C, Feyter SD, Tommasini M, Narita A, Feng X, Müllen K (2016) J Am Chem Soc 138:4726–4729
39. Alibert-Fouet S, Seguy I, Bobo JF, Destruel P, Bock H (2007) Chem Eur J 13:1746–1753
40. Rädulescu D, Ostrogovich G, Bärbulescu F (1931) Chem Ber 64:2240–2242
41. Kono Y, Miyamoto H, Aso Y, Otsubo T, Ogura F, Tanaka T, Sawada M (1989) Angew Chem Int Ed 28:1222–1223
42. Schoental R, Scott EJY (1949) J Chem Soc:1683–1696
43. Berlman IB (1973) Energy transfer parameters of aromatic compounds. Academic, London
44. Mi BX, Gao ZQ, Lee CS, Lee ST, Kwong HL, Wong NB (1999) Appl Phys Lett 75:4055–4057
45. Clar E (1948) Chem Ber 81:62

46. Arabei SM, Pavich TA (2000) J Appl Spectrosc 67:236–244
47. Hirao Y, Konishi A, Matsumoto K, Kurata H, Kubo T (2012) AIP Conf Proc 1504:863–866
48. Li J, Zhang K, Zhang X, Huang KW, Chi C, Wu J (2010) J Org Chem 75:856–863
49. Konishi A, Hirao Y, Nakano M, Shimizu A, Botek E, Champagne B, Shiomi D, Sato K, Takui T, Matsumoto K, Kurata H, Kubo T (2010) J Am Chem Soc 132:11021–11023
50. Konishi A, Hirao Y, Matsumoto K, Kurata H, Kishi R, Shigeta Y, Nakano M, Tokunaga K, Kamada K, Kubo T (2013) J Am Chem Soc 135:1430–1437
51. Konishi A, Hirao Y, Kurata H, Kubo T, Nakano M, Kamada K (2014) Pure Appl. Chem 86:497–505
52. Konishi A, Hirao Y, Kurata H, Kubo T (2013) Solid State Commun 175-176:62–70
53. Motta SD, Negri F, Fazzi D, Castiglioni C, Canesi EV (2010) J Phys Chem Lett 1:3334–3339
54. Sun Z, Wu J (2012) J Mater Chem 22:4151–4160
55. Sun Z, Ye Q, Chi C, Wu J (2012) Chem Soc Rev 41:7857–7889
56. Fort EH, Donovan PM, Scott LT (2009) J Am Chem Soc 131:16006–16007
57. Jiang DE, Dai S (2008) Chem Phys Lett 466:72–75
58. Moscardó F, San-Fabián E (2009) Chem Phys Lett 480:26–30
59. Liu J, Ravat P, Wagner M, Baumgarten M, Feng X, Müllen K (2015) Angew Chem Int Ed 54:12442–12446
60. Chase DT, Fix AG, Rose BD, Weber CD, Nobusue S, Stockwell CE, Zakharov LN, Lonergan MC, Haley MM (2011) Angew Chem Int Ed 50:11103–11106
61. Chase DT, Rose BD, McClintock SP, Zakharov LN, Haley MM (2011) Angew Chem Int Ed 50:1127–1130
62. Liu J, Narita A, Osella S, Zhang W, Schollmeyer D, Beljonne D, Feng X, Müllen K (2016) J Am Chem Soc 138:2602–2608
63. Gu X, Xu X, Li H, Liu Z, Miao Q (2015) J Am Chem Soc 137:16203–16208
64. Liu J, Osella S, Ma J, Berger R, Schollmeyer D, Beljonne D, Feng X, Müllen K (2016) J Am Chem Soc 138:8364–8367
65. Zhang X, Li J, Qu H, Chi C, Wu J (2010) Org Lett 12:3946–3949
66. Zöphel L, Berger R, Gao P, Enkelmann V, Baumgarten M, Wagner M, Müllen K (2013) Chem Eur J 19:17821–17826
67. Rogers C, Chen C, Pedramrazi Z, Omrani AA, Tsai HZ, Jung HS, Lin S, Crommie MF, Fischer FR (2015) Angew Chem Int Ed 54:15143–15146
68. Reid DH (1956) Chem Ind:1504
69. Sogo PB, Nakazaki M, Calvin M (1957) J Chem Phys 26:1343–1345
70. Reid DH, Fraser M, Molloy BB, Payne HAS, Sutherland RG (1961) Tetrahedron Lett 15:530–535
71. Goto K, Kubo T, Yamamoto K, Nakasuji K, Sato K, Shiomi D, Takui T, Kubota M, Kobayashi T, Yakusi K, Ouyang JY (1999) J Am Chem Soc 121:1619–1620
72. Zaitsev V, Rosokha SV, Head-Gordon M, Kochi JK (2006) J Org Chem 71:520–526
73. Nakasuji K, Yoshida K, Murata I (1983) J Am Chem Soc 105:5136–5137
74. Murata I, Sasaki S, Klabunde KU, Toyoda J, Nakasuji K (1991) Angew Chem Int Ed 30:172–173
75. Ohashi K, Kubo T, Masui T, Yamamoto K, Nakasuji K, Takui T, Kai Y, Murata I (1998) J Am Chem Soc 120:2018–2027
76. Kubo T, Shimizu A, Sakamoto M, Uruichi M, Yakushi K, Nakano M, Shiomi D, Sato K, Takui T, Morita Y, Nakasuji K (2005) Angew Chem Int Ed 44:6564–6568
77. Shimizu A, Uruichi M, Yakushi K, Matsuzaki H, Okamoto H, Nakano M, Hirao Y, Matsumoto K, Kurata H, Kubo T (2009) Angew Chem Int Ed 48:5482–5486
78. Kubo T, Shimizu A, Uruichi M, Yakushi K, Nakano M, Shiomi D, Sato K, Takui T, Morita Y, Nakasuji K (2007) Org Lett 9:81–84
79. Shimizu A, Hirao Y, Matsumoto K, Kurata H, Kubo T, Uruichi M, Yakushi K (2012) Chem Commun 48:5629–5631

80. Shimizu A, Kubo T, Uruichi M, Yakushi K, Nakano M, Shiomi D, Sato K, Takui T, Hirao Y, Matsumoto K, Kurata H, Morita Y, Nakasuji K (2010) J Am Chem Soc 132:14421–14428
81. Kubo T (2015) Chem Rec 15:218–232
82. Kubo T (2015) Chem Lett 44:111–122
83. Clar E, Lang KF, Schulz-Kiesow H (1955) Chem Ber 88:1520–1527
84. Staab HA, Nissen A, Ipaktschi J (1968) Angew Chem Int Ed 7:226–226
85. Mitchell RH, Sondheimer F (1970) Tetrahedron 26:2141–2150
86. Staab HA, Ipaktschi J, Nissen A (1971) Chem Ber 104:1182–1186
87. Umeda R, Hibi D, Miki K, Tobe Y (2009) Org Lett 11:4104–4106
88. Umeda R, Hibi D, Miki K, Tobe Y (2010) Pure Appl Chem 82:871–878
89. Wu TC, Chen CH, Hibi D, Shimizu A, Tobe Y, Wu YT (2010) Angew Chem Int Ed 49:7059–7062
90. Shan L, Liang Z, Xu X, Tang Q, Miao Q (2013) Chem Sci 4:3294–3297
91. Sun Z, Zeng Z, Wu J (2013) Chem Asian J 8:2894–2904
92. Sun Z, Zeng Z, Wu J (2014) Acc Chem Res 47:2582–2591
93. Li Y, Heng WK, Lee BS, Aratani N, Zafra JL, Bao N, Lee R, Sung YM, Sun Z, Huang KW, Webster RD, López Navarrete JT, Kim DH, Osuka A, Casado J, Ding J, Wu J (2012) J Am Chem Soc 134:14913–14922
94. Nakano M, Kishi R, Takebe A, Nate M, Takahashi H, Kubo T, Kamada K, Ohta K, Champagne B, Botek E (2007) Comput Lett 3:333–338
95. Weil T, Vosch T, Hofkens J, Peneva K, Müllen K (2010) Angew Chem Int Ed 49:9068–9093
96. Anthony J (2008) Angew Chem Int Ed 47:452–483
97. Zeng W, Sun Z, Herng TS, Gonçalves TP, Gopalakrishna TY, Huang KW, Ding J, Wu J (2016) Angew Chem Int Ed 55:8615–8619
98. Stępień M, Gońka E, Żyła M (2016) N. Sprutta Chem Rev 117:3479–3716
99. Liu Z, Marder TB (2008) Angew Chem Int Ed 47:242–244
100. Bosdet MJD, Piers WE (2009) Can J Chem 87:8–29
101. Campbell PG, Marwitz AJV, Liu SY (2012) Angew Chem Int Ed 51:6074–6092
102. Wang XY, Wang JY, Pei J (2015) Chem Eur J 21:3528–3539
103. Aramaki Y, Omiya H, Yamashita M, Nakabayashi K, Ohkoshi SI, Nozaki K (2012) J Am Chem Soc 134:19989–19992
104. Suzuki S, Yoshida K, Kozaki M, Okada K (2013) Angew Chem Int Ed 52:2499–2502
105. Rosenthal AJ, Devillard M, Miqueu K, Bouhadir G, Bourissou D (2015) Angew Chem Int Ed 54:9198–9202
106. Katayama T, Nakatsuka S, Hirai H, Yasuda N, Kumar J, Kawai T, Hatakeyama T (2016) J Am Chem Soc 138:5210–5213
107. Wang XY, Narita A, Zhang W, Feng X, Müllen K (2016) J Am Chem Soc 138:9021–9024
108. Wang X, Zhang F, Schellhammer KS, Machata P, Ortmann F, Cuniberti G, Fu Y, Hunger J, Tang R, Popov AA, Berger R, Müllen K, Feng X (2016) J Am Chem Soc 138:11606–11615
109. Ajayakumar M, Asthana D, Mukhopadhyay P (2012) Org Lett 14:4822–4825
110. Wu X, Guo Z, Wu Y, Zhu S, James TD, Zhu W (2013) ACS Appl Mater Interfaces 5:12215–12220
111. Jung JY, Kang M, Chun J, Lee J, Kim J, Kim J, Kim Y, Kim SJ, Lee C, Yoon J (2013) Chem Commun 49:176–178
112. Ji L, Edkins RM, Lorbach A, Krummenacher I, Brückner C, Eichhorn A, Braunschweig H, Engels B, Low PJ, Marder TB (2015) J Am Chem Soc 137:6750–6753
113. Narita A, Feng X, Hernandez Y, Jensen SA, Bonn M, Yang H, Verzhbitskiy IA, Casiraghi C, Hansen MR, Koch AHR, Fytas G, Ivasenko O, Li B, Mali KS, Tatyana B, Mahesh S, Feyter SD, Müllen K (2014) Nat Chem 6:126–132
114. Cai J, Pignedoli CA, Talirz L, Ruffieux P, Söde H, Liang L, Meunier V, Berger R, Li R, Feng X, Müllen K, Fasel R (2014) Nat Nano 9:896–900

115. Narita A, Verzhbitskiy IA, Frederickx W, Mali KS, Jensen SN, Hansen MR, Bonn M, Feyter SD, Casiragh C, Feng X, Müllen K (2014) ACS Nano 8:11622–11630
116. Cai J, Ruffieux P, Jaafar R, Bieri M, Braun T, Blankenburg S, Muoth M, Seitsonen P, Saleh M, Feng X, Müllen K, Fasel R (2010) Nature 466:470–473
117. Nakada K, Fujita M, Dresselhaus G, Dresselhaus MS (1996) Phys Rev B 54:17954–17961
118. Son YW, Cohen ML, Louie SG (2007) Phys Rev Lett 98:216803
119. Talirz L, Sode H, Cai J, Ruffieux P, Blankenburg S, Jafaar R, Berger R, Feng X, Müllen K, Passerone D, Fasel R, Pignedoli CA (2013) J Am Chem Soc 135:2060–2063
120. Ijas M, Ervasti M, Uppstu A, Liljeroth P, van der Lit J, Swart I, Harju A (2013) Phys Rev B 88:075429
121. Magda GZ, Jin XZ, Hagymasi I, Vancso P, Osvath Z, Nemes-Incze P, Hwang CY, Biro LP, Tapaszto L (2014) Nature 514:608–611
122. Ruffieux P, Wang S, Yang B, Sánchez-Sánchez C, Liu J, Dienel T, Talirz L, Shinde P, Pignedoli CA, Passerone D, Dumslaff T, Feng X, Müllen K, Fasel R (2016) Nature 531:489–492
123. Gross L, Mohn F, Moll N, Liljeroth P, Meyer G (2009) Science 325:1110–1114
124. Li Y, Zhang W, Morgenstern M, Mazzarello R (2013) Phys Rev Lett 110:216804
125. Repp J, Meyer G, Paavilainen S, Olsson FE, Persson M (2005) Phys Rev Lett 95:225503
126. Hybertsen MS, Louie SG (1986) Phys Rev B 34:5390
127. Tao C, Jiao L, Yazyev OV, Chen YC, Feng J, Zhang X, Capaz RB, Tour JM, Zettl A, Louie SG, Dai H, Crommie MF (2011) Nat Phys 7:616–620
128. van der Lit J, Boneschanscher MP, Vanmaekelbergh D, Ijas M, Uppstu A, Ervasti M, Harju A, Liljeroth P, Swart I (2013) Nat Commun 4:2023

Adv Polym Sci (2017) 278: 33–66
DOI: 10.1007/12_2017_2

Bottom-Up Synthesis of Graphene Nanoribbons on Surfaces

Felix R. Fischer

Abstract The review discusses progress in the synthesis of atomically precise graphene nanoribbons from molecularly defined precursors on surfaces. It covers the literature from 2010 through 2016.

Keywords Bottom-up synthesis • Graphene nanoribbon • Scanning tunneling microscopy/spectroscopy • Surface catalysis

Contents

F.R. Fischer (✉)
Department of Chemistry, University of California Berkeley, Berkeley, CA 94720, USA

Materials Sciences Division, Lawrence Berkeley National Laboratory, Berkeley, CA 94720, USA

Kavli Energy Nanosciences Institute at the University of California Berkeley and Lawrence Berkeley National Laboratory, Berkeley, CA 94720, USA
e-mail: ffischer@berkeley.edu

Abbreviations

AFM	Atomic force microscopy
AGNR	Armchair graphene nanoribbon
CB	Conduction band
CeGNR	Cove edge graphene nanoribbon
CGNR	Chevron graphene nanoribbon
DOS	Density of states
GNR	Graphene nanoribbon
HREELS	High-resolution electron energy loss spectroscopy
IPES	Inverse photoemission spectroscopy
LDOS	Local density of states
ncAFM	Noncontact atomic force microscopy
STM	Scanning tunneling microscopy
STS	Scanning tunneling spectroscopy
UHV	Ultrahigh vacuum
UPS	Ultraviolet photoemission spectroscopy
VB	Valence band
XPS	X-ray photoemission spectroscopy
ZGNR	Zig-zag graphene nanoribbon

1 Introduction

The outstanding transformative potential of graphene, an infinite sheet of carbon atoms tightly packed into a honeycomb lattice, has been recognized and is mostly a result of its exceptionally high charge-carrier mobility, thermal conductivity, tensile strength, and mechanical stiffness [1–3]. Yet, these undeniably very desirable properties represent only a very small facet of the true potential of all-sp^2 carbon materials and their potential to revolutionize the field of molecular electronics. The electronic properties of graphene itself can be described as those of a gapless semiconductor or semimetal (Fig. 1) [4, 5]. Its valence and conductance bands overlap in a single point. Graphene shows a strong ambipolar electric field effect. The charge carriers can be tuned continuously between holes and electrons to reach densities as high as 10^{13} cm^{-1} and mobilities in excess of 15,000 cm^2 V^{-1} s^{-1}. The charge mobility in graphene is largely dominated by impurity scattering effects and is almost independent of the temperature. Even at ambient conditions the charge carriers in graphene move ballistically over submicron distances, covering a typical gap between the source and drain electrodes of a transistor in less than 1 ps [1, 2, 6].

Over the last decade an overwhelming variety of applications for graphene have been proposed, including fillers for composite plastic materials, graphene-based batteries, supercapacitors, and field emitters [7, 8]; transparent electrodes in optoelectronics [9, 10]; carbon-based environmental sensors [11]; spin-valves [12, 13]; and field-effect transistors [1]. Research in the field of all-sp^2 carbon-based

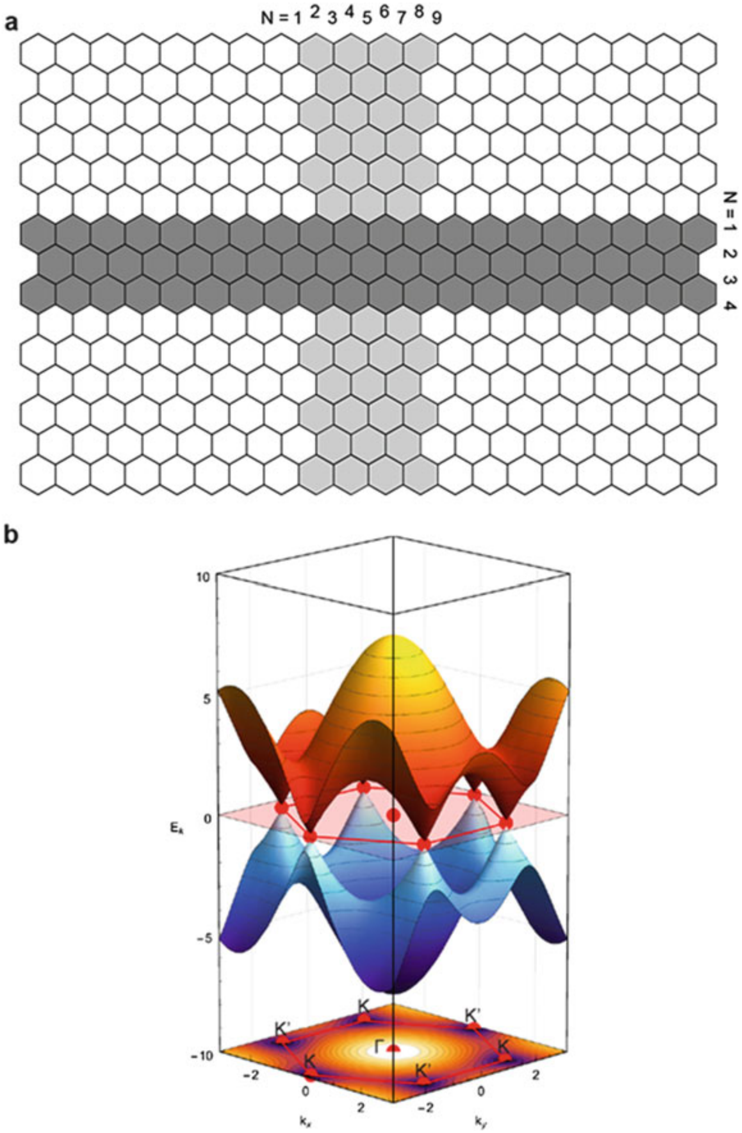

Fig. 1 (**a**) Graphene and graphene nanoribbons with armchair edges (*vertical*) and zig-zag edges (*horizontal*). The *numbering* used to define the width of the armchair GNRs (AGNRs) and zig-zag GNRs (ZGNRs) is denoted along the edges. (**b**) Electronic band structure in graphene featuring linear dispersion at the Dirac points K and K′

materials has largely been motivated by their applications in advanced functional electronics. As a result of its unique properties graphene has been identified as one of the most promising materials for post-silicon integrated circuit architectures [14]. The seamless integration of graphene into advanced electronic circuits, however, calls for semiconductors (rather than semimetals) featuring well-defined and tunable band gaps and large on–off current ratios at ambient conditions. This can be achieved by reducing the infinite two-dimensional carbon sheet to a narrow one-dimensional graphene nanoribbon (GNR) [5, 15]. This quantum mechanical confinement alters the electronic band structure and gives rise to a well-defined gap between the conductance and valence bands [16, 17]. In fact, GNRs most unusual properties (e.g., theoretically predicted edge-magnetism, exceptionally high spin-coherence, and highly tunable band gap) are intimately linked to quantum mechanical boundary conditions dictated by the dimension, symmetry, and edge structure [18]. Unfortunately, these complex structure–function relationships remain poorly understood. The exploration, realization, and implementation of these truly exotic properties rely on the development of innovative synthetic strategies that provide atomically precise control over the assembly of functional nanographene.

Superior strategies for synthesis of atomically defined and tunable GNRs must overcome several longstanding challenges. First and foremost is reliable control of the absolute dimensions (i.e., length and width). Cutting-edge top-down lithographic patterning techniques have been successfully used to fabricate individual GNRs featuring widths as narrow as 10 nm. The process, however, is exceedingly laborious, relies on the availability of sophisticated instrumentation, and is limited to the fabrication of individually unique samples. Synthetic bottom-up approaches instead have the potential to yield rationally designed GNRs in highly homogeneous batch synthesis. Structural variation of the small-molecule building blocks (precursors for the GNRs) represents a reliable strategy for obtaining a desired width and edge symmetry. Pure samples of hydrogen-terminated zig-zag (ZGNRs) or armchair (AGNRs) GNRs with homogeneous widths and highly reproducible physical properties can be obtained. Furthermore, this rational approach paves the way for assembly of GNRs featuring designer edges tailored to a variety of very specific application requirements. The extraordinary control over the structure of GNRs can also be applied to rational defect engineering or doping. Chemical synthesis of small-molecule precursors allows the introduction of functional groups or heteroatoms into the edges or into the carbon lattice of the GNR itself. The exact position of these dopants and the highly regular pattern along the length of the ribbons can easily be predicted and used to tune, for example, the Fermi energy, band gap, or the number and nature of charge carriers in the GNR.

2 Top-Down Synthetic Strategies

The controlled synthesis of GNR-based functional materials is a field still in its infancy. The techniques used to synthesize GNRs can be broadly categorized into two complementary approaches: classical top-down patterning of two-dimensional graphene sheets, and the controlled bottom-up growth of graphene nanostructures from small-molecule precursors. Early top-down approaches relied on lithographic techniques to mechanically pattern exfoliated sheets of graphene (Fig. 2). Han et al.

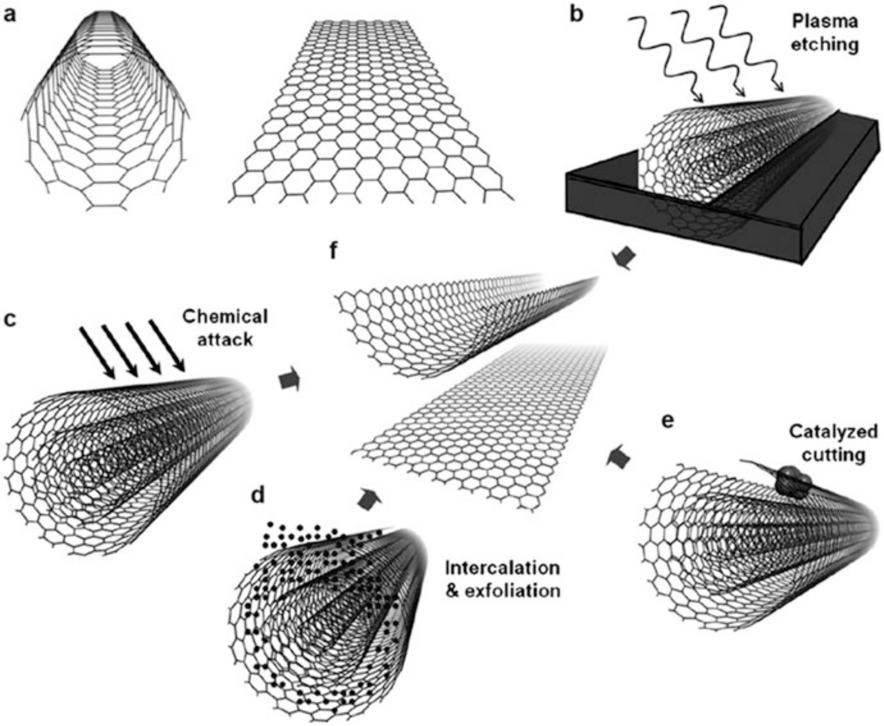

Fig. 2 (**a**) Single-walled carbon nanotubes (SWCNTs) and graphene nanoribbon (GNR). (**b**–**f**) Top-down synthetic approaches toward GNRs: (**b**) plasma etching [20], (**c**) longitudinal unzipping through chemical attack [17], (**d**) intercalation of alkali metals followed by exfoliation of CNTs [57], (**e**) metal nanoparticle catalyzed unzipping of CNTs [58], and (**f**) unfolded GNRs. Reproduced with permission from [59], Copyright (2012) John Wiley and Sons

used e-beam lithography to pattern etch masks onto single sheets of graphene [5]. Oxygen plasma etching of the unprotected graphene yielded individual GNRs with widths ranging from 10 to 100 nm and lengths of 1–2 μm. The electronic properties of these structures, however, suffer from the harsh reaction conditions. Using this technique, it is difficult to control both the edge symmetry and the substitution pattern of the GNRs. Tapasztó et al. combined the surface modification and atomic resolution imaging capabilities of scanning tunneling microscopy (STM) techniques to engineer graphene nanostructures [15]. Current etching of a single sheet of graphene at the surface of multilayer graphite yielded GNRs ranging in widths from 2.5 to 10 nm and of lengths up to 120 nm. This technique represents a significant improvement; however, the low throughput and edge irregularities or roughness in the narrower ribbons remain a common problem of top-down approaches.

Naturally occurring defect structures in graphene have been used by Li et al. to fabricate sub-10 nm wide and ~1 μm long GNRs by sonication of exfoliated graphene sheets suspended in organic solvents [19]. Although this approach yields

GNRs with well-defined edges, the random distribution of defects cannot be used to control the absolute dimensions of the ribbon. Kosynkin et al. and Jiao et al. have unzipped single-walled and multiwalled carbon nanotubes along the longitudinal axis to yield narrow GNRs [17, 20, 21]. Both techniques rely on the use of exceptionally harsh reaction conditions, large excess of strong oxidants such as $KMnO_4$, or plasma etching to induce and propagate defects along the longitudinal axis of the nanotubes. The edge structure of the resulting unfolded GNRs can be directly correlated to the chirality of the initial carbon nanotube. The use of harsh reaction conditions and the inherent inhomogeneity of carbon nanotubes, however, lead to irregularities in the substitution pattern and unpredictable edge symmetries. Carbon atoms exposed during the unzipping process can easily be oxidized to, for example, alcohols, ketones, or carboxylic acids. This irregular substitution negatively and unpredictably affects the conductive properties of narrow GNRs.

3 Rational Bottom-Up Synthesis

A significant advance in the rational synthesis of GNRs has been demonstrated by Müllen, Fasel, and coworkers [22]. Pioneering work related to the surface-supported assembly of molecular wires and covalent organic networks sparked the rational design of polymers that could be converted into GNRs through surface-catalyzed cyclodehydrogenation strategies [23–25]. Figure 3 illustrates the general concept for the rational synthesis of $N = 7$ AGNRs (7-AGNRs; where N is the integer number of carbon atoms counted across the width of the GNR) from 10,10′-dibromo-9,9′-bianthryl (**1**). The brominated small-molecule precursors are evaporated onto a clean noble metal (e.g., Au, Ag, Cu) surface held at a constant temperature (T_1) under ultrahigh vacuum (UHV). The intimate interaction with the catalytically active metal surface induces homolytic cleavage of the carbon–halogen bond to give a diradical intermediate. These intermediate carbon-centered diradicals diffuse along the surface and recombine in a step-growth polymerization to yield linear polyanthracene chains. Thermal annealing of these precursors at an elevated temperature (T_2) induces a cyclodehydrogenation sequence [26] that yields fully conjugated GNRs ranging in length from 12 to 60 nm [27]. This surface-based self-assembly technique yields 7-AGNRs with atomically defined hydrogen-substituted armchair edges. The width and crystallographic symmetry of GNRs fabricated by the bottom-up approach are primarily determined by the structure of the small-molecule precursor. The length of the ribbon largely depends on the surface coverage, average diffusion length of monomers and growing polymer chains on the surface, and the competition between chain-extension, chain-termination, and radical-transfer processes. Although this technique yields superior GNRs with hydrogen-terminated edges it is limited by the growth conditions. Efficient incorporation into devices demands GNRs with lengths in excess of 100 nm. For electronic applications in particular it is essential that the GNR is

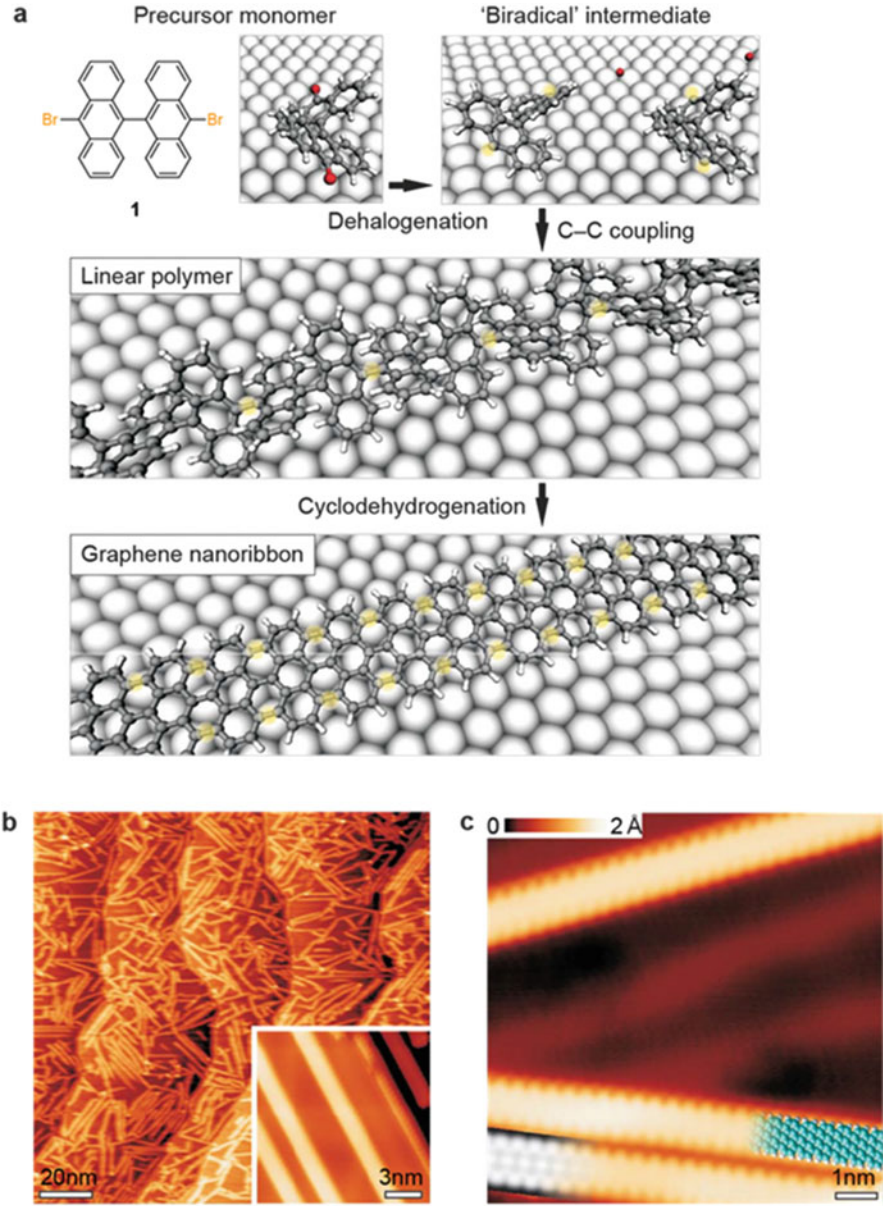

Fig. 3 (**a**) General scheme for the stepwise bottom-up synthesis of GNRs on Au(111). Key steps are activation of the monomer precursor through dehalogenation, recombination to form a new C–C bonds, and cyclodehydrogenation to form fully extended 7-AGNRs. (**b**) Large area STM image of 7-AGNRs on Au(111). (**c**) Magnified image of 7-AGNRs showing the smooth hydrogen-terminated armchair edges. A CPK model of 7-AGNR nanoribbons is overlaid as a guide for the eye. Reproduced with permission from [22], Copyright (2010) Nature Publishing Group

supported by an insulator rather than by a highly conductive metal to prevent competing conduction pathways.

3.1 Bottom-Up Synthesis on Surfaces: Mechanism and Design Strategies

A central aspect of rational bottom-up synthesis of GNRs is the design of the molecular precursors. The precursor molecules are required to meet a series of thermodynamic, kinetic, and structural criteria imposed by the dimensions and symmetry of the desired GNR, the nature of the surface used as growth substrate, and technical limitations imposed by the UHV system used in fabrication. Figure 4 summarizes a selection of building blocks used in the synthesis of AGNRs, chevron GNRs (CGNRs), and ZGNRs on surfaces. Initial work has largely focused on the synthesis of AGNRs ranging in width from $N = 5$ to $N = 13$. A common structural feature of most molecular precursors is a mirror symmetry perpendicular to the long axis of the GNR. This preferred structure, an A–A building block, ensures that the rates of radical recombination at either end of the growing polymer chain are comparable. The inherent symmetry further circumvents structural defects that could emerge from asymmetric radical recombination of A–B building blocks featuring, for example, different steric demands at either end of the monomer. A second important structural consideration is the placement of aryl rings that undergo cyclodehydrogenation during thermal annealing on the surface. As a post-polymerization step, successful defect-free cyclodehydrogenation relies on a clear preference of the aryl rings to undergo exclusively the desired cyclization that leads to the extended conjugated π-system of GNRs. Careful structural considerations ensure that the appended aryl rings form the desired C–C bonds rather than participating in side reactions that could lead to kinks or defects along the GNR backbone. Conceptually, this is illustrated in the design of the precursor for 13-AGNRs (Fig. 5). The *ortho*-substitution of the bond between the biphenyl wing and the anthracene core gives access to only one distinct cyclodehydrogenation product, in contrast to two potentially accessible orientations for the alternative *meta*-substitution pattern.

Further consideration has to be given to the choice of activating substituents. Most successful building blocks feature either C–Br or C–I bonds that undergo homolytic cleavage to generate halogen radicals and the desired Csp^2-centered radicals that participate in the step-growth polymerization. The preferential selection of Br and I substituents for the synthesis of GNRs on precious metal surfaces is not arbitrary but meets very specific kinetic and thermodynamic requirements. Key challenges are the choice of (1) a functional group that is compatible with the sublimation conditions used during deposition of molecular precursor on the target substrate, (2) a bond that can be selectively activated through external stimuli (e.g., heat, light) on the surface under conditions that do not cleave other labile

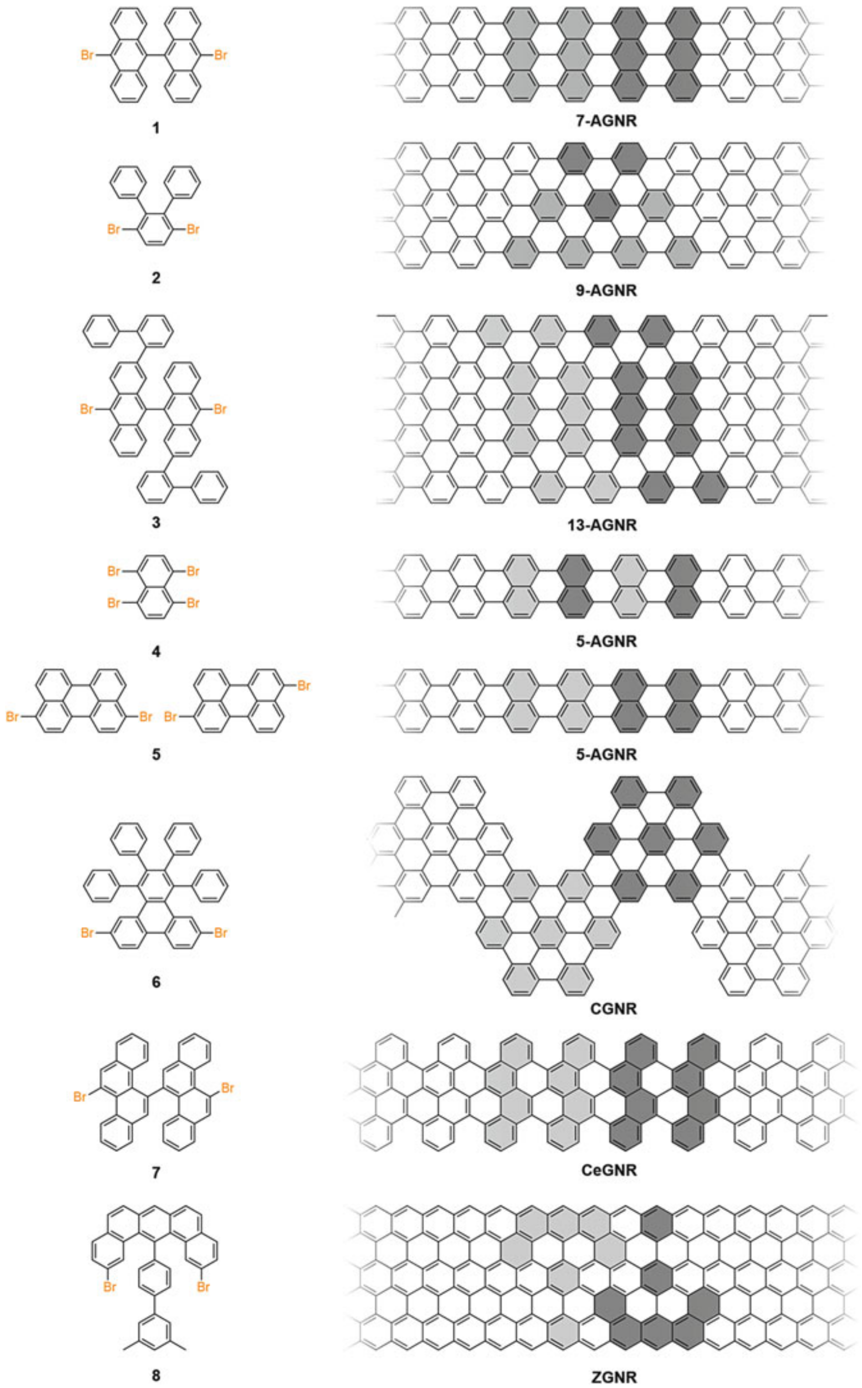

Fig. 4 Representation of AGNRs [22, 41–43], CGNRs [22], CeGNRs [47], ZGNRs [48], and the respective molecular precursors used in their synthesis on Au, Ag, or Cu surfaces

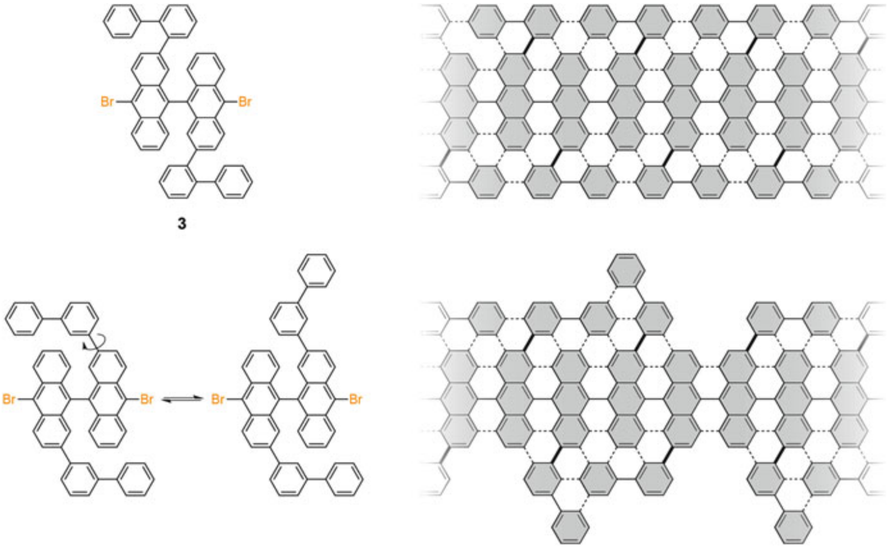

Fig. 5 Two possible designs for 13-AGNR precursors. Only precursor **3** is set up to exclusively cyclize to form the desired defect-free armchair edge. Rotation around the anthracene biphenyl C–C bond in the *meta*-substituted precursor can lead to two possible cyclodehydrogenation patterns

bonds (C–H, C–C) in the molecule, and (3) a homolytic fragmentation pattern that leaves a Csp^2-centered radical and, preferably, a small molecule behind that either irreversibly desorbs from the surface or is sufficiently deactivated that it does not interfere during the radical chain propagation step. These conditions are largely met in the activation of labile C–Br and C–I bonds over the omnipresent C–H bonds on Au, Ag, and Cu surfaces. Density functional theory (DFT) calculations by Björk et al. demonstrated that the highly exothermal bond dissociation of phenylbromide or phenyliodide (317 kJ mol^{-1} and 321 kJ mol^{-1}, respectively) turns into an endothermal process on Au(111), Ag(111), and Cu(111) surfaces [28, 29]. This unusual thermodynamic stabilization can be explained by covalent interactions between the Csp^2-centered radical on the phenyl ring and the free valences of the metal surface. Chemisorption of the high energy phenyl radical drives the reaction toward the dissociated products. The ability to stabilize the phenyl radical follows a trend in the series Au, Ag, Cu, with the latter being the most reactive surface. Along with the overall reversion of the thermodynamic parameters, the kinetic barrier for homolytic cleavage of the C–Br or C–I bond follows a similar trend. The activation energy for dissociation of C–Br and C–I bonds is highest on Au (97 and 69 kJ mol^{-1}) and lowest on Cu (64 and 38 kJ mol^{-1}). These theoretical results have been largely corroborated by experiment. Batra et al. and Simonov et al. followed the thermal activation of C–Br bonds in **1** on an Au(111) surface using X-ray photoemission spectroscopy (XPS) [30, 31]. At temperatures below 100°C, the XPS of molecule-decorated substrates indicated that **1** was only physisorbed on the surface (Fig. 6). As the temperature was raised to 120–130°C, new signals for both C1s and Br3d

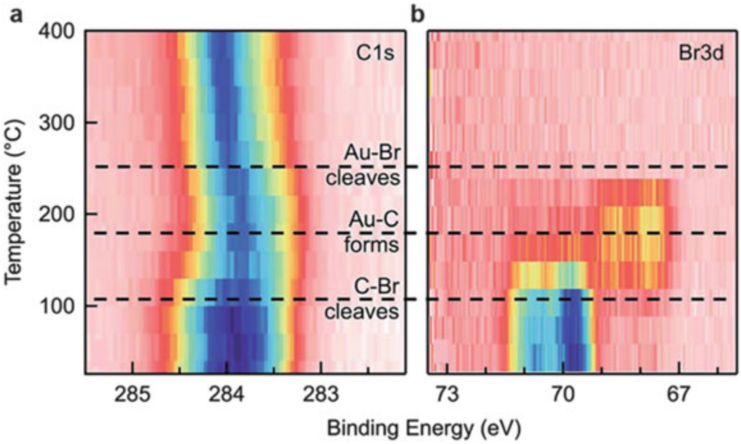

Fig. 6 Temperature-dependent XPS for (**a**) C1s and (**b**) Br3d for **1** on Au(111). The three *dashed lines* correspond to the onset of homolytic C–Br cleavage, surface stabilized radical intermediates, and desorption of Br from Au(111). Reproduced with permission from [30], Copyright (2014) Royal Society of Chemistry

appeared that were consistent with the formation of chemisorbed carbon and bromine radicals. At 180°C the reaction was complete and only the chemisorbed C and Br species could be observed. Further heating led to desorption of bromine (Br3d doublet at 68/69 eV disappeared) whereas the carbon-centered radical later underwent recombination to form the polyanthracene precursor. Experimental data indicate that the radical step-growth polymerization precedes desorption of Br from the Au(111) surface by a few degrees [32]. The subtle difference between Br desorption and C–C bond formation energy is important, as omnipresent Br atoms on the surface can act as chain termination or radical transfer reagents during the step-growth polymerization phase. Although Br and I groups are privileged motifs among molecular GNR precursors, the structural scope is not limited to carbon–halogen bonds. Recent encouraging examples include thermally induced isomerization of enediynes that efficiently and regioselectively generate Csp^2-centered radicals that can recombine to form new C–C bonds [33, 34].

A more complex factor that has to be considered in the design of competent molecular precursors is the sample preparation procedure itself. Surface-mediated GNR growth is commonly performed in a UHV system because the nature of the radical recombination that leads to the extended polymer precursors requires an atomically clean surface. The molecular building blocks for GNRs are commonly evaporated from a crucible onto the face of a single crystal of metal thin film. This step mandates a thermal stability that is compatible with the sublimation temperature, and preferably below the uncatalyzed activation of the thermally labile groups. Furthermore, an exceptionally high purity of the molecular sample is instrumental to the formation of extended polymers, as even trace impurities (<0.1%) or decomposition products can readily sublime and form a monolayer coverage on the metal substrate before the desired building blocks can evaporate. Finally, even at 10^{-9} Pa, sublimation itself places an upper limit on the size of molecular precursors that can be deposited efficiently and restricts the nature, position, and size of substituents that can be incorporated into the structure of the resulting GNR.

Even if all the above criteria are met through the rational design of a molecular building block, a series of less predictable factors remain. These include the preferred adsorption geometry and adsorption energy of the molecules on the substrate. Predicting the self-assembly of molecules on a surface solely based on routine DFT calculations in the gas phase is a daunting challenge that increases exponentially with any additional degree of freedom or decrease in symmetry inherent to the molecule itself. In addition to the numerous orientations a molecule can adopt with respect to the crystallographic axes and the unit cell of the underlying substrate, any nonplanar molecule inherently has multiple surfaces that can adsorb to the substrate. Furthermore, additional intermolecular interactions can induce formation of long-range ordered molecular islands in the monolayer. Because step-growth polymerization relies on formal radical recombination, the physisorbed or chemisorbed intermediates have to come close enough to form a covalent C–C bond. During this critical step, the relative orientation of reaction centers and the steric demand imposed by the immediate surroundings both contribute to the height of the activation barriers and, thus, to product distribution. This is illustrated by the fact that two molecules of the nonplanar dibromobisanthrene **1** adsorbed on an Au(111) surface (dihedral angle between anthracenes ~80°) can approach one another in a staggered conformation that allows the fusion of both radical centers. If a planar 9,10-dibromoanthracene is used instead, the repulsive interaction between *peri*-hydrogens effectively prevents the formation of a new C–C bond. A well-balanced molecule–surface interaction is as important as the relative orientation. Adsorbates that interact too weakly with the substrate tend to form irregular clusters along crystallographic defects and step edges or desorb prematurely during the thermal activation steps. If the adsorption energy is too large, the diffusion of activated species across the surface can become a rate-limiting step.

Although molecular designs greatly benefit from structural analogies to proven systems, even in these cases the sheer complexity inherent in balancing the multitude of intermolecular forces, along with the significant variability that comes with different metal substrates and crystallographic faces, has thus far prevented the development of any practical predictive model. An illustrative example is the growth of GNRs from **1** on Au(111) compared with Cu(111) (Fig. 7). On Au (111) substrates, **1** grows 7-AGNRs as expected from design considerations [22]. On the more active Cu(111) surface, however, the resulting GNRs feature a planar chiral (3,1) edge pattern resulting from the lateral fusion of molecular building blocks at an angle of 77° with respect to the intended axis of propagation [35–38].

The last and arguably more controllable step is the cyclodehydrogenation of the GNR polymer precursor on the metal substrate. If the molecular building blocks

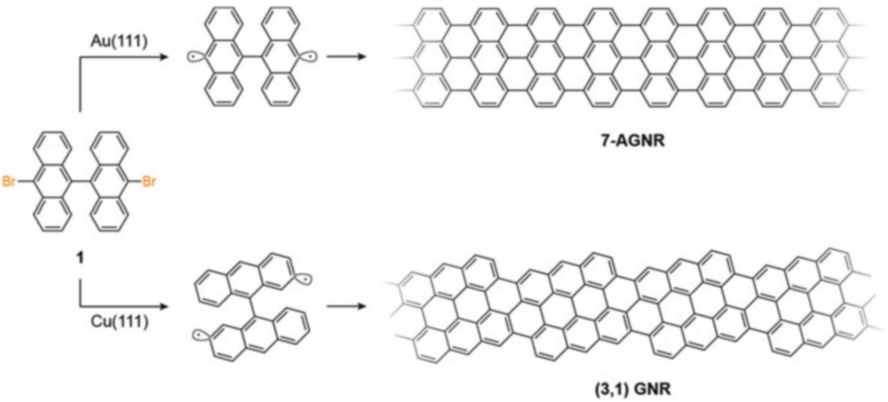

Fig. 7 7-AGNR and chiral GRNs featuring a (3,1) edge pattern formed from the same precursor **1** on Au(111) and Cu(111) surfaces, respectively [35–37]

have been carefully designed, every aryl ring can only fuse in one unique and predictable position. Björk et al. performed extensive DFT calculations based on the cyclization of a 9,9′-bianthracene model on Au(111) and demonstrated that the precious metal surface plays a key role in the cyclodehydrogenation step [26]. Although a number of plausible stepwise processes were considered, the lowest activation barrier is associated with a concerted mechanism that sees the aryl rings rotate toward one another to form a new C–C bond while the *ipso* H atoms at the corresponding positions are transferred to the Au(111) substrate as atomically chemisorbed hydrogen. The metal substrate thus acts as a catalyst that facilitates the dissociation of H atoms. An additional cooperative effect has been observed in the study of extended *oligo*-anthracene model systems. The planarization and the strain induced by the first random cyclodehydrogenation drastically decrease the activation barrier for the cyclization of immediately adjacent rings. On an Au(111) surface, cyclodehydrogenation proceeds in a cascade emanating in both directions from an initial arbitrary starting point. Although this special case of positive cooperativity is rather unique to the synthesis of 7-AGNRs from **1** and related structures, lowering of the activation barrier for adjacent cyclizations induced by the distortion imparted by the initial C–C bond formation is a commonly observed phenomenon in surface catalysis on Au, Ag, and Cu.

3.2 *Rationally Tuning the Energy Structure in Bottom-Up-Fabricated GNRs*

Quantum mechanical calculations have proven to be a valuable tool for prediction of the band structure of functional organic materials. A variety of theoretical models (e.g., tight binding, density functional theory, and *GW* approximations that include the self-energy of a many-body system of electrons) have been applied to GNRs and reflect varying levels of accuracy [39, 40]. Although the absolute numbers reflecting, for example, the magnitude of the band gap and the density of states (DOS) of the energy of the valence band (VB) and conductance band (CB) edges diverge significantly between various theoretical models, the underlying general trends are consistent throughout a family of structurally related GNRs. For consistency and to avoid confusion we will herein refer to calculations based on the *GW* approximation wherever possible.

Hydrogen-terminated GNRs featuring an armchair pattern along the edges are predicted to be intrinsic semiconductors. The magnitude of the band gap between the VB and CB edges roughly scales inversely with the width of the GNR (Fig. 8) [40]. This general trend is consistent within all three families of armchair GNRs: the width is expressed as the number of atoms $N = 3p$, $N = 3p + 1$, and $N = 3p + 2$ counted in a straight chain across a ribbon ($p = 0, 1, 2, 3, \ldots$). The smallest band gaps have been predicted for the $3p + 2$ series, whereas the largest band gaps are expected for members of the $3p + 1$ family. The width dependence of semiconducting AGNRs allows the dial-in of a desired band structure by tightly controlling the structure of the molecular precursor. Experimental determination of the band gaps in a family of AGNRs adsorbed on Au(111) supports this general trend. The quasi-particle band gaps of 7-, 9-, and 13-AGNRs determined by scanning tunneling spectroscopy (STS) are 2.3, 1.4, and 1.4 eV, respectively. Although 7- and 13-AGNRs, derived from **1** and **2** respectively, belong to the same family ($3p + 1$) and serve to illustrate the reduction in band gap for wider ribbons, 9-AGNRs derived from **3** fall into the intermediate $3p$ series and only coincidentally feature a band gap that is comparable to that of the significantly wider 13-AGNRs. Figure 9 depicts an overlay of d*I*/d*V* spectra for 7- and 13-AGNRs recorded on an Au(111) crystal [41]. The smaller intrinsic band gap of 13-AGNRs, corresponding to a peak-to-peak distance in a DOS plot, is straddled by the significantly larger gap of the

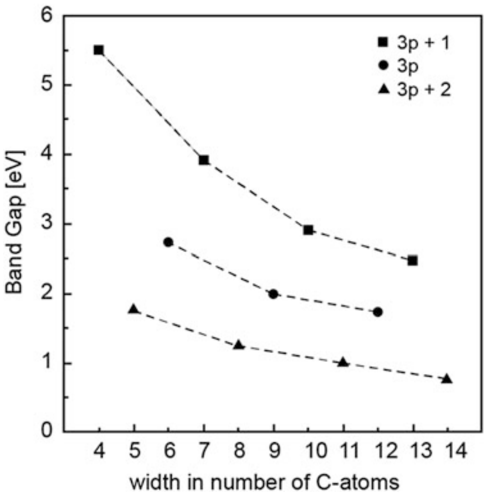

Fig. 8 Correlation of *GW* band gaps with the number of carbon atoms across the width of AGNRs. The three families of AGNRs are represented by *filled squares* ($3p + 1$), *circles* ($3p$), and *triangles* ($3p + 2$). AGNRs belonging to the same family are connected by *dotted lines* as a guide for the eye [40]

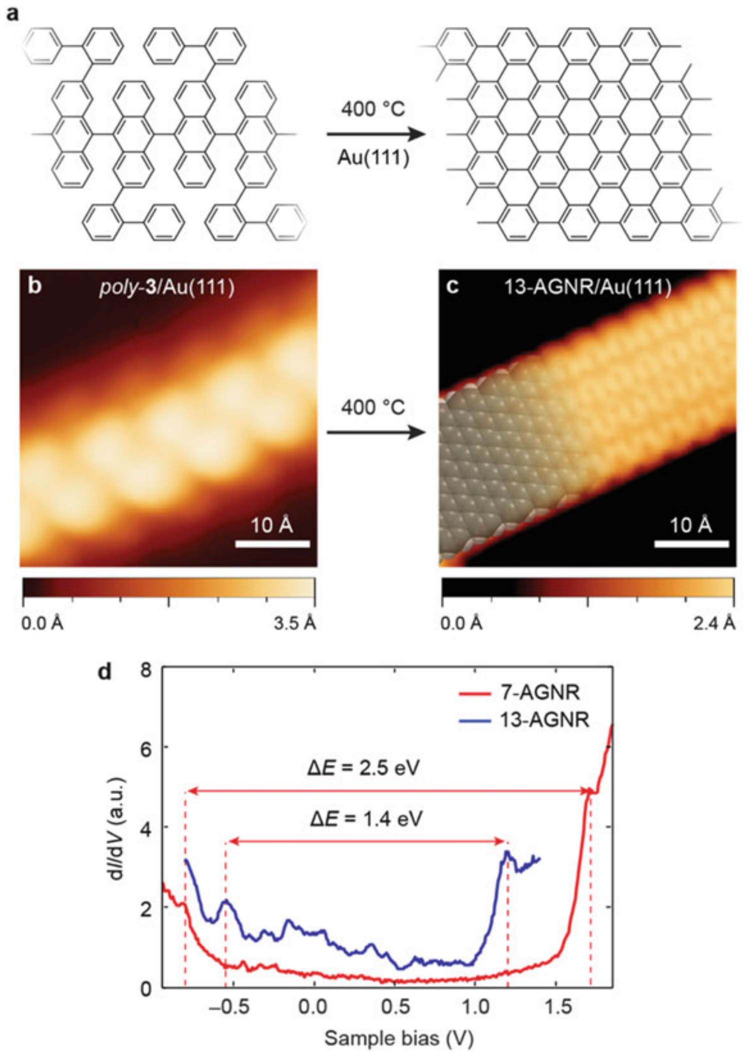

Fig. 9 (**a**) Synthesis of 13-AGNRs from **3**. At 400°C a cyclodehydrogenation sequence converts poly-**3** into 13-AGNRs. (**b**) STM image of poly-**3**. The polymers are nonplanar with an apparent height of 3.5 Å. (**c**) STM image of 13-AGNRs formed after annealing poly-**3** at 400°C. A CPK model of 13-AGNR has been overlaid onto the STM image as a guide for the eye. (**d**) d*I*/d*V* spectra of 13-AGNR (*blue*) and 7-AGNR (*red*) on Au(111). Adapted with permission from [41], Copyright (2013) American Chemical Society

7-AGNRs. It is worth noting that theoretical models based on the DFT *GW* approximation do not generally include a discrete interaction between the GNRs and the underlying metal substrate. A direct comparison between the calculated quasi-particle band gaps of isolated GNRs (3.8, 2.0, and 2.4 eV for 7-, 9-, and 13-AGNRs, respectively) and the experimentally determined band gaps is thus restricted by limitations in the accuracy of the models describing hybridization of the GNR with the surface states. Zhang et al. and Kimouche et al. expanded the series of AGNRs to include a member of the $3p + 2$ family associated with the smallest theoretically predicted band gaps. Both tetrabromonaphthalene **4** and the isomeric dibromoperylenes **5** serve as molecular precursors for 5-AGNRs [42, 43]. Although initial STS on Au(111) appeared to indicate an unusually large bandgap (2.8 eV), careful study of a series of oligomers derived from 5-AGNRs ranging in length from 2 to 14 monomer units (**5**) revealed a more detailed picture. In addition to the dominant signals previously assigned to the CB and VB edges, the study revealed a series of smaller peaks in the d*I*/d*V* spectrum that fall within the assumed band gap (Fig. 10). Reassignment of the CB and VB states led to reinterpretation of the DOS and revealed an exceptionally small band gap of 0.1 eV for ribbons featuring more than five monomer units [43]. This lower band

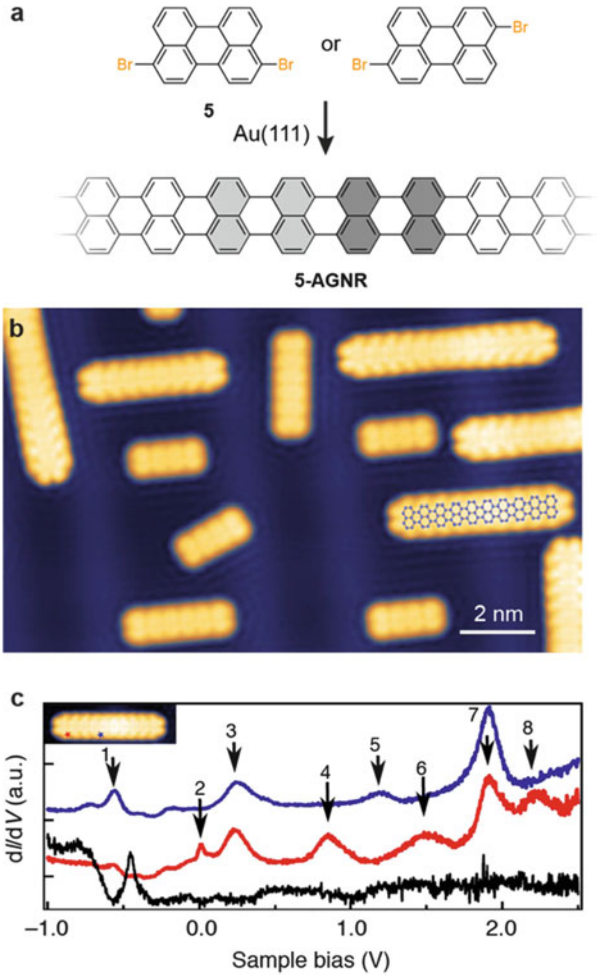

Fig. 10 (**a**) Synthesis of 5-AGNRs from **5**. (**b**) STM image of 5-AGNRs on Au (111). (**c**) d*I*/d*V* spectra acquired on short 5-AGNR segments comprised of 5 monomer units. The spectra were recorded at the positions (*red* and *blue stars*) marked in the STM inset

gap is consistent with the expected trend for the $3p + 2$ family (1.7 eV for 7-AGNRs).

In addition to varying the width of GNRs, the unique structural control inherent to a rational bottom-up synthesis offers a variety of alternative strategies for tailoring the electronic structure. CGNRs derived from the dibromotriphenylene precursor **6**, for example, can be thought of as GNRs composed of hexabenzocoronenes laterally fused at an angle of ~104° [22]. STS on Au(111) reveals an intermediate band gap of 2.0 eV [44]. For comparison, the theoretically predicted band gap calculated using the *GW* approximation is 3.5 eV. Optical spectroscopy of identical CGNRs shows a still-unresolved departure from these values. High-resolution electron energy loss spectroscopy (HREELS) and ultraviolet photoemission/inverse photoemission spectroscopy (UPS/IPES) show band gaps of 2.8 and 1.3 eV, respectively [45, 46]. A resolution of this apparent contradiction is pending further detailed investigation.

Liu et al. introduced a class of planar chiral GNRs derived from dibromobischrysene **7** [47]. The structure of these cove-edge GNRs (CeGNRs) resembles a zig-zag edge in which every fourth carbon atom has been replaced by hydrogen. Deposition of **7** on Au(111) followed by thermal annealing and cyclodehydrogenation yields GNRs ranging in length from 5 to 20 nm. The unique edge structure of these chiral GNRs is, however, unusually susceptible to unselective C–H activation. Concurrent hydrogen abstraction during the cyclodehydrogenation step leads to ubiquitous radical centers along the edges that undergo recombination or uncontrolled radical transfer processes. As a result of this insufficient selectivity, CeGNRs tend to fuse into larger irregular GNR aggregates at temperatures commensurate with the cyclodehydrogenation step. Optical spectroscopy along with ab initio DFT calculations (not including the *GW* approximation) indicate a potentially small band gap of 1.7–1.9 eV.

Narrow ZGNRs featuring a zig-zag pattern of hydrogen-terminated carbon atoms along the longitudinal edge feature a series of properties that are unique among bottom-up-fabricated GNRs. Theoretical calculations predict that the edge states are ferromagnetically coupled along one zig-zag edge and antiferromagentially with respect to the other edge. These spin-polarized electronic states are of great interest for advanced functional materials used in spintronics. Ruffieux et al. demonstrated the bottom-up synthesis of $N = 6$ ZGNRs (6-ZGNRs; where N is the number of carbon zig-zag chains counted across the width of the ribbon) from the unusual molecular precursor **8** (Fig. 11) [48]. Although all AGNRs and CGNRs feature a long axis that is aligned parallel to the armchair edge, the long axis in ZGNRs is perpendicular to the preferred growth direction of halogen-based surface polymerizations. The anchor-shaped design of molecular precursor **8** elegantly resolves this challenge by arranging in an alternating head-to-toe orientation that aligns the long axis of the GNR with the zig-zag edge while retaining the preferred relative orientation of the new C–C bond formed during radical step-growth polymerization. Lastly, the two additional methyl groups are incorporated into the structure of **8** to close the remaining gaps along the zig-zag edges of 6-ZGNRs. STS of 6-ZGNRs that have been transferred from the Au(111) gold

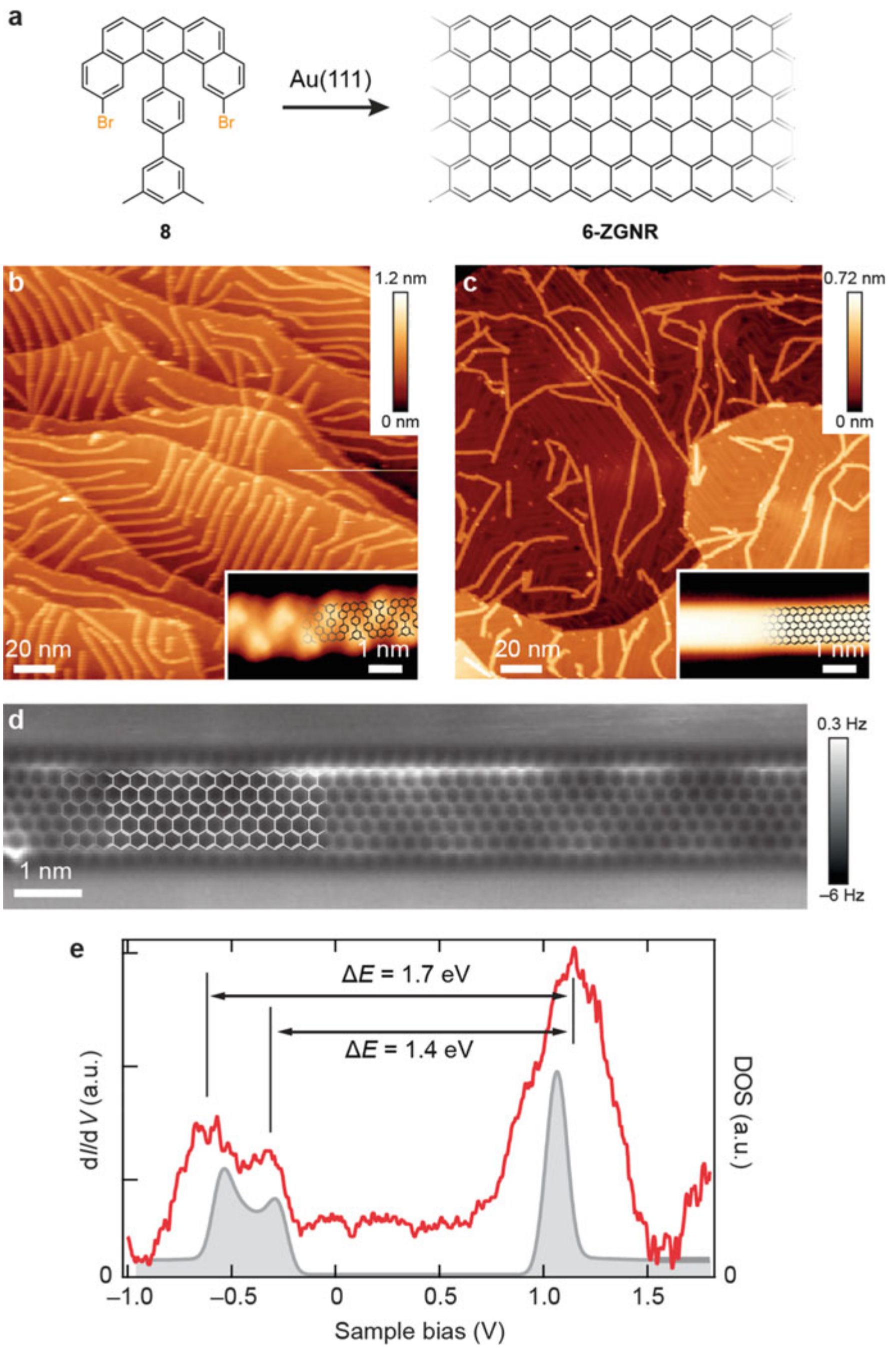

Fig. 11 (**a**) Synthesis of 6-ZGNRs from **8**. (**b**, **c**) Large area STM images of poly-**8** and 6-ZGNRs on Au(111). (**d**) ncAFM of 6-ZGNRs showing the hydrogen-terminated zig-zag edge. (**e**) d*I*/d*V* spectrum (*red*) recorded at the zig-zag edge of a 6-ZGNR partially suspended on a NaCl

substrate onto an insulating NaCl layer show a band gap of 1.5 eV. Because the 6-ZGNR is mechanically decoupled from the interaction with the Au surface states, the experimental values superbly match the theoretically predicted band gap (1.4 eV) calculated using the single particle Green's function and a screened Coulomb interaction (*GW* approximation). Further investigation of the exotic electronic and magnetic properties of ZGNRs, along with redoubled efforts to stabilize the chemically reactive zig-zag edges, is ongoing and holds great promise for the development of graphene-based spintronic devices.

3.3 Substitutional Doping in Bottom-Up-Fabricated GNRs

Although the extraordinary structural control innate to a rational bottom-up synthesis of functional graphene nanomaterials is superior to that available for classical inorganic semiconductors, the increased complexity of structure–function relationships critically limits robust performance-driven material design. Instrumental tools and strategies to tailor the band structure and the Fermi level of GNRs require a deeper understanding of how atomistic structure guides the alignment of energy states. In particular, the concept of doping in atomically defined nanoscale graphene structures extends beyond the bounds of classical theories derived for inorganic semiconductors and is the topic of extensive exploration. Theoretical models predict that the energies of the VB and CB of semiconducting GNRs can be tuned by introducing a highly regular pattern of electron-donating or electron-withdrawing functional groups or atoms along the edges of GNRs (Fig. 12). Early on, this edge-doping was at the center of investigation as it represents the least-intrusive chemical modification that can readily be incorporated into the structure of molecular precursors. Bronner et al., Cai et al., and Vo et al. demonstrated that the introduction of nitrogen atoms in the form of pyrimidine and pyridine rings into the edges of CGNRs induces a rigid band shift (Fig. 13) [44, 45, 49]. Theoretical calculations indicate that the magnitude of the band gap shift correlates with the number and, to a lesser extent, position of the heteroatoms. Electronic HREELS spectra of CGNRs derived from **6** (no N atoms), **9** (one N atom), and **10** (two N atoms) reveal that the overall magnitude of the band gap remains largely unchanged (2.8, 2.8, and 2.7 eV, respectively). UPS spectroscopy shows a rigid shift of the entire band structure to lower energy with increasing number of N atoms (~0.1 eV per atom). STS of CGNRs grown on Au(111) from dipyrimidine precursor **11** (four N atoms) show a band gap of 2.0 eV, which is comparable to that of the parent unsubstituted CGNRs. Yet, both the VB and CB of CGNRs derived from **11** are shifted by 1.1 eV to lower energy. This general trend is supported by DFT

Fig. 11 (continued) monolayer island on Au(111) and calculated DOS (*gray*). Reproduced with permission from [48], Copyright (2016) Nature Publishing Group

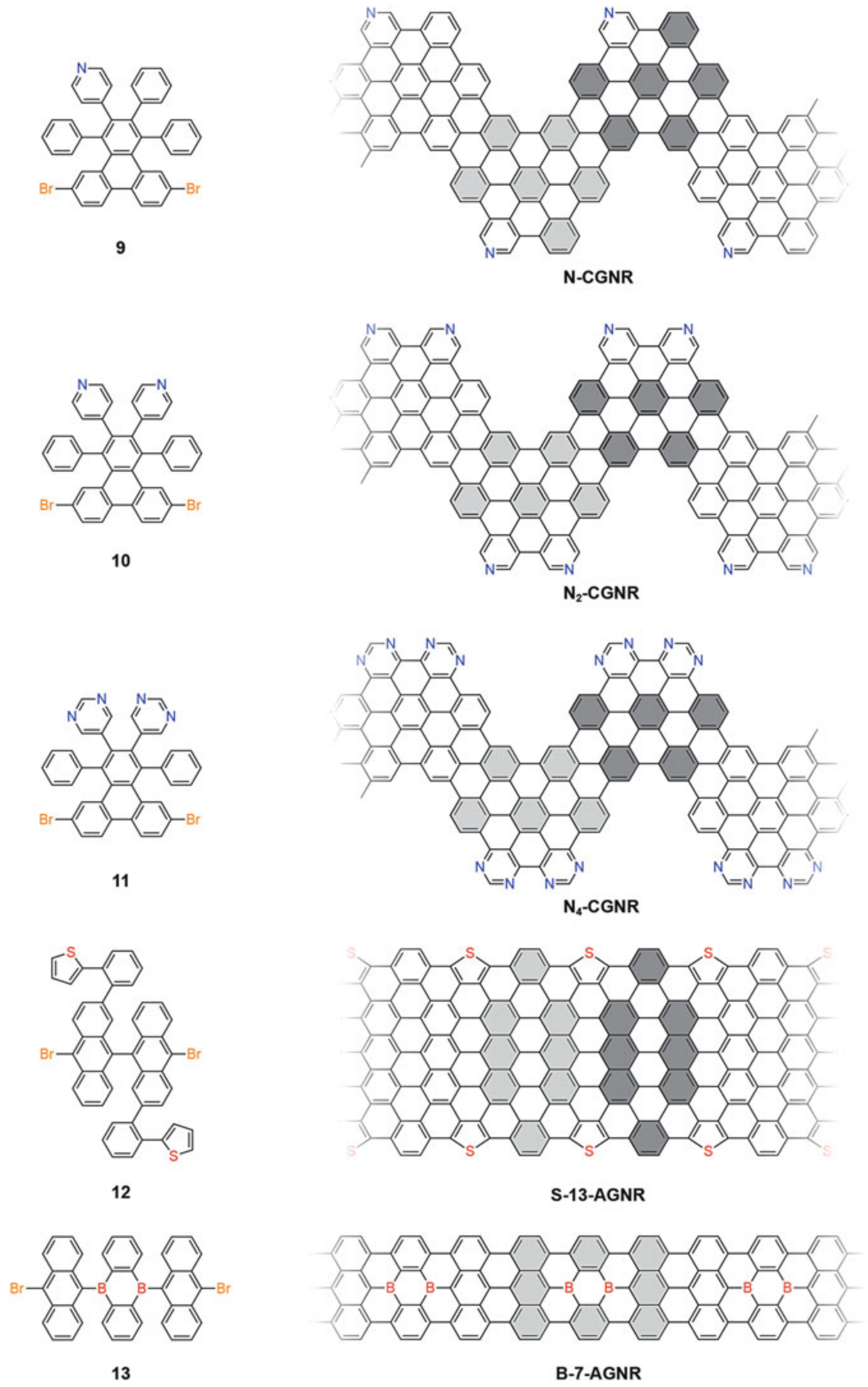

Fig. 12 Examples of nitrogen edge-doping in CGNRs [44, 45, 49], sulfur edge-doping in 13-AGNRs [50], and backbone boron doping in 7-AGNRs [51, 52]

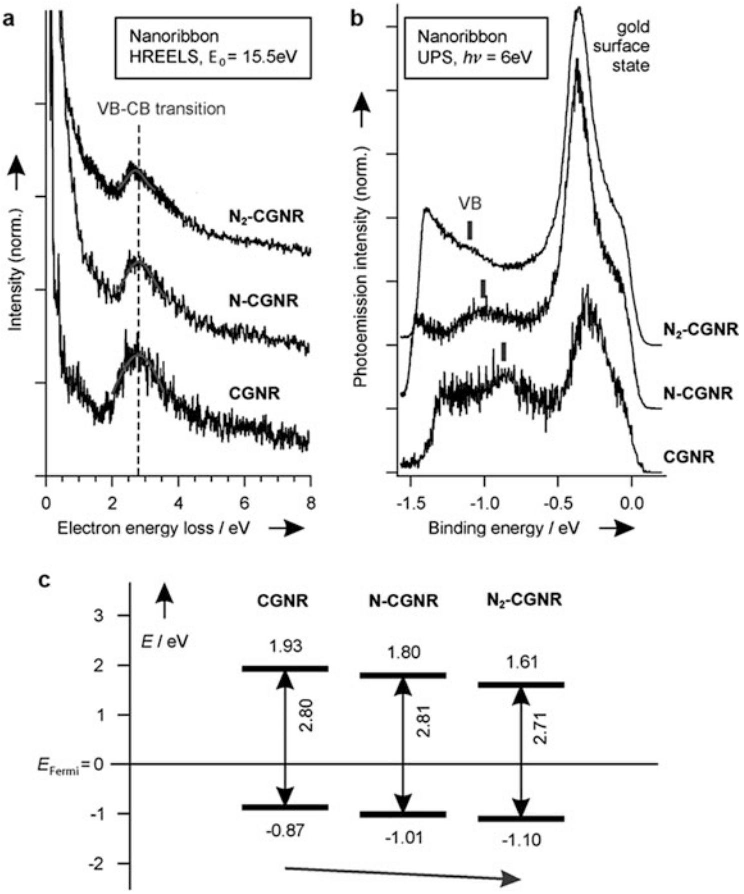

Fig. 13 (**a**) Electronic HREELS spectra for CGNRs edge-doped with zero, one, and two nitrogen atoms. The VB–CB transition is essentially unperturbed by the doping. (**b**) UPS spectra of CGNRs, N-CGNRs, and N_2-CGNRs on Au, showing a shift in the VB edge toward lower energy. (**c**) Summary of the band gap, VB, and CB alignment derived from HREELS and UPS spectroscopy. Reproduced with permission from [45], Copyright (2013) John Wiley and Sons

calculations and extends the series of nitrogen edge-doping patterns in CGNRs up to eight N atoms. Based on theory, an average shift of ~0.13 eV can be attributed to each N atom. Computationally, this concept has been applied to the introduction of boron atoms along the edges of CGNRs. As expected, the direction of the rigid band shift is inverted (toward higher energy) while the magnitude amounts to only ~0.06 eV per boron atom.

Examples of edge doping are not restricted to the CGNR family. Nguyen et al. demonstrated that a similar concept can be applied to the structurally more diverse family of AGNRs and also extended to include group VI elements [50]. The molecular precursors for sulfur-doped AGNRs (**12**) were derived from the structure

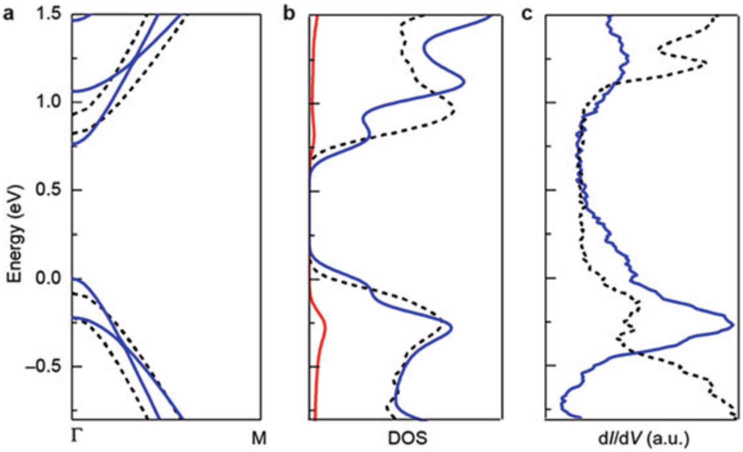

Fig. 14 Calculated band structure of (**a**) S-13-AGNR (*blue*) and undoped 13-AGNR (*black*). (**b**) Calculated DOS of S-13-AGNR (*blue*), the partial density of states (PDOS) of sulfur orbitals (*red*), and the DOS of undoped 13-AGNR (*black*). (**c**) Experimental d*I*/d*V* spectrum for S-13-AGNR (*blue*) and undoped 13-AGNR (*black*). Reproduced with permission from [50], Copyright (2016) American Chemical Society

of **2** by replacing one phenyl ring on each side by a thiophene. Even though the Pauling electronegativity of S atoms is only marginally different from that of C atoms (2.55 versus 2.58), hybridization of the heteroatom lone-pair with the conjugated π-system enhances the energy splitting between the CB (VB) and CB + 1 (VB − 1), respectively (Fig. 14). Reorganization of the energy band structure leads to an overall reduction in the intrinsic band gap compared with the parent 13-AGNRs. A notable distinction between nitrogen-doping in CGNRs and sulfur-doping in AGNRs is the overlap of the filled lone pair on sulfur (p-symmetry) with the p-orbitals on carbon atoms that form the backbone of the GNR. The nitrogen lone pair in CGNRs is orthogonal and cannot interact directly with the GNR π-system. This previously unappreciated distinction opens entirely new avenues for tailoring the DOS proximal to the band edges, a feature particularly relevant to tuning optical transitions in GNRs.

An indispensable technology required for the development of GNR-based electronic devices is the ability to tune the local charge carrier density by introducing shallow donor (n-type) and acceptor states (p-type) proximal to the CB and VB edges, respectively. Edge-doping, as outlined above, however, only shifts the energy of band edges without introducing dopant states within the band gap. Substitutional n-/p-doping, that is, the introduction of filled/empty donor or acceptor states into the intrinsic gap of atomically defined GNRs, instead requires the incorporation of dopant heteroatoms at deterministic positions, preferably along the backbone of the ribbon where the filled/empty p-orbitals are forced into conjugation with the extended π-system. Cloke et al. and Kawai et al. were the first to demonstrate rational backbone doping in AGNRs using 5,10-bis(10-bromoanthracene-9-

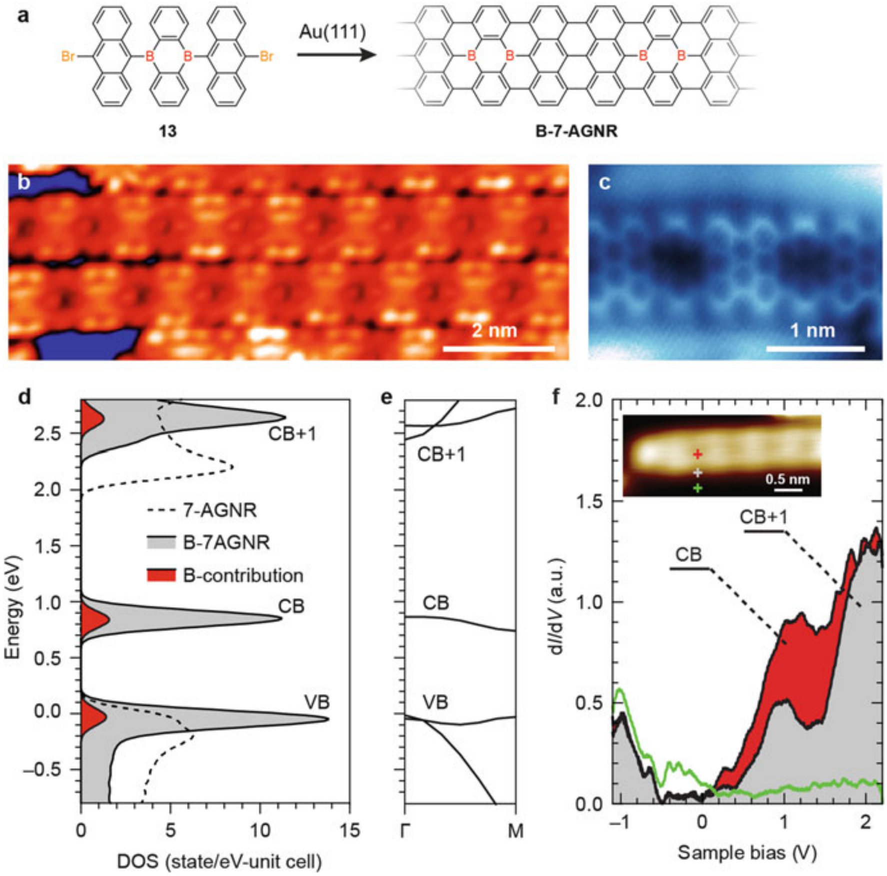

Fig. 15 (**a**) Bottom-up synthesis of B-7-AGNRs on Au(111). (**b**) STM topographic image of fully cyclized B-7-AGNRs. (**c**) ncAFM image of B-7-AGNRs. The position of boron dopants appears darker in the frequency shift image because the empty p-orbital on B atoms strongly interacts with the free valences of the underlying Au substrate. (**d**) Calculated total DOS for B-7-AGNRs (*gray*) and the contribution of B atoms to the DOS (*red*) using the *GW* approximation and including screening effects from the Au(111) substrate. For comparison, the DOS for undoped 7-AGNRs is plotted as a *dotted line*. VB maximum is set to 0 eV. (**e**) Calculated quasiparticle band structure of B-7-AGNRs (using *GW* approximation). (**f**) d*I*/d*V* spectrum of B-7-AGNRs recorded at the positions marked in the *inset*. CB and CB + 1 can clearly be identified in the spectrum. The position of the VB coincides with the surface state of the Au(111) substrate. Reproduced with permission from [51], Copyright (2015) American Chemical Society

yl)-5,10-dihydroboranthrene (**13**) as a molecular precursor for 7-AGNRs [51, 52]. Noncontact atomic force microscopy (ncAFM) with CO-functionalized tips revealed a characteristic pattern of anthracene/boranthrene/anthracene units along the backbone of the GNR. In Fig. 15, the contrast at the position of boron atoms appears darker as a result of strong interaction of the empty p-orbitals with the surface states of the underlying metal. First-principle calculations based on the

GW approximation, including screening effects from the underlying Au(111) substrate, show a new empty state in the middle of the band gap of 7-AGNRs. The DOS of both the VB and this new CB show significant contributions (~10%) from B atoms. Substitutional boron-doping along the backbone of 7-AGNRs thus introduces a deep-lying acceptor band approximately 0.9 eV above the VB maximum. The theoretically predicted quasiparticle band gap is significantly smaller than that of the undoped pristine 7-AGNRs (~2.1 eV) calculated at same level of theory. Interpretation of d*I*/d*V* spectra for boron-doped 7-AGNRs on Au(111) is challenging because the peak corresponding to the VB coincides with the surface states of the Au(111) substrate. A clearer signal can be obtained for the CB and CB + 1 states at 1.0 and 1.6 eV. Better results have recently been obtained by growing boron-doped 7-AGNRs on Ag(111) surfaces. The surface state of Ag(111) is shifted with respect to Au(111) and allows unambiguous identification of all four VB–1 (−1.0 eV), VB (−0.3 eV), CB (1.1 eV), and CB + 1 (1.5 eV) states for boron-doped 7-AGNRs. As expected, the experimental band gap of ~1.4 eV is significantly smaller than the corresponding gap for pristine 7-AGNRs (2.3 eV).

3.4 Spatial Isolation of Energy States in Segmented GNRs

Rectification, resonant tunneling, and light harvesting are just a few examples of dynamic processes that are intimately linked to the transport of charge carriers across a boundary between materials with dissimilar energy band structures. Although harnessing the corresponding performance in a single GNR holds great promise for further device miniaturization and superior energy efficiency, the microscopic structure and the underlying physics of energy band alignment at intraribbon heterojunction interfaces is still a topic of intense investigation. The unique control inherent to rational bottom-up synthesis, together with high resolution imaging (STM, ncAFM) and spectroscopic (STS) tools, provides a path to deterministic design of single GNR functional heterostructural devices. Although preparation of segmented polymers through traditional solution-based methods is well established in the literature, the surface-facilitated syntheses described herein impose a series of new challenges. The design of segmented GNRs featuring, for example, two distinctive molecular precursors, two different band structures, or two unique doping patterns requires that both building blocks A and B are structurally compatible. This requirement guarantees that cyclodehydrogenation at the interface between two segments proceeds efficiently and the resulting heterojunctions are atomically defined. The second, arguably more challenging problem, is the development of new synthetic strategies that provide control over the sequence and segmentation in GNR heterostructures. As discussed in Sect. 3.1, step-growth polymerization of activated molecular building blocks on a precious metal surface relies formally on a radical recombination mechanism. The sequence at which monomers are incorporated into the growing polymer chain is largely random and current strategies lack the exquisite control developed for block-copolymer synthesis in solution.

Cai et al. demonstrated the assembly of CGNR heterojunctions formed from molecular building blocks **6** and **11** [53]. Alternate evaporation of both precursors onto an Au(111) surface held at 200°C followed by standard cyclodehydrogenation leads to CGNRs featuring an alternating pattern of segments composed of **6** and **11**. Although sequential deposition offers rudimentary control over the concentration of activated building blocks on the surface, the random nature and unfavorable kinetics of the step-growth process do not provide GNRs with a reproducible sequence of heterojunctions. Although CGNR segments formed from **6** and **11** are structurally almost indistinguishable by topographic STM, the difference in their composition becomes apparent in STS mapping (Fig. 16). The d*I*/d*V* maps recorded at -0.35 and -1.65 V show a distinctive alternating contrast characteristic for the VBs of CGNRs formed from **6** and **11**, respectively. The band gap in the nitrogen edge-doped segments is rigidly shifted to a lower energy with respect to the undoped CGNRs. DFT calculations (Fig. 17) reveal that the electronic structure of a seamlessly fused **6/11** CGNR interface resembles a staggered gap type II heterojunction. The VB and CB are offset by 0.45 and 0.55 eV, respectively. The band bending at the interface is exceptionally sharp. The band structures reach essentially bulk properties within only 2 nm of the interface. The significant electrostatic potential across the **6/11** CGNR heterojunction has promising implications for device applications that require efficient charge separation, such as GNR-based photovoltaics.

Chen et al. successfully assembled intraribbon heterojunctions comprising fused segments of 7- and 13-AGNRs [54]. Co-deposition of molecular precursors **1** and **3** onto an Au(111) surface held at 24°C, followed by stepwise annealing at 200 and 400°C, leads to extended AGNRs featuring alternating widths (Fig. 18). The narrower segments (~1.3 nm) are composed of 7-AGNRs and the wider segments (~1.9 nm) correspond to 13-AGNRs. The d*I*/d*V* spectra recorded at the highlighted positions above the respective GNR segments reflect the expected band structure for 7- and 13-AGNRs: a large band gap (2.7 eV) for the 7-AGNR segment and a small band gap (1.5 eV) for the 13-AGNR segment. The respective band structures are highly localized in their respective segments and do not significantly extend beyond the heterojunction. If the STM tip is placed immediately above a junction between 7- and 13-AGNRs, two additional highly localized states (1.25 and 1.15 V) can be observed in the d*I*/d*V* spectrum. These states are unique to the interface and lie just below the CB of the 13-AGNRs. The relative band alignment is reminiscent of a straddling gap type I semiconductor junction. The lowest unoccupied (highest occupied) state in the $N = 13$ segment is lower (higher) than that in the $N = 7$ segment. In this unique band arrangement, a 7–13–7-AGNR sequence can be thought of as a quantum well for charge carriers trapped in the 13-AGNR segment. This architecture provides opportunities for designing graphene quantum dot devices with subnanometer feature size.

Although the above examples highlight the functional complexity that can be integrated into a single GNR, the limited control over the length and sequence of

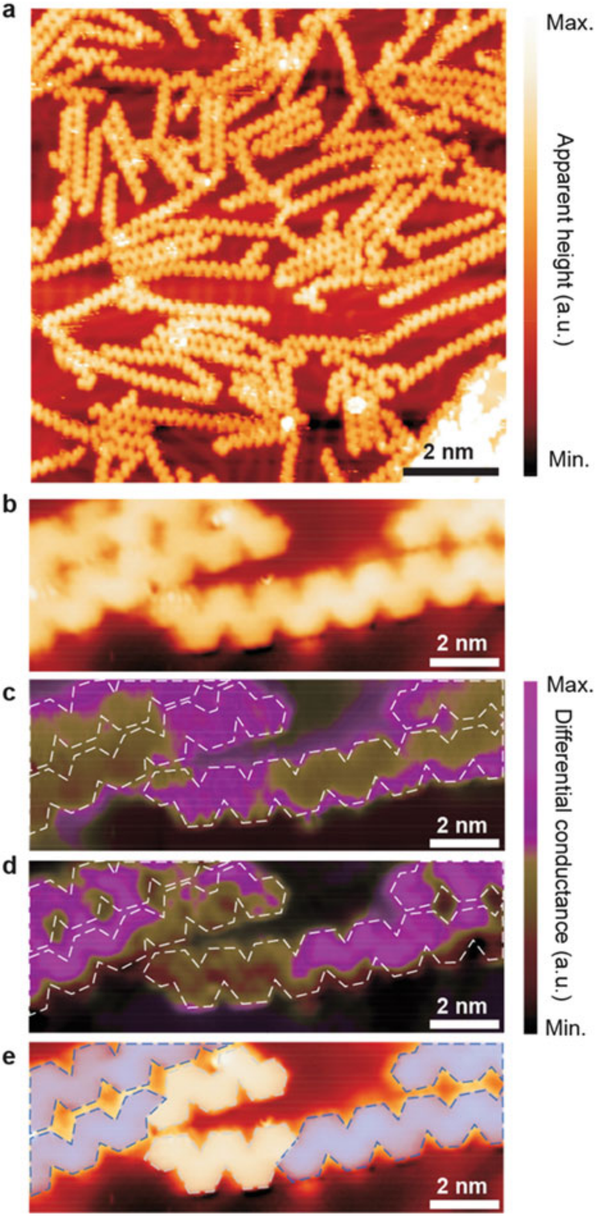

Fig. 16 (**a**) Large area STM image of segmented CGNRs formed by sequential co-deposition of **6** and **11**. (**b**) STM topographic image of a **6/11** CGRN interface. (**c**, **d**) d*I*/d*V* maps recorded at −0.35 V and −1.65 V. (**e**) Overlay of topographic STM image illustrating the segmentation pattern in **6/11** CGRNs. Reproduced with permission from [44], Copyright (2014) Nature Publishing Group

individual segments within bottom-up-fabricated GNR remains a serious challenge. An alternative to the sequential co-deposition strategy outlined above has been proposed by Blankenburg et al. [55]. They noticed that the cyclodehydrogenation of polyanthracene, the intermediate resulting from radical polymerization of **1** on Au(111) surfaces, can be stopped at an intermediate stage. Because

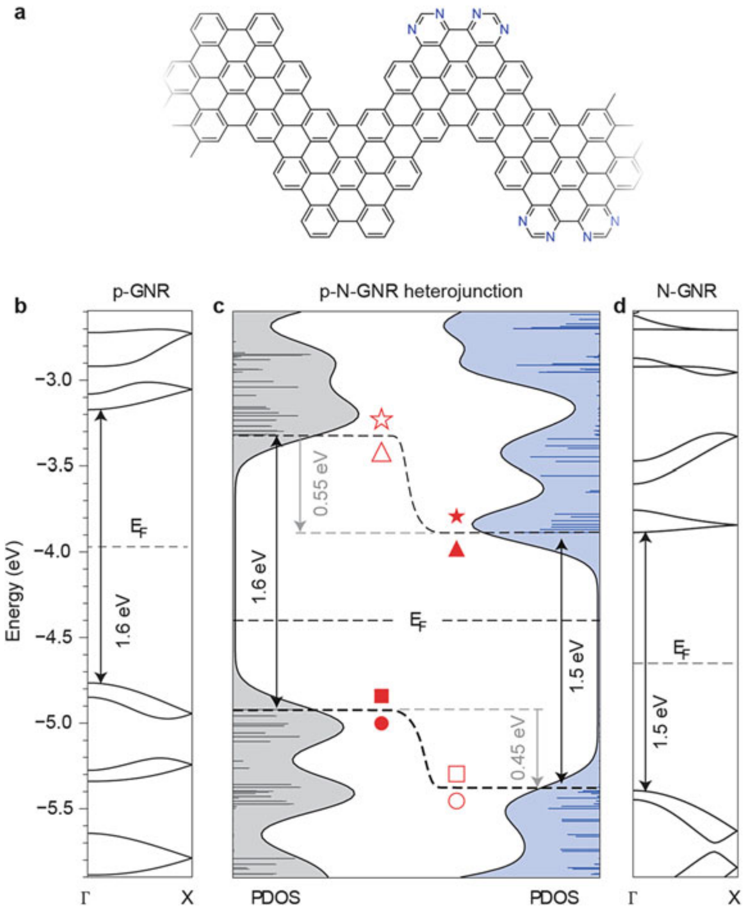

Fig. 17 (**a**) Structure of a **6/11** CGNR heterojunction interface. (**b**, **d**) DFT calculated band structure of pristine CGNR (p-GNR) (**b**) and nitrogen-doped CGNR (N-GNR) (**d**). (**c**) PDOS of the p-GNR segment (*left*, *grey*) and the N-GNR segment (*right*, *blue*) of the heterojunction shown in (**a**). The p-N-GNR heterojunction exhibits a staggered gap configuration with band offsets of 0.45 eV (VB) and 0.55 eV (CB). Reproduced with permission from [44], Copyright (2014) Nature Publishing Group

cyclodehydrogenation proceeds through a cooperative mechanism (see Sect. 3.1) along the backbone of the GNR, the reaction can be stopped at a stage where segments of fully cyclized and partially cyclized 7-AGNRs coexist within the same ribbon. STM images of 7-AGNRs featuring partially cyclized 5^+-AGNR segments are depicted in Fig. 19. Although this method formally yields GRN heterojunctions, there is no control over the sequence or the position of the junctions within the ribbon. If cyclodehydrogenation is induced by STM tip pulsing, segments of partially cyclized 5^+-AGNR could selectively be converted into 7-AGNRs. Although STM tip manipulation of individual GNRs is certainly not a viable

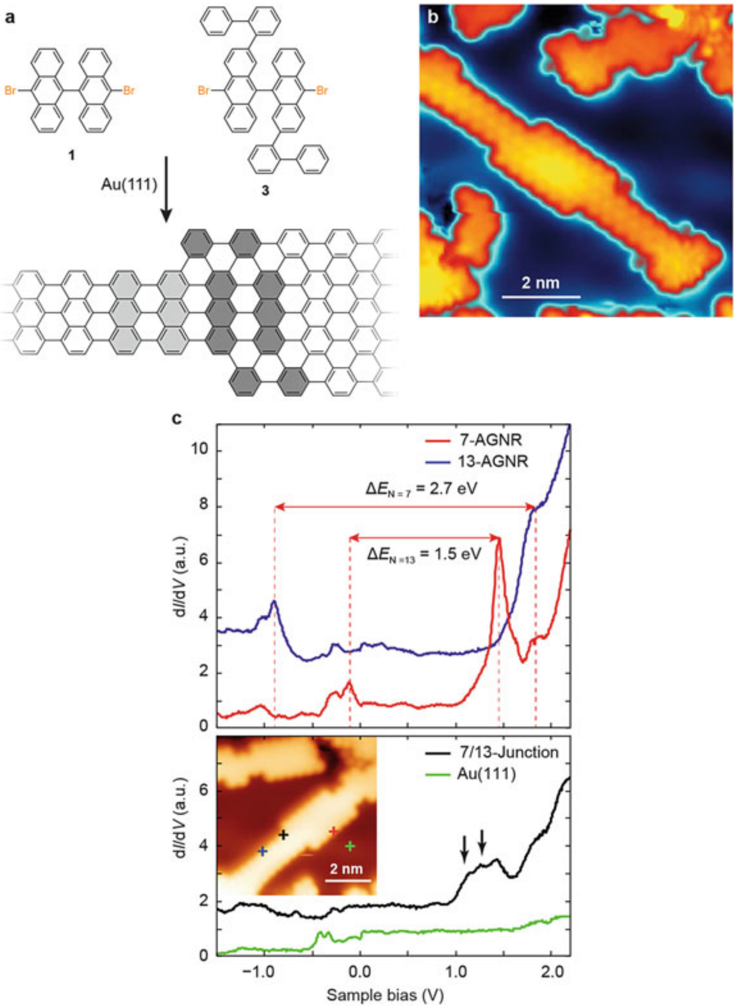

Fig. 18 (**a**) Synthesis of 7/13-AGNR heterojunctions from molecular building blocks **1** and **2**. (**b**) STM topographic image of a 7/13-AGNR heterojunction. (**c**) d*I*/d*V* spectroscopy of 7/13-AGNR heterojunction electronic structure recorded on a 7-ANGR segment (*blue*), a 13-AGNR segment (*red*), at the 7/13-AGNR heterojunction (*black*), and on the Au(111) surface. Reproduced with permission from [54], Copyright (2015) Nature Publishing Group

strategy for bulk fabrication, the use of a secondary patterning step could overcome the challenges inherent to uncontrolled step-growth polymerization.

Marangoni et al. demonstrated an alternative edge-doping strategy for obtaining segmented CGNRs that relies on late-stage interconversion of a reactive functional group [56]. Rather than relying on the co-polymerization of two dissimilar molecular precursors, the structure of dibromotriphenylene **14** incorporates a 9-methyl-9*H*-carbazole substituent as an internal reactive moiety along the convex

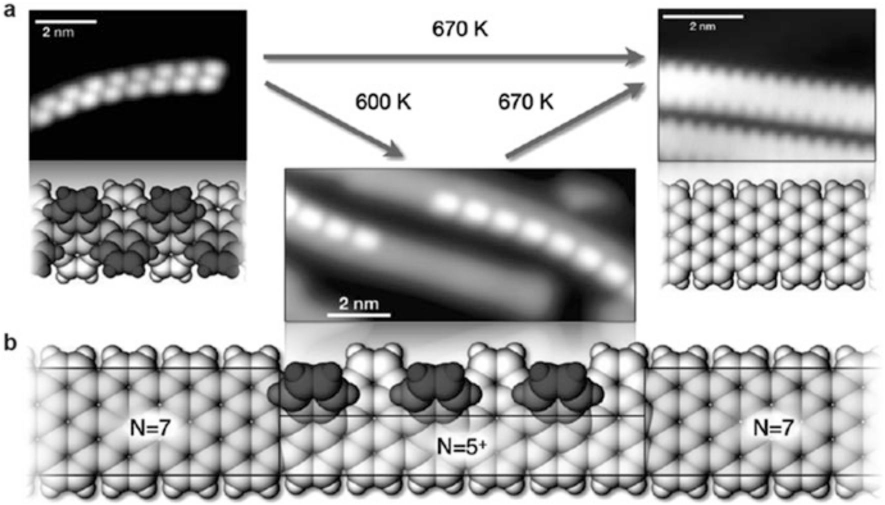

Fig. 19 GNR heterojunctions obtained by partial cyclodehydrogenation of polyanthrylene oligomers. (**a**) STM images and CPK models demonstrating the synthesis of AGNRs starting from poly-**1** on Au(111) substrate. (**b**) Annealing at a reduced temperature of 600 K results in partial cyclodehydrogenation and produces intraribbon 7/5$^+$/7-AGNR heterojunctions. Reproduced with permission from [55], Copyright (2012) American Chemical Society

protrusions of CGNR. Thermal activation of 9-methyl-9*H*-carbazole interconverts the functional group into either an electron-rich carbazole, by cleavage of the N–CH_3 bond, or an electron-deficient phenanthridine group, through a radical ring expansion mechanism. ncAFM images (Fig. 20) clearly show the segmented structure in CGNRs featuring either five-or six-membered rings along the edges of the GNR. Late-stage functionalization strategies hold great promise in the context of rational GNR heterostructure engineering as they potentially allow site-specific doping of prefabricated GNRs through a secondary activation step using, for example, light, heat or current.

4 Conclusion

The rational bottom-up synthesis of GNRs on solid supports has been instrumental in developing fundamental understanding of the exotic physical properties emerging from lateral quantum confinement effects in graphene nanostructures. The unique insights gained from width modulation, edge doping, backbone doping, and the deterministic design of intraribbon GNR heterojunctions have demonstrated their potential and inspired new perspectives for their implementation in future generations of electronic devices. Application of these visionary concepts still faces a multitude of technical challenges that require a coordinated interdisciplinary approach, including the development of novel synthetic tools and techniques

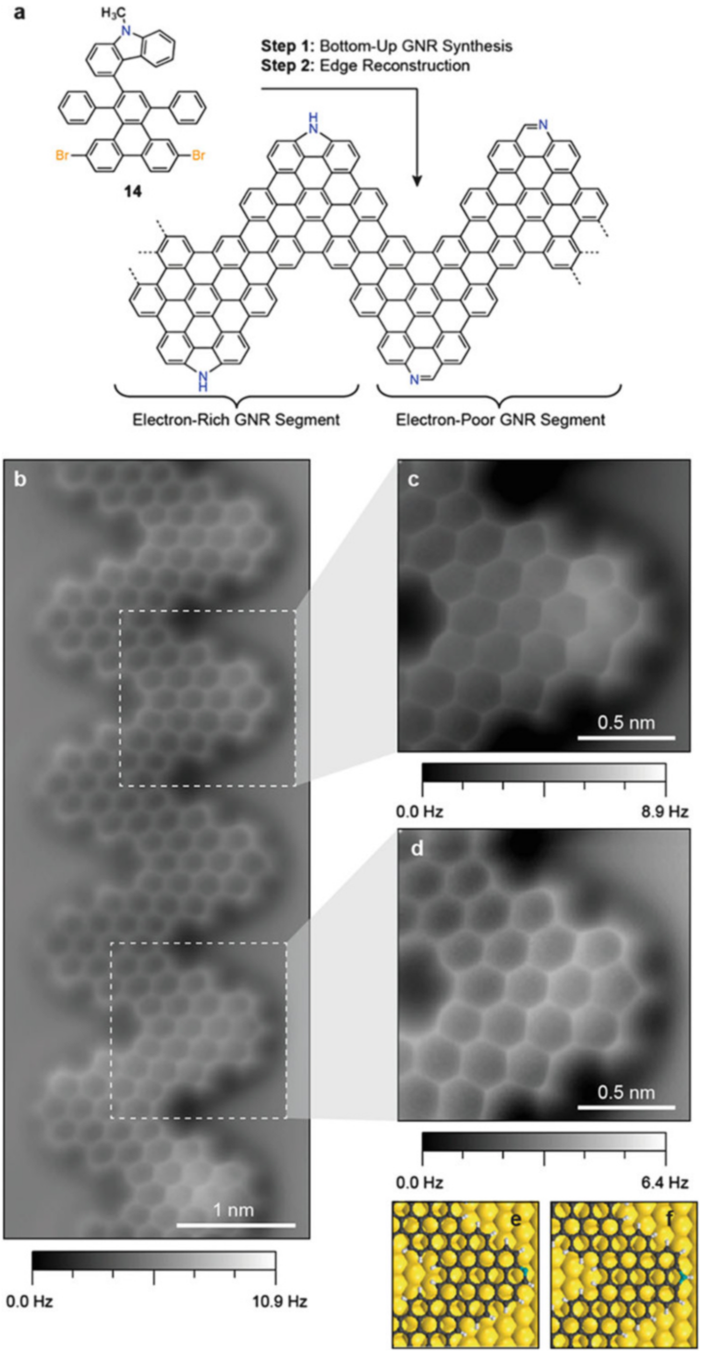

Fig. 20 (**a**) Bottom-up synthesis of segmented nitrogen-doped CGNRs through edge reconstruction. Electron-rich carbazole and electron-poor phenanthridine subunits along the edges emerge from a thermal rearrangement of the 9-methyl-9*H*-carbazole in building block **1**. (**b**) nc-AFM image of CGNR heterostructure on Au(111) featuring discrete segments of fused phenanthridine

associated with the chemistry of molecular precursors, exploration of the reactivity and physical processes governing self-assembly on surfaces, access to high-resolution and high-throughput physical characterization techniques, and, ultimately, integration with current electronic circuit architectures.

References

1. Novoselov KS, Geim AK, Morozov SV, Jiang D, Zhang Y, Dubonos SV, Grigorieva IV, Firsov AA (2004) Science 306:666–669
2. Novoselov KS, Geim AK, Morozov SV, Jiang D, Katsnelson MI, Grigorieva IV, Dubonos SV, Firsov AA (2005) Nature 438:197–200
3. Geim AK, Novoselov KS (2007) Nat Mater 6:183–191
4. Castro Neto AH, Guinea F, Peres NMR, Novoselov KS, Geim AK (2009) Rev Mod Phys 81:109–162
5. Han MY, Ozyilmaz B, Zhang YB, Kim P (2007) Phys Rev Lett 98:206805
6. Zhang YB, Tan YW, Stormer HL, Kim P (2005) Nature 438:201–204
7. Stankovich S, Dikin DA, Dommett GHB, Kohlhaas KM, Zimney EJ, Stach EA, Piner RD, Nguyen ST, Ruoff RS (2006) Nature 442:282–286
8. Dikin DA, Stankovich S, Zimney EJ, Piner RD, Dommett GHB, Evmenenko G, Nguyen ST, Ruoff RS (2007) Nature 448:457–460
9. Kim KS, Zhao Y, Jang H, Lee SY, Kim JM, Kim KS, Ahn JH, Kim P, Choi JY, Hong BH (2009) Nature 457:706–710
10. Wang X, Zhi LJ, Müllen K (2008) Nano Lett 8:323–327
11. Schedin F, Geim AK, Morozov SV, Hill EW, Blake P, Katsnelson MI, Novoselov KS (2007) Nat Mater 6:652–655
12. Hill EW, Geim AK, Novoselov K, Schedin F, Blake P (2006) IEEE T Magn 42:2694–2696
13. Heersche HB, Jarillo-Herrero P, Oostinga JB, Vandersypen LMK, Morpurgo AF (2007) Nature 446:56–59
14. Geim AK (2009) Science 324:1530–1534
15. Tapaszto L, Dobrik G, Lambin P, Biro LP (2008) Nat Nanotechnol 3:397–401
16. Wang XR, Ouyang YJ, Li XL, Wang HL, Guo J, Dai HJ (2008) Phys Rev Lett 100:206803
17. Kosynkin DV, Higginbotham AL, Sinitskii A, Lomeda JR, Dimiev A, Price BK, Tour JM (2009) Nature 458:872–875
18. Tao CG, Jiao LY, Yazyev OV, Chen YC, Feng JJ, Zhang XW, Capaz RB, Tour JM, Zettl A, Louie SG, Dai HJ, Crommie MF (2011) Nat Phys 7:616–620
19. Li X, Wang X, Zhang L, Lee S, Dai H (2008) Science 319:1229–1232
20. Jiao LY, Zhang L, Wang XR, Diankov G, Dai HJ (2009) Nature 458:877–880
21. Xie LM, Wang HL, Jin CH, Wang XR, Jiao LY, Suenaga K, Dai HJ (2011) J Am Chem Soc 133:10394–10397
22. Cai J, Ruffieux P, Jaafar R, Bieri M, Braun T, Blankenburg S, Muoth M, Seitsonen AP, Saleh M, Feng X, Müllen K, Fasel R (2010) Nature 466:470–473
23. Lafferentz L, Ample F, Yu H, Hecht S, Joachim C, Grill L (2009) Science 323:1193–1197
24. Bombis C, Ample F, Lafferentz L, Yu H, Hecht S, Joachim C, Grill L (2009) Angew Chem Int Edit 48:9966–9970

Fig. 20 (continued) and carbazole groups. (**c**, **d**) nc-AFM images of phenanthridine and carbazole fused CGNR. (**e**, **f**) Ball-and-stick models of phenanthridine and carbazole fused GNRs serve as guides for the eye. Reproduced with permission from [56], Copyright (2016) John Wiley and Sons

25. Lafferentz L, Eberhardt V, Dri C, Africh C, Comelli G, Esch F, Hecht S, Grill L (2012) Nat Chem 4:215–220
26. Björk J, Stafström S, Hanke F (2011) J Am Chem Soc 133:14884–14887
27. Linden S, Zhong D, Timmer A, Aghdassi N, Franke JH, Zhang H, Feng X, Müllen K, Fuchs H, Chi L, Zacharias H (2012) Phys Rev Lett 108
28. Bjork J, Hanke F, Stafstrom S (2013) J Am Chem Soc 135:5768–5775
29. Bjork J (2016) J Phys Condens Matter 28:083002
30. Batra A, Cvetko D, Kladnik G, Adak O, Cardoso C, Ferretti A, Prezzi D, Molinari E, Morgante A, Venkataraman L (2014) Chem Sci 5:4419–4423
31. Simonov KA, Vinogradov NA, Vinogradov AS, Generalov AV, Zagrebina EM, Martensson N, Cafolla AA, Carpy T, Cunniffe JP, Preobrajenski AB (2015) J Phys Chem C 119:880–881
32. Bronner C, Bjork J, Tegeder P (2015) J Phys Chem C 119:486–493
33. Sun Q, Zhang C, Li ZW, Kong HH, Tan QG, Hu AG, Xu W (2013) J Am Chem Soc 135:8448–8451
34. Riss A, Wickenburg S, Gorman P, Tan LZ, Tsai H-Z, de Oteyza DG, Chen Y-C, Bradley AJ, Ugeda MM, Etkin G, Louie SG, Fischer FR, Crommie MF (2014) Nano Lett 14:2251–2255
35. Han P, Akagi K, Federici Canova F, Mutoh H, Shiraki S, Iwaya K, Weiss PS, Asao N, Hitosugi T (2014) ACS Nano 8:9181–9187
36. Han P, Akagi K, Canova FF, Mutoh H, Shiraki S, Iwaya K, Weiss PS, Asao N, Hitosugi T (2015) ACS Nano 9:3404–3405
37. Simonov KA, Vinogradov NA, Vinogradov AS, Generalov AV, Zagrebina EM, Martensson N, Cafolla AA, Carpy T, Cunniffe JP, Preobrajenski AB (2015) ACS Nano 9:3399–3403
38. Sánchez-Sánchez C, Dienel T, Deniz O, Ruffieux P, Berger R, Peng XL, Müllen K, Fasel R (2016) ACS Nano 10:8006–8011
39. Son Y-W, Cohen ML, Louie SG (2006) Phys Rev Lett 97:216803
40. Yang L, Park C-H, Son Y-W, Cohen ML, Louie SG (2007) Phys Rev Lett 99:186801
41. Chen Y-C, de Oteyza DG, Pedramrazi Z, Chen C, Fischer FR, Crommie MF (2013) ACS Nano 7:6123–6128
42. Zhang HM, Lin HP, Sun KW, Chen L, Zagranyarski Y, Aghdassi N, Duhm S, Li Q, Zhong DY, Li YY, Müllen K, Fuchs H, Chi LF (2015) J Am Chem Soc 137:4022–4025
43. Kimouche A, Ervasti MM, Drost R, Halonen S, Harju A, Joensuu PM, Sainio J, Liljeroth P (2015) Nat Commun 6:10177
44. Cai JM, Pignedoli CA, Talirz L, Ruffieux P, Sode H, Liang LB, Meunier V, Berger R, Li RJ, Feng XL, Müllen K, Fasel R (2014) Nat Nanotechnol 9:896–900
45. Bronner C, Stremlau S, Gille M, Brauße F, Haase A, Hecht S, Tegeder P (2013) Angew Chem Int Ed 52:4422–4425
46. Vo TH, Shekhirev M, Kunkel DA, Morton MD, Berglund E, Kong LM, Wilson PM, Dowben PA, Enders A, Sinitskii A (2014) Nat Commun 5:3189
47. Liu JZ, Li BW, Tan YZ, Giannakopoulos A, Sanchez-Sanchez C, Beljonne D, Ruffieux P, Fasel R, Feng XL, Müllen K (2015) J Am Chem Soc 137:6097–6103
48. Ruffieux P, Wang SY, Yang B, Sanchez-Sanchez C, Liu J, Dienel T, Talirz L, Shinde P, Pignedoli CA, Passerone D, Dumslaff T, Feng XL, Müllen K, Fasel R (2016) Nature 531:489–492
49. Vo TH, Perera UGE, Shekhirev M, Mehdi Pour M, Kunkel DA, Lu H, Gruverman A, Sutter E, Cotlet M, Nykypanchuk D, Zahl P, Enders A, Sinitskii A, Sutter P (2015) Nano Lett 15:5770–5777
50. Nguyen GD, Tom FM, Cao T, Pedramrazi Z, Chen C, Rizzo DJ, Joshi T, Bronner C, Chen YC, Favaro M, Louie SG, Fischer FR, Crommie MF (2016) J Phys Chem C 120:2684–2687
51. Cloke RR, Marangoni T, Nguyen GD, Joshi T, Rizzo DJ, Bronner C, Cao T, Louie SG, Crommie MF, Fischer FR (2015) J Am Chem Soc 137:8872–8875
52. Kawai S, Saito S, Osumi S, Yamaguchi S, Foster AS, Spijker P, Meyer E (2015) Nat Commun 6:8098

53. Cai J, Pignedoli CA, Talirz L, Ruffieux P, Söde H, Liang L, Meunier V, Berger R, Li R, Feng X, Müllen K, Fasel R (2014) Nat Nano 9:896–900
54. Chen Y-C, Cao T, Chen C, Pedramrazi Z, Haberer D, de Oteyza DG, Fischer FR, Louie SG, Crommie MF (2015) Nat Nano 10:156–160
55. Blankenburg S, Cai J, Ruffieux P, Jaafar R, Passerone D, Feng X, Müllen K, Fasel R, Pignedoli CA (2012) ACS Nano 6:2020–2025
56. Marangoni T, Haberer D, Rizzo DJ, Cloke RR, Fischer FR (2016) Chem Eur J 22:13037–13040
57. Cano-Marquez AG, Rodriguez-Macias FJ, Campos-Delgado J, Espinosa-Gonzalez CG, Tristan-Lopez F, Ramirez-Gonzalez D, Cullen DA, Smith DJ, Terrones M, Vega-Cantu YI (2009) Nano Lett 9:1527–1533
58. Elias AL, Botello-Mendez AR, Meneses-Rodriguez D, Gonzalez VJ, Ramirez-Gonzalez D, Ci L, Munoz-Sandoval E, Ajayan PM, Terrones H, Terrones M (2010) Nano Lett 10:366–372
59. Ma L, Wang J, Ding F (2013) Chem Phys Chem 14:47–54

Adv Polym Sci (2017) 278: 67–98
DOI: 10.1007/12_2017_3

Surface-Assisted Reaction Under Ultrahigh Vacuum Conditions

Hong Wang, Haiming Zhang, and Lifeng Chi

Abstract Fabrication of covalently bonded molecular structures on the surface of metal single crystals is attracting increased attention because of the special synthetic strategies and potential applications (e.g., in molecular electronics). In contrast to traditional organic synthesis, surface-assisted reactions have the advantages of structural control of the produced polymers/oligomers, understanding of detailed reaction processes, and, most importantly, production of new materials that cannot be synthesized by traditional methods. The types of reactants, choice of metal surface, and initial conditions are critical parameters for control of surface-assisted reactions. Covalent bonds formed in the reaction ensure higher mechanical and thermodynamic stability of the produced structures compared with self-assembled monolayers (SAMs). Some conjugated polymers are ideal candidate organic semiconductors for next-generation carbon-based electronics. In this review, we summarize the surface-assisted reactions reported in recent years, analyzing their mechanisms and comparing them with the corresponding reactions in solution systems. We also discuss the important role that the substrate surface plays in the reaction process.

Keywords Covalent bond • Metal surface • Scanning tunneling microscopy • Surface-assisted reaction • Ultrahigh vacuum

---

H. Wang
Institute of Functional Nano & Soft Materials (FUNSOM), Jiangsu Key Laboratory for Carbon-Based Functional Materials and Devices, Soochow University, Suzhou, Jiangsu 215123, China

Physikalisches Institut, Universitaet Muenster, Wilhelm-Klemm-Str.10, Münster 48149, Germany

H. Zhang and L. Chi (✉)
Institute of Functional Nano & Soft Materials (FUNSOM), Jiangsu Key Laboratory for Carbon-Based Functional Materials and Devices, Soochow University, Suzhou, Jiangsu 215123, China
e-mail: chilf@suda.edu.cn

Contents

1 Introduction

Molecular self-assembly has been widely used in recent decades in the patterning of organic molecules and functionalization of surfaces [1, 2]. In the assembly process, molecules are collected together spontaneously through noncovalent interactions such as van der Waals’ forces, [3, 4], hydrogen bonds [5–7], halogen bonds [8, 9], and coordination bonds [10, 11]. Self-assembled monolayers (SAMs) on surfaces have the advantage of forming compact molecular structures over a large area as a result of their spontaneous and reversible growth [12]. Although weak interactions between molecules are the key requirement for reaction reversibility, they reduce the stability of these structures and thus restrict their application in molecular electronics, sensors, catalysis, and molecular templates, which all require high stability. Combination of organic molecules through on-surface reaction to produce molecular networks or polymers is a new synthetic method in chemistry, and also an effective way to fabricate stable two-dimensional (2D) structures on surfaces. In contrast to reactions taking place in solution, on-surface synthesis implements a different propagating path because of involvement of the metal surface and the totally different reaction conditions. This kind of reaction has been named “on-surface chemistry” or “surface-assisted reaction.” Investigation of different kinds of surface-assisted reactions helps in obtaining deeper understanding of the process and mechanisms. At the same time, organization of molecules using surface-assisted reactions can be used to fabricate covalently bonded 2D structures with higher stability. Several low dimensional molecular structures have been fabricated through this strategy and the advantages are as follows:

1. The strength of the covalent bond (several electronvolts) is much stronger than the weak interactions mentioned above. This kind of strong interaction in SAMs

greatly enhances the stability of the fabricated film, reflected both in higher mechanical strength and higher thermodynamic stability [13–15].

2. Surface-assisted reactions provide new strategies for synthesis of some new functional materials that cannot be produced by other methods.
3. Products fabricated on metal surfaces can easily be characterized using surface characterization techniques such as scanning tunneling microscopy (STM), X-ray photoelectron spectroscopy (XPS), infrared spectroscopy (IR), ultraviolet photoelectron spectroscopy (UPS), and near edge X-ray absorption fine structure (NEXAFS).
4. Conjugated polymers/macromolecules can work as a channel for transfer of electrons. In this case, some special electrical materials such as graphene nanoribbons (GNRs) and molecular wires can be fabricated directly on surfaces.

Similar to traditional fabrication techniques for SAMs, surface-assisted reactions are executed through bottom-up strategies. In most cases, precursor molecules containing the required functional groups can be deposited on a substrate surface under ultrahigh vacuum (UHV) conditions. The molecules diffuse over the surface and form self-assembled structures driven by weak interactions between molecules. Enough energy needs to be supplied through heating [16, 17], injection of electrons [18–20], exposure to ultraviolet light [21–23], or other methods to activate the cleavage of bonds in functional groups with the assistance of metal substrate. The formed molecular radicals connect with each other to generate macromolecules or polymers. As a result of great effort in the past decade, researchers have reported a series of surface-assisted reactions, including some classic reactions in solution, such as the Ullmann coupling reaction [24, 25], Glaser coupling reaction [26], condensation of boronic acids [27], "Click" reaction [28], cyclodehydrogenation [29], and Sonogashira coupling reaction [30], as well as some new reactions that only take place on surfaces, such as dehydrogenation of alkanes under mild conditions [31]. Here, we summarize some typical surface-assisted reactions that have been reported in the last few years and analyze the important role of the substrate surface in the reaction process. Finally, we give a vision of the future ability to fabricate functional structures based on these reactions.

2 Advantages and Challenges of Surface-Assisted Reactions Under UHV Conditions

Until recently, most reported surface-assisted reactions took place in a UHV chamber. Compared with the traditional liquid environment, the advantages of using a vacuum are very attractive, as listed below [14, 32]:

1. UHV conditions afford a perfect environment for reactions to occur, where the ultraclean environment enables metal surfaces to remain clean at the atomic scale. The metal substrate not only acts as a plane to support molecules, but also

as a kind of template to locate the adsorption molecules and as a catalyst in the reaction. Thus, the reaction ingredients can be simplified such that the precursor molecules are the primary elements, and solvents or other catalysts are not necessary. Furthermore, the negative influence of gases such as O_2 and CO_2 in air can be avoided. These advantages afford an optimized path for study of reaction mechanisms.

2. Absence of solvent allows a much larger range of reaction temperatures than for reactions in solution. Furthermore, without the requirement for solvent as intermediary in the reaction process, insoluble substances no longer restrict the reactions. This allows a larger species of materials to be chosen.
3. The structure and morphology of products on surfaces can be detected by SPM and other surface characterization instruments in situ. Importantly, the STM tip can operate on the substrate surface and measure the electronic properties of products. Additionally, a template can be used on the surface to adjust the reaction procedure.
4. The controllable active process of reactions on surfaces allows step-by-step study, which means that the reaction can be focused at some intermediate state for detailed study of the reaction procedure on surfaces.

Additionally, electronic chemistry (EC) takes place in a strictly controlled environment that also allows clean conditions and the operation of STM on single-crystal metal surfaces in situ. Moreover, EC-STM can supply an additional electric field on surfaces, which provides another important platform for study of surface-assisted reactions. In fact, some reactions studied under EC conditions have been previously reported [33–35]. In contrast to EC conditions, UHV conditions permit activation of reactions easily by the supply of energy through different techniques. More importantly, radicals are the basic elements in most reactions on surfaces and are stable in UHV conditions but might be trapped by an electrolyte.

Of course, there are some drawbacks to surface-assisted reactions under vacuum conditions. The desorption of some byproducts (e.g. H_2, H_2O) from the substrate surface under low vapor conditions and the difficulty in separation of products from each other because of the strong interaction between molecules and substrate lead to the nonreversible nature of these reactions. This hinders the fabrication of flexible, self-healing, or multimorphology structures on surfaces. Furthermore, the strong interaction between molecules and metal substrate restricts the diffusion distance of molecules on surfaces, which increases the difficulty of fabricating ordered covalent networks over a large scale. Additionally, applications based on the electronic properties of the produced materials need to be carried out on insulated surfaces, whereas surface-assisted reactions normally take place on metal single-crystal surfaces, which remains a big challenge for potential applications.

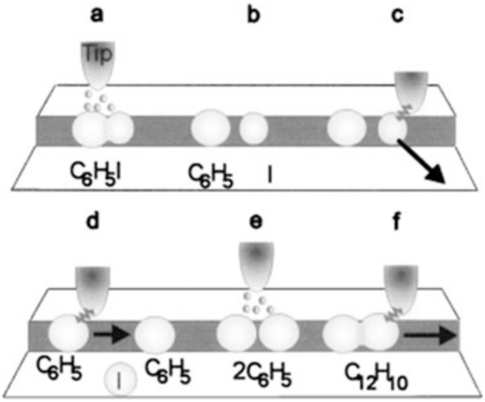

Fig. 1 STM-tip-induced synthesis of biphenyl [18]: (**a**, **b**) STM-induced abstraction of iodine from iodobenzene; (**c**) removal of iodine atom; (**d**) bringing two phenyl radicals together; (**e**) electron-induced association of two phenyls to form a biphenyl molecule; (**f**) moving one side of the biphenyl molecule to confirm the association

3 Different Kinds of Surface-Assisted Reactions

3.1 Ullmann Coupling Reaction

Ullmann coupling is a classical reaction widely used in organic synthesis. The reaction between aryl halides is catalyzed by copper to synthesize polymeric phenyl. The first study was reported in 1901 by Ullmann and Bielecki, who heated a mixture of Cu powder and iodobenzene to synthesize biphenyl [36]. Xi et al. [37] reported the reaction of iodobenzene on a Cu(111) surface to produce biphenyl through annealing, which was the first time realize the initiation of Ullmann coupling was realized on a metal surface. The reaction proceeds as follows: iodobenzene dissociates iodine atoms on a Cu(111) surface to form phenyl radicals by heating; those phenyl radicals diffuse over the surface and combine into biphenyl when annealed to a higher temperature [38]. In 2000, Hla et al. [18] succeeded in synthesizing biphenyl from iodobenzene by manipulation of the STM tip step by step on a Cu(111) surface. As shown in Fig. 1, iodobenzene molecules deposited on a Cu(111) surface were kept at low temperature in the vacuum chamber. The STM tip was moved above one iodobenzene molecule and supplied a positive voltage to cleave off the iodine atom. Two phenyl radicals were brought together, followed by a positive voltage to combine them together. The STM tip acted to manipulate the molecules in the reaction process and, more importantly, as a versatile tool at the submolecule scale to detect the structure of components at every step and reveal the detailed procedure of reaction on the Cu(111) surface. However, the limitation is that the STM tip operation is slow and multifarious, which make it unsuitable for large-scale fabrication.

In 2007, Grill et al. [25] reported production of poly-phenylporphyrin on an Au (111) surface from brominated porphyrin-derived molecules through the Ullmann reaction. In the experimental strategy, poly-phenylporphyrin was fabricated in two different ways. First, the brominated porphyrin derivates were evaporated from the crucible onto an Au(111) surface kept at low temperature and were subsequently

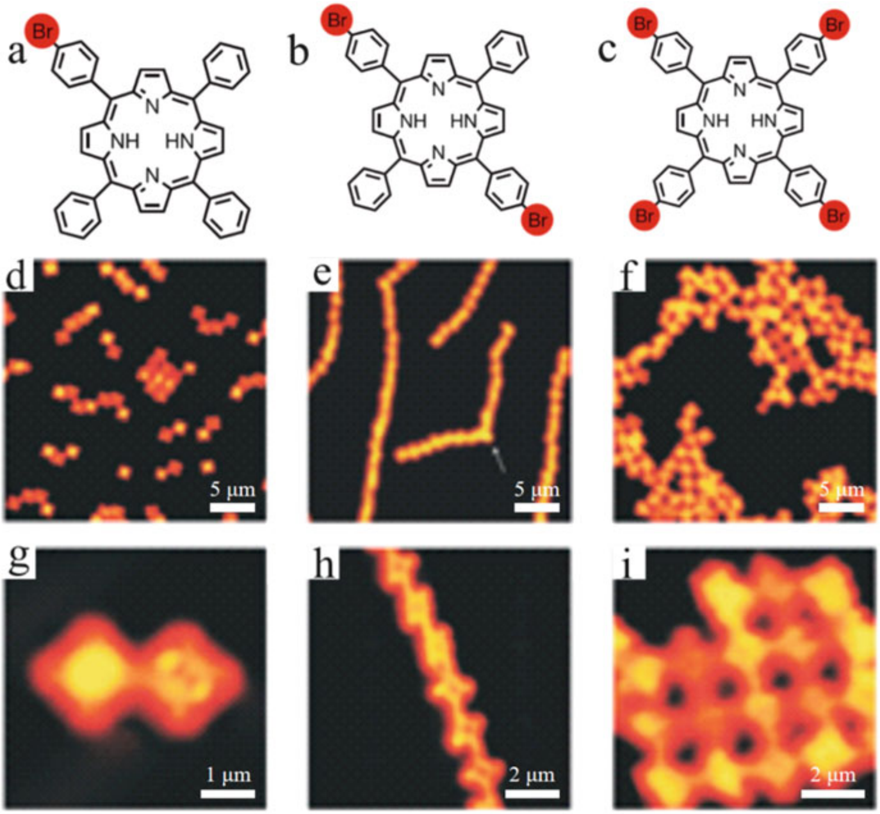

Fig. 2 Structural formulae (**a–c**) and corresponding STM images (**d**–**i**) of different kinds of brominated porphyrin-derived molecules [25]: (**d**, **g**) dimer; (**e**, **h**) molecular line; and (**f**, **i**) molecular network

activated by heating the sample to dissociate the substituted Br atoms. The formed radicals diffused over the surface and connected into polymers. The second method was to evaporate molecules at a high temperature (more than 590 K) in a Knudsen cell, where cleavage of C–Br bonds was completed; subsequent deposition of the radicals on an Au(111) surface induced combination of those radicals. Interestingly, the obtained polymerized structures could be controlled by adjusting the number and position of the substituted Br atoms in the monomers. Figure 2a–c shows the molecular structures of different precursor molecules with one, two and four Br atoms substituted in tetraphenylporphyrin (TPP). The resulting products were dimers, molecular wires, and molecular networks, respectively. Compared with the tip-induced reaction, thermo-induced Ullmann reaction benefits from simplified operation and has set a precedent for disseminating surface-assisted reactions. Grill's group later exchanged two of the bromine atoms for iodine atoms in the precursor molecule Br_4TPP, in which the halogen atoms can be cleaved off at

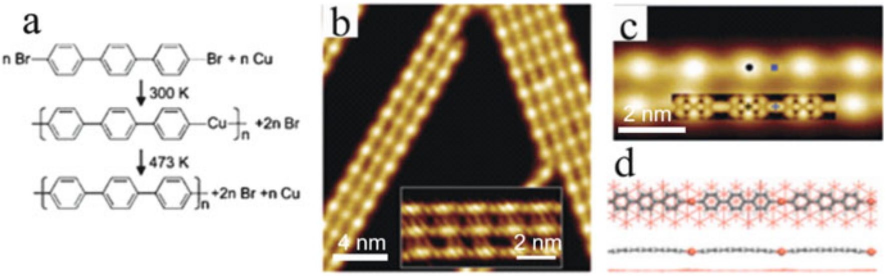

Fig. 3 (**a**) Ullmann coupling reaction of 4,4″-dibromo-*p*-pterphenyl (Br-(ph)$_3$-Br) on a Cu(111) surface. (**b**) STM topography and high-resolution image (*inset*) of the sample after annealing to 300 K. (**c**) Simulated STM image covered on the STM topography of the intermediate. (**d**) *Top* and *side* views of the intermediate structure on a Cu(111) surface, obtained through DFT calculation [41]

different temperature to explore the sequential reaction process. In this experiment, they first deposited precursor molecules on an Au(111) surface kept at 80 K to obtain the self-assembled structure, subsequently annealed the sample to 393 K to produce covalently bonded molecular linear structures through cleavage of iodine atoms, and then annealed the sample to 523 K to obtain the final product with dissociation of Br and subsequent combination of the linear polymer chains into 2D networks [16]. This kind of step-by-step procedure affords a new bottom-up strategy for production of nanomolecular frameworks.

The general view of the mechanism of this surface Ullmann coupling is that there exits an important intermediate between the dissociation of the halogen atoms and the formation of C–C bonds. At first, researchers considered the intermediates to be coordination structures attached by dehalogenated molecules to metal atoms on the surface [38–40]. Later works provided more unambiguous evidence to prove that the intermediates are stable metal–organic coordination structures linked by molecular radicals to free metal atoms on the substrate surface. Wang et al. [41] observed this kind of structure when they studied the Ullmann reaction of 4.4′-dibromo-*p*-terphenyl [Br-(ph)$_3$)-Br] on a Cu(111) surface. Figure 3a shows the reaction procedure of the experiment, where a set of molecular wires were detected by STM when the sample was annealed to 300 K. As shown in Fig. 3b, a series of bright dots can be clearly identified in every linear structure, uniformly distributed between every two molecules. Furthermore, these molecular linear structures possessed high stability, which even grew across the atomic steps on the surface, and behaved similarly to the coordination structures reported previously [42]. The authors attributed the bright dots to free Cu atoms on surface, linked by molecular radicals. The simulated coordination structure calculated by density functional theory (DFT) agreed well with the STM result (see Fig. 3c). At the same time, the DFT-calculated intermediate on the Cu(111) surface in Fig. 3d shows that both the molecules and the Cu atoms were located in the same plane, far from the substrate surface. Additionally, in the inset of Fig. 3b, lots of bright dots can be observed between the linear structures and were attributed to Br atoms dissociated from the precursor molecules and adsorbed on the Cu(111) surface. The authors confirmed this stable metal–organic coordination structure to be the intermediate in surface Ullmann reactions, with a Cu–C bond length of 0.211 nm. Further annealing of the intermediates to 473 K produced covalently bonded linear polymers. Other works have also been presented that give further evidence for the existence of metal-linked intermediates [43–47].

One important reason for study of Ullmann coupling is the fabrication of covalently bonded conjugated structures, such as molecular wires and organic semiconductors. Grill et al. [48] succeeded in fabrication of a set of molecular wires of different lengths on an Au(111) surface by annealing the deposited dibromoterfluorene (DBTF) to 520 K, with the longest wire being over 100 nm. Furthermore, the STM tip can be used to drag up one side of the wire to determine the conductance. The conjugated products can be used as organic semiconductors in the fabrication of various organic devices by adjusting the precursor molecules to have different configurations and symmetries [16, 49].

3.2 Schiff Base Reaction

Schiff base reactions refer to those reactions in which an amine reacts with an oxo-compound (aldehyde and ketone) through nucleophilic addition to form the hemiaminal intermediate, followed by dehydration to generate imine (the reaction procedure is shown in Fig. 4a) [51]. Weigelt et al. [50] reported the first Schiff base reaction between dialdehyde and octylamine on an Au(111) surface. Dialdehyde molecules were first deposited on Au(111) and then exposed to a vapor of octylamine ($p \approx 1$–5×10^{-8} mbar). The reaction took place at room temperature and resulted in self-assembly of the produced imines. Compared with the self-assembled structure of imines synthesized in solution, the morphology and inner structure of the SAMs were exactly the same, giving strong evidence for initiation of the Schiff base reaction on the Au(111) surface. The mechanism of a surface-assisted Schiff base reaction is different from that in solution. Normally, the solvent plays a very important role in catalysis of the transformation from intermediate to final product in solution, but this is impossible in a vacuum chamber. Learning from DFT calculations, the authors estimated that the hydroxyl group in phenol acted as acceptor/donor and, at the same time, played as the factor of solvent in the reaction in solution. Furthermore, the DFT-calculated activation energy of this reaction is 1.17 eV, and the reaction initiated at room temperature, which is much lower than estimated. This is a result of the catalytic effect of the Au(111) surface in reducing the activation energy of the reaction.

More importantly, Schiff base reactions involve two reactants, which enhances the controllability of the product structures through adjusting the precursor molecules or reaction parameters. Weigelt et al. [52] tried using trialdehyde to react with 1,6-diaminohexane to fabricate covalently bonded networks. They found that the parameters of the network (e.g., pore size and shape) can be easily adjusted by using different amines. Furthermore, the reaction also depended on the reaction

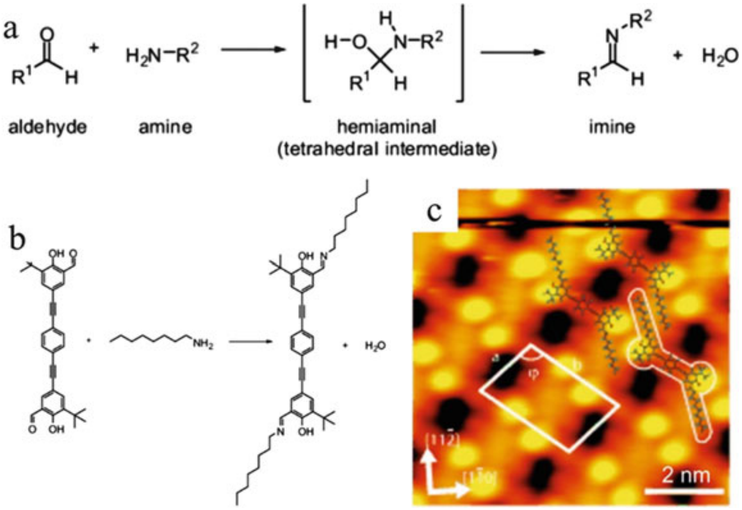

Fig. 4 (**a**) Schiff base reaction in solvent. (**b**) Schiff base reaction from dialdehyde and octylamine to diimine on an Au(111) surface. (**c**) STM topography of the self-assembled structure of diamine, overlaid with the structural model [50]

conditions. For example, reactants handled using two different paths gave different connected networks. In method A, after the deposition of trialdehyde, the sample was exposed to 1,6-diaminohexane ($p = 1\text{–}5 \times 10^{-7}$ mbar) and subsequently annealed to 400–450 K to initiate the reaction. The products were small oligomers. In method B, after the deposition of trialdehyde, the sample was heated to 400 K and exposed to 1,6-diaminohexane (5×10^{-9} mbar). In this case, the products were extended polymers. Comparing the two products synthesized using different procedures, the trialdehyde connected with more 1,6-diaminohexane molecules in method B, inducing a more compact network structure. In addition to fabrication of oligomers and anomalous polymers, a honeycomb network can also be produced through optimizing the reaction [53].

3.3 Condensation Reaction of Boronic Acids

Condensation of boronic acids is often applied for fabrication of covalent organic frameworks (COFs) in solution [54, 55]. More recently, this reaction has also been used in the synthesis of surface covalent organic frameworks (SCOFs). Zwaneveld et al. [27] first reported the fabrication of large scale 2D frameworks from condensation of boronic acids on a metal surface. The reaction was initiated when the precursor molecules 1,4-benzenediboronic acid (BDBA) reached the Ag(111) surface at room temperature. The formed framework was detected by STM, as shown in Fig. 5a. The pore size was 1.52 nm, agreeing with the calculated structure.

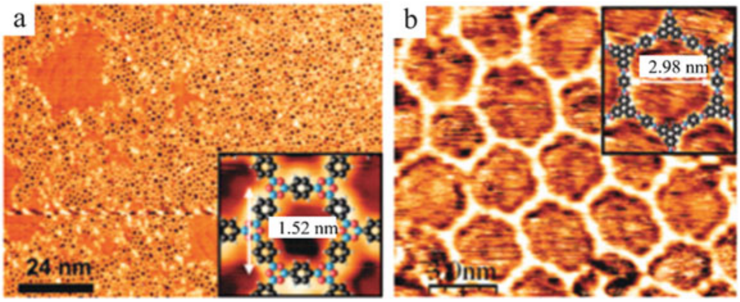

Fig. 5 STM images of surface covalent organic framework (SCOF) structures synthesized from different precursors on an Au(111) surface [27]: (**a**) 1,4-benzenediboronic acid (BDBA); (**b**) co-adsorption of BDBA and 2,3,6,7,10,11-hexahydroxytriphenylene (HHTP)

Learning from the fabrication of 3D COF structures, 2D SCOFs structure can also be produced from multireactants. As an example, BDBA and 2,3,6,7,10,11-hexahydroxytriphenylene (HHTP) were simultaneously deposited on an Ag(111) surface, producing a framework with pore size of 2.98 nm. In addition to the flexibility of controllable pore size, other advantages of the reaction using double reactants are that the produced SCOF structure has higher stability (even annealed to 750 K) and less defects. With the assistant of HHTP, dioxaborole formation is a bimolecular reaction, in contrast to the trimolecular boroxine reaction, and thus follows a more favorable kinetic path. As shown in Fig. 5b, in addition to the majority existence of hexagons, other structures such as five-, seven-, and eight-membered rings are also present. That is probably due to the fact that, although the hexagon is the optimal structure in the reaction, in the experimental process some molecules might not have enough time or space to reach the right position when the reaction is initiated, thus inducing the formation of other structures. Meanwhile, the produced water molecules are desorbed from the surface during the reaction process, which causes the irreversible nature of this reaction. Consequently, all defects created in the process are kept on the metal surface. Defects can be reduced by optimizing the reaction conditions, such as increasing the deposition flux rate or raising the substrate temperature to enhance transformation of molecules on the surface [56]. It is worth mentioning that the condensation reaction of boronic acids can be excited not only by heating, but also by an STM tip or electronic beam. This confers the ability to control the reaction area as well as the activation sequence [57].

3.4 Dehydrogenation

Dehydrogenation, as a convenient strategy for generating C–C coupling structures through cleaving the C–H bond directly with the assistance of catalytic metals, is widely used in standard organic synthesis. To break a C–H bond, an activation

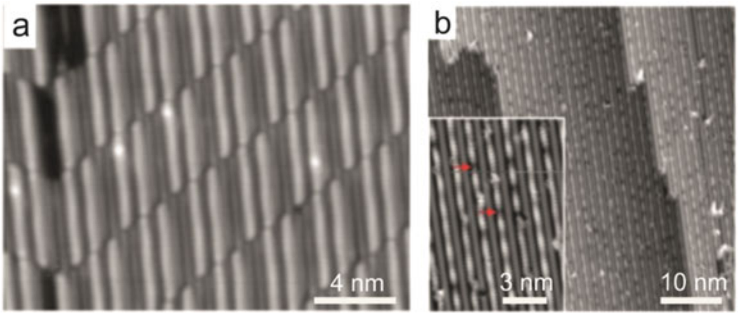

Fig. 6 STM images of self-assembled and polymerized structures formed by dotriacontane ($C_{32}H_{66}$) [31]: (**a**) self-assembled structure on an Au(110)-(1 × 2) surface at 300 K; (**b**) parallel polyethylene chains on a reconstructed Au(110)-(1 × 3) surface at 440 K

energy of more than 4.5 eV is needed [58]. However, on a single-crystal metal surface, especially one with high reactivity, the cleavage energy can be significantly reduced. For example, on a Cu(110) surface, tetra(mesityl)porphyrin (TAP) molecules dehydrogenated in the methyl group form a combinatorial mixture of covalent nanostructures when annealed to 423 K [59]. Furthermore, Zhong et al. [31] succeeded in combining alkane molecules into linear polymers on the more 'inert' Au surface. Dotriacontane ($C_{32}H_{66}$) was deposited on reconstructed Au (110)-(1 × 3) surface and subsequently annealed to 440 K. One of the H atoms in every methyl was dissociated from the alkyl chains, combined into H_2, and released into the vacuum chamber. The alkyl radicals moved along the grooves and connected with each other to generate linear alkane polymers. The self-assembled structure as well as the polymerized alkyl chains are shown in Fig. 6. In comparison, this reaction did not occur on an Au(111) surface. DFT calculation shows that the selected polymerization is a result of the special structure of reconstructed Au (110)-(1 × 3) surfaces. The grooves of the Au(110)-(1 × 3) surface enhanced the interaction between molecules and substrate, which reduced the energy barrier for dehydrogenation. More importantly, the grooves restricted the movement of molecules on the surface, limiting molecules to a "head-to-tail" connection mode. The benefit of producing polymers through dehydrogenation is the clean synthetic process, because only H_2 is produced as byproduct in this reaction and is released from the surface immediately after combination of H atoms, affecting neither the formation of product nor the substrate surface activity. More recently, the polymerization of porphyrin molecules through cleavage of C–H bonds on an Ag(111) surface was reported [60].

3.5 *Cyclodehydrogenation*

Cyclodehydrogenation is a common method for fabricating planar aromatic structures in solution [61]. $AlCl_3$ or $FeCl_3$ is normally used as catalyst for cleaving neighboring C–H bonds. Analogously, C–C coupling through cyclodehydrogenation can also be carried out to synthesize monolayer GNRs or graphene nanoplates on metal substrate surfaces. For example, Cai et al. [62] fabricated GNRs from 10,10′-dibromo-9,9′-bianthryl (DBBA) precursor monomers. The experimental procedures are shown in Fig. 7a. The authors deposited DBBA on an Au(111) surface and subsequently annealed to 473 K to generate the tortuous connected linear polymers via Ullmann reaction. A consecutive second annealing step at 673 K was executed to transfer the linear polymers into GNRs via cyclodehydrogenation. The produced GNRs were imaged by STM and are shown in Fig. 7b. The type of nanoribbon obtained is related to the choice of precursor monomers. As an example, a chevron-type GNR fabricated from tetraphenyl-triphenylene monomers is shown in Fig. 7c. More recently, the fabrication of other GNRs with much more complicated structures has been reported [63, 64]. Björk et al. [65] analyzed the cyclization mechanism through DFT calculation and explained the detailed procedure for cyclodehydregenation of anthracene polymer. Hydrogen atoms are first adsorbed on the metal surface, subsequently cleaved off by the catalytic substrate, combined into H_2 with other hydrogen atoms, and desorbed from the surface. On the other hand, the molecular radicals connect with each other spontaneously to generate GNRs. Interestingly, only one energy barrier exists in the cyclodehydregenation process in a single chain. The formation of GNR proceeds from one end of the linear chain. After activation of the first molecule, subsequent energy barriers are reduced, which induces the cyclodehydregenation to propagate unit-by-unit through the entire polymer in a domino-like fashion. Treier et al. [66] studied the cyclodehydrogenation process of cyclohexa-o-p-o-p-o-p-phenylene on a Cu(111) surface by STM and DFT calculation and found that the reaction contained six steps, in which two intermediates were stable enough to be detected by STM.

Fullerenes, as special carbon materials, have been extensively used for various biomedical applications and are mostly obtained through vaporization of graphite. Researchers are continuously searching for routes to avoid uncontrolled procedures [67]. A promising path is to catalyze the cyclization of planar precursors. This strategy has the advantages of mild conditions and predesigned products. Furthermore, various fullerenes and their derivatives that cannot be produced in other ways can be synthesized by this method. There are also obvious disadvantages of this method, such as low efficiency and complicated operation [68, 69]. However, the synthesis is simplified when taking place on noble metal substrate surfaces, where the precursor molecules can be reproduced into fullerenes or fullerene derivatives through spontaneous cyclodehydrogenation. For example, open-cage $C_{57}H_{33}N_3$ precursor molecules were deposited on a Pt(111) surface and annealed to 750 K to generate ball-shaped $C_{57}N_3$ molecules. The benefits are not only the simplified experimental procedure, but also enhanced yield, from less than 1% in solution to about 100% on a surface [29]. Figure 8a, b shows STM images of the precursor molecules $C_{57}H_{33}N_3$ adsorbed on a Pt(111) surface. Because of the strong interaction between molecules and Pt surface, the molecules rotate into a special state to reduce the distance between the hydrogen atoms and Pt surface. Subsequently, the

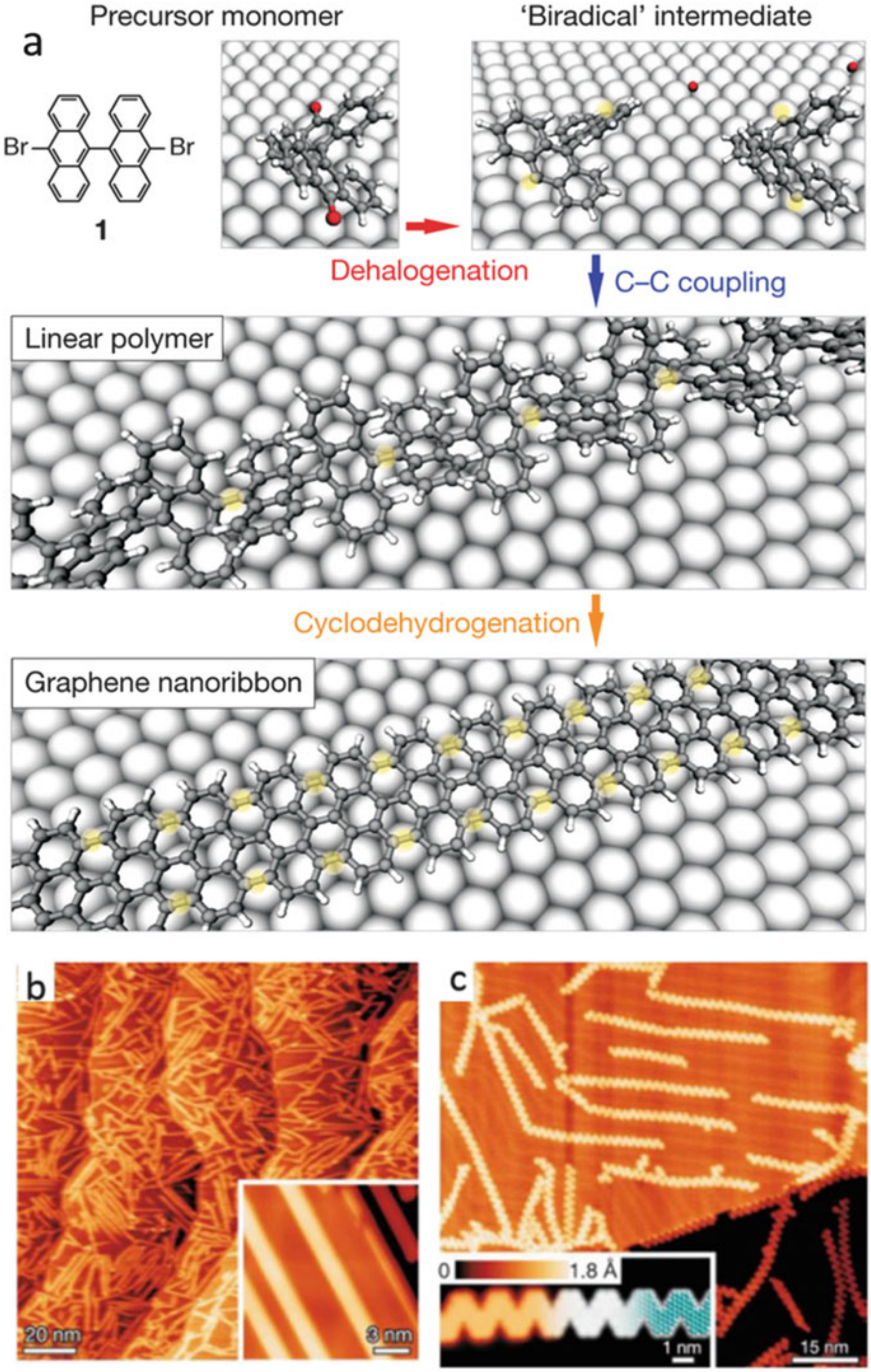

Fig. 7 Strategy for synthesis of graphene nanoribbon (GNR) and STM images of two kinds of GNR [62]: (**a**, **b**) GNRs synthesized from 10,10′-dibromo-9,9′-bianthryl (BDDA) on an Au(111) surface; (**c**) GNRs fabricated from 6,11-dibromo-1,2,3,4-tetraphenyltriphenylene monolayer

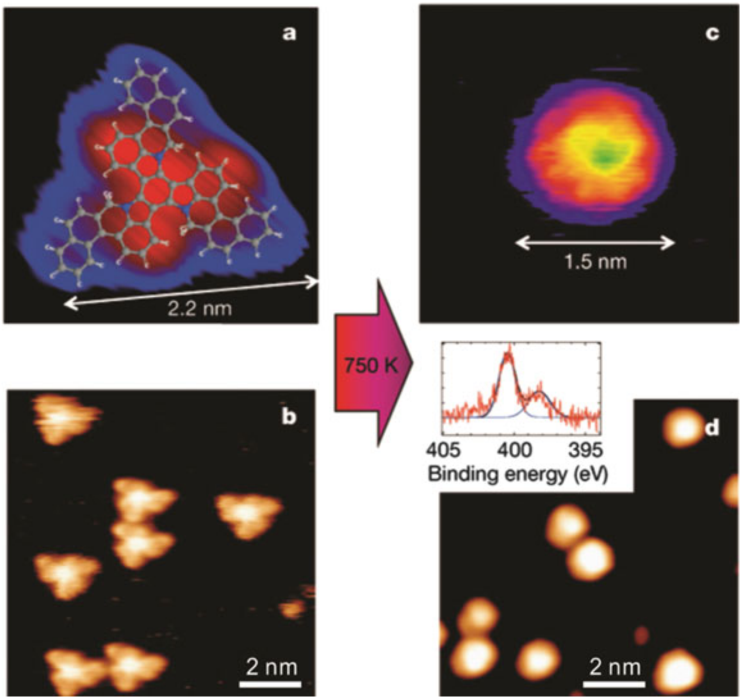

Fig. 8 STM images of $C_{57}H_{33}N_3$ and $C_{57}H_{33}N_3$ on a Pt(111) surface [29]: (**a**) high resolution and (**b**) large area STM images of $C_{57}H_{33}N_3$ deposited on a Pt(111) surface; (**c**) high resolution and (**d**) large area STM images of the produced $C_{57}N_3$ after annealing at 750 K

C–H bond was cleaved by the substrate in the annealing process, inducing cyclization of the molecules into $C_{57}N_3$. Figure 8c, d shows STM images of the produced $C_{57}N_3$. It is noteworthy that the strong interaction between molecule and substrate acts as a crucial factor in the reaction. For comparison, annealing the same precursor molecules on an Au(111) surface, which has a low adsorption interaction with $C_{57}H_{33}N_3$, resulted in very low yield (less than 1%). Consequently, the strong interaction induced deformation of the $C_{57}N_3$ cages. STM measurement showed the diameter of the formed $C_{57}N_3$ to be 1.5 nm and the height 0.38 nm. Amsharov et al. [70] pointed out that the transformation from precursor to fullerene is not a random combination of inner functional groups, but an ordered process in which hydrogen atoms dissociate and the radicals formed are connected step by step, without any rearrangement of C–C bonds. This means that the type and structure of the produced fullerene or derivative is only dependent on the structure of the precursor.

3.6 Glaser Coupling Reaction

Glaser coupling was first reported in the 1860s and is catalyzed by cuprous salts in alkaline solution [71]. This kind of reaction can also take place on single-crystal surfaces. Zhang et al. [26] first reported the Glaser reaction on Ag(111) surfaces in 2012. The scheme of the reaction process is shown in Fig. 9a. By depositing 1,3,5-triethynyl-benzene (TEB) on an Ag(111) surface kept at 170 K, the self-assembled structures shown in Fig. 9c were obtained. Because the molecules might desorb from the surface before the initiation of reaction in the annealing process, the TEB was directly deposited on an Au(111) surface held at 330 K. A new self-assembled structure composed of dumbbell-like molecules was obtained, as shown in Fig. 9d. Analysis of these structures by STM and DFT calculation, enabled the dumbbell like structures to be attributed to coupled TEB molecules. In contrast to the Ullmann reaction, XPS characterization and DFT calculation both showed that there is no analogous intermediate such as C–Ag–C in the reaction procedure. During on-surface Glaser coupling, two neighboring alkynyl groups combine together first, followed by the cleavage of H atoms to form a dimer. Another precursor molecule of larger size, 1,3,5-tris-(4-ethynylphenyl)benzene (Ext-TEB), was also investigated. The self-assembly structure shown in Fig. 9e was obtained when Ext-TEB was deposited on an Ag(111) surface at 152 K. Subsequent annealing to 300 K produced dimer structures. When the sample was further annealed to a higher temperature (400 K), another new covalent bonded network was obtained (shown in Fig. 9f). Moreover, Eichhorn et al. [72] observed several different underlying reaction schemes when they studied the coupling of 1,4-diethynylbenzene on a Cu(111) surface. In this case, it was difficult to control the polymerization path by adjusting experimental parameters such as annealing temperature or time. Gao et al. [73] introduced hexyl groups into the aromatic ring to enhance steric hindrance between molecules to prevent creation of other polymers, and succeeded in generating linear polymerized chains on an Ag(111) surface, which was thought to be impossible using conventional organic synthesis. However, the substrate material also affects the selectivity of this reaction. It was found that Glaser coupling is more efficient on Ag(111) surfaces than on Au(111) and Cu(111) [23].

3.7 Sonogashira Coupling Reaction

The Sonogashira reaction is a crosscoupling reaction used in organic synthesis to form C–C bonds and has also been implemented on metal surfaces by Kanuru et al. [30]. Phenylacetylene and iodobenzene were co-deposited on a 90 K Au(111) surface and subsequently annealed to 200 K to generate the polymerized diphenylacetylene. XPS and NEXAFS characterization were applied to find the mechanism of this reaction. After the deposition of two precursor molecules, they

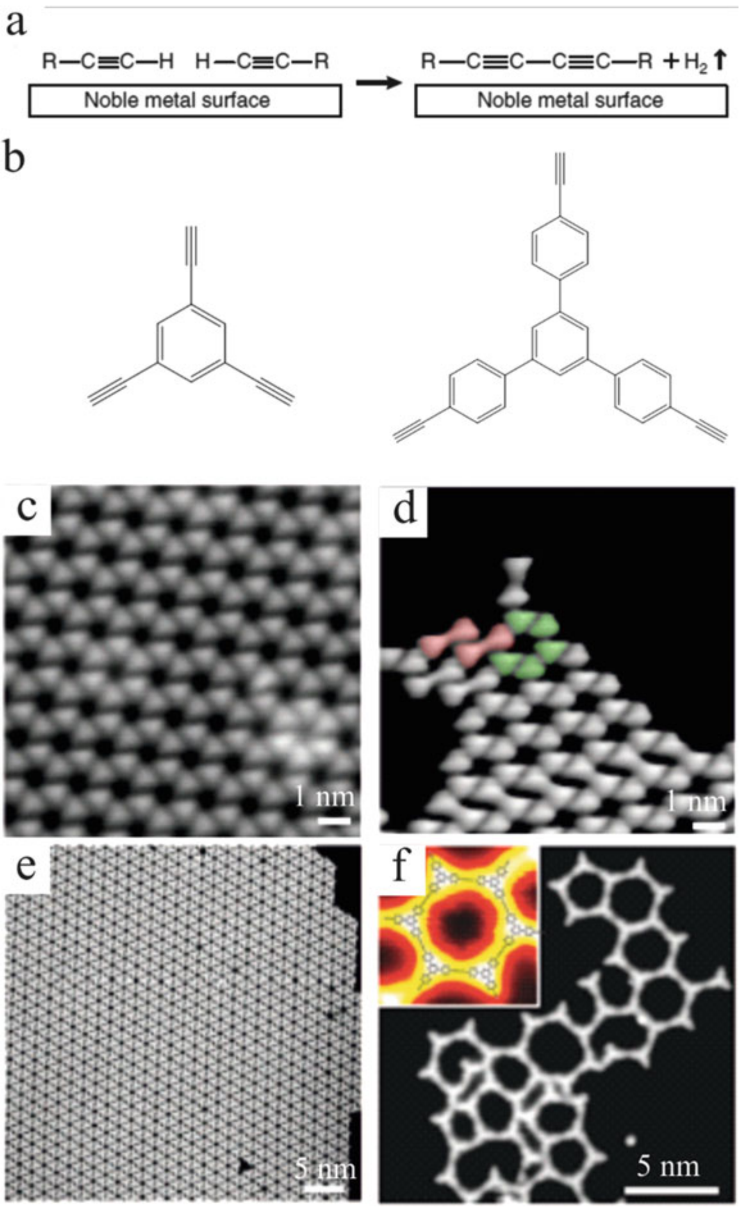

Fig. 9 (**a**) Scheme of Glaser coupling reaction on a metal surface. (**b**) Molecular structures of 1,3,5-triethynylbenzene (TEB) and 1,3,5-tris-(4-ethynylphenyl)benzene (Ext-TEB). (**c**, **d**) STM images of TEB deposited on an Ag(111) surface kept at 170 K (**c**) and 330 K (**d**). (**e**, **f**) STM images of Ext-TEB deposited on Ag(111) kept at 152 K (**e**) and annealed to 400 K (**f**). The *inset* shows the high-resolution image with a structural model [26]

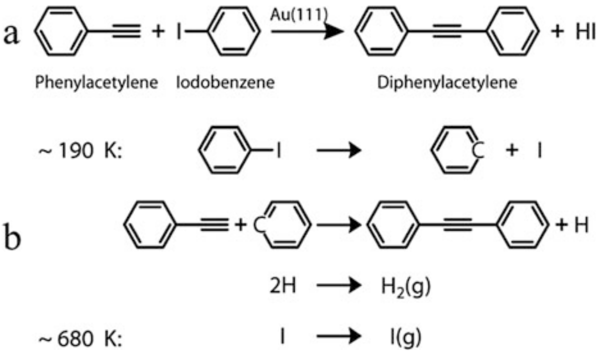

Fig. 10 (**a**) Reaction equation and (**b**) step-by-step process of the Sonogashira coupling reaction on an Au(111) surface [30]

both adsorbed on the surface in planer state, forming separated self-assembled structures because of their different adsorption behaviors on the Au(111) surface. The annealing process induced cleavage of the I atom on iodobenzene, while the produced phenyl radicals reacted with phenylacetylene located at the boundary of neighboring phenylacetylene islands (reaction scheme is shown in Fig. 10). Compared with the reaction in solution, the absence of Pt and base promoted the Au atoms to act as base, inducing a different reaction procedure. In this case, only the reactants located at the boundary possessed the ability to initiate Sonogashira coupling, whereas the inner iodobenzene/phenylacetylene islands initiated the Ullmann reaction/Glaser coupling. On-surface Sonogashira coupling had a low yield of about 10%, but it should be possible to increase this by expanding the boundary area of the two kinds of islands.

Furthermore, Sonogashira coupling reactions are very sensitive to the properties of the substrate surface. On Au(111), the coupling process prefers to occur on a flat surface, because the low coordinated Au sites on a rough surface can cause decomposition of the adsorbed phenylacetylene molecules. In contrast, Sánchez-Sánchez et al. [74] reported that rough Au(100) surfaces have advantages for Sonogashira coupling. The difference is a result of the different distribution of nucleation centers on the two kinds of surfaces. Au(100) is not suitable for nucleation of either phenylacetylene or iodobenzene molecules to form separate islands; thus, roughening treatment affords new nucleation centers for those molecules to grow more islands. However, on an Au(111) surface, the main nucleation centers are herringbone reconstruction structures [75], which disappear if the surface is roughened. In this case, the rough Au(111) surface is no longer suitable for growth of small molecular islands.

3.8 Azide–Alkyne Cycloaddition (“Click” Reaction)

Azide–alkyne cycloaddition catalyzed by cuprous salts has attracted wide attention because of the advantages of no byproducts and low activation energy (0.65 eV).

Fig. 11 Scheme of azide–alkyne cycloaddition reaction and STM image of the products after cycloaddition [28]: (**a**) comparison of azide–alkyne cycloaddition reaction in solution (*A*) and on Cu(111) surface (*B*); (**b**) co-deposition of 9-ethynylphenanthrene and 4-azidobiphenyl on a Cu (111) surface kept at room temperature. The 1,4-triazole reaction products are marked in *quadrangles*

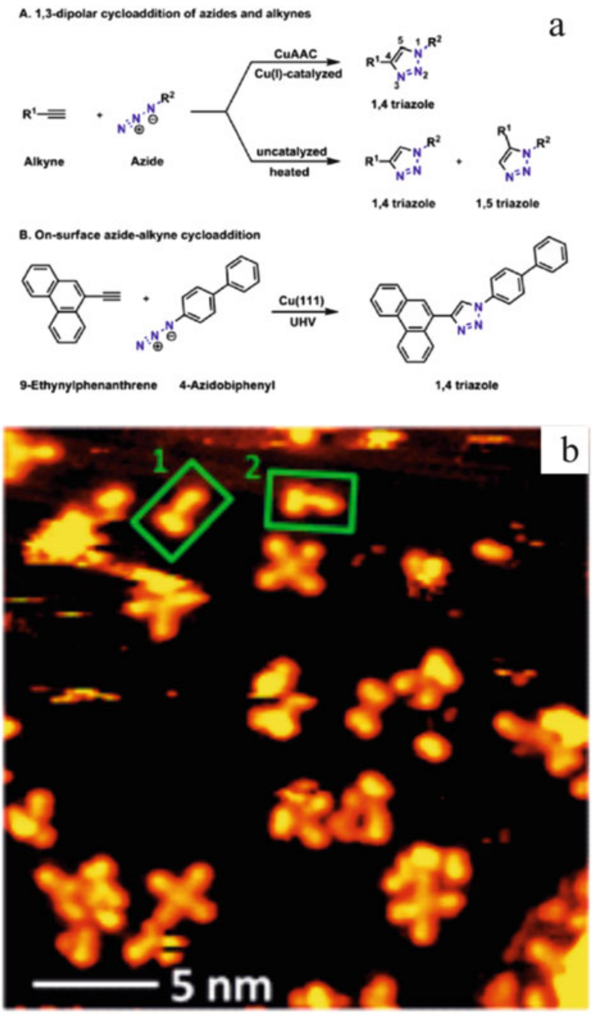

This reaction was implemented on metal surfaces by Bebensee et al. in 2013 [28]. 9-Ethynylphenanthrene (alkyne) and 4-azidobiphenyl (azide) were simultaneously deposited on Cu(111) at room temperature, and spontaneously generated 1,4-triazole by 1,3-cycloaddition (the reaction scheme is shown in Fig. 11a). Figure 11b shows the STM image of the products, where the molecules marked by quadrangles are the formed 1,4-triazole molecules. To confirm the initiation of this reaction, the authors compared the self-assembly structure of 1,4-triazole produced in solution with that synthesized on a surface and found no difference in the STM measurements. In contrast to the high yield obtained for reaction in solution, the surface-assisted reaction gave a very low yield. XPS detection showed that the alkyne molecules were not stable on the surface and degraded rapidly after reaching the surface. Most of the alkyne molecules were not integral when the reaction was initiated. The loss of alkyne molecules induced the low reaction yield. In the reaction taking place in solution, Cu ions act as catalyst in the cycloaddition process. By contrast, Arado et al. [76] found that Cu atoms were not an essential agent for cycloaddition of *N*-(4-azidophenyl)-4-ethynyl-benzamide (AEB) on an Au(111) surface. Both STM detection and DFT calculation proved that the surface only acted as a support to locate the molecules.

3.9 Other Reactions

Some other surface-assisted reactions have also been reported recently, with some exciting examples. The formation of imide from anhydride and amine through condensation in a 2D plane was previously considered to be impossible because initiation of the reaction requires the amine to attack the anhydride in a nonplanar manner. However, with the assistance of metal substrate to locate the two reactants under high vacuum conditions, the reaction took place on a metal substrate surface [77]. 4,4′-Diamino-*p*-terphenyl (DATP) and 3,4,9,10-perylenetetracarboxylic-dianhydride (PTCDA) molecules (the chemical structures are shown in Fig. 12a) were deposited on an Au(111) surface and subsequently annealed to 570 K for 15 min to achieve the polyimide structures shown in Fig. 12b. The authors estimated that it is the high transfer ability of the amine molecules that allow them to attack the anhydride. When the substrate was heated to the critical temperature for desorbing DATP, the diffusion of DATP on surfaces was greatly enhanced, which increased the amount of nucleophilic attack in the reaction procedure. In this case, 2D covalent networks were fabricated by this reaction to combine 2,4,6-tris (4-aminophenyl)-1,3,5-triazine (TAPT) and PTCDA.

Marele et al. [78] reported the condensation between 1,3,5-tri(4-hydroxyphenyl) benzene (TPB) and benzene-1,3,5-tricarbonyl trichloride (TMC) to generate polyester-based SCOF structures. In this work, TPB was deposited on an Au(111) surface and heated to 575 K; exposure to TMC vapor provided honeycomb networks through the condensation reaction.

Bergman cyclization is an important cycloaromatization reaction, which was first reported for on-surface synthesis in 2013 [79]. Sun et al. [80] studied the Bergman cyclization of 1,6-di-2-naphthylhex-3-ene-1,5-diyne (DNHD) on a Cu (110) surface and obtained linear polyphenylene chains. It was thought that the cyclization of DNHD induced formation of diradicals on the surface, which subsequently combined to form polyphenylene chains. Furthermore, the movement of precursor molecules was restricted to one direction by the Cu(110) surface, which led to a tendency to generate long polymer chains.

Cyclotrimerization is another important method for solution fabrication of COF crystals [81, 82]. Yang et al. [83] first introduced the method into the family of surface-assisted reactions for production of 2D conjugated SCOF structures. Precursor molecules of 1,3,5-tris(4-acetylphenyl)benzene (TAPB) were deposited on

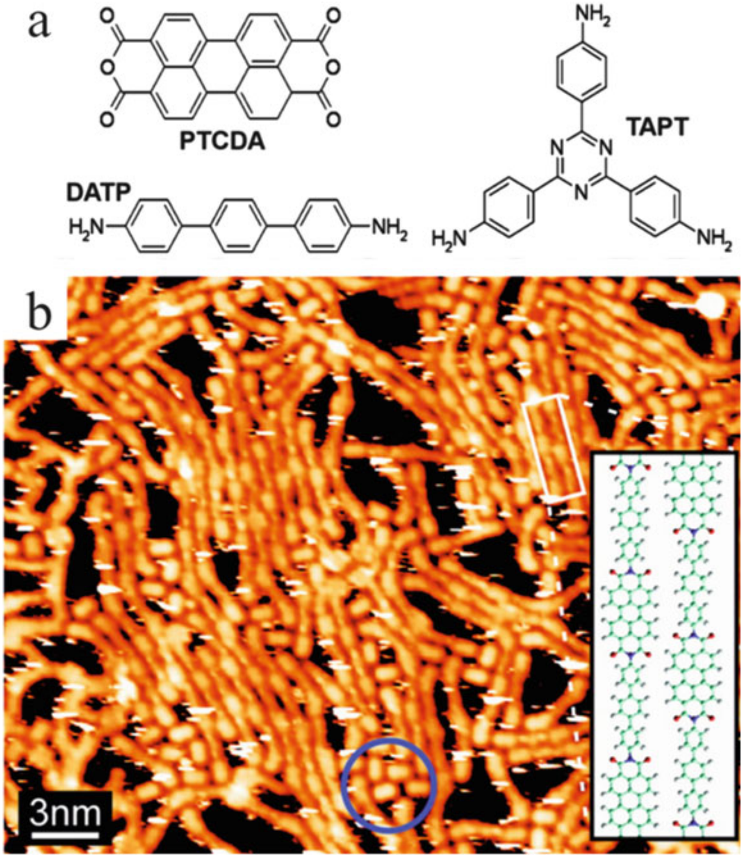

Fig. 12 Chemical structures of the precursors and STM image of the products formed in imidization condensation reaction [77]: (**a**) 3,4,9,10-perylenetetracarboxylic-dianhydride (PTCDA), 4,4′-diamino-*p*-terphenyl (DATP), and 2,4,6-tris(4-aminophenyl)-1,3,5-triazine (TAPT); (**b**) parallel polyimide formed from annealing at 570 K of DATP and PTCDA molecules co-deposited on Au(111)

an Ag(111) surface kept at 590 K to generate conjugated SCOF structures through cyclotrimerization. The products were imaged by STM, as shown in Fig. 13a. The reaction mechanism was studied by DFT calculation and XPS characterization, and the proposed procedure is shown in Fig. 13b. To activate the reaction, one C–H bond in a methyl group is cleaved. Then, the formed radical attacks the nearby molecule, with subsequent dissociation of a hydroxyl to obtain a dimer. The dimer reacts with a third molecule to produce the final trimerization product. It is worth noting that this reaction is universal on other surfaces such as Au(111) and Cu(111), whereas Ag(111) was the best choice because of the high mobility of the precursor molecules on Ag surfaces.

Fig. 13 (**a**) STM image of SCOF structure formed from 1,3,5-tris (4-acetylphenyl) benzene (TAPB) on an Ag(111) surface and (**b**) schematic representation of the reaction [83]

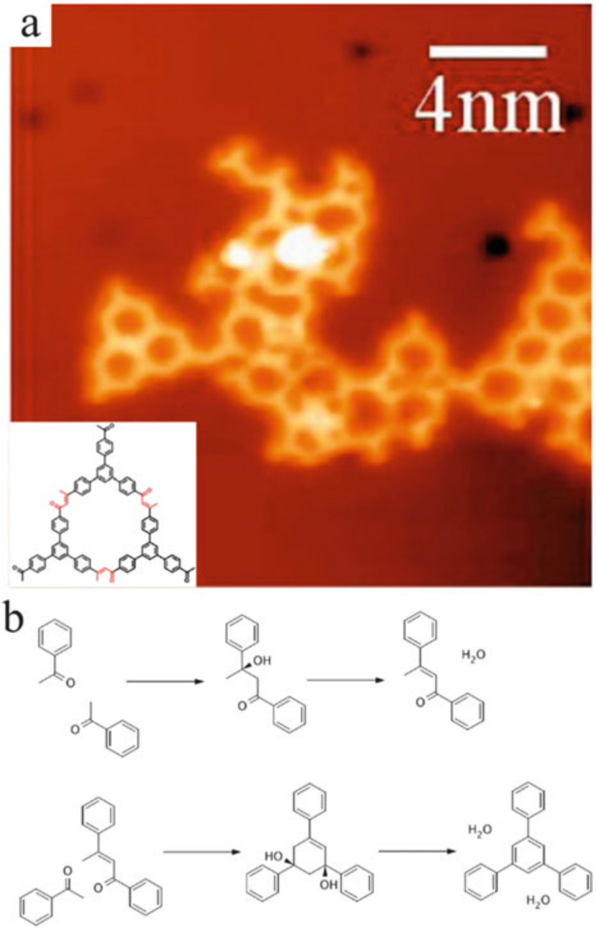

4 Choice of Substrate Surface

Many surface-assisted reactions have been successfully implemented on metal surfaces. Compared with the corresponding reactions in solution, the same products can be synthesized from the same reactants; the difference is that they may proceed through different reaction paths. In surface-assisted reactions, without the presence of solvent or other catalyst, the metal surfaces play a crucial role. In fact, the basic effect of the substrate surface is to afford a 2D plane to support adsorption and promote the movement of precursor molecules. Additionally, the periodic electronic structures on metal surfaces can reduce the activation energy barriers of on-surface reactions, which allows the metal surface to serve as catalyst in the reaction process. Thus, the material and the surface orientation of the substrate both need to be carefully chosen when designing a surface-assisted reaction.

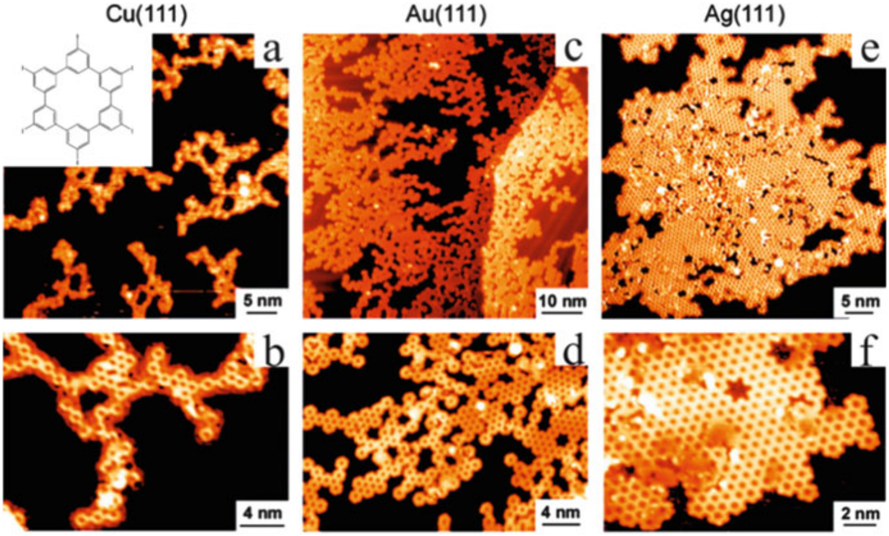

Fig. 14 STM images of hexaiodo-substituted macrocycle cyclohexa-*m*-phenylene (CHP) deposited on different surfaces [84]:. (**a**, **b**) Cu(111); (**c**, **d**) Au(111); (**e**, **f**) Ag(111); *inset* chemical structure of CHP

Taking the Ullmann reaction as an example, Bieri et al. [84] investigated the influence of different surfaces on Ullmann coupling. The hexaiodo-substituted macrocycle cyclohexa-*m*-phenylene (CHP) was employed as precursor, deposited on Cu(111), Ag(111), and Au(111) and subsequently annealed to different temperatures to activate the reactions. On Cu(111), the reaction initiated at 475 K and generated dendritic network structures with single-molecule-wide branches; on Ag (111), an activation temperature of 575 K was used, and the products were extended and well-ordered 2D networks; on Au(111), the activation temperature was 525 K and 2D networks in small domains were obtained (shown in Fig. 14). These differences were the result of variations in the reactivity and mobility of the three surfaces. Cu surfaces show higher reactivity than Ag surfaces, but have a higher diffusion barrier (2.2 eV) than Ag(111) surfaces (0.8 eV) [85]. In this case, CHP polymerization on Cu(111) surfaces can be activated at low temperature, but the movement of molecules is hindered by the large diffusion barrier on the surface; thus, formation of loose polymerized structures is induced. By contrast, coupling of CHP on Ag(111) surfaces requires a higher activation temperature because of the low reactivity of the substrate, whereas the low diffusion barrier promotes the formation of large-scale 2D networks. Au(111) surfaces exhibit properties between those of Cu(111) and Ag(111) surfaces, with an activation temperature between the two, and the formed products being a mixture of branched polymers and 2D networks.

It is worth noting that not only the excitation conditions of reaction, but also the proceeding paths, are related to the properties of the substrate surface. The Ullmann

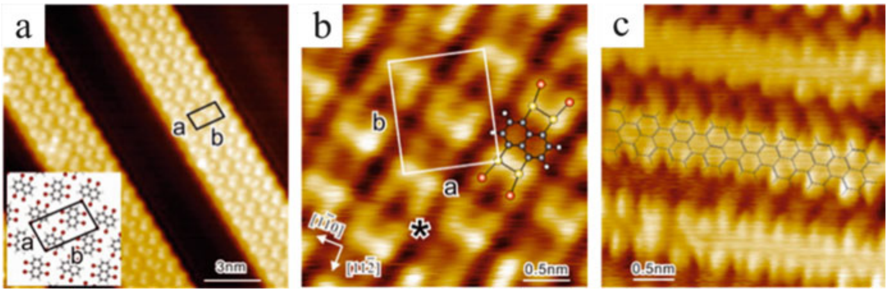

Fig. 15 STM images of 1,4,5,8-tetrabromonaphthalene (TBN) molecules deposited on Au(111) surfaces held at different temperatures [89]: (**a**) 273 K; (**b**) 370 K; (**c**) 470 K

reactions on Cu(111) [41, 86] and Ag(111) [87] contain metal–organic coordination structures as intermediates. On Au(111), only direct transformation of reactants to the final covalently bonded structures was detected. It was thought that the C–Au–C structure is not stable enough to be detected [24]. However, Zhang et al. [88] successfully fabricated stable C–Au–C structures when they studied the coupling of chlorosubstituted perylene-3,4,9,10-tetracarboxylic acid bisimides (PBIs) on Au (111) surfaces. Additionally, study of the coupling of 1,4,5,8-tetrabromonaphthalene (TBN) proved that the C–Au–C coordination structure is the intermediate of the Ullmann reaction on an Au(111) surface. The authors deposited TBN molecules on an Au(111) surface at 273 K and obtained the self-assembled structure shown in Fig. 15a. However, the molecules desorbed before reaching the activation temperature for Ullmann coupling on the surface. TBN deposited on an Au(111) surface held at 370 K produced a stable coordination structure intermediate (STM image and molecular model are shown in Fig. 15b). Subsequent annealing of the coordination structures at higher temperatures (400–470 K) gave GNRs with the width of only five carbon atoms [89]. Therefore, this work proved the stability of the coordinated intermediate in the Ullmann reaction on an Au surface, and also indicated another way to synthesize GNRs under gentle conditions without involving the cyclodehydregenation process.

Walch et al. [90] studied the Ullmann coupling of 1,3,5-tris(4-bromophenyl) benzene (TBB) on Ag(111) and Ag(110) surfaces to identify the effect of substrate surface orientation. They found that the reaction only occurred on Ag(110) surfaces and not Ag(111) surfaces at room temperature. They attributed the difference to the higher catalytic ability of an Ag(110) surface than that of an Ag(111) surface, as well as the unique anisotropy structure on Ag(110) surfaces that enhanced the directional combination. Another example is the linear polymerization of alkane molecules through dehydrogenation on Au(110) because of the special properties of the surface, but not on Au(111) under the same conditions [31].

One important application of surface-assisted reactions is the fabrication of conjugated 1D or 2D organic materials, which can be further used as organic semiconductors or molecular wires in organic devices. However, until now, most of the reactions took place on metal [23, 91] or semiconductor [92] surfaces under vacuum conditions. This hindered the application of such organic materials because device fabrication requires them to be transferred from these conductive surfaces onto insulator substrates. Stripping the organic polymers from metal surfaces proved to be difficult, whereas directly producing the conjugated polymers on an insulator surface seems to be difficult because of the low catalytic properties of insulating surfaces [93]. Bombis et al. [94] tried to fabricate organic wires from dibromoterfluorene (DBTF) on NaCl crystal surfaces and found that it is impossible to fabricate poly(9,9-dimethylfluorene) on an NaCl surface because of the low surface reactivity. They found a circuitous path for solving this problem, that is, initial synthesis of poly(9,9-dimethylfluorene) on an Au(111) surface by the Ullmann reaction followed by deposition of NaCl molecules on the sample kept at 270 K. The NaCl crystal thin film grew under the polymer chains to give a set of molecular wires with the middle part laid on insulating NaCl crystal films and two ends connected with gold substrate. Later, Abel et al. [95] succeeded in fabrication of polymeric Fe-phthalocyanine single sheet on an Ag(100) surface covered by single layer of NaCl film through co-evaporating Fe and 1,2,4,5-tetracyanobenzene (TCNB). More recently, researchers have explored the polymerization of molecules on bulk insulated $CaCO_3$ (104) surface and obtained polymers of linear, zig-zag, and dimer structure [96, 97]. A speculated explanation of the initiation of these reactions is that the strong anchoring of the molecules on the substrate surface reduces the activation barrier, although exploration of detailed mechanisms is still in progress.

5 Outlook

In summary, we have reviewed a series of surface-assisted reactions on single-crystal metal surfaces for preparation of various macromolecules and polymers. Various activation methods, such as heat, exposure to light, or electron injection, can be used to trigger reactions on metal surfaces under vacuum conditions. In these on-surface reactions, the metal substrate plays an important role in determining the activation barrier of the reaction and the final structure of products. In each specific reaction, the structure of precursor molecules, substrate temperature, type of metal substrate, and the orientation of single-crystal planes are important factors that deserve particular concern. Compared with physisorbed SAMs, SCOF structures are much more stable as a result of the covalently bonded connections between molecular moieties. Such a stable and structurally controllable monolayer can be used as a chemically protective layer for metal surfaces, and as molecular template to selectively host guest molecules (e.g., C_{60}) [98]. Specifically, conjugated structures (e.g., molecular chains and GNRs) prepared by on-surface reactions are potential candidates for next-generation carbon-based semiconductors. Surface-assisted reactions are still in their infancy and there are many challenges and open questions that need to be addressed.

First, surface-supported polymers (e.g., GNRs on metal substrate) cannot be efficiently transferred onto insulating surfaces, which significantly impedes their application in electronics. In contrast to the direct etching of metal substrate [99], other possible methods can be taken into consideration, such as synthesis of the polymer on an insulating surface. Because a bulk insulating substrate is not suitable for STM measurements, an alternative substrate could be a metal substrate with a thin insulating film (about 1–4 atomic thickness) on top. The insulating film can decouple the hybridization of electrons from metal substrate and, at the same time provide sufficient tunneling current for STM investigations. Furthermore, the insulating film can remarkably reduce the charge transfer between organic materials and metal surfaces, enabling investigation of the intrinsic properties of the molecules (polymers) (e.g., electronic structure and molecular vibration).

Second, there is no effective method for controlling the reaction in terms of the pathway and the structure of products. Surface-assisted reactions frequently take place on metal surfaces with high catalytic activity, mostly leading to the formation of other byproducts. Byproducts are adsorbed steadily on the metal substrate and thus limit subsequent investigation of the physical and chemical properties of the products. Although there are several examples where high yields of the pure product have been achieved in terms of molecule–surface interactions [16, 31, 73, 100], the methods are still not general enough to avoid byproducts in different reactions.

Finally, the strong covalently bonded connections between molecules are a double-edged sword. On the one hand, they provides a stable connection between molecular moieties, but, on the other hand, they also prevent the reversibility of the reaction. The lack of reversibility leads to the formation of random defects in produced structures. Reduction of defects in produced polymers and exploration of controllable synthesis of functional materials are both urgent tasks in the study of surface-assisted reactions. Under UHV conditions, because of the irreversibility of the reaction, defects are preserved and present in the final product on surfaces. However, it seems possible to solve this problem using a solution system established in air. Recently, researchers have succeeded in fabricating large-scale, ordered and defect-free SCOF structures in the condensation reaction of boronic acids [101] and the Schiff base reaction [102, 103] on HOPG in ambient conditions. Those reactions proceed reversibly by controlling the surrounding environment, which makes it possible to decrease defects in the final products. In conclusion, the exploration of surface-assisted reactions is still in progress. Many traditional solution chemistry reactions will be reevaluated under UHV conditions. More importantly, practical application of the synthesized materials is still highly challenging and requires further study.

References

1. Barth JV, Costantini G, Kern K (2005) Engineering atomic and molecular nanostructures at surfaces. Nature 437:671–679
2. Ciesielski A, Palma C-A, Bonini M, Samorì P (2010) Towards supramolecular engineering of functional nanomaterials: pre-programming multi-component 2D self-assembly at solid-liquid interfaces. Adv Mater 22:3506–3520
3. Xie Z-X, Huang Z-F, Xu X (2002) Influence of reconstruction on the structure of self-assembled normal-alkane monolayers on Au(111) surfaces. Phys Chem Chem Phys 4:1486–1489
4. Tahara K, Furukawa S, Uji-i H, Uchino T, Ichikawa T, Zhang J, Mamdouh W, Sonoda M, De Schryver FC, De Feyter S, Tobe Y (2006) Two-dimensional porous molecular networks of dehydrobenzo[12]annulene derivatives via alkyl chain interdigitation. JACS 128:16613–16625
5. Griessl SJH, Lackinger M, Jamitzky F, Markert T, Hietschold M, Heckl WM (2004) Incorporation and manipulation of coronene in an organic template structure. Langmuir 20:9403–9407
6. Madueno R, Raisanen MT, Silien C, Buck M (2008) Functionalizing hydrogen-bonded surface networks with self-assembled monolayers. Nature 454:618–621
7. Wasio NA, Quardokus RC, Forrest RP, Lent CS, Corcelli SA, Christie JA, Henderson KW, Kandel SA (2014) Self-assembly of hydrogen-bonded two-dimensional quasicrystals. Nature 507:86–89
8. Silly F (2013) selecting two-dimensional halogen–halogen bonded self-assembled 1,3,5-tris (4-iodophenyl)benzene porous nanoarchitectures at the solid–liquid interface. J Phys Chem C 117:20244–20249
9. Gutzler R, Ivasenko O, Fu C, Brusso JL, Rosei F, Perepichka DF (2011) Halogen bonds as stabilizing interactions in a chiral self-assembled molecular monolayer. Chem Commun 47:9453–9455
10. Schlickum U, Decker R, Klappenberger F, Zoppellaro G, Klyatskaya S, Ruben M, Silanes I, Arnau A, Kern K, Brune H, Barth JV (2007) Metal−organic honeycomb nanomeshes with tunable cavity size. Nano Lett 7:3813–3817
11. Shi Z, Lin N (2009) Porphyrin-based two-dimensional coordination kagome lattice self-assembled on a Au(111) surface. JACS 131:5376–5377
12. Bonifazi D, Mohnani S, Llanes-Pallas A (2009) Supramolecular chemistry at interfaces: molecular recognition on nanopatterned porous surfaces. Chem – A Eur J 15:7004–7025
13. El Garah M, MacLeod JM, Rosei F (2013) Covalently bonded networks through surface-confined polymerization. Surf Sci 613:6–14
14. Franc G, Gourdon A (2011) Covalent networks through on-surface chemistry in ultra-high vacuum: state-of-the-art and recent developments. Phys Chem Chem Phys 13:14283–14292
15. Lackinger M, Heckl WM (2011) A STM perspective on covalent intermolecular coupling reactions on surfaces. J Phys D: Appl Phys 44:464011
16. Lafferentz L, Eberhardt V, Dri C, Africh C, Comelli G, Esch F, Hecht S, Grill L (2012) Controlling on-surface polymerization by hierarchical and substrate-directed growth. Nat Chem 4:215–220
17. Bieri M, Blankenburg S, Kivala M, Pignedoli CA, Ruffieux P, Mullen K, Fasel R (2011) Surface-supported 2D heterotriangulene polymers. Chem Commun 47:10239–10241
18. Hla S-W, Bartels L, Meyer G, Rieder K-H (2000) Inducing all steps of a chemical reaction with the scanning tunneling microscope tip: towards single molecule engineering. Phys Rev Lett 85:2777–2780
19. Dinca LE, MacLeod JM, Lipton-Duffin J, Fu C, Ma D, Perepichka DF, Rosei F (2014) Tip-induced C-H activation and oligomerization of thienoanthracenes. Chem Commun 50:8791–8793

20. Jiang Y, Huan Q, Fabris L, Bazan GC, Ho W (2013) Submolecular control, spectroscopy and imaging of bond-selective chemistry in single functionalized molecules. Nat Chem 5:36–41
21. Basagni A, Colazzo L, Sedona F, DiMarino M, Carofiglio T, Lubian E, Forrer D, Vittadini A, Casarin M, Verdini A, Cossaro A, Floreano L, Sambi M (2014) Stereoselective photopolymerization of tetraphenylporphyrin derivatives on Ag(110) at the sub-monolayer level. Chem – A Eur J 20:14296–14304
22. Basagni A, Ferrighi L, Cattelan M, Nicolas L, Handrup K, Vaghi L, Papagni A, Sedona F, Valentin CD, Agnoli S, Sambi M (2015) On-surface photo-dissociation of C-Br bonds: towards room temperature Ullmann coupling. Chem Commun 51:12593–12596
23. Gao H-Y, Franke J-H, Wagner H, Zhong D, Held P-A, Studer A, Fuchs H (2013) Effect of metal surfaces in on-surface Glaser coupling. J Phys Chem C 117:18595–18602
24. Dong L, Liu PN, Lin N (2015) Surface-activated coupling reactions confined on a surface. Acc Chem Res 48:2765–2774
25. Grill L, Dyer M, Lafferentz L, Persson M, Peters MV, Hecht S (2007) Nano-architectures by covalent assembly of molecular building blocks. Nat Nano 2:687–691
26. Zhang Y-Q, Kepčija N, Kleinschrodt M, Diller K, Fischer S, Papageorgiou AC, Allegretti F, Björk J, Klyatskaya S, Klappenberger F, Ruben M, Barth JV (2012) Homo-coupling of terminal alkynes on a noble metal surface. Nat Commun 3:1286
27. Zwaneveld NAA, Pawlak RM, Abel M, Catalin D, Gigmes D, Bertin D, Porte L (2008) Organized formation of 2D extended covalent organic frameworks at surfaces. JACS 130:6678–6679
28. Bebensee F, Bombis C, Vadapoo S-R, Cramer JR, Besenbacher F, Gothelf KV, Linderoth TR (2013) On-surface azide–alkyne cycloaddition on Cu(111): does it “click” in ultrahigh vacuum? JACS 135:2136–2139
29. Otero G, Biddau G, Sanchez-Sanchez C, Caillard R, Lopez MF, Rogero C, Palomares FJ, Cabello N, Basanta MA, Ortega J, Mendez J, Echavarren AM, Perez R, Gomez-Lor B, Martin-Gago JA (2008) Fullerenes from aromatic precursors by surface-catalysed cyclodehydrogenation. Nature 454:865–868
30. Kanuru VK, Kyriakou G, Beaumont SK, Papageorgiou AC, Watson DJ, Lambert RM (2010) Sonogashira coupling on an extended gold surface in vacuo: reaction of phenylacetylene with iodobenzene on Au(111). JACS 132:8081–8086
31. Zhong D, Franke J-H, Podiyanachari SK, Blömker T, Zhang H, Kehr G, Erker G, Fuchs H, Chi L (2011) Linear alkane polymerization on a gold surface. Science 334:213–216
32. Gourdon A (2008) On-surface covalent coupling in ultrahigh vacuum. Angew Chem Int Ed 47:6950–6953
33. Sakaguchi H, Matsumura H, Gong H, Abouelwafa AM (2005) Direct visualization of the formation of single-molecule conjugated copolymers. Science 310:1002–1006
34. Lapitan Jr LDS, Tongol BJV, Yau S-L (2012) In situ scanning tunneling microscopy imaging of electropolymerized poly(3,4-ethylenedioxythiophene) on an iodine-modified Au(111) single crystal electrode. Electrochim Acta 62:433–440
35. Lapitan LDS, Tongol BJV, Yau S-L (2010) Molecular assembly and electropolymerization of 3,4-ethylenedioxythiophene on Au(111) single crystal electrode as probed by in situ electrochemical STM in 0.10 M HClO4. Langmuir 26:10771–10777
36. Ullmann F, Bielecki J (1901) Ueber synthesen in der biphenylreihe. Ber Dtsch Chem Ges 34:2174–2185
37. Xi M, Bent BE (1992) Iodobenzene on Cu(111): formation and coupling of adsorbed phenyl groups. Surf Sci 278:19–32
38. Xi M, Bent BE (1993) Mechanisms of the Ullmann coupling reaction in adsorbed monolayers. JACS 115:7426–7433
39. Blake MM, Nanayakkara SU, Claridge SA, Fernández-Torres LC, Sykes ECH, Weiss PS (2009) Identifying reactive intermediates in the Ullmann coupling reaction by scanning tunneling microscopy and spectroscopy. J Phys Chem A 113:13167–13172

40. Lipton-Duffin JA, Ivasenko O, Perepichka DF, Rosei F (2009) Synthesis of polyphenylene molecular wires by surface-confined polymerization. Small 5:592–597
41. Wang W, Shi X, Wang S, Van Hove MA, Lin N (2011) Single-molecule resolution of an organometallic intermediate in a surface-supported Ullmann coupling reaction. JACS 133:13264–13267
42. Heim D, Écija D, Seufert K, Auwärter W, Aurisicchio C, Fabbro C, Bonifazi D, Barth JV (2010) Self-assembly of flexible one-dimensional coordination polymers on metal surfaces. JACS 132:6783–6790
43. Koch M, Gille M, Viertel A, Hecht S, Grill L (2014) Substrate-controlled linking of molecular building blocks: Au(111) vs. Cu(111). Surf Sci 627:70–74
44. Cardenas L, Gutzler R, Lipton-Duffin J, Fu C, Brusso JL, Dinca LE, Vondracek M, Fagot-Revurat Y, Malterre D, Rosei F, Perepichka DF (2013) Synthesis and electronic structure of a two dimensional [small pi]-conjugated polythiophene. Chem Sci 4:3263–3268
45. Fan Q, Wang T, Liu L, Zhao J, Zhu J, Gottfried JM (2015) Tribromobenzene on Cu(111): temperature-dependent formation of halogen-bonded, organometallic, and covalent nanostructures. J Chem Phys 142:101906
46. Fan Q, Wang C, Liu L, Han Y, Zhao J, Zhu J, Kuttner J, Hilt G, Gottfried JM (2014) Covalent, organometallic, and halogen-bonded nanomeshes from tetrabromo-terphenyl by surface-assisted synthesis on Cu(111). J Phys Chem C 118:13018–13025
47. Eichhorn J, Strunskus T, Rastgoo-Lahrood A, Samanta D, Schmittel M, Lackinger M (2014) On-surface Ullmann polymerization via intermediate organometallic networks on Ag(111). Chem Commun 50:7680–7682
48. Lafferentz L, Ample F, Yu H, Hecht S, Joachim C, Grill L (2009) Conductance of a single conjugated polymer as a continuous function of its length. Science 323:1193–1197
49. Bieri M, Treier M, Cai J, Ait-Mansour K, Ruffieux P, Groning O, Groning P, Kastler M, Rieger R, Feng X, Mullen K, Fasel R (2009) Porous graphenes: two-dimensional polymer synthesis with atomic precision. Chem Commun 2009:6919–6921
50. Weigelt S, Busse C, Bombis C, Knudsen MM, Gothelf KV, Strunskus T, Wöll C, Dahlbom M, Hammer B, Lægsgaard E, Besenbacher F, Linderoth TR (2007) Covalent interlinking of an aldehyde and an amine on a Au(111) surface in ultrahigh vacuum. Angew Chem Int Ed 46:9227–9230
51. Cordes EH, Jencks WP (1962) On the mechanism of Schiff base formation and hydrolysis. JACS 84:832–837
52. Weigelt S, Busse C, Bombis C, Knudsen MM, Gothelf KV, Lægsgaard E, Besenbacher F, Linderoth TR (2008) Surface synthesis of 2D branched polymer nanostructures. Angew Chem 120:4478–4482
53. Weigelt S, Bombis C, Busse C, Knudsen MM, Gothelf KV, Lægsgaard E, Besenbacher F, Linderoth TR (2008) Molecular self-assembly from building blocks synthesized on a surface in ultrahigh vacuum: kinetic control and topo-chemical reactions. ACS Nano 2:651–660
54. El-Kaderi HM, Hunt JR, Mendoza-Cortés JL, Côté AP, Taylor RE, O'Keeffe M, Yaghi OM (2007) Designed synthesis of 3D covalent organic frameworks. Science 316:268–272
55. Côté AP, El-Kaderi HM, Furukawa H, Hunt JR, Yaghi OM (2007) Reticular synthesis of microporous and mesoporous 2D covalent organic frameworks. JACS 129:12914–12915
56. Ourdjini O, Pawlak R, Abel M, Clair S, Chen L, Bergeon N, Sassi M, Oison V, Debierre J-M, Coratger R, Porte L (2011) Substrate-mediated ordering and defect analysis of a surface covalent organic framework. Phys Rev B 84:125421
57. Clair S, Ourdjini O, Abel M, Porte L (2011) Tip- or electron beam-induced surface polymerization. Chem Commun 47:8028–8030
58. Streitwieser A, Heathcock CH (1985) Introduction to organic chemistry. Macmillan, New York
59. In't Veld M, Iavicoli P, Haq S, Amabilino DB, Raval R (2008) Unique intermolecular reaction of simple porphyrins at a metal surface gives covalent nanostructures. Chem Commun 2008:1536–1538

60. Wiengarten A, Seufert K, Auwärter W, Ecija D, Diller K, Allegretti F, Bischoff F, Fischer S, Duncan DA, Papageorgiou AC, Klappenberger F, Acres RG, Ngo TH, Barth JV (2014) Surface-assisted dehydrogenative homocoupling of porphine molecules. JACS 136:9346–9354
61. Simpson CD, Mattersteig G, Martin K, Gherghel L, Bauer RE, Räder HJ, Müllen K (2004) Nanosized molecular propellers by cyclodehydrogenation of polyphenylene dendrimers. JACS 126:3139–3147
62. Cai J, Ruffieux P, Jaafar R, Bieri M, Braun T, Blankenburg S, Muoth M, Seitsonen AP, Saleh M, Feng X, Mullen K, Fasel R (2010) Atomically precise bottom-up fabrication of graphene nanoribbons. Nature 466:470–473
63. Chen Y-C, Cao T, Chen C, Pedramrazi Z, Haberer D, de OteyzaDimas G, Fischer FR, Louie SG, Crommie MF (2015) Molecular bandgap engineering of bottom-up synthesized graphene nanoribbon heterojunctions. Nat Nano 10:156–160
64. Rogers C, Chen C, Pedramrazi Z, Omrani AA, Tsai H-Z, Jung HS, Lin S, Crommie MF, Fischer FR (2015) Closing the nanographene gap: surface-assisted synthesis of peripentacene from 6,6′-bipentacene precursors. Angew Chem Int Ed 54:15143–15146
65. Björk J, Stafström S, Hanke F (2011) Zipping up: cooperativity drives the synthesis of graphene nanoribbons. JACS 133:14884–14887
66. Treier M, Pignedoli CA, Laino T, Rieger R, Müllen K, Passerone D, Fasel R (2011) Surface-assisted cyclodehydrogenation provides a synthetic route towards easily processable and chemically tailored nanographenes. Nat Chem 3:61–67
67. Mendez J, Lopez MF, Martin-Gago JA (2011) On-surface synthesis of cyclic organic molecules. Chem Soc Rev 40:4578–4590
68. Scott LT, Boorum MM, McMahon BJ, Hagen S, Mack J, Blank J, Wegner H, de Meijere A (2002) A rational chemical synthesis of C_{60}. Science 295:1500–1503
69. Gómez-Lor B, Echavarren AM (2004) Synthesis of a triaza analogue of crushed-fullerene by intramolecular palladium-catalyzed arylation. Org Lett 6:2993–2996
70. Amsharov K, Abdurakhmanova N, Stepanow S, Rauschenbach S, Jansen M, Kern K (2010) Towards the isomer-specific synthesis of higher fullerenes and buckybowls by the surface-catalyzed cyclodehydrogenation of aromatic precursors. Angew Chem Int Ed 49:9392–9396
71. Hay AS (1962) Oxidative coupling of acetylenes. II1. J Org Chem 27:3320–3321
72. Eichhorn J, Heckl WM, Lackinger M (2013) On-surface polymerization of 1,4-diethynylbenzene on Cu(111). Chem Commun 49:2900–2902
73. Gao H-Y, Wagner H, Zhong D, Franke J-H, Studer A, Fuchs H (2013) Glaser coupling at metal surfaces. Angew Chem Int Ed 52:4024–4028
74. Sánchez-Sánchez C, Yubero F, González-Elipe AR, Feria L, Sanz JF, Lambert RM (2014) The Flexible surface revisited: adsorbate-induced reconstruction, homocoupling, and Sonogashira cross-coupling on the Au(100) surface. J Phys Chem C 118:11677–11684
75. Yokoyama T, Yokoyama S, Kamikado T, Okuno Y, Mashiko S (2001) Selective assembly on a surface of supramolecular aggregates with controlled size and shape. Nature 413:619–621
76. Díaz Arado O, Mönig H, Wagner H, Franke J-H, Langewisch G, Held PA, Studer A, Fuchs H (2013) On-surface azide–alkyne cycloaddition on Au(111). ACS Nano 7:8509–8515
77. Treier M, Richardson NV, Fasel R (2008) Fabrication of surface-supported low-dimensional polyimide networks. JACS 130:14054–14055
78. Marele AC, Mas-Balleste R, Terracciano L, Rodriguez-Fernandez J, Berlanga I, Alexandre SS, Otero R, Gallego JM, Zamora F, Gomez-Rodriguez JM (2012) Formation of a surface covalent organic framework based on polyester condensation. Chem Commun 48:6779–6781
79. de Oteyza DG, Gorman P, Chen Y-C, Wickenburg S, Riss A, Mowbray DJ, Etkin G, Pedramrazi Z, Tsai H-Z, Rubio A, Crommie MF, Fischer FR (2013) Direct imaging of covalent bond structure in single-molecule chemical reactions. Science 340:1434–1437
80. Sun Q, Zhang C, Li Z, Kong H, Tan Q, Hu A, Xu W (2013) On-surface formation of one-dimensional polyphenylene through Bergman cyclization. JACS 135:8448–8451

81. Liu J, Lam JWY, Tang BZ (2009) Acetylenic polymers: syntheses, structures, and functions. Chem Rev 109:5799–5867
82. Dong H, Zheng R, Lam JWY, Häussler M, Qin A, Tang BZ (2005) A New Route to hyperbranched macromolecules: syntheses of photosensitive poly(aroylarylene)s via 1,3,5-regioselective polycyclotrimerization of bis(aroylacetylene)s. Macromolecules 38:6382–6391
83. Yang B, Björk J, Lin H, Zhang X, Zhang H, Li Y, Fan J, Li Q, Chi L (2015) Synthesis of surface covalent organic frameworks via dimerization and cyclotrimerization of acetyls. JACS 137:4904–4907
84. Bieri M, Nguyen M-T, Gröning O, Cai J, Treier M, Aït-Mansour K, Ruffieux P, Pignedoli CA, Passerone D, Kastler M, Müllen K, Fasel R (2010) Two-dimensional polymer formation on surfaces: insight into the roles of precursor mobility and reactivity. JACS 132:16669–16676
85. Hammer BN, Norskov JK (2000) Theoretical surface science and catalysis—calculations and concepts. In: Gates B, Knoezinger H (eds) Advances in catalysis, vol 45. Academic, San Diego 2000, pp 71–129
86. Chen M, Xiao J, Steinrück H-P, Wang S, Wang W, Lin N, Hieringer W, Gottfried JM (2014) Combined photoemission and scanning tunneling microscopy study of the surface-assisted Ullmann coupling reaction. J Phys Chem C 118:6820–6830
87. Chung K-H, Koo B-G, Kim H, Yoon JK, Kim J-H, Kwon Y-K, Kahng S-J (2012) Electronic structures of one-dimensional metal-molecule hybrid chains studied using scanning tunneling microscopy and density functional theory. Phys Chem Chem Phys 14:7304–7308
88. Zhang H, Franke J-H, Zhong D, Li Y, Timmer A, Arado OD, Mönig H, Wang H, Chi L, Wang Z, Müllen K, Fuchs H (2013) Surface supported gold–organic hybrids: on-surface synthesis and surface directed orientation. Small 10:1361–1368
89. Zhang H, Lin H, Sun K, Chen L, Zagranyarski Y, Aghdassi N, Duhm S, Li Q, Zhong D, Li Y, Müllen K, Fuchs H, Chi L (2015) On-surface synthesis of rylene-type graphene nanoribbons. JACS 137:4022–4025
90. Walch H, Gutzler R, Sirtl T, Eder G, Lackinger M (2010) Material- and orientation-dependent reactivity for heterogeneously catalyzed carbon−bromine bond homolysis. J Phys Chem C 114:12604–12609
91. Matena M, Riehm T, Stöhr M, Jung TA, Gade LH (2008) Transforming surface coordination polymers into covalent surface polymers: linked polycondensed aromatics through oligomerization of N-heterocyclic carbene intermediates. Angew Chem Int Ed 47:2414–2417
92. Kolmer M, Ahmad Zebari AA, Prauzner-Bechcicki JS, Piskorz W, Zasada F, Godlewski S, Such B, Sojka Z, Szymonski M (2013) Polymerization of polyanthrylene on a titanium dioxide (011)-(2×1) surface. Angew Chem 125:10490–10493
93. Gutzler R, Walch H, Eder G, Kloft S, Heckl WM, Lackinger M (2009) Surface mediated synthesis of 2D covalent organic frameworks: 1,3,5-tris(4-bromophenyl)benzene on graphite (001), Cu(111), and Ag(110). Chem Commun 2009:4456
94. Bombis C, Ample F, Lafferentz L, Yu H, Hecht S, Joachim C, Grill L (2009) Single molecular wires connecting metallic and insulating surface areas. Angew Chem Int Ed 48:9966–9970
95. Abel M, Clair S, Ourdjini O, Mossoyan M, Porte L (2010) Single layer of polymeric Fe-phthalocyanine: an organometallic sheet on metal and thin insulating film. JACS 133:1203–1205
96. Kittelmann M, Nimmrich M, Lindner R, Gourdon A, Kühnle A (2013) Sequential and site-specific on-surface synthesis on a bulk insulator. ACS Nano 7:5614–5620
97. Kittelmann M, Rahe P, Nimmrich M, Hauke CM, Gourdon A, Kühnle A (2011) On-surface covalent linking of organic building blocks on a bulk insulator. ACS Nano 5:8420–8425
98. Blunt MO, Russell JC, Champness NR, Beton PH (2010) Templating molecular adsorption using a covalent organic framework. Chem Commun 46:7157–7159

99. Bennett PB, Pedramrazi Z, Madani A, Chen Y-C, de Oteyza DG, Chen C, Fischer FR, Crommie MF, Bokor J (2013) Bottom-up graphene nanoribbon field-effect transistors. Appl Phys Lett 103:253114
100. Faury T, Clair S, Abel M, Dumur F, Gigmes D, Porte L (2012) Sequential linking to control growth of a surface covalent organic framework. J Phys Chem C 116:4819–4823
101. Guan C-Z, Wang D, Wan L-J (2012) Construction and repair of highly ordered 2D covalent networks by chemical equilibrium regulation. Chem Commun 48:2943–2945
102. Liu X-H, Guan C-Z, Ding S-Y, Wang W, Yan H-J, Wang D, Wan L-J (2013) On-surface synthesis of single-layered two-dimensional covalent organic frameworks via solid–vapor interface reactions. JACS 135:10470–10474
103. Xu L, Zhou X, Yu Y, Tian WQ, Ma J, Lei S (2013) Surface-confined crystalline two-dimensional covalent organic frameworks via on-surface schiff-base coupling. ACS Nano 7:8066–8073

Adv Polym Sci (2017) 278: 99–126
DOI: 10.1007/12_2017_4

On-Surface Polymerization: From Polyarylenes to Graphene Nanoribbons and Two-Dimensional Networks

Matthias Koch, Stefan Hecht, and Leonhard Grill

Abstract On-surface polymerization is a novel technique for the fabrication of one- and two-dimensional molecular networks confined on a surface and is a rapidly developing field in surface science. The molecular building blocks exhibit pre-defined connection sites at which, after thermal activation and diffusion on the surface, the molecules are linked in a clean environment. Depending on the position and number of these connection sites, activated molecules polymerize to yield chains or two-dimensional networks. The chemical composition of the resulting polymer is precisely defined by the precursor molecules. We review current developments in the field of on-surface polymerization and present different examples, including the fabrication of graphene nanoribbons. We introduce reductive Ullmann-type coupling as well as Scholl-type cyclodehydrogenation for fabrication of graphene nanoribbons of increasing width. The surface plays a crucial role during the activation and polymerization processes because it serves as a catalyst, promotes molecular diffusion, and has a huge influence on the final molecular architecture. One-dimensional polymers can act as molecular wires and their conductance has been studied at the level of individual chains. In addition, we discuss two-dimensional networks and describe recent progress in attempts to improve their quality using sequential activation or defect-healing.

M. Koch
Department of Physical Chemistry, Fritz Haber Institute of the Max Planck Society, 14195 Berlin, Germany

S. Hecht
Department of Chemistry & IRIS Adlershof, Humboldt-Universität zu Berlin, 12489 Berlin, Germany

L. Grill (✉)
Department of Physical Chemistry, University of Graz, Heinrichstrasse 28, 8010 Graz, Austria
e-mail: leonhard.grill@uni-graz.at

Keywords Carbon-based materials • C–C coupling reactions • Molecular conductance • On-surface polymerization • On-surface synthesis • Scanning tunneling Microscopy • Step-growth polymerization • Surface chemistry • Surface science

Contents

On-surface polymerization is a recently developed bottom-up approach for the fabrication of one-dimensional polymer chains, including ladder-type polymers and ribbons, as well as two-dimensional sheets and networks. In many cases these structures are not accessible by solution synthesis or top-down fabrication [1]. The technique requires suitable monomers, typically (polycyclic) (hetero) aromatic building blocks, which react at specific predefined connection sites during the polymerization step. To prevent uncontrolled growth, the monomers need to be chemically inert and their reactivity unleashed only after an activation step. One particularly popular approach for this "turn on" reactivity is equipping the molecular building blocks with halogen substituents, which can readily be cleaved by heat, and stabilizing the formed carbon-based radicals on the underlying metal surface. The activated monomer can form covalent aryl–aryl bonds at these reactive sites, allowing fabrication of large macromolecules in a very well-defined manner and in an extremely clean environment. The absence of solvent means that there is no need to solubilize side chains. In contrast, deposition of macromolecules by conventional evaporation techniques in ultrahigh vacuum is difficult to achieve because the high temperatures required typically lead to decomposition.

1 On-Surface Polymerization by Dehalogenation

The process of on-surface polymerization can be separated into three subsequent steps: (1) deposition, when monomers, carrying halogen atoms to mask the desired reaction sites, are deposited onto the surface; (2) activation, when the halogen–carbon bonds are cleaved; and (3) coupling, when covalent bonds are formed

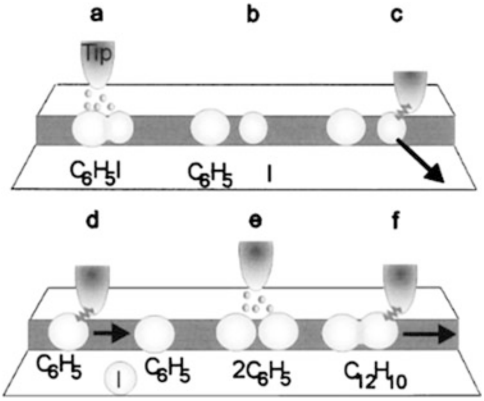

Fig. 1 Different synthesis steps induced by an STM tip: selective dissociation of the C–I bond in iodobenzene induced by electrons (**a, b**), lateral manipulation to remove the cleaved-off iodide (**c**), lateral manipulation to bring two phenyl moieties together (**d**), inelastic tunneling-induced phenyl–phenyl coupling (**e**), and lateral manipulation of the formed biphenyl to confirm successful reaction (**f**). Reproduced from [2]. Copyright (2000) by the American Physical Society

between activated monomers, leading to polymerization. As early as 2000, using iodobenzene molecules on Cu(111), Saw Hla et al. demonstrated each of these steps at the level of single molecules with the help of a low temperature scanning tunneling microscope (STM) (see Fig. 1) [2].

These experiments were performed at a temperature of 20 K to freeze the diffusion of iodobenzene molecules. By applying a bias pulse with the STM tip right on top of the molecule, dissociation of the iodine atom can be induced and a reactive phenyl radical, which is stabilized by interaction with the copper step edge, is generated. In the next step, lateral manipulation is used to move two of such reactive phenyl species next to each other. Finally, coupling of the two radicals is induced by another lower voltage pulse, which induces rotation and subsequently leads to formation of a covalent C–C bond in the biphenyl product, resembling an Ullmann-type coupling reaction [3] on the single molecule level. The beauty of this procedure is that each individual step of the reaction is induced by the STM tip and, hence, each intermediate stage can be studied. This pioneering work laid the foundation for what has become the field of on-surface polymerization.

Although this degree of control over a chemical process is more than sensational, the growth of large polymeric structures requires at least bifunctional building blocks (monomers) and automation of both activation and coupling reactions. For this, a constant stimulus is needed, supplying the activation energy for both processes. The most convenient form of energy to apply is heat in combination with the proper surface. An appropriate surface is crucial because it is much more than a template for performing the reaction and many studies have shown that the

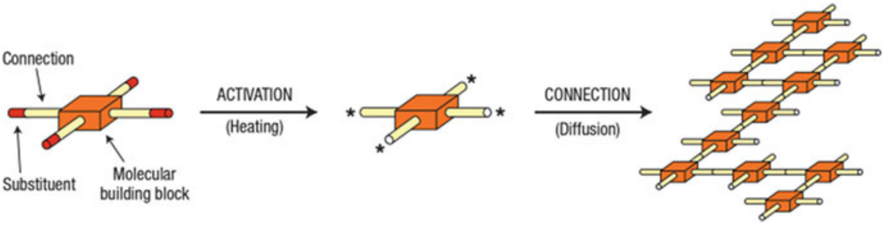

Fig. 2 Principle of the on-surface polymerization technique [1, 7]. Reproduced from [7]

choice of surface has a strong influence on the occurrence of the polymerization process and the resulting final product. For example, the activation energy required to dissociate a halogen atom and the mobility of the monomer and oligomer building blocks vary with the choice of substrate [4]. Thereby, not only the composition of the substrate (e.g,. Cu versus Ag versus Au) but also the surface reconstruction play important roles, specific sites sometimes displaying enhanced reactivity [5].

To automate polymerization, monomers are deposited on the surface and the molecules self-assemble in more or less extended two-dimensional (2D) islands, depending on the coverage. These monomers are, as in the experiment discussed before, equipped with (at least two) halogen atoms at defined sites. The monomer is designed such that the bond between the halogen atom and the molecular framework is the weakest bond in the overall system. For example, the average bond energies of C–C and C–H bonds present on such aromatic systems are between 85 and 103 kcal/mol, whereas the C–Br and C–I bonds have bond dissociation energies of only 68 kcal/mol and 51 kcal/mol, respectively [6]. Monomers can be activated either by evaporating them at a higher temperature or, alternatively and more reliably, by heating the substrate to an elevated temperature. In contrast to local STM-tip-induced activation, this global heating step simultaneously addresses all molecular building blocks adsorbed on the surface. The elevated temperature of the substrate furthermore promotes both diffusion of the monomers (and oligomeric intermediates) and provides the necessary activation energy for their coupling. Therefore, the right combination of surface and monomer structure, together with a properly chosen reaction temperature to provide the necessary thermal activation for the dissociation, diffusion, and coupling steps, indeed allows their automation and integration into a powerful and highly efficient on-surface polymerization scheme (Fig. 2) [1, 7].

Using these powerful techniques, architectural control can be achieved by judicious choice of the monomer structure, including both the number and kind of halogen atoms as well as their relative orientation. Two halogen atoms provide either one-dimensional (1D) chains or cycles, whereas three or more halogens lead to formation of 2D networks.

2 One-Dimensional Oligomers

In early work, Weiss and coworkers studied 1,4-diiodobenzene on Cu(111) and observed formation of so-called “protopolymers” [8]. Later, Rosei, Perepichka, and coworkers found that the same monomer on Cu(110) was readily activated by C–I bond cleavage, yet required additional heating to 500 K to trigger formation of the covalent C–C bonds to yield poly(*para*-phenylene) [9]. When changing from the strictly linear *para*-relationship of the two iodine substituents in the monomer to *meta* (i.e., 1,3-diiodobenzene), they found formation of both *transoid* poly(*meta*-phenylene) chains as well as hexameric cycles (Fig. 3).

If the monomer units are connected to each other by more than one bond, ladder polymers are formed. Using Ullmann-type couplings in this fashion, 1,4,5,8-tetrabromonaphthalene can be polymerized at 470 K on Au(111) to yield such ladder polymers, resembling the narrowest possible graphene nanoribbon (GNR) with armchair edges (Fig. 4) [10]. The authors could show that the Au-bridged metallosupramolecular polymer is an intermediate of the polymerization process; it could be observed at 400 K and underwent reductive elimination to the GNR at 470 K.

Obtaining GNRs with increased width using solely Ullmann-type couplings is limited by the efficiency of the reaction, in particular in adjacent positions on the zig-zag edge of acenes. To circumvent this issue, the groups of Müllen and Fasel developed a two-step procedure to first polymerize a suitable dihalogenated

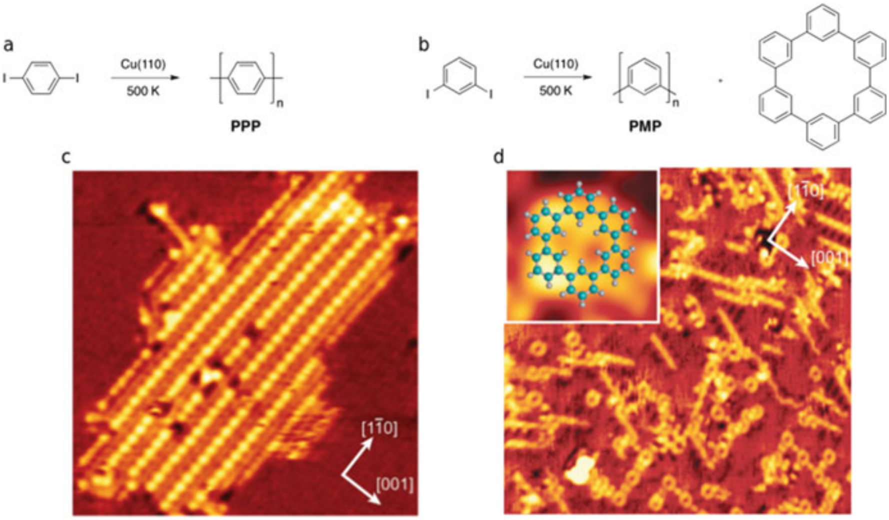

Fig. 3 On-surface polymerization on Cu(110) of either 1,4-diiodobenzene (**a**) or 1,3-diiodobenzene (**b**), resulting in formation of poly(*para*-phenylene) (PPP; **c**) and poly(*meta*-phenylene) (PMP) as well as hexameric macrocycles (**d**), respectively. Reproduced in part from [9]. Copyright (2009) by Wiley-VCH

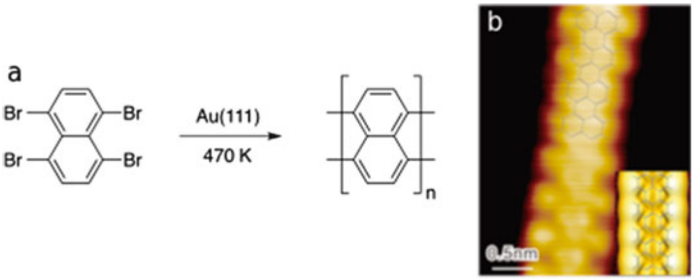

Fig. 4 Polymerization of 1,4,5,8-tetrabromonaphthalene (**a**) to yield narrow armchair graphene nanoribbons (**b**). Reproduced in part from [10]. Copyright (2015) American Chemical Society

monomer via single C–C bonds made with on-surface Ullmann-type coupling, followed by a second annealing step leading to cyclodehydrogenation, known in solution as the Scholl reaction [11]. This powerful route (Fig. 5) led to the successful bottom-up growth of armchair-edge GNRs from dibromodianthracene (DBDA) monomers [12]. After deposition on Au(111), the DBDA monomers arrange in large islands. Heating the substrate to 470 K cleaves the C–Br bonds, and anthracene oligomers (connected by C–C single bonds) are formed. In these oligomers/polymers, the neighboring anthracene units can be fused by a cyclodehydrogenation step, which is induced by increasing the temperature to 670 K.

For the formation of anthracene oligomers it is crucial that the DBDA monomers adsorb in a nonplanar twisted geometry on the Au(111) surface to minimize steric hindrance in the coupling step. This is in good agreement with a study using 9,10-dibromoanthracene (9,10-DBA), a single anthracene with two bromines in the opposing central *meso*-positions, which does not polymerize on Au(111) (Fig. 6) [13].

Even heating the substrate to 670 K does not lead to polymer formation; instead, desorption takes place. This finding is attributed to the planar adsorption geometry of 9,10-DBA and the associated steric hindrance of C–C coupling, whereas the approach of two twisted activated DBDA monomers is presumably associated with a much lower kinetic barrier.

The power of the on-surface polymerization strategy clearly lies in its inherent chemical precision. The structure of the resulting polymer on the surface is precisely determined by the monomer building blocks, in particular their symmetry and position of the reactive groups, which encode their connectivity. This has been beautifully demonstrated by the recent work of the Müllen and Fasel groups on the synthesis of various types of GNRs, in particular achieving precise control over edge structure, ranging from armchair (see Fig. 5) [12] all the way to zig-zag edges [14]. In the latter work, a cleverly designed monomer provided access to a

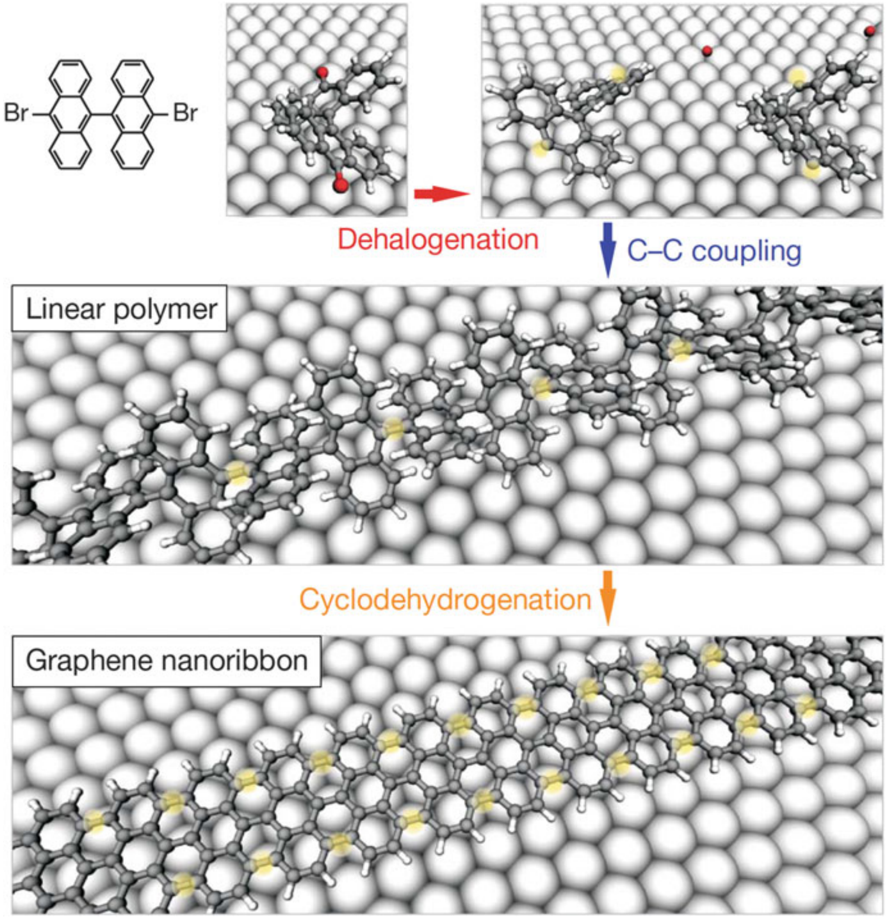

Fig. 5 On-surface polymerization of dibromodianthracene (DBDA) monomers to yield narrow armchair graphene nanoribbons. Reproduced from [12]. Copyright (2010) Nature Publishing Group

polyarylene precursor, which after subsequent cyclodehydrogenation yielded zig-zag edge GNRs of considerable width and length with atomic precision (Fig. 7).

In addition to the monomer structure, several other parameters should be considered in the design. For example, the monomers have to be sufficiently stable upon thermal treatment to enable their evaporation onto the surface under typically used UHV conditions at temperatures below the activation temperature.

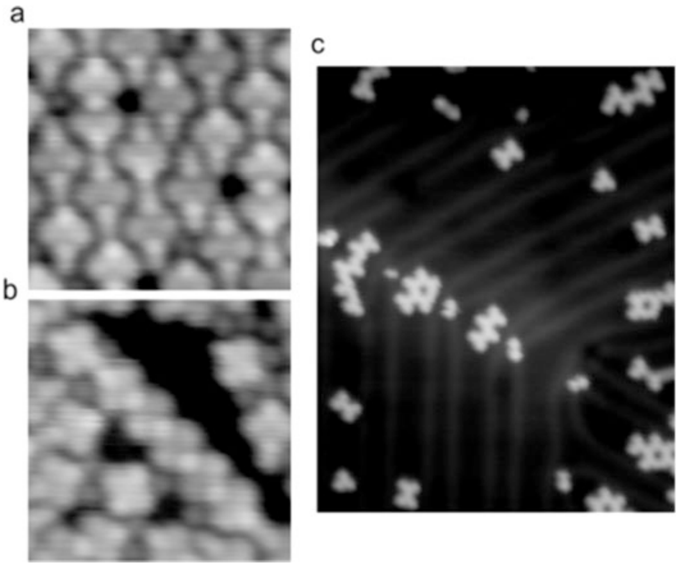

Fig. 6 Inhibited polymerization of 9,10-dibromoanthracene (9,10-DBA) on Au(111), presumably as a result of steric hindrance during coupling of planar activated monomers: 9,10-DBA on Au (111) before heating (**a**) and after heating the substrate to 470 K (**b**) and 670 K (**c**). Reproduced from [13]

3 Influence of the Surface

In addition to the molecular design criteria detailed above, the surface itself plays a decisive role during monomer activation and coupling (and potential annealing) and has a major influence on the occurrence and outcome of the on-surface polymerization process. As mentioned above, the surface can act as a catalyst for the initial activation step. Step edges, defects, and adatoms are highly reactive sites for promoting chemical reactions. At the same time, the surface stabilizes the formed radical species and enables diffusion of monomers. Reconstruction of the surface changes the binding energy and adsorption geometry. As discussed above, a larger binding energy can limit polymerization because of steric hindrance. Also, orientation of the monomers and the shape and size of the molecular networks and islands depends on the surface reconstruction.

We have studied 2,3-dibromoanthracene (2,3-DBA) on Au(111) and Au(100) surfaces (Fig. 8) [13]. The intact and nonactivated molecules arrange in a parallel manner on Au(111). This is in contrast to Au(100), where the molecules face each other. The appearance and length of a single 2,3-DBA molecule was similar on both surfaces, and to activate them the substrates were heated to 520 K.

On Au(111), the formation of narrow rod-like structures (Fig. 8d, e) and star-shaped molecules (Fig. 8g, h) has been observed. The rods appear to be dimers formed via a formal [2+2]cycloaddition, whereas the star-shaped molecules

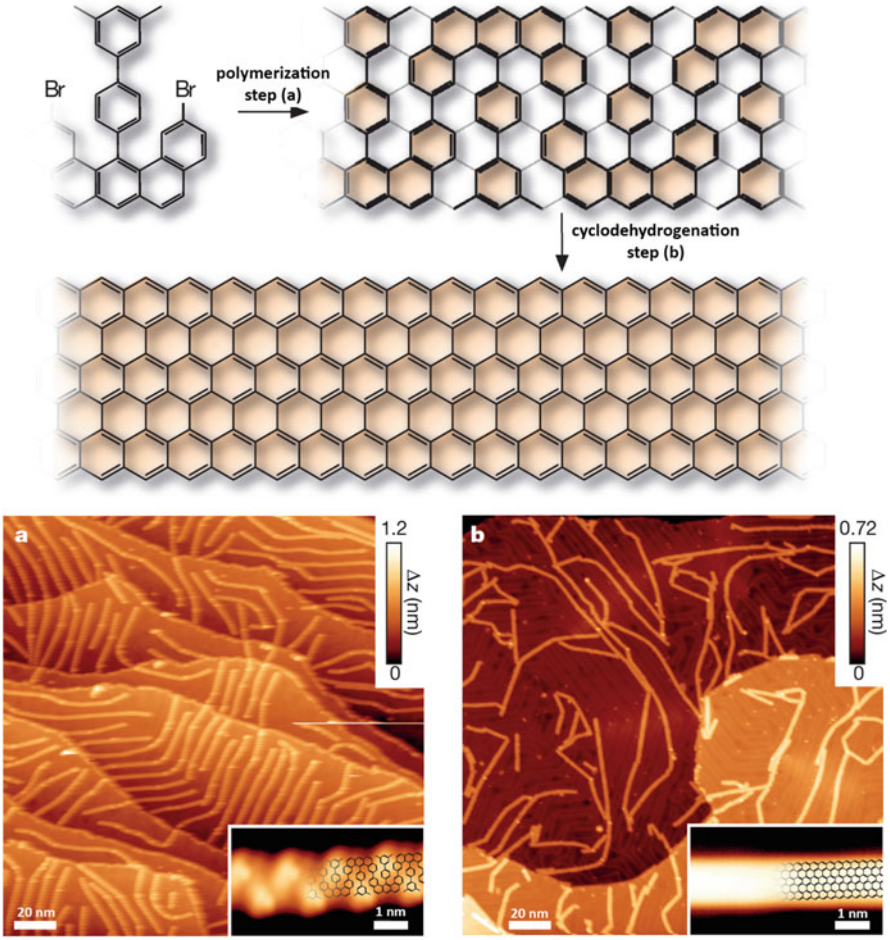

Fig. 7 On-surface polymerization of appropriately chosen monomer leads to formation of a polyarylene precursor (**a**), which after cyclodehydrogenation yields zig-zag edge graphene nanoribbons (**b**), sketched in the *upper panel*. Reproduced from [14]. Copyright (2016) Nature Publishing Group

resemble trimers arising from a [2+2+2]cycloaddition. In contrast, exclusively rod-like structures and no stars were formed on Au(100) (Fig. 8f). It appears that the parallel rows of the Au(100) surface favor dimerization in a head-to-head fashion, whereas the threefold symmetry on the Au(111) surface allows both dimerization and cyclotrimerization pathways.

In addition to the surface reconstruction, the type of metal substrate also plays an important role. This was exemplarily illustrated by a study of Cu(111), Ag(111), and Au(111) surfaces that suggested a different coupling probability for each surface [4]. In general, two effects oppose each other: activation by carbon–halogen dissociation is facilitated on the more reactive Cu(111) surface, but diffusion of the

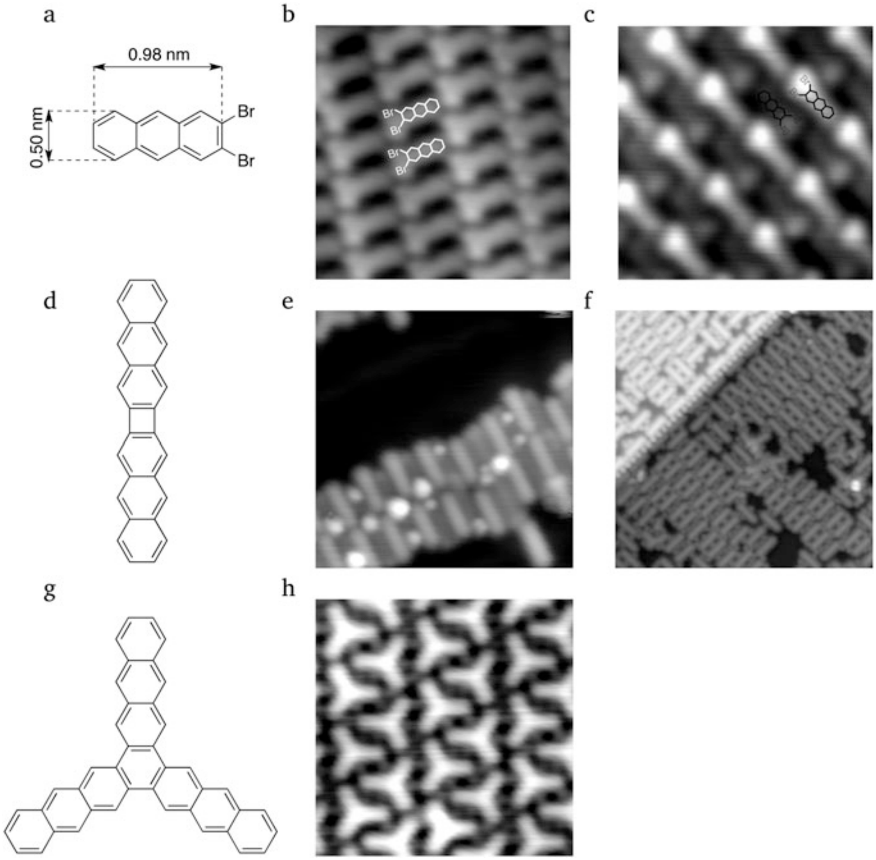

Fig. 8 Oligomerization of 2,3-dibromoanthracene (2,3-DBA) on Au(111) and Au(100). *Left*: 2,3-DBA monomer (**a**), observed linear dimer (**d**), and star-shaped trimer (**g**). *Center*: Intact tdDBA molecules adsorbed on Au(111) (**b**) and two species observed after heating the Au(111) sample (**e, h**). *Right*: Intact tdDBA molecules adsorbed on Au(100) (**c**) and species observed after heating the substrate (**f**). Reproduced from [13]

activated monomers and, hence, their coupling efficiency is decreased on the same surface. More specifically, Monte Carlo simulations showed that lower coupling probabilities lead to more closed networks, whereas higher coupling probability and lower mobility lead to branched network structures. Clearly, the choice of substrate is crucial for achieving efficient polymerization reactions and can dictate the resulting polymer architecture.

The fully aromatic framework of hexabenzocoronene (HBC), which can be considered as small graphene fragment, is known to adsorb in a flat and planar fashion on noble metal surfaces. The results of Soe et al. [15] suggest that the electronic states of two HBC molecules are able to hybridize, rendering HBC oligomers/polymers promising candidates for molecular wires (Fig. 9).

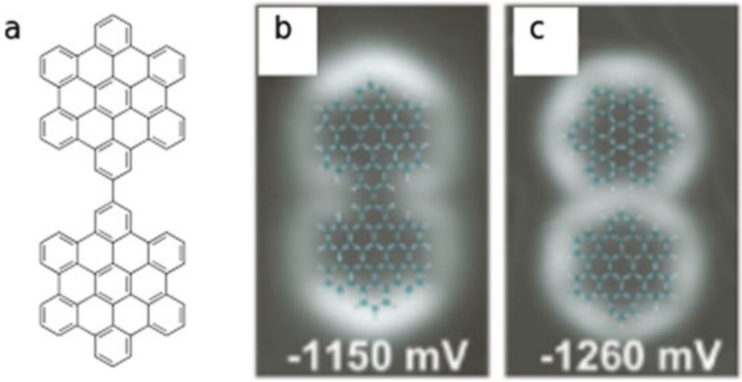

Fig. 9 Hexabenzocoronene dimer: chemical structure (**a**) and STM images at different bias voltages (**b, c**). Reproduced from [15]. Copyright (2012) American Chemical Society

In order to grow such molecular wires composed of linked HBC units, we investigated dibromohexabenzocoronene (DBHBC) equipped with two bromines in a *trans*-type relationship on Au(111) and Cu(111) surfaces [16]. Similar to the results of Walch and coworkers [17], we found that activation takes place at room temperature when depositing DBHBC onto a Cu(111) surface. The activation temperature depends strongly on the type of halogen but also on the substrate, as DBHBC is activated below room temperature on Cu(111), whereas a heating step to 520 K is required on Au(111). This can be explained by the higher catalytic reactivity of the Cu(111) substrate. The energy required to remove an atom from a Cu(111) step is lower than for Au(111), which results in more diffusing copper adatoms at room temperature, thus supporting the reaction. In accordance with the general trend that C–I bonds cleave at lower temperatures than C–Br bonds, as a result of lower bond dissociation energy, we found that diiodohexabenzocoronene (DIHBC) cleaves on Au(111) at 390 K. However, a much higher activation temperature is necessary in the absence of a catalytically active metal substrate. For example, on calcite ($CaCO_3$) cleavage of C–I bonds takes place only at temperatures above 570 K [18].

The bond that is formed between activated monomers depends on the substrate as well as temperature. On Au(111), a heating step to 520 K is required to activate the DBHBC precursor, leading to formation of covalent bonds between HBC monomers. In strong contrast, on Cu(111), activation occurs at room temperature and metal-coordination bonds are subsequently formed, connecting HBC monomers via Cu atoms (Fig. 10) [16].

Metal–carbon bonds are typically less stable than covalent C–C bonds but offer the advantage that the activation barrier associated with their formation is lower. This fact can be crucial for molecules that decompose at elevated temperatures, as illustrated by work on the assembly of molecular wagons [19]. On Cu(111), the formation of chains based on metal–carbon bonds is possible, but on Au(111) the required temperature for polymerization leads to decomposition of the molecules. Interestingly, during polymerization of tetrabromonaphthalene, gold–organic

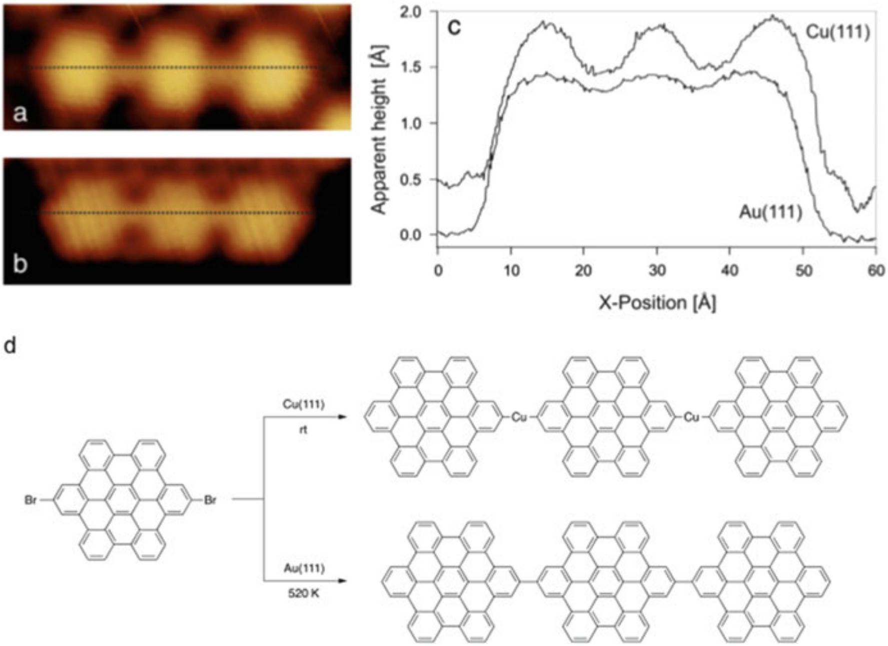

Fig. 10 Oligomerization of dibromohexabenzocoronene (DBHBC) on Cu(111) and Au(111): STM image of a HBC chain on Au(111) (**a**) and Cu(111) (**b**), including their height profiles (**c**). Chemical reaction pathways on Cu(111) and Au(111) (**d**). Reproduced from [16]

hybrids were observed if the sample was annealed below 470 K [10]. The formation of copper–organic hybrids is very common for Cu adatoms but has been rarely reported for Au. This intermediate stage, where Au-bridged metallosupramolecular polymers are formed, might be the reason why no products except GNRs are observed [10]. As a result of less stable Au–C linking, these bonds may be reversible and allow defect-healing to occur.

4 Doping of Molecular Chains

The electronic structure of $N = 7$ GNRs (N being the number of carbon atoms counted across the width of the GNR; see Fig. 5) has been characterized with scanning tunneling spectroscopy and other techniques [20–23]. The lowest unoccupied molecular orbital (LUMO) has been found at 1.6 eV and the highest occupied state (HOMO) at -1.1 eV on Au(111), leading to a HOMO–LUMO gap of 2.7 eV [20]. Both states are delocalized along the edges of the GNR. In addition to the HOMO and LUMO, an edge state located at the zig-zag edges of the GNR was observed close to the Fermi energy.

Different results have been reported for the band gap of chevron-shaped GNRs (Fig. 11). These GNRs have been fabricated with 6,11-dibromo-1,2,3,4-

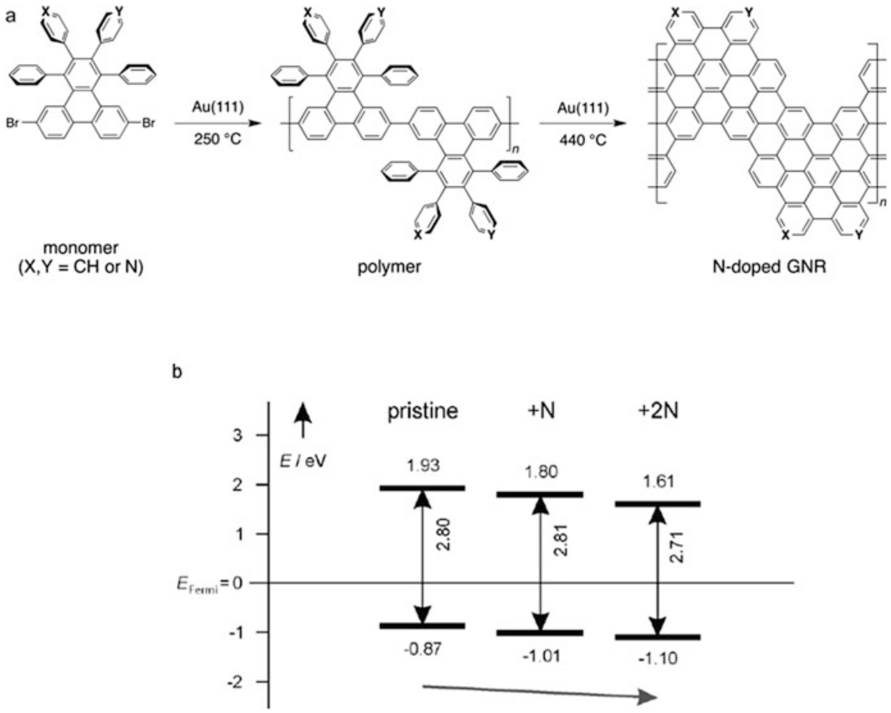

Fig. 11 Chevron-type GNRs with varying degree of n-doping in the armchair edge by on-surface polymerization of mono- and bispyridyl substituted monomers on Au(111) (**a**), showing that the band structure is shifted with each additional N atom (**b**). Reproduced in part from [25]. Copyright (2013) by Wiley-VCH

tetraphenyl-triphenylene as molecular building block [12, 24, 25]. Fasel et al. found a band gap of 2.0 eV [24], whereas high-resolution electron energy loss spectroscopy (HREELS) indicated a band gap of 2.8 eV [25].

The LUMO of pristine chevron-shaped nanoribbons is located at −0.87 eV. The ribbons are p-doped because of interaction with the Au(111) substrate [24]. By replacing carbon atoms in the precursor molecule it is possible to create GNRs with an atomically precise doping pattern [24, 25]. By exchanging one or two carbon atoms in the molecular building block with nitrogen, the entire band structure is shifted by 0.1 eV or 0.2 eV, respectively (see Fig. 11) [25]. Each nitrogen atom shifts the band structure by about 0.1 eV, whereas the band gap is only weakly influenced by n-doping. By mixing pristine 6,11-dibromo-1,2,3,4-tetraphenyl-triphenylene with n-doped 5,5′-(6,11-dibromo-1,4-diphenyl-triphenylene-2,3-diyl)dipyrimidine, p-N-GNR heterojunctions are formed. According to Fasel and coworkers, the band gap of ~2.0 eV is similar for both GNRs on Au(111) but the position of the valence band maximum of the p-doped pristine GNRs is closer to the Fermi level of the metallic substrate [24]. Local density of states (LDOS) maps

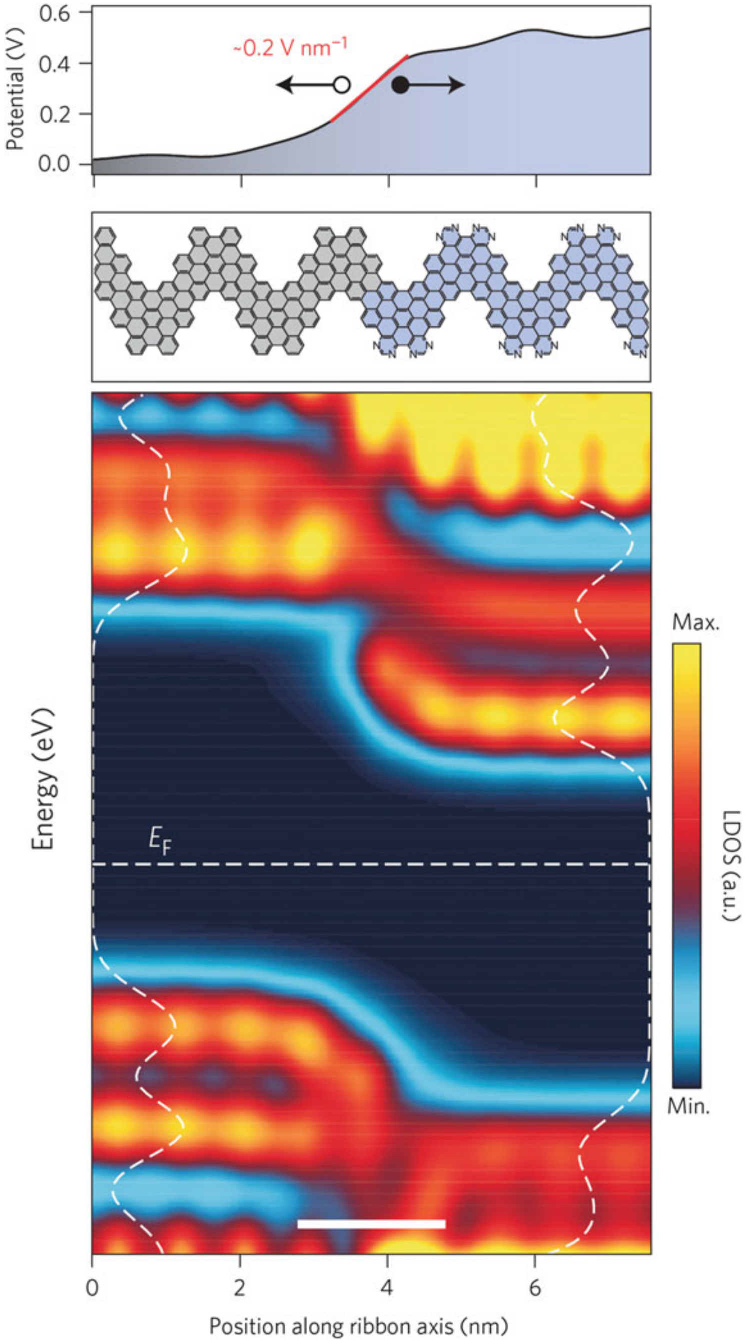

Fig. 12 Copolymerization of phenyl- and pyrimidyl-substituted monomers on Au(111), leading to p-n junctions of chevron-type GNRs. Reproduced from [24]. Copyright (2014) Nature Publishing Group

show that the interface is very sharp and that band bending is only 2 nm wide in its spatial extension (Fig. 12).

A different approach for synthesis of good conducting molecular wires is based on alternating donor–acceptor chains [26]. The coupling of donor and acceptor units lowers the HOMO–LUMO gap significantly. We prepared and polymerized bis(5-bromo-2-thienyl)-benzobis(1,2,5-thiadiazole) as the donor–acceptor–donor (DAD) monomer (Fig. 13) to obtain highly conducting, yet flexible, molecular wires [27]. The benzobis(thiadiazole) groups function as acceptor units, connected via bithiophene units formed during Ullmann-type on-surface coupling that act as donor moieties. Due to nature of the connecting C–C single bond, and in strong contrast to the stiff GNRs, the resulting conjugated donor–acceptor polymer wires are highly flexible, which enables characterization of their conductance using pulling experiments. This flexibility leads to closed structures (i.e., highly ordered rings) that are composed of only very few molecular building blocks and exhibit rather small diameters that reflect the high curvature angles that can be achieved. Specifically, $(DAD)_6$ rings (the most abundant closed structure, containing six DAD monomers) with a curvature radius of about 13.9 ± 0.2 Å and even $(DAD)_5$ rings with a radius of only 11.5 ± 0.2 Å have been found [27]. These structures indicate the high degree of conformational flexibility that can be achieved in such structures.

DAD monomers and DAD_n oligomers show a very homogeneous contrast (i.e., apparent height) in constant-current STM images (Fig. 13). Detailed information about their electronic states, in particular about the spatial distribution of these states within the molecules, can be obtained by dI/dV conductance spectroscopy

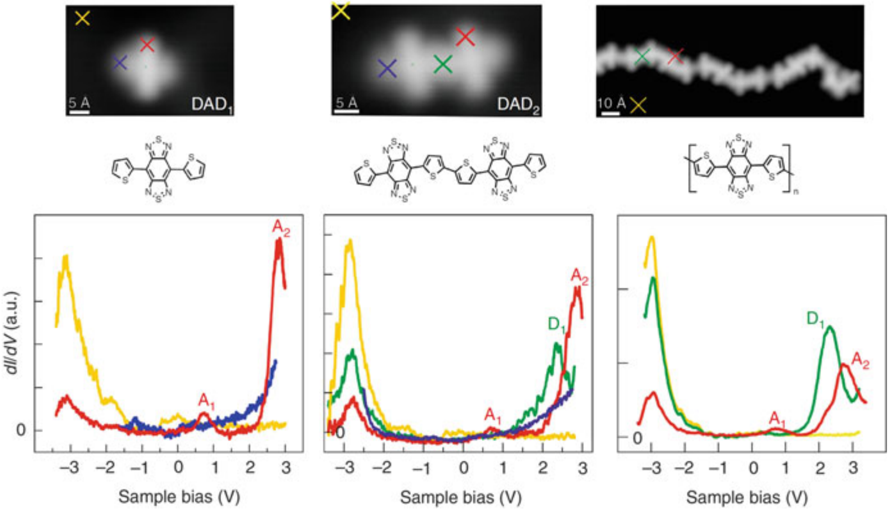

Fig. 13 Flexible wires based on alternating donor–acceptor polymers prepared by on-surface polymerization on Au(111) [27]

(at the bottom of Fig. 13), which probes the LDOS. Different unoccupied states can be identified there (all being in the range of positive bias voltages as this refers to the sample potential), named A_1, A_2, and D_1 (Fig. 13). The first two are exclusively found on the acceptor groups of the DAD_n oligomers, whereas the latter is only present on the donor groups, a finding that is valid for various lengths of chain without any significant energy shift. Hence, no efficient electron delocalization takes place for these states, otherwise they would smear out over the molecular structure and could not be as clearly distinguished on different positions along the molecular chain as reported by d*I*/d*V* maps over the oligomers [27]. Hence, the characteristic electronic states of donor and acceptor groups within an oligomer adsorbed on an Au(111) surface can be identified in terms of their spatial position and electronic energy for different oligomer lengths.

Note that the donor state D_1 is spatially located at the site of the bithiophene within the oligomer, but no feature is visible in the d*I*/d*V* spectra at this energy position at the thiophene site for the DAD monomer or at the chain terminus. The D_1 state is therefore clearly related to the linking of two thiophenes to a bithiophene unit, which is the actual donor moiety in the DAD oligomer [27]. Such an effect on the optoelectronic properties (via the energy positions of electronic states) with increasing chain length is well established in the field of π-conjugated oligomers.

5 Conductance of Molecular Wires

The conductance (G) of a molecular wire of length d decays exponentially and can be described by $G(d) = Go\ \mathrm{e}^{-\beta d}$, where Go is the contact conductance and β is the inverse decay length. The inverse decay length depends on the position of the HOMO and LUMO relative to the Fermi level E_F as well as on their energy gap (E_g) and on the effective mass of the electron in the tunneling junction. Large E_g leads to high β values and, consequently, to low junction conductance, for instance for alkane chains. If the molecule in the junction exhibits electronic states that are located close to the Fermi level, another transport regime is active. In such a case, β becomes very small, for example when d-states of an organometallic compound or π-states of a conjugated organic molecule are available. Consequently, a pseudoballistic transport regime with $G < 2e^2/h$ (i.e., the quantum of conductance) occurs because the electronic structure of the molecular wire differs from that of the metallic electrodes.

To measure the conductance of a single molecule, it can be lifted off the surface by controlled STM pulling (Fig. 14) [28]. One end of the molecular chain is attached to the tip and the other to the (metallic) surface. Before and after a pulling experiment, the molecular chain can be characterized by imaging and spectroscopy. While the tip is retracted, the effective transport length through the molecular chain is modified, because the current is only passing through the part of the molecule that does not interact with the surface. If the molecule is successfully lifted from the

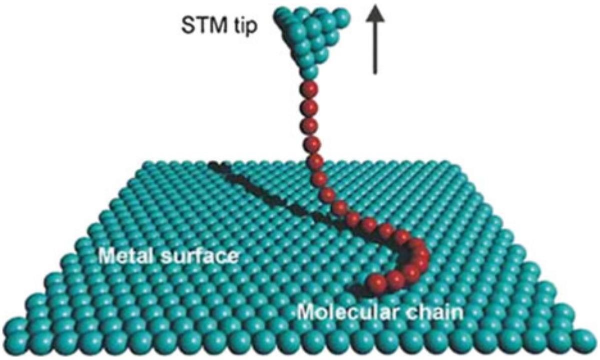

Fig. 14 In situ characterization of molecular chains, prepared by on-surface polymerization, by pulling experiments, which provide direct access to current (conductance) versus distance (chain length) curves at the single-molecule level [28]

surface, a smaller slope of the STM current signal $I(z)$ (i.e., higher conductance) than for the vacuum junction is measured during pulling.

Poly(9,9-dimethylfluorene) prepared by on-surface polymerization from dibromoterfluorene (DBTF) monomers was the first molecular wire studied using STM pulling experiments [28]. The high mobility of (activated) monomers allows formation of very long and well-defined polyfluorene chains on the Au(111) surface. Defect-free polymers with lengths exceeding 100 nm have been observed. These oligomers are highly flexible and the polyfluorene chains can be strongly curved during STM manipulation experiments.

To pull a polyfluorene chain from the surface, the tip is approached at the terminus of the chain. When contact is established, the tip is retracted while the current is being measured (Fig. 15). The current decays exponentially and regular oscillations appear in the conductance trace. These oscillations are attributed to fluorene units, which are lifted one-by-one from the surface, as shown by subsequent measurement of the same system by atomic force microscopy (AFM) [29]. The inverse decay rate is 0.38 Å^{-1} for a bias voltage of 100 mV, in good agreement with theory [28].

To study the influence of molecular orbitals on transport we studied the pristine GNRs mentioned above [20]. Scanning tunneling spectroscopy showed that the HOMO and LUMO are delocalized along the edges of the GNR. We performed STM pulling experiments on these ribbons but with varied applied bias voltage. This means that we retracted the STM tip to -10 Å and then increased the bias voltage to the value of interest. We found inverse decay length values of around 0.45 Å^{-1} in the HOMO–LUMO gap.

If the bias voltage is increased so that the HOMO or LUMO participate in charge transport, the inverse decay length decreases to values as low as 0.1 Å^{-1} (Fig. 16). Nevertheless, no ballistic transport ($\beta = 0\ \text{Å}^{-1}$) is achieved, as predicted by theory for flat GNRs [20], which we explain by the curvature of the ribbons during pulling experiments. The nonplanar conformation modifies the electronic structure and perturbs electronic delocalization along the molecule.

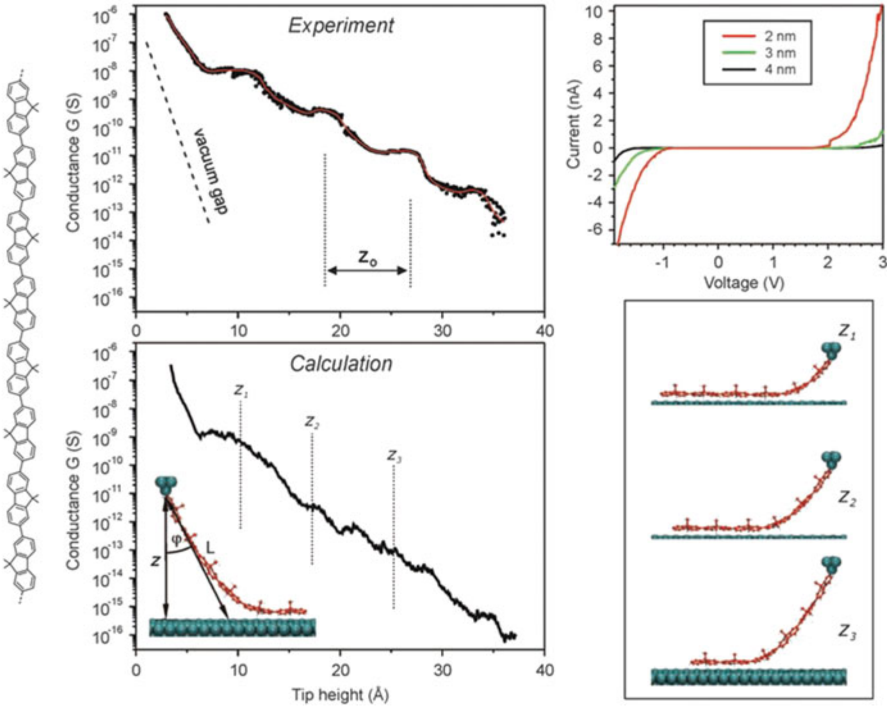

Fig. 15 Experimental and calculated conductance of an individual poly(9,9-dimethylfluorene) chain pulled off an Au(111) surface. The chemical structure of the oligomer is shown on the *left*. Reproduced from [28]

Conjugated polymer chains based on alternating donor and acceptor units (see Fig. 13) combine the high flexibility of polyfluorene chains with the inherent conductivity of GNRs. STM pulling experiments show an inverse decay length of 0.21 Å^{-1} for bias voltages between -100 mV and 100 mV [27], being only weakly influenced by the applied bias voltage. This value is very low considering that these alternating donor–acceptor polymers do not have delocalized states along the molecular chain.

Direct comparison of the inverse decay lengths β, reflecting the electrical conductance, revealed a variety of values for different molecular structures [27]. Typical β values are 0.38 Å^{-1} for polyfluorene (see Fig. 15) and about 0.4 Å^{-1} for GNRs (see Fig. 16); polyanthracene is a rather bad conductor with a β value of about 0.8 Å^{-1} as a result of its twisted structure. The smallest value of 0.21 Å^{-1}, and therefore best conductance, is found for the DAD_n oligomers. It should be noted that a homogeneous polymer consisting only of thiophene units (i.e., the donor groups in DAD chains) exhibits a clearly reduced conductance as compared with DAD_n oligomers [27]. Hence, it is the combination of alternating donor and acceptor groups that gives good conductance values, in combination with the molecular flexibility.

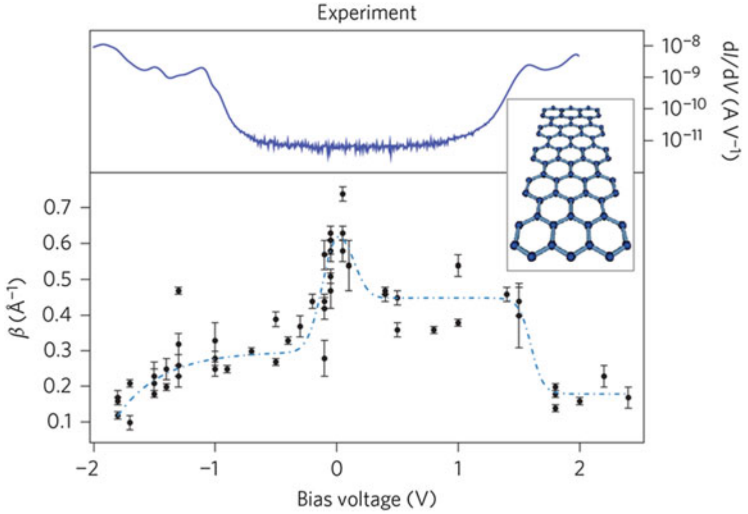

Fig. 16 Inverse decay lengths from various $N = 7$ GNRs (shown in the *inset*) for different bias values during a pulling experiment. Reproduced from [20]

6 Two-Dimensional Networks

So far we have discussed the on-surface growth of 1D structures. By increasing the number of halogen atoms (i.e., the number of reactive sites), branched structures and ideally 2D networks can be fabricated on the surface. In our initial work, porphyrin molecules were equipped with one, two, and four bromine atoms [7]. Depending on the number of bromine atoms, dimers, chains, or 2D networks were observed after heating the Au(111) substrate and activating the monomers (Fig. 17).

Whereas Ullmann-type homocoupling connects identical (het)aryl halides, the condensation of amine and aldehydes allows coupling of two different (orthogonal) reaction partners and the formed imines are typically too labile to be deposited directly onto a metal substrate by evaporation. Imine formation has been demonstrated by evaporating a star-shaped trifunctional salicyl aldehyde (1,3,5-tris [(5-*tert*-butyl-3-formyl-4-hydroxyphenyl)ethynyl]benzene) and octylamine onto Au(111) at room temperature [30]. Subsequently, the substrate was annealed at temperatures between 300 K and 400 K to trigger imine condensation and desorb the formed water and unreacted octylamine. The generated trisimine product self-assembles on the surface, either in interdigitating row-like or hexagonal honeycomb structures (Fig. 18).

After optimizing deposition of the two reactants and the conditions for imine formation, the authors employed a bifunctional amine, such as hexamethylenediamine, to perform a formal A3 + B2 polycondensation and generate covalent polymeric networks on the surface (Fig. 18, bottom) [31]. Because of

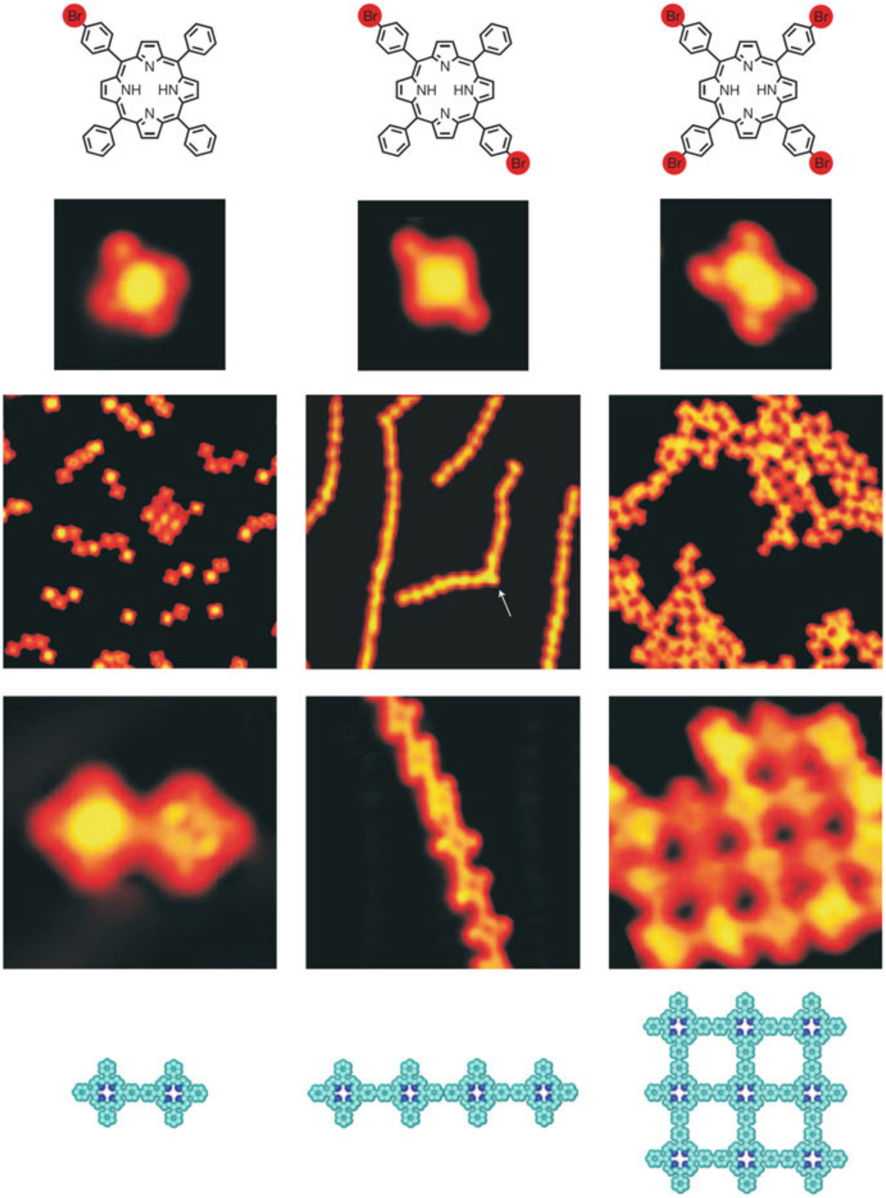

Fig. 17 On-surface polymerization of porphyrins equipped with one, two, and four bromine atoms gives rise to dimers (*left*), 1D chains (*center*), and 2D networks (*right*). Reproduced from [7]

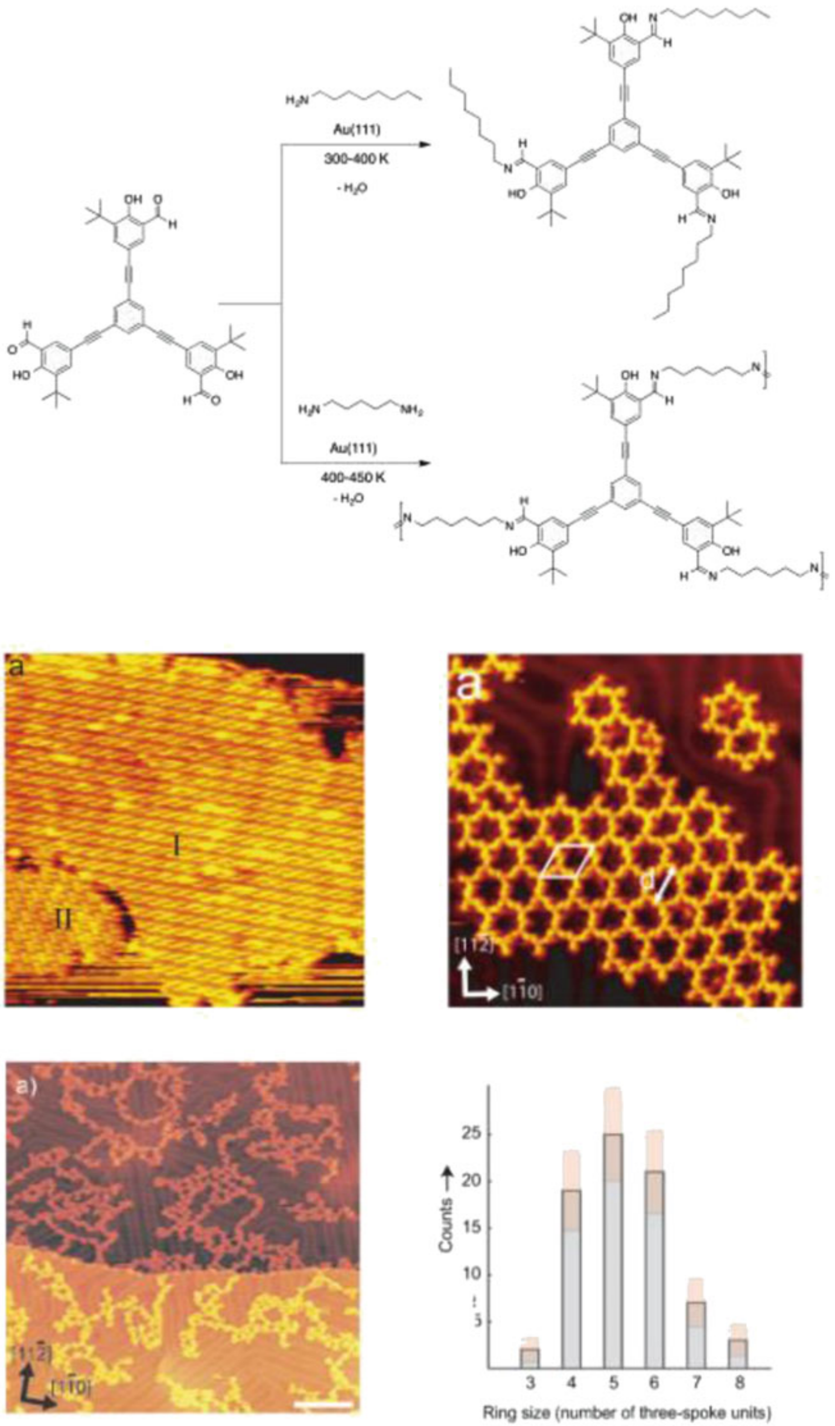

Fig. 18 Reaction of a trifunctional aldehyde with mono- and bifunctional amines on Au(111) (*top*) can lead to formation of trisimines self-assembled in rows or honeycombs (*middle*) and polyimine

the flexible structure of the diamine linker, the formed polymer network is structurally ill-defined, as exemplified by the various ring sizes formed (Fig. 18, bottom).

Although imine bonds are reversible covalent bonds, enabling defect-healing [32], in the above example the dynamic character could not be exploited, presumably because of the non-equilibrating conditions. Exploiting boroxine formation by reversible boronic acid trimerization under equilibrating conditions, Lackinger and coworkers were able to grow extended hexagonal networks (2D COFs) from 1,4-phenylenebisboronic acid in a humid atmosphere [33]. Shortly thereafter, a similar effect was shown during network formation of the extended homologue 1,4′-diphenylbisboronic acid, where equilibration was induced by intentional addition of water [34].

These two examples show that reversible connectivities allow the growth of extended 2D networks; however, the types of dynamic covalent bonds, which allow for exchange under mild conditions, are rather limited. In the context of benzene-based structures (i.e., graphene and porous phenylene networks), equilibration of aryl–aryl connections cannot typically be achieved and, hence, network formation is solely kinetically controlled.

7 Optimizing the Polymerization Process

To improve the 2D polymerization process in order to increase the size and quality of the network under kinetically controlled conditions (i.e., during C–C bond formation), the monomer concentration and reactivity are of utmost importance. Given a specific dosage/coverage, the local concentration relates to the mobility of the monomers, which is dependent on adsorbate–surface interactions and temperature. A detailed study has been carried out by the Lackinger group, showing that low surface temperatures typically favor open pores, which is explained by decreased monomer mobility on the substrate [35]. With an increase in temperature fewer open pores are found, yet increasing the temperature too far induces defects in the network (Fig. 19).

In addition, the influence of molecular flux has been studied by heating the sample to the activation temperature during deposition of monomers. Although very low deposition rates reduce the number of open pores, they also lead to formation of more pentagonal and tetragonal pores, indicating premature ring closure in the absence of new monomers. Higher deposition rates did not have a significant effect in experiments in which deposition and activation were conducted separately. Interestingly, at around 200°C or higher the authors found no difference between using BIB and tetra(*p*-bromophenyl)-quaterphenyl (TBQ), formed after initial iodine cleavage of BIB and subsequent dimerization.

Fig. 18 (continued) networks (*bottom*), respectively. Reproduced in part from [30, 31]. Copyright (2008) American Chemical Society and by Wiley-VCH, respectively

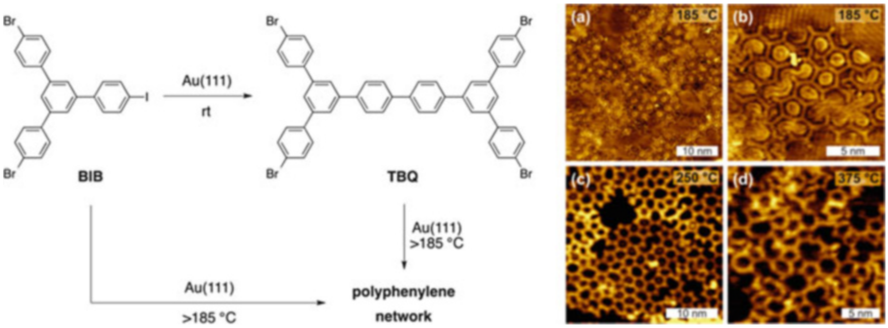

Fig. 19 Influence of the temperature of the Au(111) surface on network formation during deposition of 1,3-bis(*p*-bromophenyl)-5-(*p*-iodophenyl)benzene (BIB) and subsequent 15 min annealing. Reproduced in part from [35]. Copyright (2014) American Chemical Society

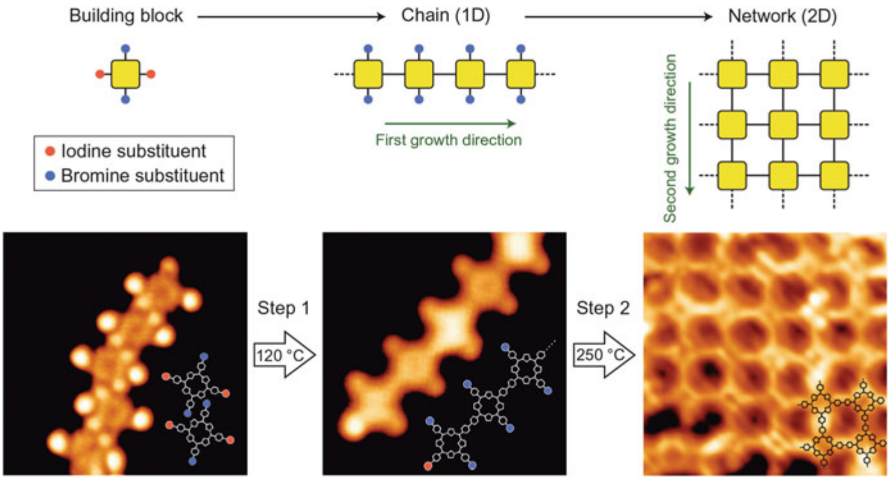

Fig. 20 Hierarchical growth of rectangular porphyrin networks by sequential activation of porphyrin monomers, in which cleavage of the iodine substituents leads to initial formation of chains, which are subsequently connected after bromine dissociation. Reproduced from [36]

Prior to these experiments, sequential activation of C–I and C–Br bonds had been used to control the 2D growth of porphyrin networks [36]. The approach is based on the different halogen–carbon bond dissociation energies (i.e., 272 kJ/mol in the case of phenyl iodide and 336 kJ/mol for phenyl bromide), which lead to different activation temperatures. In other words, monomer building blocks equipped with iodine and bromine substituents have two different activation temperatures, which enables polymerization to take place first at the cleaved iodine sites and subsequently at the cleaved bromine sites. We chose porphyrin building blocks because their fourfold symmetry allows attachment of two iodine and two bromine atoms in orthogonal directions (Fig. 20). The initial heating step to 390 K activates only the iodine sites of the porphyrin building block. The reactive sites are

Fig. 21 Coupling selectivities observed in copolymerization using sequential activation. Reproduced from [36]

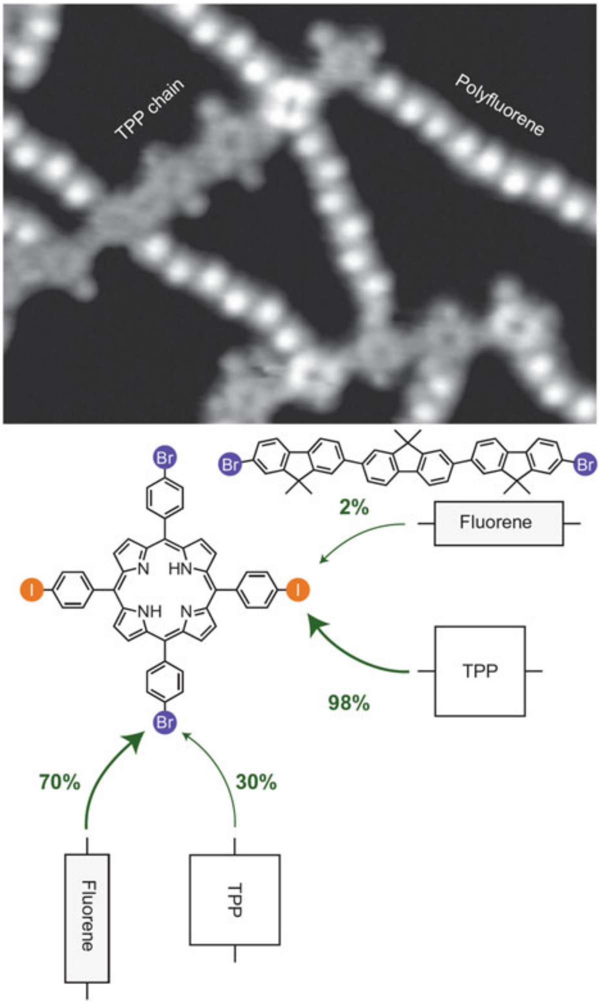

in a *trans* relationship, which leads to formation of 1D porphyrin chains. Subsequently, heating to 470 K activates orthogonal bromine sites and the porphyrin chains are connected to yield 2D networks (Fig. 20). The size and quality of the 2D porphyrin networks is higher when the chains are polymerized first (compared with 2D network formation in one step only; see Fig. 17). Although polymerization of the porphyrin chains is not reversible, it leads to preorganization of the reactive sites after bromine dissociation, and this zipper effect facilitates network formation.

Note that the fourfold symmetry of the porphyrin building blocks is ideally suited for two orthogonal growth directions.

This sequential activation technique could also be used to connect different monomer building blocks. For example, *trans*-dibromo-diiodo-porphyrin monomers were mixed with dibromoterfluorene (DBTF; see Fig. 21) and both species deposited onto the surface intact (i.e., not activated). On raising the temperature to 520 K, two reactions take place sequentially: First, only iodine atoms are cleaved and porphyrin chains are exclusively created. Then, the bromine sites are activated and DBTF forms polyfluorene chains, which attach to the porphyrins. Note that both molecular monomers are present on the surface during the entire procedure. Hence, a heterogeneous network can be formed based, on the one hand, on sequential activation and, on the other, on the relative chemoselectivities of the activated monomer building blocks (Fig. 21).

8 Outlook

Over the past decade, a joint effort by synthetic chemists and surface physicists has led to the development of on-surface synthesis, which allows polymers of various types and topologies to be prepared directly on an atomically defined surface under controlled (UHV) conditions. The growing body of work has contributed to our fundamental understanding of chemical surface reactivity and enabled preparation of a large potpourri of nanostructures, such as GNRs and nanosheets of various composition, as interesting materials for emerging applications. Although much progress has been made, several challenges remain at least partially open: (1) the degree of structure perfection utilizing reversible covalent reactions, (2) preparation of specific heterostructures involving regioselective doping and copolymers, (3) compatibility with catalytically inactive surfaces, and (4) potential transfer of reaction products. In particular, with regard to benzene-derived graphene-like structures, such as GNRs and (nano)graphene, the future will witness a continued evolution of bottom-up chemical methods and integration of these functional nanomaterials – the topic of this particular volume – into electronic devices and other applications.

References

1. Nacci C, Hecht S, Grill L (2016) The emergence of covalent on-surface polymerization. In: Gourdon A (ed) On-surface synthesis. Springer, Switzerland, pp 1–21
2. Hla S-W, Bartels L, Meyer G, Rieder KH (2000) Inducing all steps of a chemical reaction with the scanning tunneling microscope tip: towards single molecule engineering. Phys Rev Lett 85:2777–2780
3. Ullmann F, Bielecki J (1901) Über Synthesen in der Biphenylreihe. Chem Ber 34:2174–2185

4. Bieri M, Nguyen M-T, Gröning O, Cai J, Treier M, Aït-Mansour K, Ruffieux P, Pignedoli CA, Passerone D, Kastler M, Müllen K, Fasel R (2010) Two-dimensional polymer formation on surfaces: insight into the roles of precursor mobility and reactivity. J Am Chem Soc 132:16669–16676
5. Saywell A, Schwarz J, Hecht S, Grill L (2012) Polymerization on stepped surfaces: alignment of polymers and identification of catalytic sites. Angew Chem Int Ed 51:5096–5100
6. Cram D, Hendrickson J, Hammond G (1970) Organic chemistry, 3rd edn. McGraw-Hill, New York
7. Grill L, Dyer M, Lafferentz L, Persson M, Peters MV, Hecht S (2007) Nano-architectures by covalent assembly of molecular building blocks. Nat Nanotechnol 2:687–691
8. McCarthy GS, Weiss PS (2004) Formation and manipulation of protopolymer chains. J Am Chem Soc 126:16772–16776
9. Lipton-Duffin JA, Ivasenko O, Perepichka DF, Rosei F (2009) Synthesis of polyphenylene molecular wires by surface-confined polymerization. Small 5:592–597
10. Zhang H, Lin H, Sun K, Chen L, Zagranyarski Y, Aghdassi N, Duhm S, Li Q, Zhong D, Li Y, Müllen K, Fuchs H, Chi L (2015) On-surface synthesis of rylene-type graphene nanoribbons. J Am Chem Soc 137:4022–4025
11. Scholl R, Seer C (1912) Abspaltung aromatisch gebundenen Wasserstoffs und Verknüpfung aromatischer Kerne durch Aluminiumchlorid. Justus Liebigs Ann Chem 394:111–177
12. Cai J, Ruffieux P, Jaafar R, Bieri M, Braun T, Blankenburg S, Muoth M, Seitsonen AP, Saleh M, Feng X, Müllen K, Fasel R (2010) Atomically precise bottom-up fabrication of graphene nanoribbons. Nature 466:470–473
13. Koch M (2013) Growth and characterization of single molecular wires on metal surfaces. Dissertation, Freie Universität Berlin
14. Ruffieux P, Wang S, Yang B, Sánchez-Sánchez C, Liu J, Dienel T, Talirz L, Shinde P, Pignedoli CA, Passerone D, Dumslaff T, Feng X, Müllen K, Fasel R (2016) On-surface synthesis of graphene nanoribbons with zigzag edge topology. Nature 531:489–492
15. Soe W-H, Wong HS, Manzano C, Grisolia M, Hliwa M, Feng X, Müllen K, Joachim C (2012) Mapping the excited states of single hexa-peri-benzocoronene oligomers. ACS Nano 6:3230–3235
16. Koch M, Gille M, Viertel A, Hecht S, Grill L (2014) Substrate-controlled linking of molecular building blocks: Au(111) vs. Cu(111). Surf Sci 627:70–74
17. Walch H, Gutzler R, Sirtl T, Eder G, Lackinger M (2010) Material- and orientation-dependent reactivity for heterogeneously catalyzed carbon−bromine bond homolysis. J Phys Chem C 114:12604–12609
18. Kittelmann M, Rahe P, Nimmrich M, Hauke CM, Gourdon A, Kühnle A (2011) On-surface covalent linking of organic building blocks on a bulk insulator. ACS Nano 5:8420–8425
19. Villagomez CJ, Sasaki T, Tour JM, Grill L (2010) Bottom-up assembly of molecular wagons on a surface. J Am Chem Soc 132:16848–16854
20. Koch M, Ample F, Joachim C, Grill L (2012) Voltage-dependent conductance of a single graphene nanoribbon. Nat Nanotechnol 7:713–717
21. Söde H, Talirz L, Gröning O, Pignedoli CA, Berger R, Feng X, Müllen K, Fasel R, Ruffieux P (2015) Electronic band dispersion of graphene nanoribbons via Fourier-transformed scanning tunneling spectroscopy. Phys Rev B 91:045429
22. Bronner C, Leyssner F, Stremlau S, Utecht M, Saalfrank P, Klamroth T, Tegeder P (2012) Electronic structure of a subnanometer wide bottom-up fabricated graphene nanoribbon: end states, band gap, and dispersion. Phys Rev B 86:085444
23. Linden S, Zhong D, Timmer A, Aghdassi N, Franke JH, Zhang H, Feng X, Müllen K, Fuchs H, Chi L, Zacharias H (2012) Electronic structure of spatially aligned graphene nanoribbons on Au(788). Phys Rev Lett 108:216801
24. Cai J, Pignedoli CA, Talirz L, Ruffieux P, Söde H, Linag L, Meunier V, Berger R, Li R, Feng X, Müllen K, Fasel R (2014) Graphene nanoribbon heterojunctions. Nat Nanotechnol 9:896–900

25. Bronner C, Stremlau S, Gille M, Brauße F, Haase A, Hecht S, Tegeder P (2013) Aligning the band gap of graphene nanoribbons by monomer doping. Angew Chem Int Ed 52:4422–4425
26. Mullekom HAMV, Vekemans JAJM, Havinga EE, Meijer EW (2000) Developments in the chemistry and band gap engineering of donor-acceptor substituted conjugated polymers. Mater Sci Eng 32:1–40
27. Nacci C, Ample F, Bléger D, Hecht S, Joachim C, Grill L (2015) Conductance of a single flexible molecular wire composed of alternating donor and acceptor units. Nat Commun 6:7397
28. Lafferentz L, Ample F, Yu H, Hecht S, Joachim C, Grill L (2009) Conductance of a single conjugated polymer as a continuous function of its length. Science 323:1193–1197
29. Kawai S, Koch M, Gnecco E, Sadeghi A, Pawlak R, Glatzel T, Schwarz J, Goedecker S, Hecht S, Baratoff A, Grill L, Meyer E (2014) Quantifying the atomic-level mechanics of single long physisorbed molecular chains. Proc Natl Acad Sci 111:3968–3972
30. Weigelt S, Bombis C, Busse C, Knudsen MM, Gothelf KV, Lægsgaard E, Besenbacher F, Linderoth TR (2008) Molecular self-assembly from building blocks synthesized on a surface in ultrahigh vacuum: kinetic control and topo-chemical reactions. ACS Nano 2:651–660
31. Weigelt S, Bombis C, Busse C, Knudsen MM, Gothelf KV, Lægsgaard E, Besenbacher F, Linderoth TR (2008) Surface synthesis of 2D branched polymer nanostructures. Angew Chem Int Ed 47:4406–4410
32. Belowich ME, Stoddart JF (2012) Dynamic imine chemistry. Chem Soc Rev 41:2003–2024
33. Dienstmaier JF, Gigler AM, Goetz AJ, Knochel P, Bein T, Lyapin A, Reichlmaier S, Heckl WM, Lackinger M (2011) Synthesis of well-ordered COF monolayers: surface growth of nanocrystalline precursors versus direct on-surface polycondensation. ACS Nano 12:9737–9745
34. Guan C-Z, Wang D, Wan L-J (2012) Construction and repair of highly ordered 2D covalent networks by chemical equilibrium regulation. Chem Commun 48:2943–2945
35. Eichhorn J, Nieckarz D, Ochs O, Samantha S, Schmittel M, Szabelski PJ, Lackinger M (2014) On-surface ullmann coupling: the influence of kinetic reaction parameters on the morphology and quality of covalent networks. ACS Nano 8:7880–7889
36. Lafferentz L, Eberhardt V, Dri C, Africh C, Comelli G, Esch F, Hecht S, Grill L (2012) Controlling on-surface polymerization by hierarchical and substrate-directed growth. Nat Chem 4:215–220

Adv Polym Sci (2017) 278: 127–146
DOI: 10.1007/12_2017_7

Rational Synthesis of Fullerenes, Buckybowls, and Single-Walled Carbon Nanotubes by a Surface-Assisted Approach

Konstantin Amsharov

Abstract The sp^2 carbon-based structures with nanoscale dimension, such as fullerenes, nanographenes, nanoribbons, nanocones, and nanotubes, remain at the forefront of nanotechnology research. These unique structures appear to be the most promising building blocks for future nanotechnology applications and electronic devices. One of the main challenge in this field is to develop facile synthetic methods for production of these unique materials with fully controlled structure on the bulk scale. Here, we review studies on controlled surface-assisted synthesis of fullerenes, buckybowls, and single-walled carbon nanotubes that have been published to date. The relevance and prospects of on-surface synthesis strategies for construction of nonplanar sp^2 carbon-based nanostructures are highlighted.

Keywords Bottom-up approach • Buckybowls • Chirality pure SWCNTs • Fullerenes • On-surface synthesis

Contents

K. Amsharov (✉)
Institute of Organic Chemistry II, University Erlangen-Nuernberg, Henkestr. 42, 91054 Erlangen, Germany
e-mail: konstantin.amsharov@fau.de

1 Introduction

Nanographenes, nanoribbons, fullerenes, nanotubes, and other related sp^2 carbon-based systems attract considerable attention as a result of their intriguing properties and potential technological applications [1–3]. For instance, these materials are believed to be the best candidates for future replacement of silicon-based systems in conventional microelectronic technology because they are able to address many of the limitations of silicon technology and push traditional microelectronics to the nanometer scale [4]. These molecules are polycyclic aromatic compounds based on sp^2 hybridized carbon and display a specific geometric organization. Nanographenes are essentially fragments of graphene; nanoribbons are narrow strips of graphene; and fullerenes are molecules composed in the form of hollow spheres or ellipsoids. Buckybowls represent fragments of the fullerene surface or can be considered as "defect" nanographenes with pentagons embedded into the graphene lattice. Nanotubes are carbon allotropes with a cylindrical structure, which can be imagined as "rolled up" nanoribbons or infinitely elongated fullerenes (Fig. 1). Despite the apparent similarity, the chemical, mechanical, optical, and electronic properties of these materials are remarkably distinct and largely dependent on the structural organization [1–3]. The virtually unlimited number of possible fullerenes and isomeric nanotube structures provides the possibility to "tune" the required properties for certain applications, offering vital flexibility in technological design. On the other hand, application of these materials has remained elusive because an efficient preparative production technique for fullerenes, nanotubes, and other related structures with well-defined structure is still lacking [5]. Conventional production of fullerenes and nanotubes is based on various graphite evaporation techniques, including laser ablation [6, 7], resistive heating [8], arc-discharge [9, 10], and the radio frequency method [11]. Several alternative techniques, such as pyrolysis of polycyclic aromatic compounds [12, 13] and a ton-scale combustion approach, have been developed [14]. Chemical vapor deposition (CVD) has become the most prevalent technique for synthesis of carbon nanotubes (CNTs) because it offers better control of growing conditions [15–17]. As a result of the random nature of formation, little control over the structure can be achieved. Thus, none of the existing synthesis techniques can provide access to those materials in isomerically pure form, which is crucial for many applications.

Typically, as-produced CNTs and fullerenes are highly heterogeneous materials that vary significantly in structure. Isolation of individual species requires an elaborate multistep separation procedure, which has been successfully realized in only a few cases. Thus, for example, two soluble fullerenes, namely C_{60}-Ih and C_{70}-$D5h$, were easily obtained in pure form by single-step high-performance liquid chromatography (HPLC) separation of fullerene soot extract [18]. So far, only these two fullerene members have been the subject of in-depth investigations [19], although the fullerene family represents a huge class of carbon-cage molecules. In contrast to C_{60} and C_{70}, all higher fullerenes have several structural isomers that obey the so-called isolated pentagon rule (IPR), stating that all pentagons have to be

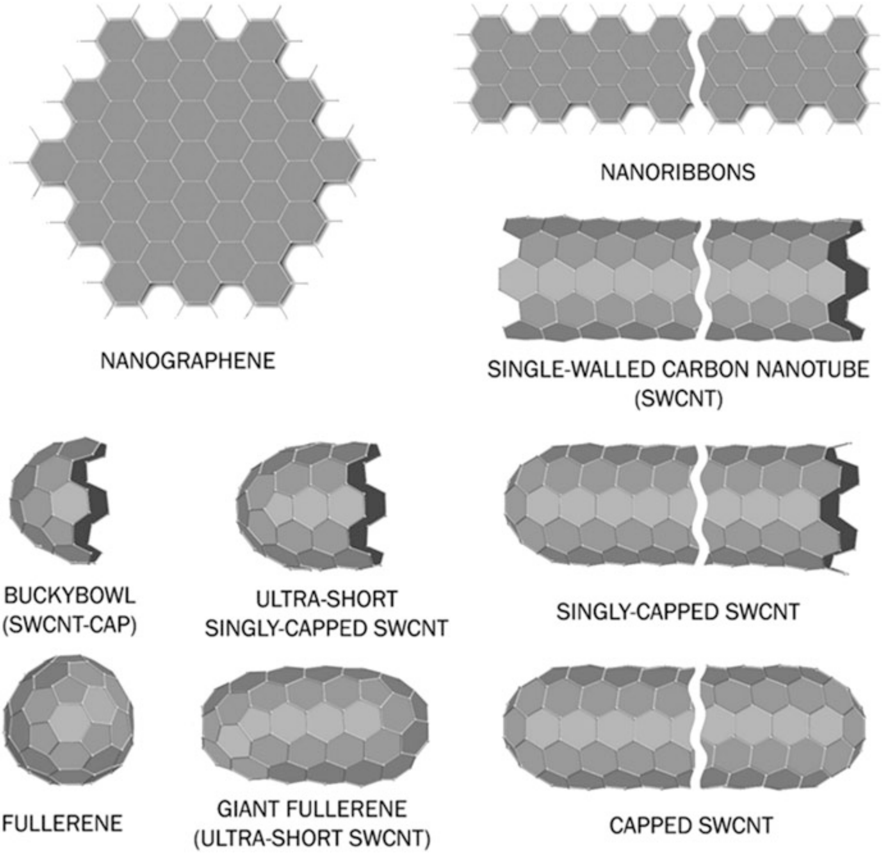

Fig. 1 Relationship between different sp^2 hybridized carbon-based nanostructures: planar nanographenes and nanoribbons, buckybowls, ball-shaped fullerenes, and cylindrical nanotubes

completely surrounded by hexagons [20]. The number of possible IPR isomers surges exponentially with increasing number of carbon atoms in the cage. For example, C_{100} has 450 IPR isomers whereas C_{200} has 15,655,672 [20]. Each of these molecules possesses its own set of unique properties, such as HOMO–LUMO gap, electron affinity, and optical and magnetic characteristics. Despite intense research in the fullerene field, only a small fraction of all possible members of the fullerene family have been synthesized and an even smaller number have been isolated and characterized [1, 19]. The higher fullerenes still remain poorly explored, mainly as a result of the very low yield and purification issues. Separation of CNTs is an even more challenging task, due to their polymer-like nature and lack of solubility. Many efforts have been made in the past few years to isolate this material in isomer-pure form, and several methods for the separation of individual nanotubes have been developed. Importantly, all "separation" techniques developed are actually fractionalization or sorting of short (in length) CNTs by diameter, band gap, or electronic type. The best results obtained so far are for fractionalization of individual single-walled carbon nanotubes (SWCNTs) at purities ranging from 70% to 90% [21–27]. Despite the great progress made in this field, the post-production separation processes are limited by their small scale, high cost, and rather low efficiency, which is not suitable for many applications, especially in nanoelectronics. Alternative approaches have attempted to achieve SWCNT structure control by controlling the composition and shape of metal catalyst particles [28]. Recently Yang et al. demonstrated highly selective SWCNT growth utilizing well-defined W-Co bimetallic nanoparticles [29]. Templated CVD growth resulted in the formation of (12,6)-SWCNTs, which were obtained with abundance higher than 92% [29]. Although single chirality-enriched SWCNT samples can be obtained by developed separation methods as well as by templated CVD growth, the ultimate goal of obtaining only one type of nanotube remains a challenge [30]. Therefore, new synthetic approaches are needed for the production of desired fullerenes, buckybowls, and CNTs that are free from impurities, defects, and other isomers. In this respect, bottom-up approaches are of great interest and appear to be the most promising strategies for synthesis of buckybowls, individual fullerenes, and CNTs with predefined chirality, including isomers that do not form using conventional techniques [31].

2 Zipping Approach

The zipping approach to fullerenes, buckybowls, and CNTs is based on the synthesis of specially "preprogrammed" precursor molecules (polycyclic aromatic hydrocarbons; PAHs) containing the carbon framework required for formation of the target nanostructure. The precursor molecule can be "zipped" to the desired carbon nanostructure by tandem surface-assisted intramolecular aryl–aryl coupling. The concept of this approach is schematically presented in Fig. 2 for C_{60} fullerene synthesis as an example. The characteristic feature of this approach is a zipper mechanism of cyclization (intramolecular domino-fashion cyclization) in the final synthetic step. The regiospecifity of each condensation step can be pronouncedly predefined by proper "design" of the precursor structure, thereby exclusively inducing the formation of isomer-pure nanostructure. The type of nanostructure (fullerene, buckybowl, nanotube, or nanoribbon) can be unambiguously preprogrammed by the precursor connectivity. Thus, if no pentagons are involved, a planar graphene-like system forms (Fig. 3, precursor A). The introduction of pentagons in the honeycomb lattice of graphene causes deviation from planarity and finally results in the formation of bowl-shaped molecules (buckybowls), representing fragments of the fullerene "surface." The exact 12 pentagons "placed" in proper positions give a closed cage structure – a fullerene (Fig. 3, precursors B and C). The nanotubes can be considered as a combination of both graphene-like and bowl-shaped blocks, which can be incorporated directly into the precursor structure (Fig. 3, precursor D). Alternatively, the hemispherical buckybowls

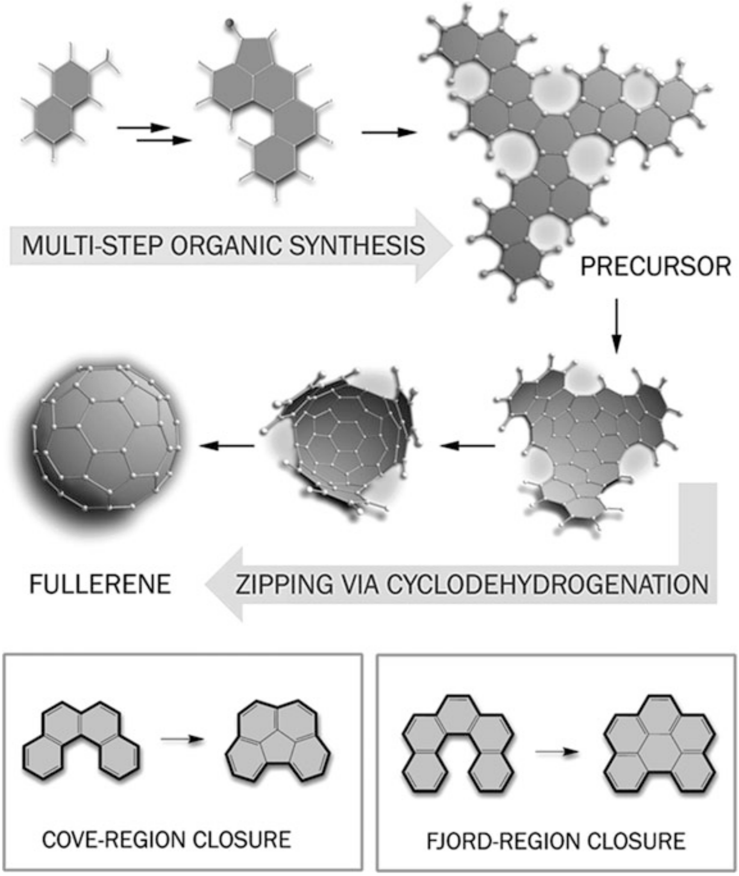

Fig. 2 Zipping strategy for C_{60}-I_h fullerene formation from $C_{60}H_{30}$ precursor via intramolecular aryl–aryl domino-coupling. The cove and fjord regions where direct aryl–aryl coupling can take place are highlighted by *grey shadow*. Each subsequent condensation leads to formation of new cove (or fjord) regions; thus, the reaction can proceed in a domino fashion (tandem condensation) until the desired structure is completed

representing SWCNT caps can be used further as seeds for templated nanotube growth. It is important to mention that the zipping approach can be applied for the synthesis of many other related sp^2 carbon-based nanostructures because the corresponding precursor molecules can be derived retrosynthetically by formal "unrolling" of the target molecule.

As shown in Fig. 2, the synthetic route can be formally divided into two main steps. The first stage is multistep organic synthesis of quasi-planar precursor molecules and the second is transformation of the precursor to the target nanostructure by zipping via consecutive cyclodehydrogenation. The zipping step is a key transformation in the bottom-up approach. Because many new C–C bonds have to be established during precursor zipping, the selectivity and efficiency of each

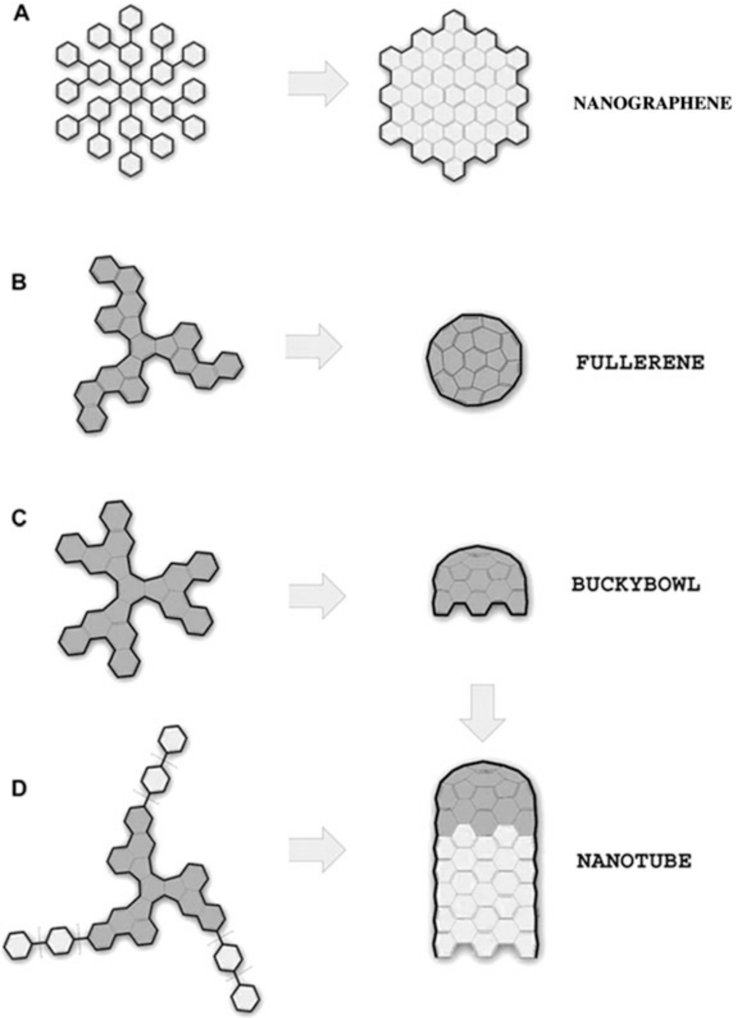

Fig. 3 Bottom-up approach for construction of nanographenes, buckybowls, fullerenes, and nanotubes via precursor zipping. Graphene fragments are highlighted by *light grey* and fullerene fragments by *dark grey*. For clarity, the same coding is used to show respective fragments in the precursor molecule

condensation step needs to be exceptionally high in order to achieve reasonable yield of the target nanostructure. Traditional methods for intramolecular aryl–aryl coupling such as the Scholl reaction, Pschorr reaction, or Wurtz and Ullmann couplings tend to involve harsh reaction conditions and, as a consequence, are characterized by low selectivity and yield and are usually unsuitable for tandem cyclodehydrogenation [32]. On the other hand, it was shown that various polyphenylenes readily undergo oxidative intramolecular cyclodehydrogenation under modified Scholl reaction conditions [33]. Recently, this approach has become of high practical interest for the synthesis of large planar PAHs, nanographenes, and nanoribbons [34]. In particular, this method was found to be highly effective for fabrication of extra-large full-benzoid nanographenes [35, 36]. In several cases, successful multifold cyclization was realized with good to excellent yields, even in the case of strained saddle-shaped systems [37]. Polyphenylenes and related PAH structures frequently undergo intramolecular cyclization under UV irradiation in the presence of an oxidant such as oxygen or iodine [38]. Mallory's photocyclization method was found to be very effective for the synthesis of various PAHs and is widely used for the synthesis of large polycyclic systems. The big advantage of this method is high tolerance for many functionalities and no need for introduction of any functional groups to induce cyclization. On the other hand, the reaction is frequently capricious and the yields can vary from quantitative to virtually zero depending on the system and conditions. Considering the synthesis of "classic" geodesic systems composed on hexagons and pentagons exclusively, two different types of cyclodehydrogenations can be selected (Fig. 2). Fjord region closure leads to formation of new hexagons, whereas cove region closure leads to formation of new pentagons. Although the fjord region closure in planar systems can be effectively realized utilizing the methods discussed above [39], these techniques are usually not effective for cove region closure and frequently not suitable for the synthesis of bowl-shaped PAHs in general. The bottom-up construction of fullerenes, buckybowls, and nanotubes appears to be much more difficult to perform than the synthesis of inherently planar nanographenes and/or nanoribbons. Perturbation of the inherently planar π-system causes enormous enhancement of the strain energy, which has to be overcome during cyclization. The strain energy stems mainly from the "cost" involved in the changes in valent angles and curvature-induced pyramidalization of the carbon atoms, as a result of deviation from the energetically ideal values observed in planar graphene lattices. It is not surprising that aryl–aryl coupling techniques developed for synthesis of planar PAHs usually fail in the case of geodesic PAHs. In this regard, the flash vacuum pyrolysis (FVP) approach, which is able to address the issue of high strain energy, remains the most powerful method for construction of buckybowls and related geodesic PAH structures [31, 40–44]. FVP is achieved by passing precursor molecules through a hot zone of the reactor under an inert gas atmosphere where the molecules are heated to a very high temperature for a very short time. The high temperature applied in FVP causes intramolecular cyclization via a radical mechanism and provides enough energy to form highly strained molecules. Many small buckybowls have been successfully obtained by this route via intramolecular cyclization of quasi-planar precursors [31, 40–44]. Unfortunately, the utilizing of nonfunctionalized PAH precursors results in low conversion and low selectivity of the process. The introduction of chlorine or bromine functionalities into the initial precursor was found to be essential for facilitating the cyclization via a free radical mechanism [31]. Although the FVP approach has proven to be very prolific for the synthesis of many small nonplanar PAHs, the high-yield synthesis of large bowls and isomer-pure fullerenes has remained challenging. The general possibility of selective fullerene cage formation through FVP has been demonstrated by the examples of C_{60} [45, 46], C_{78} [47], and C_{84} [48]. However, the rates of conversion to the target molecules have remained disappointingly low. The usually employed bromine or chlorine functionalizations reach their limits in the case of large molecules, because of decomposition of precursors during sublimation. Apart from modest yield and difficulty in scale-up, the main drawback of the FVP technique is minimum functional group tolerance and numerous side reactions caused by the harsh reaction conditions. To overcome these disadvantages, several alternative wet chemical methods have been developed. Palladium(0)-catalyzed direct arylation, utilizing bromo and chloro derivatives or aryl triflates, was effective for construction of small buckybowls [49–52]. Recently, alternative methods for synthesis of bowl-shaped molecules by ring closure via C–F bond activation have been reported [53, 54]. All these methods necessitate the introduction of various functional groups into the cove/fjord regions, which is often associated with synthetic difficulties and generally not suitable for the construction of large strained PAH systems such as fullerenes and nanotubes.

3 Surface-Assisted Synthesis

The formation of complex nanostructures directly on surfaces is a highly promising strategy for the fabrication of nanoscale devices by a bottom-up approach. In this respect, on-surface studies under ultrahigh vacuum (UHV) conditions offer an extraordinary degree of control in experiments [55]. Among the many advantages of this strategy over solution synthesis, the use of atomically clean and flat single-crystal surfaces allows observation of the reaction process at the single molecule level by means of scanning tunneling microscopy (STM) [56]. Recent progress in this field clearly demonstrates a high potential for the synthesis of complex two-dimensional (2D) molecular architectures via surface-assisted C–C coupling of organic molecules on single-crystal metal surfaces [57, 58]. Recently, it has been demonstrated that fjord ring closure via thermally induced cyclodehydrogenation, leading to planar nanographenes and nanoribbons, can be realized with exceptionally high efficiency on Cu(111) and Au(111) surfaces [59–62]. However, attempts to perform a similar cove region closure and to fabricate geodesic PAH molecules by cyclodehydrogenation on Au(111) or Cu(111) surfaces were unsuccessful because the high mobility of precursor molecules leads to random intermolecular merging of precursor molecules. These results clearly indicate that transformation to nonplanar PAHs require stronger catalysts that are able to address the strain energy erased during cyclodehydrogenation. The Pt group metals are well-known catalysts widely used for dehydrogenation of organic compounds [63]. The first examples of intramolecular cyclodehydrogenation using Pt/C catalyst were reported more than 50 years ago for the synthesis of triphenylene [64] and benzo [*ghi*]perylene [65]. The possibility of cove region closure in PAHs using a Pt group catalyst was demonstrated for the first time by Studt and Win in 1983. It was shown

Fig. 4 Examples of cyclodehydrogenations catalyzed by Pt and Pd metals

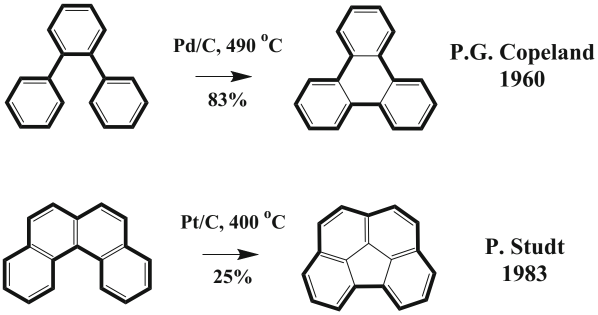

that benzo[*c*]phenanthrene, representing the smallest PAH molecule bearing a cove region, can be converted to benzo[*ghi*]fluorathrene using a Pd/C catalyst at 400°C with 25% yield (Fig. 4) [66]. Despite the fact that the cyclodehydrogenation on Pt group metals has been known for a long time, this technique has only recently been successfully applied for the synthesis of geodesic PAHs.

The first step toward on-surface synthesis of buckybowls was made by Rim et al., who demonstrated the formation of the C_{48} hemispherical buckybowl from quasi-planar hexabenzocoronene precursor [67]. The surface-assisted sixfold closure of cove regions on the precursor periphery was achieved via cyclodehydrogenation by annealing (at 600°C) a sample as-deposited on an Ru (0001) surface. The Ru surface serves as catalyst for the cyclodehydrogenation and prevents intermolecular coupling as a result of bonding to the surface. Importantly, the surface also acts as a support for the precursors and final products, enabling the use of STM investigations at the single-molecule level. STM analysis has revealed a high selectivity and exceptionally high conversion ratio of the deposited precursors into nonplanar buckybowl structures (Fig. 5). As a result of the high reactivity of the Ru surface and high temperature applied, the dehydrogenation process does not stop at the formation of the $C_{48}H_{12}$ bowl. The molecule undergoes exhaustive dehydrogenation, leading to an all-carbon C_{48} bowl covalently bonded to the Ru surface by at least 12 C–Ru bonds [67]. The efficiency of the surface-assisted approach was demonstrated by Otero et al. for the synthesis of C_{60} fullerene on a Pt surface [68]. In their study, $C_{60}H_{30}$ fullerene precursor molecules (Fig. 6, precursor A) were deposited onto a Pt(111) surface under UHV conditions and annealed at around 480°C. The simple annealing step led to the formation of the corresponding C_{60} cages with an unprecedented high efficiency of close to 100%. STM analysis of the surface covered with about 0.2 monolayers of precursor before and after annealing showed that the molecular coverage did not change during temperature-induced reaction and that all of the triangular molecules were converted into round fullerenes [68]. Despite the variety of experimental and theoretical methods employed to characterize the process, general readiness to form and the particular stability of the target C_{60} prevented conclusive demonstration of the selectivity of the process. At least, the C–C bond rearrangement, leading to formation of the most stable 60-carbon atom cluster (C_{60} fullerene), cannot be

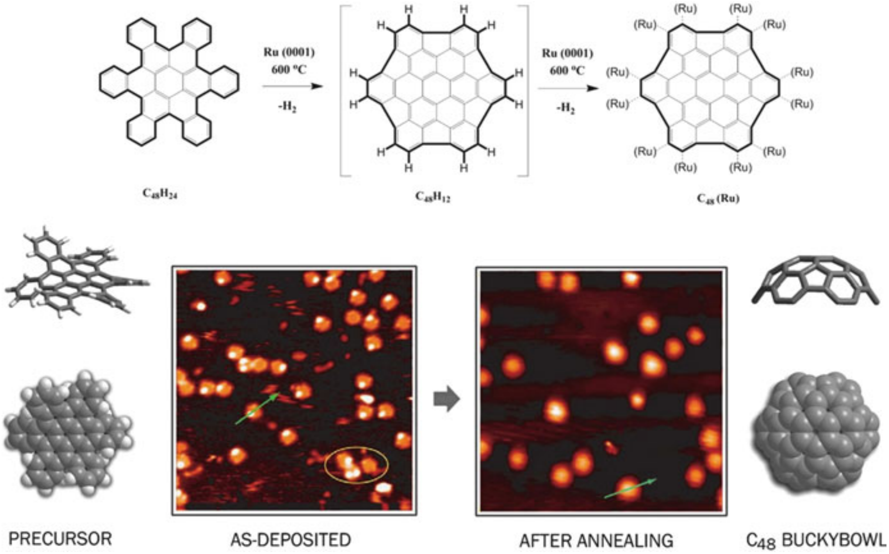

Fig. 5 Surface-assisted synthesis of the hemispherical C_{48} buckybowl (*left*) via exhaustive cyclodehydrogenation of hexabenzocoronene (*right*) on an Ru(0001) surface. STM images of the precursor before and after annealing at 600°C (reprint with permission from [67])

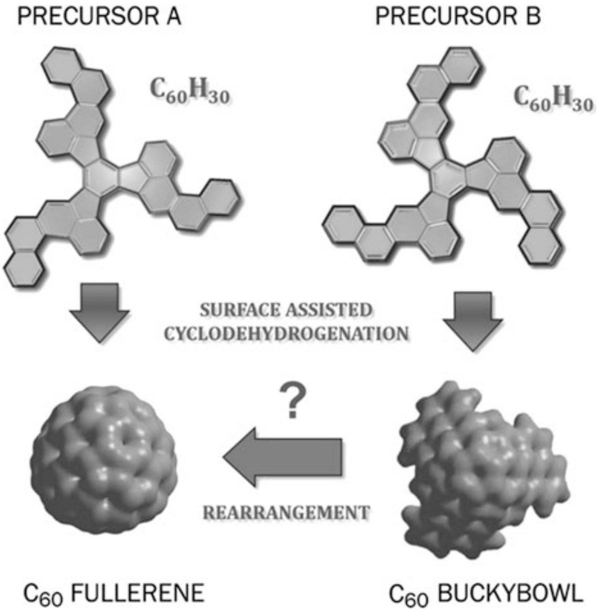

Fig. 6 Structures of C_{60} fullerene precursor (**A**) and C_{60} buckybowl precursor (**B**) and their cyclodehydrogenation products

excluded under the applied conditions. Obviously, synthesis of isomer-pure higher fullerenes cannot be realized if any kind of C–C rearrangements take place during or after condensation. This important issue has been addressed by investigation of surface catalyzed cyclodehydrogenation of a specifically designed precursor molecule (Fig. 6, precursor B) preprogrammed for the formation of the C_{60} buckybowl structure with unique triangular shape [69]. On-surface cyclodehydrogenation of two isomeric $C_{60}H_{30}$ precursors (Fig. 6, precursor A and precursor B) gave convincing evidence that the reaction occurs in a highly selective manner [69]. In contrast to the condensation of precursor A, whose cyclodehydrogenation leads to a closed C_{60} cage, the zipping of precursor B should result in the formation of a triangular-shaped C_{60} buckybowl whose formation can be readily distinguished by STM because of its unique triangular geometry.

Indeed, upon annealing of precursor B deposited on a Pt(111) surface at 480°C, STM analysis revealed full conversion into triangular species, all with similar size and shape (Fig. 7). The molecules are imaged as triangular protrusions, suggesting that the rim is connected to the platinum surface by strong C–Pt bonds. The parameters of the formed structures indicate that, although precursor B has all the necessary C atoms to form the C_{60}-I_h fullerene, cyclodehydrogenation resulted exclusively in the formation of triangular C_{60} buckybowls, as no C–C bond

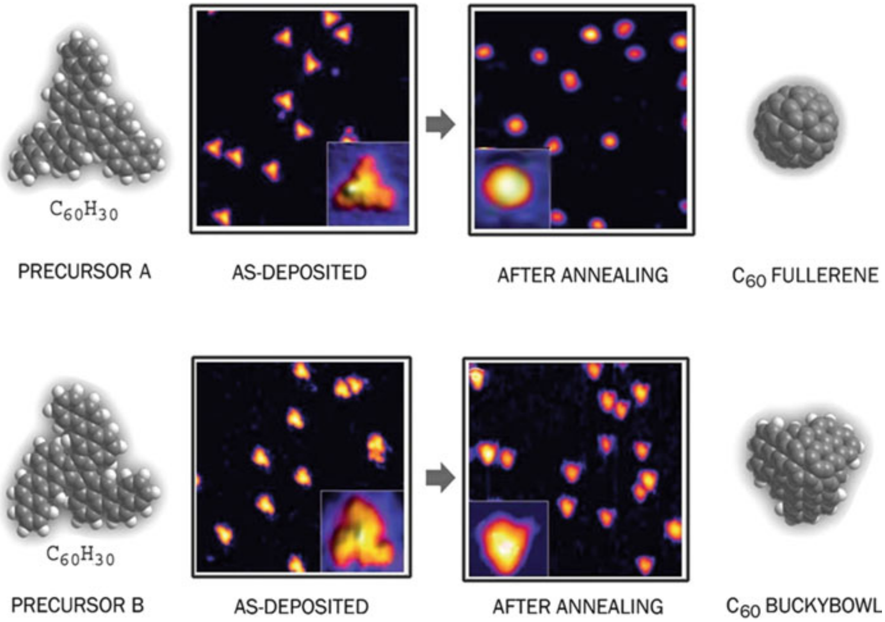

Fig. 7 Surface-assisted synthesis of fullerene C_{60}-I_h (*top*) and C_{60} buckybowl (*bottom*) via cyclodehydrogenation of their respective precursors on a Pt(111) surface. STM images (reprint with permission from [69]) of the precursor before and after annealing at 480°C

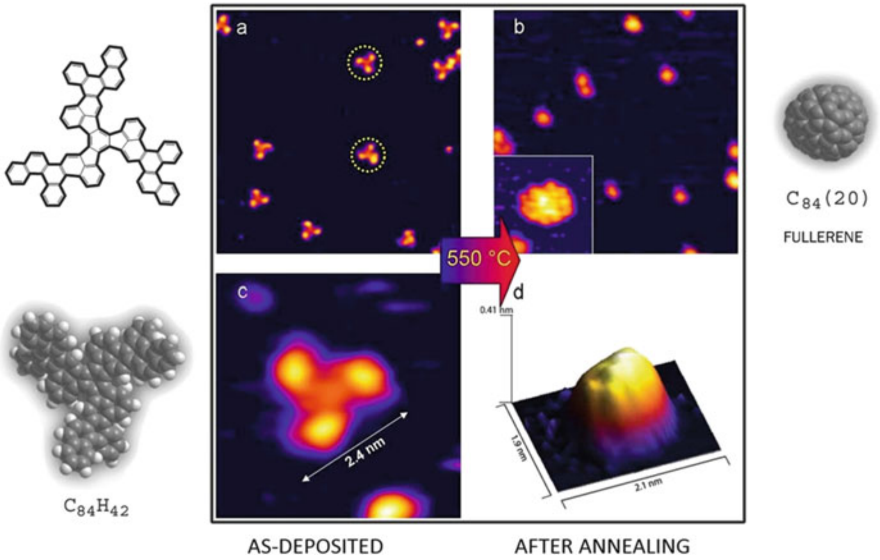

Fig. 8 Surface-assisted synthesis of fullerene $C_{84}(20)$ via cyclodehydrogenation of $C_{84}H_{42}$ precursors on a Pt(111) surface. STM images (reprint with permission from [69]) of the precursor before and after annealing at 550°C

rearrangement occurred during the annealing. The observation of intermediate products along with final products additionally supports the zipper mechanism of the reaction, whereby only preselected bonds are formed [69]. The results demonstrate that the surface-assisted cyclodehydrogenation process is selective in nature and can be used to produce various specifically designed carbon-based nanostructures.

The approach was successfully applied for the first rational synthesis of isomer-pure higher fullerene $C_{84}(20)$ from the respective $C_{84}H_{42}$ precursor molecules [69]. Upon annealing at 550°C on a Pt(111) surface, STM monitoring showed that the shape of all of precursor molecules changed and all species became spherical with a lateral size expected for C_{84} fullerene (Fig. 8). Formation of the C_{84} fullerene cages was additionally confirmed by mass spectrometry [69]. Although the quantities of the final products were too small to permit direct confirmation of fullerene connectivity, the structural uniformity of formed fullerene molecules, as indicated by STM analysis, indicated regiospecific zipping to the single fullerene isomer. Furthermore, it was demonstrated that the approach can be extended to the synthesis of highly interesting heterocarbon nanostructures. The first successful fabrication of heterofullerenes by the surface-assisted approach was demonstrated by Otero et al. for synthesis of $C_{57}N_3$ [68] (Fig. 9). In their study, a structurally related precursor was quantitatively converted to the heterofullerene $C_{57}N_3$ upon annealing of the respective precursor on a Pt(111) surface at 477°C [68].

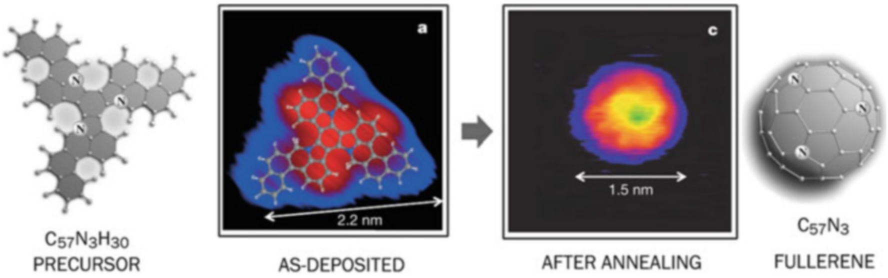

Fig. 9 Surface-assisted synthesis of fullerene $C_{57}N3$ via cyclodehydrogenation of $C_{57}N_3H_{30}$ precursors on a Pt(111) surface. STM images (reprint with permission from [68]) of the precursor before and after annealing at 477°C

4 Seed-Templated Growth of SWCNTs

Hemispherical buckybowls representing nanotube caps appear to be highly attractive molecular seeds for chirality-controlled nanotube growth. Scott and coworkers formulated a general strategy for the growth of chirality-pure SWCNTs starting from CNT cap templates, which can be synthesized by means of FVP [70]. In 2011, the Scott group succeeded in the first rational synthesis of such a CNT cap [71], which recently showed selectivity in nearly exclusive growth of semiconducting nanotubes by vapor phase epitaxy elongation under metal-free conditions [72]. Deviation from the “preprogrammed” chirality was caused by C–C rearrangements in the CNT seeds under the applied conditions. Another approach, suggested by Bertozzi and Jasti [73], envisions the synthesis of defined CNT segments as suitable CNT seeds [74]. Recent results have demonstrated the selectivity in diameter distribution of SWCNTs, although the preprogrammed chirality was not kept because of seed rearrangement during activation [75]. On the other hand, progress in SWCNT “cloning” demonstrates that the original chiralities of nanotube seeds can be preserved during growth, suggesting that the approach is highly feasible for production of chirality-pure SWCNT from well-defined CNT seeds [30, 76–78]. Considering the metal-assisted strategy, the synthesis of CNT seeds and subsequent SWCNT growth can be performed as a one-pot process on the same metal surface (Fig. 10) [79]. This approach mimics conventional CVD growth whereby the usual nucleation step, leading to formation of an end-cap with accidental geometry, is avoided by introducing a predefined end-cap molecule whose structure should unambiguously dictate nanotube chirality. The strategy offers the possibility of performing several challenging steps (synthesis of large buckybowl systems, correct placing of CNT caps on a metal surface, and activation of CNT growth) as a one-pot reaction with unprecedentedly high efficiency. The seeds obtained are already bonded to the metal in an appropriate way and can be used directly for SWCNT fabrication on the same metal surface.

Several routes for the synthesis of quasi-planar CNT precursors for different chiralities have been recently suggested [70, 71, 79–82]. It was also shown that the

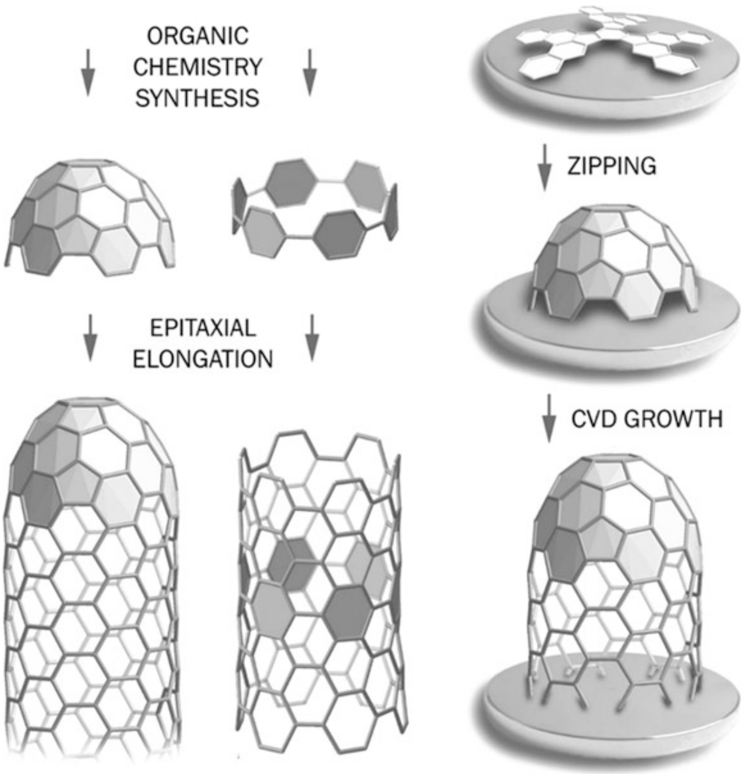

Fig. 10 Three different template-mediated approaches for the chirality-controlled synthesis of SWCNTs

respective precursors can be effectively transformed to CNT caps on Pt group metal surfaces under UHV conditions (Fig. 11) [67, 69, 83].

First attempts to grow CNTs by a surface-assisted strategy revealed the activity of fabricated CNT seeds in nanotube growth initiation, leading to the formation of multiwalled nanotubes [84]. Attempts to grow SWCNTs from CNT caps under UHV conditions were also not successful, because of the decomposition of CNT caps before growth initiation, indicating that the activation barrier for the insertion of carbon into the CNT caps is too high [83]. This is most probably connected with the high local strain on the boundary between the "fullerene fragment" (CNT cap) and the all-hexagon part (CNT segment). The localization of high strain in such fragments is well known for higher fullerenes and is responsible for their high reactivity [85]. This problem can be overcome by employing more stable seed molecules bearing already completed nanotube segments in the structure (ultrashort nanotubes). Indeed, recently it has been demonstrated that ultrashort (6,6) SWCNTs, generated in situ via cyclodehydrogenation of the respective precursors, can be effectively elongated on the Pt surface at 400–500°C, resulting in chirality-pure (6,6) SWCNTs [86]. As a result of the very mild CVD conditions used, defect-

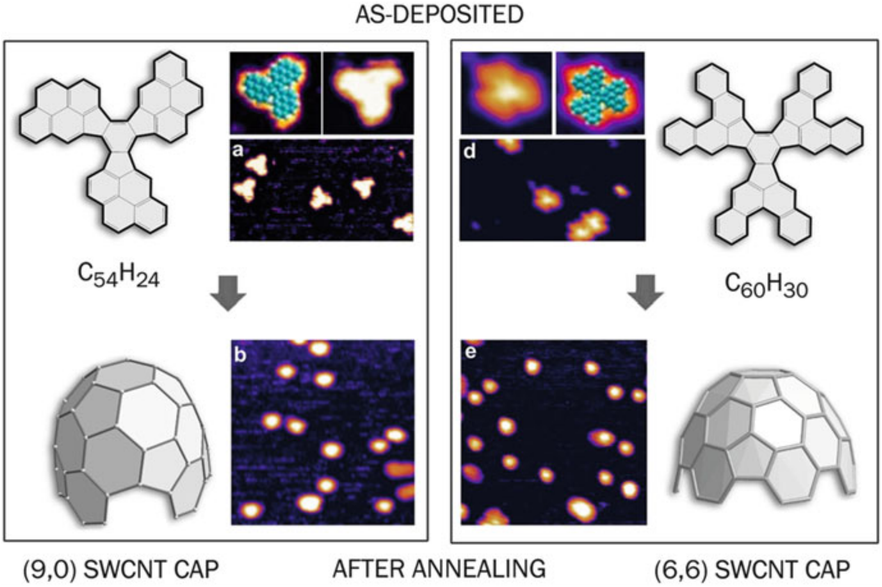

Fig. 11 Surface-assisted synthesis of (9,0) and (6,6) SWCNT caps via cyclodehydrogenation of $C_{54}H_{24}$ and $C_{60}H_{30}$ precursors on a Rh(111) surface. STM images of the precursor before and after annealing at 547°C and at 577°C, respectively

free and 100% chirality-pure SWCNTs were generated, as indicated by Raman spectroscopy measurements (Fig. 12). Importantly, this approach allows the synthesis of pure SWCNT free from metal nanoparticles, because growth is carried out on a flat metal surface (no metal nanoparticles are used) [86]. This method is currently the only one that provides full control over SWCNT chirality and SWCNT purity. The big advantage of the approach is that virtually any required CNT chirality can be unambiguously preprogrammed by the precursor engineering. Furthermore, because of thousand-fold elongation of the seed molecules during SWCNT growth, only milligram amounts of the respective precursor molecules are needed for multigram-scale SWCNT production. Because the process of SWCNT fabrication under STM conditions imitates conventional CVD production, a high level of transferability is expected, which could ultimately provide access to chirality-pure SWCNTs in bulk amounts in the future.

5 Future Prospects

Surface-assisted strategies have proved to be very prolific for the synthesis of nonplanar sp^2-based carbon nanostructures. Recent progress in this field has clearly demonstrated the possibility of fabrication of carbon-based nanostructures such as higher fullerenes and SWCNTs in a fully controllable manner. Production of these

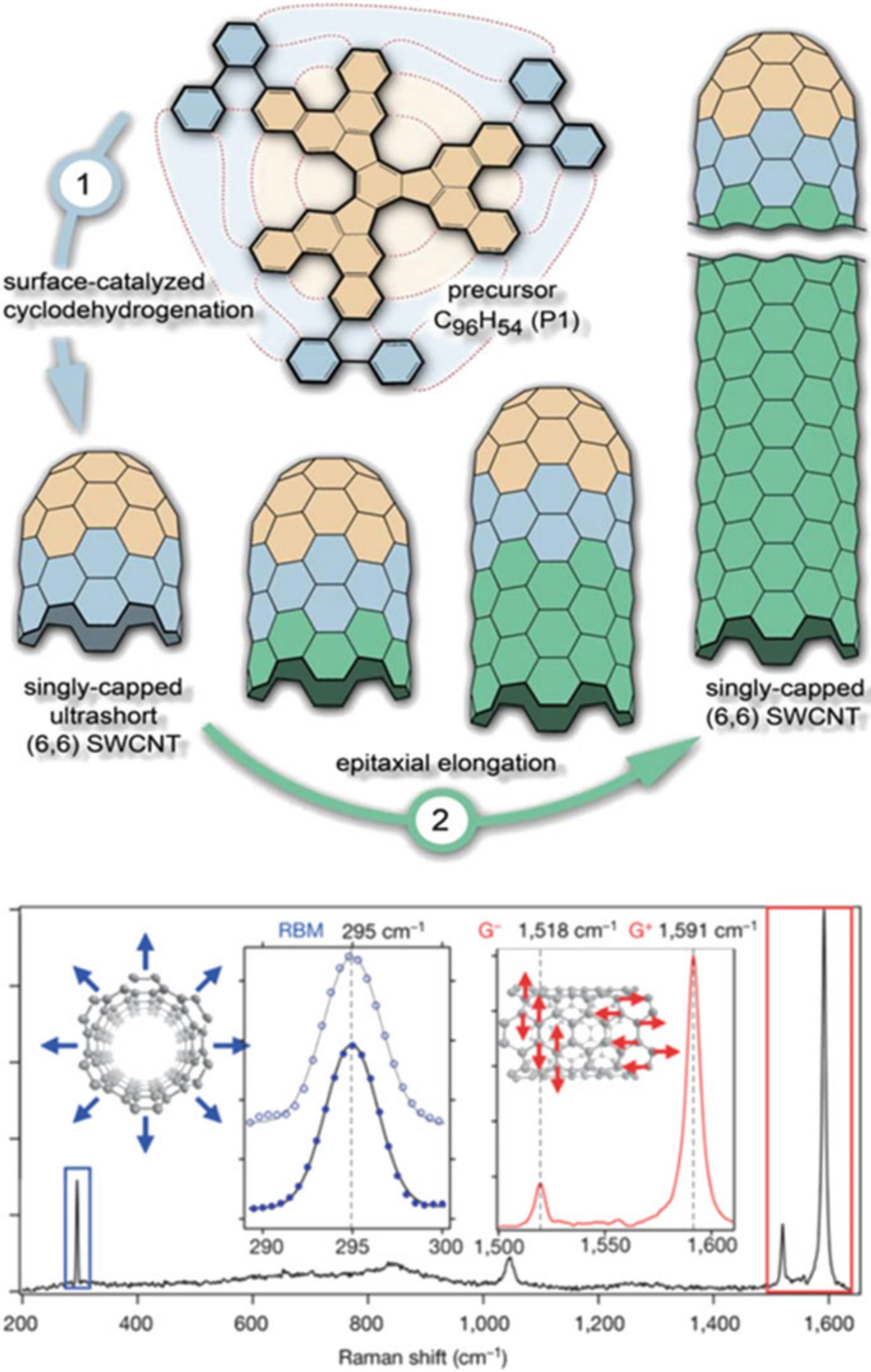

Fig. 12 Surface-assisted synthesis of single-chirality (6,6) SWCNTs, showing the formation of singly capped ultrashort CNT seeds via surface-catalyzed cyclodehydrogenation, and SWCNT growth via surface-catalyzed epitaxial elongation. *Bottom*: Raman spectrum of a bulk sample,

unique materials in isomer-pure form in bulk amounts no longer appears elusive and there are promising prospects that such compounds will become available in macroscopic amounts in the near future. For the surface-assisted zipping approach, there are virtually no factors limiting its application in assembling complex precursor structures, so there are no important obstacles to extending the approach to other highly interesting carbon-based nanostructures, such as endohedral and exohedral fullerenes, heterofullerenes, heteronanotubes, nanocones, and other more complex sp^2 carbon-based architectures.

References

1. Langa F, Nierengarten JF (2011) Fullerenes: principles and applications. RSC, Cambridge
2. O'Connell MJ (2006) Carbon nanotubes: properties and applications. CRC, Boca Raton
3. Jorio A, Dresselhaus MS, Dresselhaus G (2008) Carbon nanotubes: advanced topics in the synthesis, structure, properties and applications. Springer, Berlin
4. Guisinger NP, Arnold MS (2010) MRS Bull 35:273–279
5. Zhang J, Terrones M, Park CR, Mukherjee R, Monthioux M, Koratkar N, Kim YS, Hurt R, Frackowiak E, Enoki T, Chen Y, Chen YS, Bianco A (2016) Carbon 98:708–732
6. Kroto HW, Heath JR, O'Brien SC, Curl RF, Smalley RE (1985) Nature 318:162–164
7. Guo T, Nikolaev P, Thess A, Colbert DT, Smalley RE (1995) Chem Phys Lett 243:49–54
8. Krätschmer W, Lamb LD, Fostiropoulos K, Huffman DR (1990) Nature 347:354–358
9. Haufler RE, Conceicao J, Chibante LPF, Chai Y, Byrne NE, Flanagan S, Haley MM, Obrien SC, Pan C, Xiao Z, Billups WE, Ciufolini MA, Hauge RH, Margrave JL, Wilson LJ, Curl RF, Smalley RE (1990) J Phys Chem 94:8634–8636
10. Ebbesen TW, Ajayan PM (1992) Nature 358:220–222
11. Peters G, Jansen M (1992) Angew Chem Int Ed 31:223
12. Taylor R, Langley GJ, Kroto HW, Walton DRM (1993) Nature 366:728–731
13. Amsharov KY, Jansen M (2007) Carbon 45:117–123
14. Takehara H, Fujiwara M, Arikawa M, Diener MD, Alford JM (2005) Carbon 43:311–319
15. Endo M, Takeuchi K, Igarashi S, Kobori K, Shiraishi M, Kroto HW (1993) J Phys Chem Solids 54:1841–1848
16. Kumar M, Ando Y (2010) J Nanosci Nanotechnol 10:3739–3758
17. Zhang Q, Huang JQ, Zhao MQ, Qian WZ, Wei F (2011) ChemSusChem 4(7):864–889
18. Jinno K (2001) Separation of fullerenes by liquid chromatography. RSC, Cambridge
19. Hirsch A, Brettreich M (2004) Fullerenes: chemistry and reactions. Wiley-VCH, Weinheim
20. Fowler PW, Manolopoulos DE (1995) An atlas of fullerenes. Clarendon, Oxford
21. Tu X, Manohar S, Jagota A, Zheng M (2009) Nature 460:250–253
22. Liu H, Nishide D, Tanaka T, Kataura H (2011) Nat Commun 2:309–316
23. Khripin CY, Fagan JA, Zheng M (2013) J Am Chem Soc 135(18):6822–6825
24. Tulevski GS, Franklin AD, Afzali A (2013) ACS Nano 7(4):2971–2976
25. Subbaiyan NK, Cambre S, Parra-Vasquez ANG, Haroz EH, Doorn SK, Duque JG (2014) ACS Nano 8(2):1619–1628
26. Flavel BS, Moore KE, Pfohl M, Kappes MM, Hennrich F (2014) ACS Nano 8(2):1817–1826
27. Liu HP, Tanaka T, Kataura H (2014) Nano Lett 14(11):6237–6243

Fig. 12 (continued) revealing formation of defect-free (absence of a D peak) and chirality-pure (single and very narrow RGB signal) SWCNTs (reprinted with permission from [86])

28. Wang H, Yuan Y, Wie L, Goh K, Yu D, Chen Y (2015) Carbon 81:1–19
29. Yang F, Wang X, Zhang DQ, Yang J, Luo D, Xu ZW, Peng F, Li X, Li R, Li Y, Li M, Bai X, Ding F, Li Y (2014) Nature 510:522–524
30. Liu J, Wang C, Tu XM, Liu BL, Chen L, Zheng M, Zhou CW (2012) Nat Commun 3:1–7
31. Petrukhina MA, Scott LT (2012) Fragments of fullerenes and carbon nanotubes. Wiley, New York
32. Harvey RG (1997) Polycyclic aromatic hydrocarbons. Wiley-VCH, New York
33. Grzybowski M, Skonieczny K, Butenschon H, Gryko DT (2013) Angew Chem Int Ed 52:9900–9930
34. Chen L, Hernandez Y, Feng XL, Müllen K (2012) Angew Chem Int Ed 51:7640–7654
35. Simpson CD, Brand JD, Berresheim AJ, Przybilla L, Räder HJ, Müllen K (2002) Chem Eur J 8:1424–1429
36. Zhi L, Müllen K (2008) J Mater Chem 18:1472–1484
37. Cheung KY, Xu XM, Miao Q (2015) J Am Chem Soc 137:3910–3914
38. Mallory FB, Mallory CW (1984) Org React 30:1–456
39. Kivala M, Wu D, Feng X, Li C, Müllen K (2013) Cyclodehydrogenation in the synthesis of graphene-type molecules. In: Materials science and technology. Wiley-VCH, Weinheim, pp. 373–420
40. Mehta G, Rao HSP (1998) Tetrahedron Lett 54:13325–13370
41. Plater MJ, Praveen M, Schmidt DM (1997) Fuller Nanotub Carbon Nanostruct 5:781–800
42. Scott LT (1996) Pure Appl Chem 68:291–300
43. Scott LT (2004) Angew Chem Int Ed 43:4994–5007
44. Tsefrikas VM, Scott LT (2006) Chem Rev 106:4868–4884
45. Scott LT, Boorum MM, McMahon BJ, Hagen S, Mack J, Blank J, Wegner H, de Meijere A (2002) Science 295:1500–1502
46. Kabdulov M, Jansen M, Amsharov KY (2013) Chem Eur J 19:17262–17266
47. Amsharov KY, Jansen M (2005) J Org Chem 73(7):2931–2934
48. Amsharov KY, Jansen M (2009) Chem Commun 19:2691–2693
49. Echavarren AM, Gomez-Lor B, Gonzalez JJ, De Frutos O (2003) Synlett 2003:585–597
50. Alberico D, Scott ME, Lautens M (2007) Chem Rev 107:174–238
51. Pascual S, de Mendoza P, Echavarren AM (2007) Org Biomol Chem 5:2727–2734
52. Steinberg BD, Jackson EA, Filatov AS, Wakamiya A, Petrukhina MA, Scott LT (2009) J Am Chem Soc 131:10537–10545
53. Allemann O, Duttwyler S, Romanato P, Baldridge KK, Siegel JS (2011) Science 332:574–577
54. Amsharov KY, Kabdulov MA, Jansen M (2012) Angew Chem Int Ed 51(19):4594–4597
55. Tait SL (2008) ACS Nano 2:617–621
56. Hla SW, Rieder KH (2003) Annu Rev Phys Chem 54:307–330
57. Gourdon A (2008) Angew Chem Int Ed 47:6950–6953
58. Mendez J, Lopez MF, Martin-Gago JA (2011) Chem Soc Rev 40:4578–4590
59. Weiss K, Beernink G, Dötz F, Birkner A, Müllen K, Wöll CH (1999) Angew Chem Int Ed 38:3748–3752
60. Cai J, Ruffieux P, Jaafar R, Bieri M, Braun T, Blankenburg S, Muoth M, Seitsonen AP, Saleh M, Feng X, Müllen K, Fasel R (2010) Nature 466:470–473
61. Treier M, Pignedoli CA, Laino T, Rieger R, Müllen K, Passerone D, Fasel R (2011) Nat Chem 3:61–67
62. Abdurakhmanova N, Amsharov N, Stepanow S, Jansen M, Kern K, Amsharov K (2014) Carbon 77:1187–1190
63. Rylander PN (1987) Organic syntheses with noble metal catalysts. Academic, New York
64. Copeland PG, Dean RE, McNeil D (1960) J Chem Soc 1960:1687–1689
65. Altman Y, Ginsburg D (1959) J Chem Soc 1959:466–468
66. Studt P, Win T (1983) Liebigs Ann Chem 1983:519

67. Rim KT, Siaj M, Xiao SX, Myers M, Carpentier VD, Liu L, Su CC, Steigerwald ML, Hybertsen MS, McBreen PH, Flynn GW, Nuckolls C (2007) Angew Chem Int Ed 46:7891–7895
68. Otero G, Biddau G, Sanchez-Sanchez C, Caillard R, Lopez MF, Rogero C, Palomares FJ, Cabello N, Basanta MA, Ortega J, Mendez J, Echavarren AM, Perez R, Gomez-Lor B, Martin-Gago JA (2008) Nature 454:865–867
69. Amsharov K, Abdurakhmanova N, Stepanow S, Rauschenbach S, Jansen M, Kern K (2010) Angew Chem Int Ed 49:9392–9396
70. Hill TJ, Hughes RK, Scott LT (2008) Tetrahedron 64:11360–11369
71. Scott LT, Jackson EA, Zhang Q, Steinberg BD, Bancu M, Li B (2011) J Am Chem Soc 134:107–110
72. Liu BL, Liu J, Li HB, Bhola R, Jackson EA, Scott LT, Page A, Irle S, Morokuma K, Zhou CW (2015) Nano Lett 15:586–595
73. Jasti R, Bertozzi CR (2010) Chem Phys Lett 494:1–7
74. Bunz UHF, Menning S, Martin N (2012) Angew Chem Int Ed 51:7094–7101
75. Omachi H, Nakayama T, Takahashi E, Segawa Y, Itami K (2013) Nat Chem 5:572–576
76. Smalley RE, Li YB, Moore VC, Price BK, Colorado R, Schmidt HK, Hauge RH, Barron AR, Tour JM (2006) J Am Chem Soc 128:15824–15829
77. Ren ZF (2007) Nat Nanotechnol 2:17–18
78. Yao YG, Feng CQ, Zhang J, Liu ZF (2009) Nano Lett 9:1673–1677
79. Mueller A, Amsharov KY, Jansen M (2010) Tetrahedron Lett 51:3221–3225
80. Mueller A, Amsharov KY (2012) Eur J Org Chem 2012:6155–6164
81. Mueller A, Amsharov KY (2015) Eur J Org Chem 2015:3053–3056
82. Amsharov KY (2015) Phys Status Solidi B 252:2466–2471
83. Abdurakhmanova N, Mueller A, Stepanow S, Rauschenbach S, Jansen M, Kern K, Amsharov KY (2015) Carbon 84:444–447
84. Mueller A, Amsharov KY, Jansen M (2012) Fullerenes, Nanotubes, Carbon Nanostruct 20:401–404
85. Amsharov KY, Simeonov KS, Jansen M (2010) Fullerenes, Nanotubes, Carbon Nanostruct 18:427–430
86. Sanchez-Valencia JR, Dienel T, Groning O, Shorubalko I, Mueller A, Jansen M, Amsharov K, Ruffieux P, Fasel R (2014) Nature 512:61–64

Adv Polym Sci (2017) 278: 147–172
DOI: 10.1007/12_2017_5

Chemical Synthesis of Carbon Nanomaterials Through Bergman Cyclization

Youfu Wang, Shudan Chen, and Aiguo Hu

Abstract Bergman cyclization, an organic reaction that forms 1,4-benzene diradicals via intramolecular cyclization of enediyne (EDY) compounds, is a fascinating reaction and can be used to fabricate polyarylenes with various side chains and construct carbon nanomaterials with diverse morphologies. Bergman cyclization has had a strong impact on a number of fields, including pharmaceutics, polymer chemistry, and materials science. The homopolymerization of EDYs through Bergman cyclization is an ingenious strategy for fabrication of functional polyarylenes and has the advantages of facial operation, high efficiency, tailored structure, and being catalyst-free. Moreover, the obtained functionalized polyarylenes show many remarkable properties, such as excellent thermal stability, good solubility, and processability, which enable these polyarylenes to be further manufactured into carbon nanomaterials. Recently, extensive efforts have been devoted to the application of Bergman cyclization in polymer chemistry, materials science, and nanodevices. This chapter summarizes the synthetic strategies that have been developed for fabrication of structurally unique carbon-rich materials using Bergman cyclization, including formation of nanoparticles by intramolecular collapse of single polymer chains, fabrication of conjugated microporous polymers, and construction of carbon nanomembranes with different morphologies and their applications in nanodevices. The future development of Bergman cyclization in materials science is discussed, especially in the construction and application of carbon nanomaterials by altering the template types and morphologies to precisely control the microstructures and properties of carbon nanomaterials.

Y. Wang, S. Chen, and A. Hu (✉)
Shanghai Key Laboratory of Advanced Polymeric Materials, School of Materials Science and Engineering, East China University of Science and Technology, Shanghai 200237, China
e-mail: hagmhsn@ecust.edu.cn

Keywords Bergman cyclization • Carbon dots • Carbon nanomembranes • Confined catalysis • Enediyne • Microporous polymer • Polyarylenes • Single chain nanoparticles • Supercapacitor

Contents

Abbreviations

AFM	Atomic force microscopy
APTES	*N*-Aminopropyltriethoxysilane
BET	Brunauer–Emmett–Teller
BODA	Bis-*ortho*-diynylarene
C-dot	Carbon quantum dot
CMP	Conjugated microporous polymer
CNM	Carbon nanomembrane
CN	Cyclo-1,4-naphthylene
CV	Cyclic voltammetry
DMA	Dynamic mechanical spectroscopy
DMF	*N*,*N*-Dimethylformide
DNHD	*cis*-1,6-di-2-naphthylhex-3-en-1,5-diyne
EC	Electrochemical capacitor
EDLC	Electric double layer capacitor
EDY	Enediyne
FAR	Fused aromatic ring
GPC	Gel permeation chromatography
HOMO	Highest occupied molecular orbital
LUMO	Lowest unoccupied molecular orbital
MMA	Methyl methacrylate
MWNT	Multiwalled carbon nanotube
NMP	*N*-Methylpyrrolidone
PAA	Poly(acrylic acid)
PBzA	Poly(benzyl acrylate)
PEG	Polyethylene glycol

PL	Photoluminescence
PMA	Poly(methyl acrylate)
PN	Polynaphthalene
PPP	Poly(*p*-phenylene)
QD	Quantum dot
QY	Quantum yield
SAED	Selected area electron diffraction
SAM	Self-assembly monolayer
SCMP	Soluble conjugated microporous polymer
SCNP	Single-chain polymer nanoparticle
SERS	Surface-enhanced Raman scattering
SS-CNM	Silica-supported carbon nanomembrane
STM	Scanning tunneling microscopy
TBAF	Tetrabutylammonium fluoride
TEM	Transmission electron microscopy
TMS	Trimethylsilyl

1 Introduction

The past three decades, especially the last decade, have witnessed a vigorous extension of carbon nano-allotropes with various dimensions and abundant nanostructures [1]. All of them have been a sensation in science for their surprising properties and diverse potential applications [2]. Although they demonstrate excellent performance, optimization is still a challenge because it requires elaboration of their nanostructures to figure out the structure–behavior relationships. Over the past few years, the previously existing gap between small organic molecules and macroscopic carbon materials has been partially filled by the development of a range of bottom-up strategies for the construction of carbon nano-allotropes with atomic precision, especially for graphene or graphene-like nanomaterials [3]. Various classical reactions such as the Diels–Alder reaction, cyclotrimerization, Suzuki coupling, and Ullmann coupling have been adopted for the synthesis of nanographenes [4]. Nevertheless, catalyst-free and/or byproduct-free reactions are demanded in polymer chemistry and materials science for the construction of carbon-rich polymers and carbon nanomaterials. Bergman cyclization is a unique organic reaction that forms 1,4-benzene diradicals via intramolecular cyclization of enediyne (EDY) compounds. The formed diradical intermediates further couple with each other to construct carbon-rich polymers in a facial manner. Bergman cyclization can be triggered by a variety of stimuli either in bulk or in solution. Considering the broad scope of the structures and the simplicity of the operation, Bergman cyclization has been extensively investigated in polymer chemistry and materials science for fabrication of polyarylenes with various side chains and for subsequent construction of carbon nanomaterials with diverse morphologies.

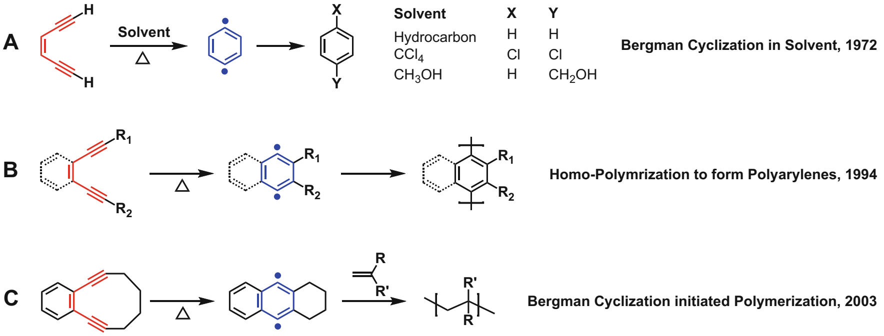

Fig. 1 Prototypical EDY structure and Bergman cyclization in solution (**a**) and the development of Bergman cyclization in polymer chemistry. The diradical generated from Bergman cyclization can act as monomer for homopolymerization to form polyarylenes (**b**) or as initiator to polymerize vinyl monomers (**c**)

The seminal work in the field of Bergman cyclization was that of Bergman and colleagues in the early 1970s [5, 6]. They found that *cis*-hex-3-en-1,5-diyne underwent an exclusively thermal rearrangement to generate a 1,4-didehydrobenzene intermediate that could be easily trapped by external reagents to yield benzene derivatives (Fig. 1a). However, Bergman cyclization did not received much attention until the late 1980s when the EDY-type core structures of many naturally occurring antibiotics, such as calicheamicin [7, 8], dynemicin A [9], esperamicin A_1 [10–12], and kedarcidin chromophore [13], were reported. The EDY "warheads" of these antibiotics are readily triggered in vivo to generate 1,4-benzene diradicals, which can cause DNA cleavage or crosslinking [14]. The strong cytotoxicity arising from Bergman cyclization has initiated a flurry of activity on the synthesis of biosimilar enediyne compounds, especially hetero-EDYs and metallo-EDYs, for potential applications in antitumor treatment [15–21].

The therapeutic applications of these EDY antitumor antibiotics has also triggered connected study of EDY chemistry, including quantum chemical theory and the thermodynamics and kinetics of the Bergman cyclization [22]. From these studies, it was found that the activation barrier of the Bergman cyclization is influenced by three dominant factors: (1) the proximity effect [23], stating that the critical distance between the two EDY carbon atoms forming a new bond should be in the range of 3.31–3.20 Å for spontaneous Bergman cyclization at physiological temperatures; (2) the molecular-strain differences [24, 25], leading to significant activation of some cyclic EDYs; and (3) the electronic effects [26], influencing the stability of the rearranged EDY, the transition state, and the formed diradical intermediate. In general, all these factors act synergistically to drive the process of diradical generation at a physiologically relevant temperature (the onset temperature). These factors therefore play an instrumental role in the design strategies for EDYs, especially in the case of thermally triggered Bergman cyclization. Besides heat, Bergman cyclization can also be triggered by other stimuli such as light, acid, and organometallic catalysts [18, 27–30].

Bergman cyclization has also proven to be a promising tool in polymer chemistry and materials science [31]. In 1994, Tour [32] first carried out radical polymerization of EDY compounds via thermally triggered Bergman cyclization and obtained conjugated polyarylenes such as poly(*p*-phenylene)s (PPPs) and polynaphthalenes (PNs) (Fig. 1b), highlighting the Bergman cyclization as a new synthetic tool for polymers and other materials. Smith [33, 34] later used Bergman cyclization of bis (*ortho*-diynylarene) (BODA) to form branched oligomers at 210°C, which could either react with carbon nano-onions to improve their solubility, or be carbonized to generate glassy carbon. Moore [35, 36] used the diradicals generated from Bergman cyclization to initiate the radical polymerization of a variety of vinyl monomers (Fig. 1c). The results showed that the diradicals tend to terminate intramolecularly to produce oligomeric byproducts. The high polymers produced in diradical-initiated systems are only expected to result from monoradicals formed after the diradicals undergo chain transfer with monomer, polymer, or other available chain-transfer agents. Following this line, Barner-Kowollik [37] reported the first reversible addition fragmentation chain transfer (RAFT) polymerization of methyl methacrylate (MMA) initiated with aryl diradical, employing a cyclic EDY as the diradical source and cyanoisopropyldithiobenzoate (CPDB) as the RAFT agent. They successfully obtained very high molecular weights up to almost 400,000 Da, with narrow polydispersity under mild reaction conditions.

The homopolymerization of EDYs through Bergman cyclization is a fascinating strategy for fabrication of functional polyarylenes because of the advantages of facial operation, high efficiency, tailored structure, and being catalyst-free. Moreover, the generated functionalized polyarylenes show many remarkable properties, such as excellent thermal stability, good solubility, and processability, which enable these polyarylenes to be further manufactured into carbon nanomaterials with diverse morphologies. These studies established ideal platforms for the preparation of polyarylenes and carbon nanomaterials with unique electronic and photovoltaic properties and excellent thermal stability and processability, which aroused our curiosity to explore this field further. Therefore, considerable research has been conducted in our laboratory on the preparation of novel functional materials and the development of new synthetic methods based on Bergman cyclization. During the past few years, we have successfully prepared a variety of structurally unique materials, such as nanoparticles collapsed from single polymer chain, conjugated microporous polymers, and carbon nanomembranes with different morphologies. In this chapter, we summarize our recent research results on this topic together with some closely related work from other groups.

2 Mechanism of Bergman Cyclization

The Bergman cyclization is especially attractive for the synthesis of linear polyarylenes because it is a simple, byproduct-free synthetic route involving one component and with no strict requirement in terms of catalyst or additives. Despite the progress in pharmaceutics and polymer chemistry [38], limitations still exist for Bergman cyclization, especially in the ambiguous main chain structure of the formed polymers. Matzger and colleagues [39] proposed a mechanism for Bergman cyclization polymerization, combining radical chain growth with step-growth pathways (Fig. 2). EDY is first attacked by radical A (formed from Bergman cyclization) at the 1- or 2-position of the alkynyl group to form a vinyl radical intermediate (intermediate B or D). Subsequent 5-exo-dig cyclization of B and 5-endo-dig cyclization of D gives radicals with an indene moiety, while 6-endo-dig cyclization of B gives a radical with a naphthalene moiety. This leads to "polynaphthalene" as a random copolymer of naphthalene and indenylenemethylene. This mixed mechanism limits the further development of Bergman cyclization in the field of controllable synthesis of conjugated polymers and graphene-like materials.

By utilizing the designable structure of EDYs, it is very easy to modulate the reaction conditions and vary the structure, performance, and application of the obtained polyarylenes. Unfortunately, the fundamental mechanism of Bergman cyclization polymerization [39] remained obscure although the construction of polyarylenes through homopolymerization of EDY is very interesting. To resolve this issue, we studied on-surface Bergman cyclization, taking advantage of the ultrahigh resolution of scanning tunneling microscopy (STM), and reported for the first time the formation of structurally well-defined one-dimensional (1D) PPP chains on a Cu(110) surface [40].

Initially, an EDY compound, *cis*-1,6-di-2-naphthylhex-3-en-1,5-diyne (DNHD), terminated with two naphthyl groups was designed as the monomer (Fig. 3). After deposition of DNHD molecules on a Cu(110) substrate held at ~170 K, heart-shaped molecules with two elliptical lobes and one round protrusion were

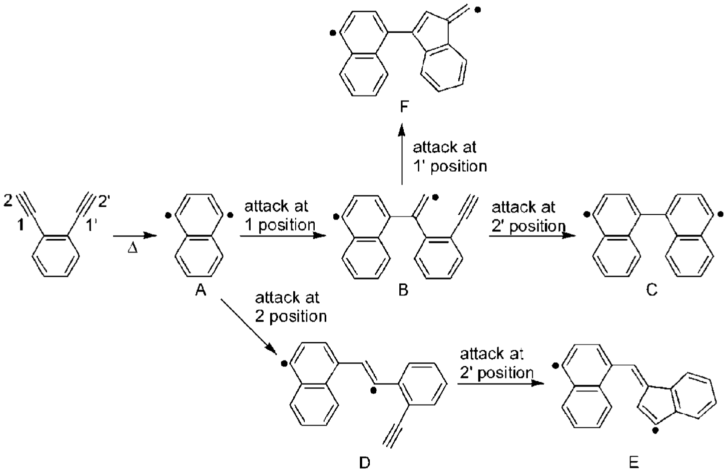

Fig. 2 Possible mechanism of Bergman cyclization. Reproduced from [39] with permission from ACS

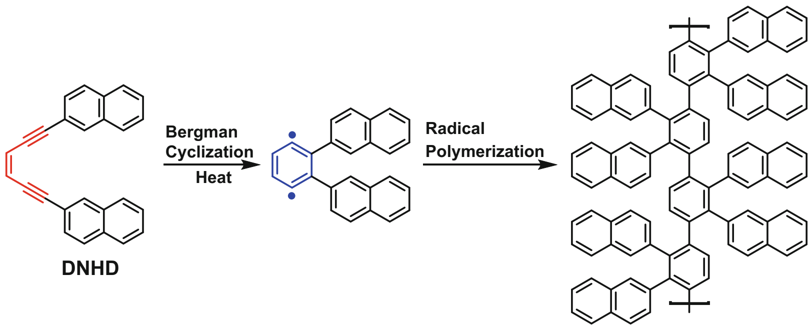

Fig. 3 Mechanism of Bergman cyclization and radical homopolymerization of DNHD

distributed in an isolated way on the substrate, as illustrated by the STM. When the sample was annealed to ~400 K, the heart-shaped motifs disappeared and dispersed 1D chains grew along the $[1\bar{1}0]$ direction of the substrate (Fig. 4). It is plausible to deduce that the on-surface formation of 1D polyphenylene through Bergman cyclization of the EDY precursor was successfully achieved. The result was validated by comparison with STM images of the monomeric product of Bergman cyclization of DNHD via ex situ synthesis. The findings demonstrated that Bergman cyclization is a promising tool for the construction, with submolecular precision, of molecular nanostructures containing conjugated backbones. This could shed light on the design of molecular nanodevices with engineered chemical and electronic properties.

Because of the submolecular precision of the polyarylenes obtained through homopolymerization of EDYs via Bergman cyclization, it is interesting to prepare rod-like polymers with pendant polyesters [41], dendrimers [42], multi-donor/ acceptors [43], and chiral imides [44, 45] as side chains.

In addition to applications in the synthesis of linear conjugated polymers, Bergman cyclization has been used to covalently modify carbon nanomaterials, such as carbon nano-onions [34], fullerene [46], multiwalled carbon nanotubes (MWNTs) [47, 48], and pristine graphene [49] via radical addition to the sp^2 carbons, thus improving their solubility and dispersibility in organic solvents.

3 Carbon-Rich Polymers Fabricated Through Bergman Cyclization

3.1 Carbon-Rich Nanoparticles

With the development of nanochemistry, it is desirable that molecules or particles of any possible size, morphology, and functionality can be facially synthesized. For

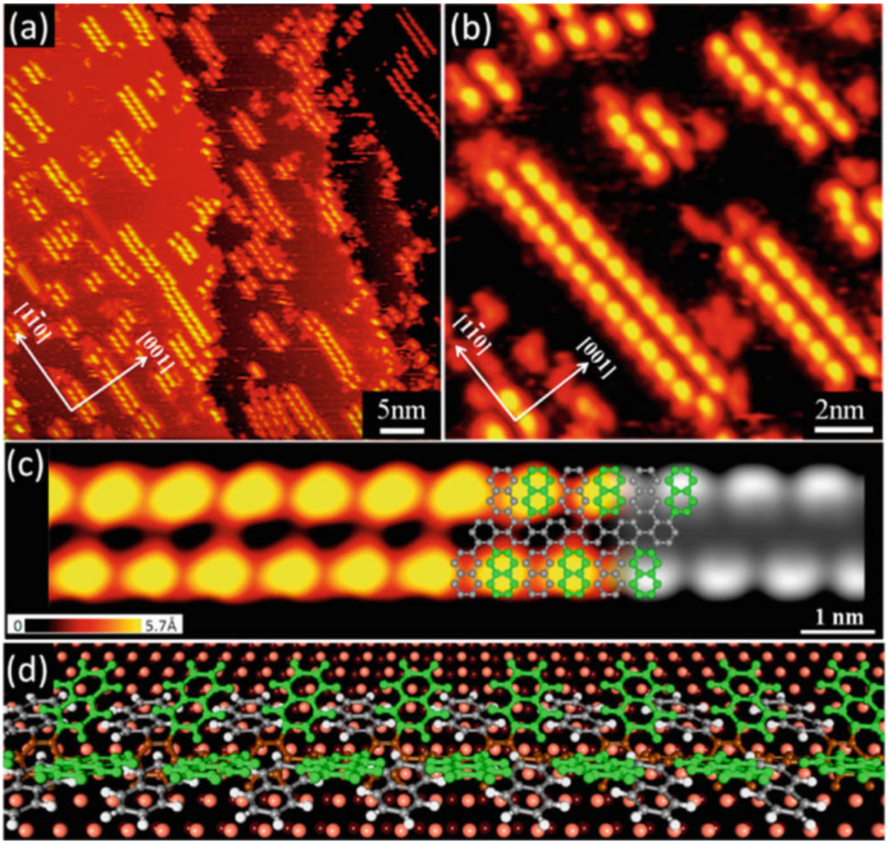

Fig. 4 Bergman cyclization of DNHD on a Cu(110) surface to form PPPs. (**a**) Large-scale and (**b**) close-up STM images showing the formation of 1D molecular chain structures along the $[1\bar{1}0]$ direction of the substrate after the sample with adsorbed molecules was annealed at 400 K. (**c**) High-resolution close-up STM image of the molecular chain and a DFT-based STM simulation (*black*-and-*white* part). An equivalently scaled model of the PPP structure is superimposed. (**d**) Perspective view of the structural model showing the tilted naphthyl groups (*green*). Reproduced from [40] with permission from ACS

example, single-molecule dendrimer synthesis gives access to particles up to approximately 5 nm in size [50], and self-assembly of amphiphiles or miniemulsion polymerizations lead to particle constructs down to around 20 nm. However, particles of 5–20 nm have attracted significant interest in the past decade because of their diverse applications in catalysis, drug-delivery systems [51, 52], light- and energy-harvesting [53], and nanoporous low dielectric constant materials for microelectric applications [54]. Intramolecular collapse of single polymer chains is a promising approach for this type of nanoparticle [55–57]. Since Mecerreyes [54] first used a radical initiator to radically crosslink the pendant acrylate functionalities along a polycaprolactone or polymethylmethacrylate backbone under ultradilute conditions, the development of slow addition methods has resulted in the ability to feasibly synthesize single-chain polymer nanoparticles (SCNPs) on a larger scale. Up to now, a variety of crosslinking methods have been used in SCNP synthesis, including high temperature self-condensation of benzocyclobutene [55, 58], benzoxazines [59], and sulfonyl azides [60]. Click chemistry, Glaser–Hay coupling of alkynes, and the tetrazine-norbornene reaction have also been employed for single polymer chain collapse [61]. Bergman cyclization produces crosslinkable diradical intermediates under various conditions, which can be advantageous for preparation of polymeric nanoparticles, and can be further applied for fabrication of size-controlled carbon dots (C-dots) and encapsulation of quantum dots (QDs).

Two strategies were used for the synthesis of linear polymer precursors [62]: (1) copolymerization of EDY-containing methacrylate with MMA through living radical polymerization (Fig. 5); and (2) attaching the EDY-containing compound to polymers via post-polymerization modification. After removal of the trimethylsilyl (TMS) protection group, the polymer was subjected to Bergman cyclization-mediated intramolecular chain collapse in hot diphenyl ether under ultradilute conditions or using continuous addition to give polymeric nanoparticles. As expected, a significant drop in the apparent molecular weights was observed for all systems after Bergman cyclization, implying the formation of nanoparticles. This is reasonable because nanoparticles are much more compact after crosslinking, showing smaller hydrodynamic volumes. No shoulder peak was observed on either the high or low molecular weight side during gel permeation chromatography (GPC), indicating that no intermolecular crosslinking process or chain scission occurred. The "tightness" of the carbon-rich nanoparticles is controllable by adjusting the EDY content in the linear polymer precursors. This is not surprising because higher EDY content results in a much more densely crosslinked network. SCNPs were well separated when spin-coated on silicon wafer (Fig. 6). Assuming the particles to be half an ellipsoid on the flat surface, the diameters of the nanoparticles were calculated to be 4.7–8.7 nm, with an average of 6.36 nm. These ultrasmall nanoparticles were then used as sacrificial pore generators to fabricate low-k spin-on dielectrics.

Because the harsh reaction conditions (>200°C) against thermally sensitive polymers such as poly(*t*-butyl acrylate) could suppress the universality of Bergman cyclization in the preparation of SCNPs, phototriggered Bergman cyclization was

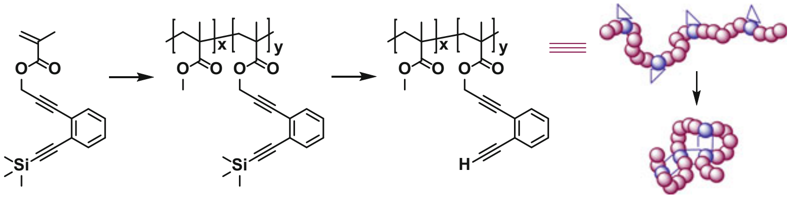

Fig. 5 Synthesis of carbon-rich nanoparticles through Bergman cyclization of EDY-containing copolymers via copolymerization of EDY-containing methacrylate with methyl methacrylate (MMA). Reproduced from [62] with permission from RSC

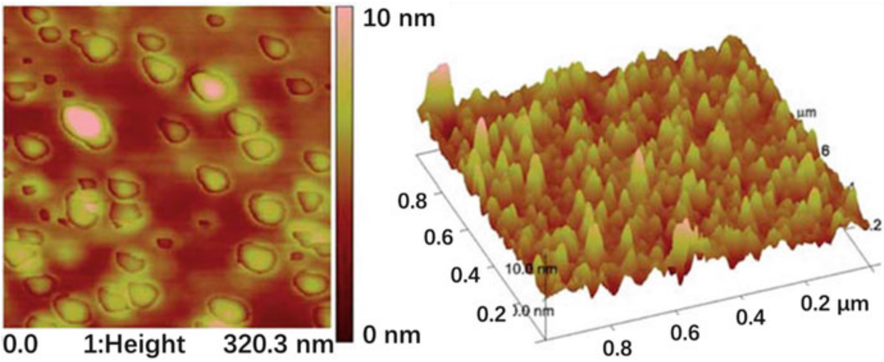

Fig. 6 Atomic force microscope (AFM) images of single-chain polymer nanoparticles on silicon wafer. Reproduced from [62] with permission from RSC

also integrated with intramolecular chain collapse to yield nanoparticles with a calculated diameter of ~10 nm [63]. The EDY motif was carefully designed to possess high photoreactivity, with the double bond locked in a methyl benzoate ring and triple bonds substituted with phenyls. Vinyl monomers were used to further verify its applicability, including methyl acrylate, ethyl acrylate, butyl acrylate, and tertbutylacrylate.

Carbon quantum dots (CQDs, C-dots or CDs), which are generally small carbon nanoparticles (less than 10 nm in size) with various photoelectric properties, have found wide application in biomedicine, optronics, catalysis, and sensors during the last few years [64]. Although various strategies have been developed for synthesis of C-dots, the photoluminescence (PL) mechanism of C-dots is still not completely understood. Size-tunable SCNPs can serve as ideal precursors for the controllable fabrication of photoluminescent C-dots [65]. As shown in Fig. 7, the transesterification reaction between EDY and poly(methyl acrylate) (PMA) was carried out to obtain the EDY-modified copolymer P(MA-*r*-EDY), followed by deprotection of TMS and Bergman cyclization. The obtained PN nanoparticles were mixed with pure PMA and carbonized at 500°C, generating each C-dot from single PN nanoparticle. With this so-called bijective approach, the sizes of the C-dots were tunable by varying the molecular weight of PMA and the molar fraction of the EDY moiety in the copolymer. The composition and surface chemistry of these C-dots are controlled during carbonization and surface treatment. To further investigate the PL mechanism of C-dots, three series of uniform C-dots (CD-1 – CD-3) with average diameters of 4.5, 2.1, and 2.0 nm were fabricated. After surface modification with a diamine-terminated polyethylene glycol (PEG_{2000N}), all C-dots gave effective and stable PL, as shown in Fig. 8 (only CD-1 and CD-2 are shown).

In contrast to the trends typically found in semiconductor quantum dots and C-dots prepared from graphitized materials, the optimal emission wavelength of these C-dots red-shifts when the size decreases. On the other hand, PL spectra of

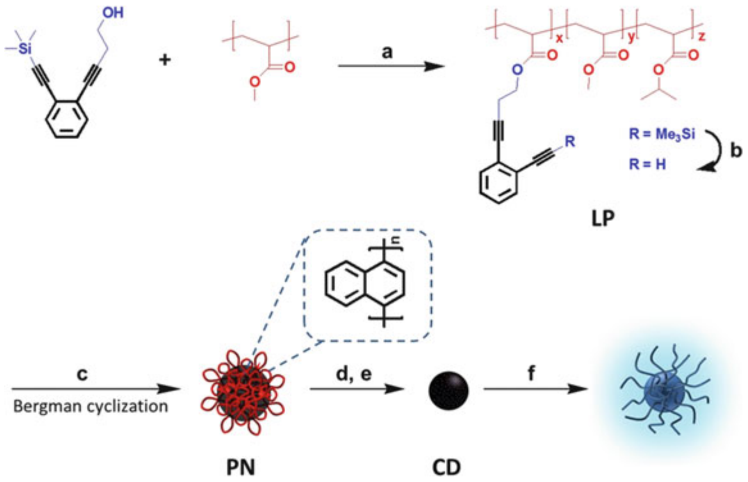

Fig. 7 Preparation of photoluminescent C-dots: (**a**) Ti(OiPr)$_4$, diphenylmethane, 120°C, 24 h; (**b**) tetrabutylammonium fluoride (TBAF), *p*-toluenesulfonic acid, tetrahydrofuran, room temperature, 2 h; (**c**) diphenyl ether, reflux, 6 h; (**d**) 500°C, 30 min; (**e**) 5 M HNO_3, reflux, 12 h; and (**f**) PEG_{2000N}, H_2O, reflux, 72 h. Reproduced from [65] with permission from RSC

surface-reduced C-dots (treated with $NaBH_4$) exhibit the same emission wavelengths as their surface-oxidized counterparts under the same excitation conditions, but the quantum yields (QYs) decrease significantly. Thus, we rationalized that the surface chemistry does not affect the energy gap of the C-dots and that the PL solely originates from the electron–hole pair recombination in the localized sp^2 carbon clusters, which are composed of two entirely different classes of carbon (crystalline and amorphous). The PL mechanism of C-dots formed from these two different sources was studied theoretically using density functional theory (DFT), choosing fused aromatic rings (FARs) and cyclo-1,4-naphthylenes (CNs) as model compounds (Fig. 9). For C-dots with a graphitized carbon core, the energy gap between the highest occupied molecular orbital (HOMO) and the lowest unoccupied molecular orbital (LUMO) decreases with increasing size of these sp^2 clusters. For C-dots with a disordered carbon core, however, the smaller size of CNs releases more strain energy in the excited state, resulting in a narrower energy gap

SCNPs were also used as size-tunable nanoreactors to fabricate and encapsulate inorganic quantum dots (QDs) in a one-pot reaction [66]. Poly(benzyl acrylate) (PBzA) nanoparticles were prepared by the same method as mentioned above, followed by hydrogenolysis on Pd/C to obtain hydrophilic poly(acrylic acid) (PAA)-based nanoreactors. Carboxy groups in these nanoreactors can interact with zinc ions and trap them internally. Subsequent reaction with S^{2-} gives ZnS QDs in situ. TEM images showed that almost spherical QDs with an average diameter of 4.1 nm were well-dispersed on the copper grid. Larger PAA nanoparticles led to ZnS QDs of similar size and emission wavelength, but decreased QYs from QDs@PN$_1$ to QDs@PN$_3$ (17, 6, and 2%). The latter was

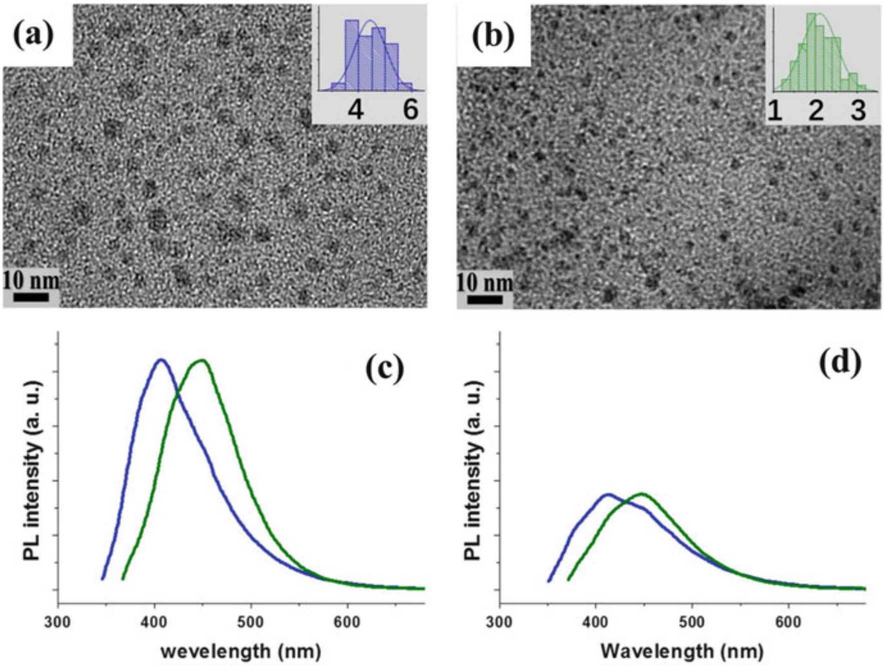

Fig. 8 Sizes and size-dependent PL spectra of C-dots. Transmission electron microscope (TEM) image and size histogram (*inset*) of (**a**) CD-1 and (**b**) CD-2. (**c**) PL spectra of surface-oxidized CD-1 (*blue line*) and CD-2 (*green line*) excited at 340 nm. (**d**) PL spectra of surface-reduced CD-1 (*blue line*) and CD-2 (*green line*) excited at 340 nm. Reproduced from [65] with permission from RSC

probably due to the fact that PAA nanoparticles of larger size can hold many ZnS QDs, which decreases the distance between neighboring QDs and results in fluorescence quenching. Nevertheless, CdS QDs@PN$_1$ exhibited bright fluorescence centered at 450 nm, with an average diameter of about 4.7 nm and a calculated QY of 45%.

3.2 *Carbon-Rich Three-Dimensional Networks*

Conjugated microporous polymers (CMPs) [67], a class of organic porous polymers that combine π-conjugated skeletons with permanent micropores, have shown great potential for solving challenging energy and environmental issues, as exemplified by their excellent performance in gas adsorption, heterogeneous catalysis, light emission, light harvesting, and electrical energy storage. As an emerging material platform, CMPs offer high flexibility for the molecular design of conjugated skeletons and nanopores. To construct a conjugated skeleton, the synthetic reaction

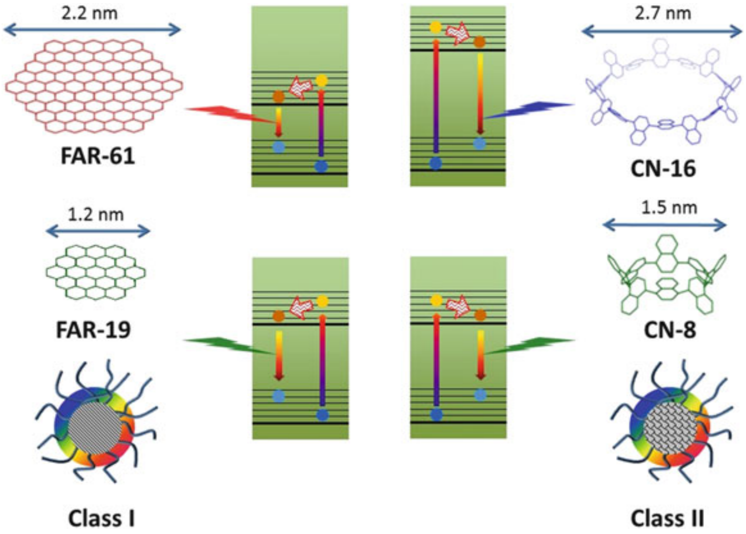

Fig. 9 PL mechanism of C-dots. The number after FARs represents the number of hexagonal rings. The number after CNs represents the number of repeating units. Reproduced from [65] with permission from RSC

must covalently link building blocks with a π-conjugated bond. Classic chemical reactions utilized for the preparation of linear conjugated polymers can also be employed for the synthesis of CMPs. Metal-containing catalysts are needed in most of these reactions, such as the Suzuki crosscoupling reaction [68], Yamamoto reaction [69], Sonogashira–Hagihara reaction [70], oxidative coupling reaction [71], Friedel–Crafts reaction [72], phenazine ring fusion reaction, and cyclotrimerization [73]. The residual metal catalysts can affect the performance of the obtained CMPs. In this respect, Bergman cyclization of EDY (a π-conjugated block) to form 1,4-benene diradicals via a catalyst-free method exactly fits chemists' wishes for a method of preparing CMPs.

Compounds containing multi-EDY moieties can be regarded as novel and multifunctional precursors for CMPs and carbon materials. Smith [74] was aware of this as early as 1998 when Bergman cyclization was rarely regarded as a tool for polymer synthesis. However, polyarylenes prepared in this way were limited to linear systems, as either soluble oligomers with fair stability or insoluble polymers with excellent thermal stability but which could not be easily processed. To tackle these issues, Smith pioneered the use of tetraynes, namely BODA [33, 75], which went through Bergman cyclization at around 200°C and led to branched oligomers containing pendant and terminal aryldiynes. Multifunctionality could be achieved through changing the spacer group X and/or terminal group. Purified oligomers with molecular weights of 3,000–24,000 and polydispersity index of 3–11 (GPC versus polystyrene) could be dissolved in organic solvents such as triisopropylbenzene, mesitylene, *N*-methylpyrrolidone (NMP), or diphenyl ether.

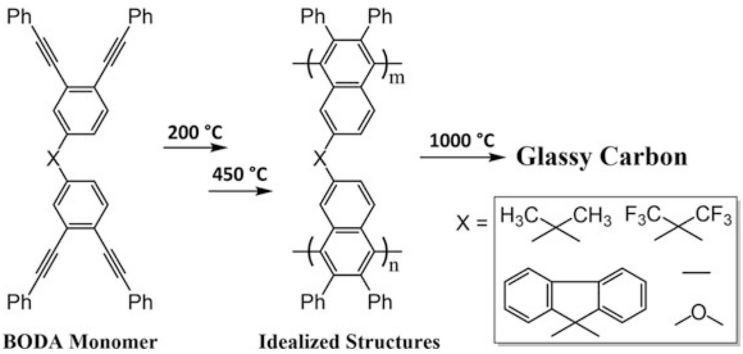

Fig. 10 Polymerization and conversion of BODA monomers to glassy carbon

Predominantly, large melt processing windows of 4–5 h at 210°C were exhibited in dynamic mechanical spectroscopy (DMA), which indicated that the oligomers could be used as melt- and solution-processible precursors for PN networks.

The hyperbranched network of BODA-DPO [75] (X = O) was converted into electrically conductive glassy carbon upon pyrolysis above 900°C in an inert atmosphere (Fig. 10). Electrical conductivity of the glassy carbons increased with temperature, which is similar to the semiconductive behavior. A rapid weight loss ensued when annealed from 450 to 1,000°C, giving a total weight loss of about 25%. No apparent weight loss was observed with continuous heating at 1,000°C, which indicated a high (>75%) yield of conductive glassy carbon. Subsequent heating from 1,100 to 1,600°C resulted in gradual weight loss, representing further carbonization or/and graphitization.

Given their high carbonization efficiency (75–80%) and excellent melt- and solution-processability, BODA monomers were investigated as novel resources for production of low-shrinkage glassy carbon microstructures, such as high temperature thin film dielectrics and inverse carbon opal photonic crystal structures [33, 76].

Recently, CMPs were prepared through Bergman cyclization of 2,3,6,7,10,11-hexaethynyltriphenylene (HET) by a thermal process in solid phase reaction or in solution without any additives (Fig. 11) [77]. Triggered by heat, the rigid intermediate trinaphthylene derivative is formed with three pairs of linkage sites, which then crosslink with each other. Although the monomer is totally planar, the trinaphthylene derivatives link with each other in a nonplanar mode, resulting in a rigid polymer with a three-dimensional (3D) structure. The Brunauer–Emmett–Teller (BET) specific surface area of the polymer was as high as 820 $m^2\ g^{-1}$, and the microporous specific surface area obtained using the *t*-plot method was up to 230 $m^2\ g^{-1}$. The obtained polymer displayed high adsorption capacity for both hydrogen and carbon dioxide. The hydrogen storage and carbon dioxide uptake reached 1.76 wt% (1.0 bar and 77 K) and 10.5 wt% (1.0 bar and 273 K), respectively. It is expected that this novel approach could be widely utilized in the formation of porous organic polymers based on Bergman cyclization.

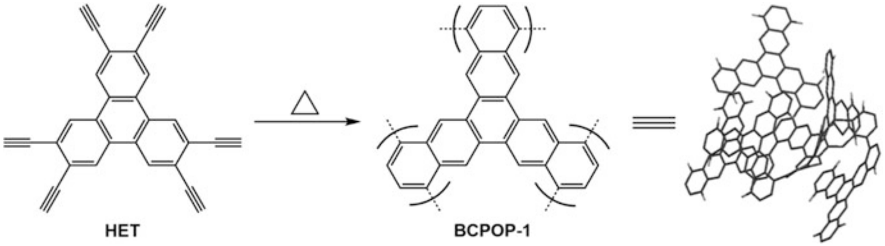

Fig. 11 Preparation of conjugated microporous polymers through Bergman cyclization of 2,3,6,7,10,11-hexaethynyltriphenylene (HET)

4 Carbon Nanomembranes Fabricated Through Bergman Cyclization

Carbon-based materials possess a broad range of properties as a result of the existence of different allotropes and various microstructures [1, 2]. They play important roles in modern technologies as commodity materials. Conjugated polymers with extensive polyarylene networks stemming from Bergman cyclization can be regarded as novel and multifunctional precursors for carbon materials that exhibit extreme thermal, chemical, and structural stability; metallic electrical conductivity; and catalytic, electrochemical, and electromechanical properties. The structural variability of EDYs makes it possible to design carbon materials with various nanoscopic morphologies, such as glassy carbon, carbon nanotubes, nanoplates, and nanospheres (Fig. 12). Based on these materials, a variety of nanodevices have been fabricated in our laboratory.

Initial work was performed by installing a tethering group on an EDY moiety and immobilizing this compound onto the surface of mesoporous silica (SBA-15) to construct tubular carbon monolayers [78]. EDY-containing imine was synthesized by two consecutive Sonogashira coupling reactions and imidization with *N*-aminopropyltriethoxysilane (APTES). After the formation of EDY SAMs on surface-activated SBA-15, Bergman cyclization of these surface-bound EDYs was performed by heating to 260°C under vacuum, yielding PN networks. Successive carbonization at 750°C was carried out to remove volatile components, followed by etching off the SBA-15 template with aqueous HF. Finally, the powder was heated under vacuum at 900°C to obtain ultrathin carbon nanotubes. TEM images of the tubular CNMs in Fig. 13 indicate successful replication of the SBA-15 template. Two well-separated rings were observed in the selected area electron diffraction (SAED) pattern of this carbonaceous material, which correlated with the major indices [100] and [110] of graphite nanostructures. In addition, by changing the template, this work was extended to the synthesis of carbon nanoplates [79] (Fig. 14b), ordered porous carbon [80] (Fig. 14a), and CNM-coated Fe_3O_4 nanoparticles [81].

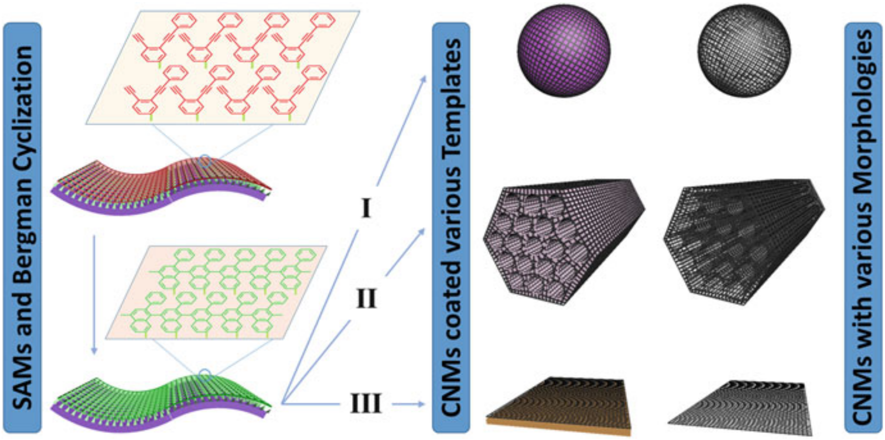

Fig. 12 Preparation of carbon nanomembranes (CNMs) through Bergman cyclization of self-assembly monolayers (SAMs) of EDY on templates with various microstructures and subsequent carbonization (and template removal). After SAM formation on various templates and Bergman cyclization, CNM-coated templates can be prepared via carbonization. Free CNMs with various morphologies can be obtained via template removal

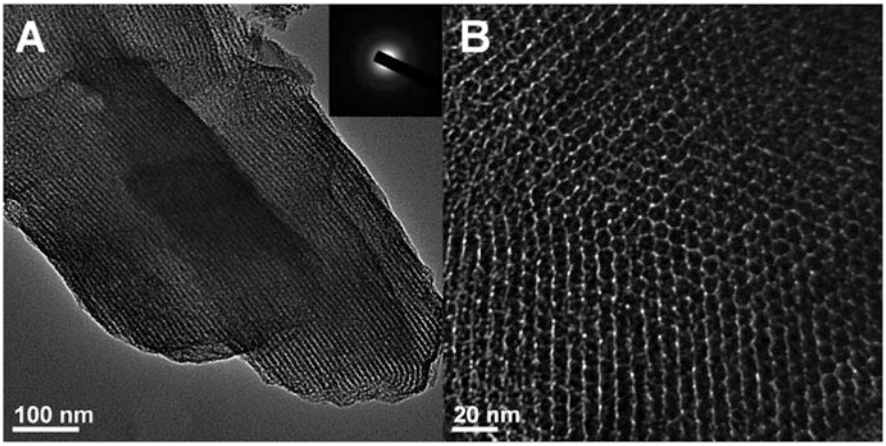

Fig. 13 TEM images of tubular CNMs viewed along [110] (**a**) and [001] (**b**) directions; *inset* shows SAED pattern of tubular carbon monolayers. Reproduced from [78] with permission from ACS

5 Application of Carbon Nanomembranes

The uniform pore size, outstanding electronic conductivity, and high surface area of CNMs promise many applications in nanodevices, especially in supercapacitor and catalysis. The ultrathin skeleton of the tubular CNMs means that the silica-

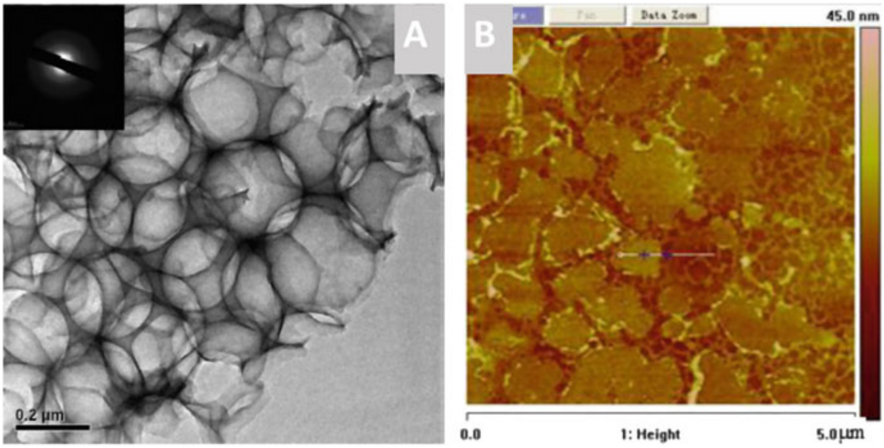

Fig. 14 (**a**) TEM image of ordered porous CNMs [80] and (**b**) AFM image of plate-like CNMs [79]. Reproduced from [80] with permission from ACS

supported carbon nanomembranes (SS-CNMs) can be directly applied in various nanodevices. As shown in Fig. 15, tubular SS-CNMs with different pore sizes were obtained by tuning the parameters of the mesoporous silica support. The relationship between pore size and supercapacitance capacity was then investigated. To further improve the supercapacitance performance, we embedded metal oxide nanocrystals into the pores of SS-CNMs. They showed very high specific capacitance and excellent electrochemical stability. We also immobilized palladium nanoparticles in the pores of SS-CNMs and used this system as a nanoreactor for heterogeneous catalysis and confined catalysis. Furthermore, we coated noble metal nanoparticles with CNMs to serve as robust and reusable probes for surface-enhanced Raman scattering (SERS).

5.1 Carbon Nanomembranes for Supercapacitors

The complex relationship between the texture parameters of electrode materials and the supercapacitance of electrochemical capacitors (ECs) was studied using SS-CNMs of similar geometries but different mesopore sizes [82]. In this study, four SS-CNMs (SS-CNM-1, SS-CNM-2, SS-CNM-3, and SS-CNM-4) with pore sizes of 3.05, 4.14, 6.68, and 8.02 nm (as determined using the BET equation) were prepared from MCM-41, SBA-15, and pore-expanded SBA-15s, respectively. All samples gave quasi-rectangular cyclic voltammetry (CV) curves along the current–potential axis (Fig. 16a), indicating that the samples display ideal capacitive behavior. The galvanostatic charge–discharge curves were linear and symmetrical (Fig. 16b), which are typical characteristics of an ideal electrical double layer (EDL)

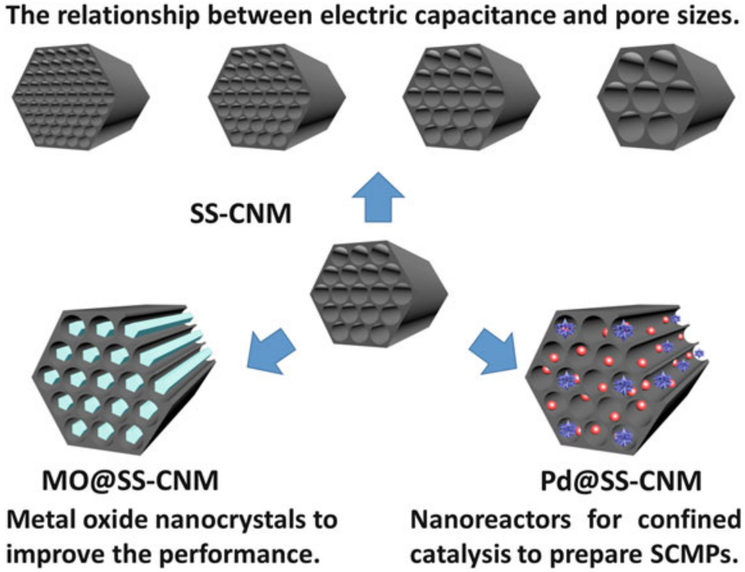

Fig. 15 Applications of tubular CNMs in supercapacitors and catalysis, as investigated by our group

capacitor. Moreover, it is notable that high specific capacitance of 305 F g^{-1} was obtained for SS-CNM-2 at 10 mV s^{-1}, which was superior to 68, 173, and 75 F g^{-1} for SS-CNM-1, SS-CNM-3, and SS-CNM-4 composites, respectively. Theoretical modeling further validated this curved dependence of supercapacitance on the pore size of mesoporous electrode materials, indicating that the optimal capacitance of ECs can be achieved using porous carbon electrode materials with open pores of 3.0–5.0 nm (Fig. 17).

Inspired by this work, we synthesized porous 3D CNMs through Friedel–Crafts crosslinking of phenyl SAMs on silica nanoparticles (SNPs), followed by high temperature treatment and template removal [83, 84]. The CNMs show a hierarchic 3D connected porous structure, and the pore size can be facilely tuned by varying the particle size of the SNP template. CNMs with high surface area, large pore volume, and partially graphitized frameworks exhibited good performances as supercapacitor electrode materials. The specific capacitance of the porous 3D CNMs reached 202 F g^{-1} at a current density of 0.5 A g^{-1} in an aqueous electrolyte [83].

To improve the capacitance performance of SS-CNMs in supercapacitors, we embedded metal oxide nanocrystals inside SS-CNMs. The SS-CNMs acted as host electrode materials as a result of their high surface area, tunable structure, and good conductivity; Co_3O_4 nanoparticles were used as the electronic active component [85]. A series of Co_3O_4@SS-CNM-2 composites with different Co_3O_4 contents (24, 50, 66, and 80 wt%) were synthesized by a facile wetness impregnation method with $Co(NO_3)_2$ as the precursor, followed by oxidation in air. Co_3O_4(66%)@SS-CNM-2 showed the highest specific capacitance, probably as a result of better

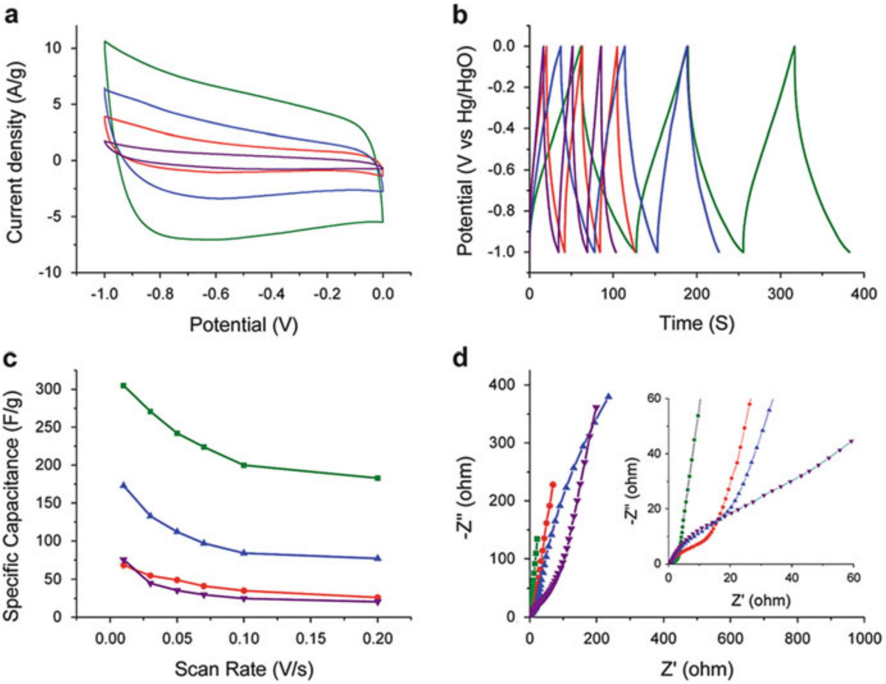

Fig. 16 Electrochemical evaluation of SS-CNM electrode materials (SS-CNM-1, *red*; SS-CNM-2, *green*; SS-CNM-3, *blue*; SS-CNM-4, *purple*) using an aqueous electrolyte of 6.0 M potassium hydroxide dissolved in deionized water. (**a**) Cyclic voltammetry curves for four SS-CNM electrode materials at a scan rate of 0.05 V s^{-1}. (**b**) Galvanostatic charge–discharge curves of SS-CNM electrode materials operated at a current density of 5 A g^{-1}. (**c**) Stack capacitance values calculated from cyclic voltammetry curves as a function of the scan rate. (**d**) Impedance Nyquist plots for the SS-CNMs. Reproduced from [82] with permission from RSC

dispersion of Co_3O_4, which improved electron transmission inside the channels and further increased both the electrical conductivity of the composites and electrochemical utilization of the pristine Co_3O_4 during the charge/discharge process. This supercapacitor electrode material exhibited a maximum specific capacitance of 1,086 F g^{-1} (1,645 F g^{-1} based on Co_3O_4) in 6 M KOH solution. After 10,000 cycles, retention of 90% of the initial capacitance was observed, indicating excellent electrochemical stability of the electrode. Highly ordered metal oxide nanorods (MnO_2, SnO_2, NiO) embedded inside SS-CNM-2 were also applied as electroactive materials for fabrication of symmetrical supercapacitors [86]. Maximum specific capacitance of the obtained cells reached 964, 745, and 620 F g^{-1} in aqueous electrolytes with energy densities of 33.5, 25.7, and 21.6 Wh kg^{-1} for a 1 V voltage window for MnO_2, SnO_2, and NiO, respectively. These values are among the highest for two-electrode supercapacitor cells employing similar metal oxide/carbon materials. The high performance is attributed to the synergic effect between the conductive CNMs and well-ordered pseudocapacitive metal oxide nanorods.

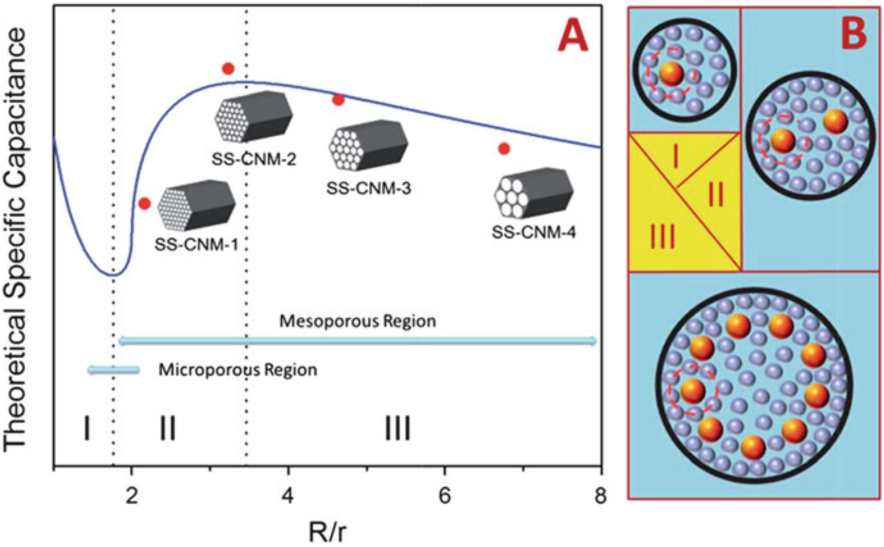

Fig. 17 (**a**) Fitting the specific capacitances of SS-CNMs with the model plot. (**b**) Drawings of solvated ions residing in pores with *R*/*r* values of 1.5 (*top left*), 2 (*top right*), and 4 (*bottom*). Reproduced from [82] with permission from RSC

5.2 Palladium Nanoparticle-Loaded Carbon Nanomembranes for Confined Catalysis

Further modification of SS-CNMs, such as embedding Pd nanoparticles inside the nanotubes, have created new desirable nanoreactors for catalytic applications [87]. Pd@SS-CNM (Fig. 18b) nanoreactors with Pd contents of 3.5% were prepared by wetness impregnation with H_2PdCl_4 followed by reduction of Pd(II) to Pd (0) under a hydrogen atmosphere. This nanoreactor revealed high efficiency in heterogeneous Suzuki crosscoupling reactions in aqueous media, and was easily separated and recovered from the reaction mixture. Its catalytic activity did not deteriorate, even after being reused several times, indicating high stability of the nanoreactor (mainly as a benefit of the CNM lining). Kinetic studies showed that the addition of naphthalene or anthracene significantly decelerated the coupling reactions, whereas the addition of decalin only slightly slowed the reactions. These results confirmed that the CNM is essential for the high reactivity of the catalyst because it provides a hydrophobic environment (aromatic compounds prefer to coordinate with the graphene layer of a carbonaceous surface through π–π interactions).

Exploration of this newly designed nanoreactor in the synthesis of soluble conjugated microporous polymers (SCMPs) offered exciting results [88]. Preparation of CMPs through hyperbranching polycondensation is generally hard to control, which usually leads to insoluble polymer particles regardless of the solvent

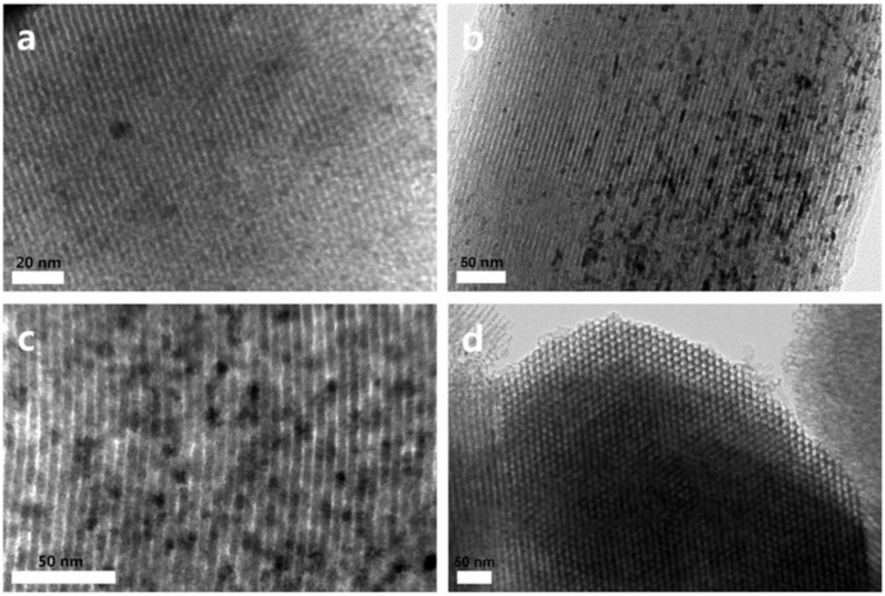

Fig. 18 TEM images of Pd@SS-CNM-1 (**a**), Pd@SS-CNM-2 (**b**), and Pd@SS-CNM-3 (**c**, **d**). Reproduced from [88] with permission from Wiley-VCH

used. To solve the solubility problem, we limited the Suzuki-type polycondensation so that it took place exclusively inside Pd@SS-CNM nanoreactors, and successfully synthesized size-controlled SCMPs. In this study, SS-CNM-1, SS-CNM-2, and SS-CNM-3 with pore sizes of 3.4, 5.4, and 7.2 nm were prepared from MCM-41, SBA-15, and pore-expanded SBA-15, respectively. TEM images (Fig. 18) showed that all the palladium nanoparticles were well dispersed inside the channels and no palladium nanoparticles were found outside the nanoreactors, which is essential for the confined growth of the SCMPs. Polycondensations performed in DMF with Pd@SS-CNMs as the catalyst and tetrabutylammonium fluoride (TBAF) as the base gave three series of narrowly dispersed SCMPs (SCMP1, SCMP2, and SCMP3) with average sizes of 2.4, 3.8, and 5.4 nm, respectively (Fig. 19). These were only slightly smaller than the pore sizes of the nanoreactors, implying that the sizes of SCMPs are controlled by the pore sizes of the nanoreactors, because the polycondensations take place exclusively inside the confined pores of SS-CNM nanoreactors. Based on theoretical simulations, the calculated sizes of generation 2, 3, and 4 dendrimers match quite well with the experimental values for SCMP1, SCMP2, and SCMP3, respectively. More interestingly, the smallest SCMP (SCMP1) can diffuse into the mesochannels of larger nanoreactors (SS-CNM-2 and SS-CNM-3) to further react with iodobenzene. In contrast, the middle-sized SCMP2 can only enter the largest nanoreactors. The largest polymer, SCMP3, can hardly enter either nanoreactor, leading to negligible consumption of iodobenzene (as monitored by gas chromatography). This set of experiments unambiguously

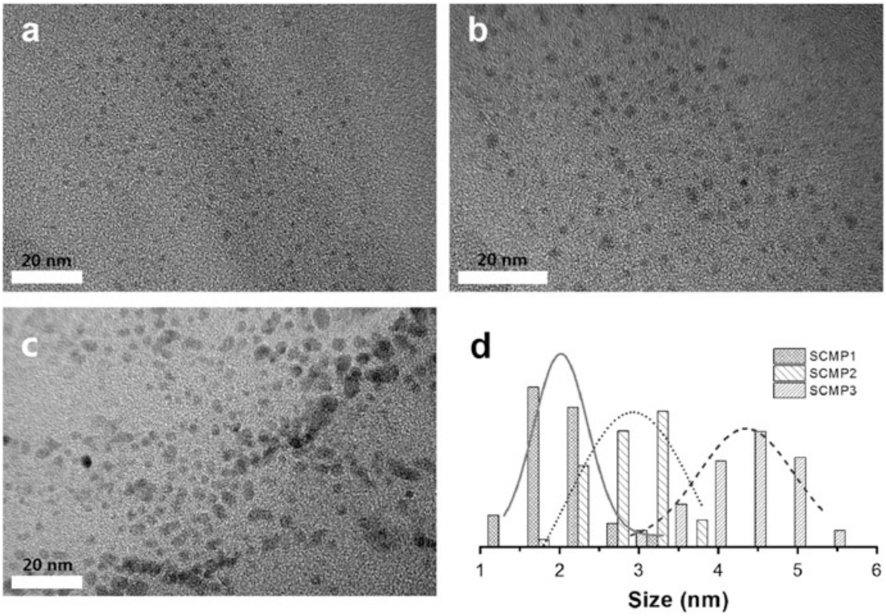

Fig. 19 High resolution TEM images of SCMP1 (**a**), SCMP2 (**b**), and SCMP3 (**c**). (**d**) Size histogram of three SCMPs, obtained using high resolution TEM. Reproduced from [80] with permission from Wiley-VCH

demonstrated that the polycondensation is a truly confined growth, with the monomers accessing palladium nanoparticles through the open channels. This catalyst@pore strategy can also be generally appreciated in the synthesis of other types of soluble hyperbranched polymers using different types of monomers, and the sizes of different kinds of SCMPs are exactly controlled by the nanoreactors. In addition, the controllable preparation of SCMPs has been extended to a heterogeneous catalysis system [89]. The combination of physical stability and processability offered by SCMPs makes them particularly attractive in polymer light-emitting diodes (PLEDs) and polymer solar cells.

6 Conclusions and Perspectives

Bergman cyclization has attracted increasing attention as an emerging and extraordinary strategy for the preparation of aromatic polyarylenes and carbon-rich nanomaterials. Considerable efforts have been directed at understanding and expanding the various processes involved in the synthesis of EDYs, polymerization strategies and functionalization, and further conversion to carbon nano-allotropes. Recent years have witnessed broad achievements for Bergman cyclization in materials science, especially in the development of new synthetic routes for carbon-rich nanoparticles/networks, carbon nanomembranes, and nanodevices. However, this field is still in its infancy and has much room for improvement. For example, PPPs formed from DNHD on a surface of Cu(110) cannot be converted to graphene nanoribbons directly (Fig. 4). Another example is that graphene nanoplates can be obtained using silicon as template, but it is a challenge to growth large-scale graphene in this way (Fig. 14b). The problem here could be that rapid chain transfer or termination of the radicals causes unwanted five-membered cyclization to form "indene" structure defects [39] that encumber further growth of the nanographene. This mixed mechanism limits the further development of Bergman cyclization in the field of controllable synthesis of conjugated polymers. Solving this problem requires a strategy for closing the reaction pathways of the step-growth mechanism, which seems to be unattainable with the diradical nature of the intermediates. This issue has inspired our attempts to extend research into the mechanism of Bergman cyclization and develop a novel ionic cycloaromatization of EDYs. Much effort has been devoted to redirecting the Bergman cyclization from the usual formation of a diradical toward a zwitterionic or ionic pathway, and polymerizations based on ionic cycloaromatization of EDYs are likely to be discovered in the near future.

Acknowledgements Financial support by the National Natural Science Foundation of China (21674035, 21474027, 91023008, 20874026, 20704013), Shanghai Shuguang Project (07SG33), National Postdoctoral Program for Innovative Talents (BX201600101), New Century Excellent Talents in University, PhD Programs Foundation of Ministry of Education of China, and Shanghai Leading Academic Discipline Project (B502) are gratefully acknowledged. A.H. thanks the "Eastern Scholar Professorship" support from Shanghai local government. Y.W. thanks the scholarship from China Scholarship Council (CSC) to support his study at the University of Chicago.

References

1. Hirsch A (2010) Nat Mater 9:868
2. Georgakilas V, Perman JA, Tucek J, Zboril R (2015) Chem Rev 115:4744
3. Chen L, Hernandez Y, Feng X, Mullen K (2012) Angew Chem Int Ed 51:7640
4. Sun Z, Wu JS (2014) In: Siegel JS, Wu YT (eds) Polyarenes I, vol 349. Springer, Berlin, p 197
5. Jones RR, Bergman RG (1972) J Am Chem Soc 94:660
6. Bergman RG (1973) Acc Chem Res 6:25
7. Lee MD, Dunne TS, Siegel MM, Chang CC, Morton GO, Borders DB (1987) J Am Chem Soc 109:3464
8. Lee MD, Dunne TS, Chang CC, Ellestad GA, Siegel MM, Morton GO, McGahren WJ, Borders DB (1987) J Am Chem Soc 109:3466
9. Konishi M, Ohkuma H, Tsuno T, Oki T, VanDuyne GD, Clardy J (1990) J Am Chem Soc 112:3715
10. Golik J, Clardy J, Dubay G, Groenewold G, Kawaguchi H, Konishi M, Krishnan B, Ohkuma H, Saitoh K, Doyle TW (1987) J Am Chem Soc 109:3461
11. Golik J, Dubay G, Groenewold G, Kawaguchi H, Konishi M, Krishnan B, Ohkuma H, Saitoh K, Doyle TW (1987) J Am Chem Soc 109:3462
12. Long BH, Golik J, Forenza S, Ward B, Rehfuss R, Dabrowiak JC, Catino JJ, Musial ST, Brookshire KW, Doyle TW (1989) Proc Natl Acad Sci 86:2

13. Leet JE, Schroeder DR, Hofstead SJ, Golik J, Colson KL, Huang S, Klohr SE, Doyle TW, Matson JA (1992) J Am Chem Soc 114:7946
14. Nicolaou KC, Smith AL, Yue EW (1993) PNAS 90:5881
15. Smith AL, Nicolaou K (1996) J Med Chem 39:2103
16. Biggins JB, Onwueme KC, Thorson JS (2003) Science 301:1537
17. Basak A, Mandal S, Bag SS (2003) Chem Rev 103:4077
18. Kar M, Basak A (2007) Chem Rev 107:2861
19. Hatial I, Jana S, Bisai S, Das M, Ghosh AK, Anoop A, Basak A (2014) RSC Adv 4:28041
20. Song D, Sun S, Tian Y, Huang S, Ding Y, Yuan Y, Hu A (2015) J Mater Chem B 3:3195
21. Song D, Tian Y, Huang S, Li B, Yuan Y, Hu A (2015) J Mater Chem B 3:8584
22. Kraka E, Cremer D (2014) Wiley Interdiscip Rev Comput Mol Sci 4:285
23. Nicolaou KC, Ogawa Y, Zuccarello G, Schweiger EJ, Kumazawa T (1988) J Am Chem Soc 110:4866
24. Magnus P, Fortt S, Pitterna T, Snyder JP (1990) J Am Chem Soc 112:4986
25. Snyder JP (1990) J Am Chem Soc 112:5367
26. Klein M, Walenzyk T, Konig B (2004) Collect Czechoslov Chem Commun 69:945
27. Alabugin IV, Yang WY, Pal R (2012) In: Griesbeck A, Oelgemoeller M, Ghetti F (eds) CRC handbook of organic photochemistry and photobiology. Taylor and Francis, Boca Raton, p 549
28. Kaya K, Johnson M, Alabugin IV (2015) Photochem Photobiol 91:748
29. Campolo D, Arif T, Borie C, Mouysset D, Vanthuyne N, Naubron JV, Bertrand MP, Nechab M (2014) Angew Chem Int Ed 53:3227
30. Nösel P, Müller V, Mader S, Moghimi S, Rudolph M, Braun I, Rominger F, Hashmi ASK (2015) Adv Synth Catal 357:500
31. Xiao Y, Hu A (2011) Macromol Rapid Commun 32:1688
32. John JA, Tour JM (1994) J Am Chem Soc 116:5011
33. Smith DW, Shah HV, Perera KPU, Perpall MW, Babb DA, Martin SJ (2007) Adv Funct Mater 17:1237
34. Rettenbacher AS, Perpall MW, Echegoyen L, Hudson J, Smith DW (2007) Chem Mater 19:1411
35. Rule JD, Wilson SR, Moore JS (2003) J Am Chem Soc 125:12992
36. Rule JD, Moore JS (2005) Macromolecules 38:7266
37. Gerstel P, Barner-Kowollik C (2011) Macromol Rapid Commun 32:444
38. Chen S, Hu A (2015) Science China Chem 58:1710
39. Johnson JP, Bringley DA, Wilson EE, Lewis KD, Beck LW, Matzger AJ (2003) J Am Chem Soc 125:14708
40. Sun Q, Zhang C, Li Z, Kong H, Tan Q, Hu A, Xu W (2013) J Am Chem Soc 135:8448
41. Cheng X, Ma J, Zhi J, Yang X, Hu A (2010) Macromolecules 43:909
42. Ma J, Ma X, Deng S, Li F, Hu A (2011) J Polym Sci Polym Chem 49:1368
43. Dong L, Zheng Z, Wang Y, Li X, Hua J, Hu A (2015) J Mater Chem A 3:11607
44. Miao C, Zhi J, Sun S, Yang X, Hu A (2010) J Polym Sci Polym Chem 48:2187
45. Sun S, Huang B, Li F, Song D, Hu A (2015) Chin J Polym Sci 33:743
46. Saito K, Rettenbacher AS, Smith DW, Fukuzumi S (2008) J Mater Chem 18:3237
47. Ma J, Cheng X, Ma X, Deng S, Hu A (2010) J Polym Sci Polym Chem 48:5541
48. Ma J, Deng S, Cheng X, Wei W, Hu A (2011) J Polym Sci Polym Chem 49:3951
49. Ma X, Li F, Wang Y, Hu A (2012) Chem Asian J 7:2547
50. Taranekar P, Park JY, Patton D, Fulghum T, Ramon GJ, Advincula R (2006) Adv Mater 18:2461
51. Tekade RK, Kumar PV, Jain NK (2009) Chem Rev 109:49
52. Parrott MC, Benhabbour SR, Saab C, Lemon JA, Parker S, Valliant JF, Adronov A (2009) J Am Chem Soc 131:2906
53. Helms B, Meijer EW (2006) Science 313:929
54. Mecerreyes D, Lee V, Hawker CJ, Hedrick JL, Wursch A, Volksen W, Magbitang T, Huang E, Miller RD (2001) Adv Mater 13:204

55. Adkins CT, Muchalski H, Harth E (2009) Macromolecules 42:5786
56. Moreno AJ, Lo Verso F, Sanchez-Sanchez A, Arbe A, Colmenero J, Pomposo JA (2013) Macromolecules 46:9748
57. Wong EHH, Lam SJ, Nam E, Qiao GG (2014) ACS Macro Lett 3:524
58. Croce TA, Hamilton SK, Chen ML, Muchalski H, Harth E (2007) Macromolecules 40:6028
59. Ergin M, Kiskan B, Gacal B, Yagci Y (2007) Macromolecules 40:4724
60. Jiang XY, Pu HT, Wang P (2011) Polymer 52:3597
61. Hansell CF, Lu A, Patterson JP, O’Reilly RK (2014) Nanoscale 6:4102
62. Zhu B, Ma J, Li Z, Hou J, Cheng X, Qian G, Liu P, Hu A (2011) J Mater Chem 21:2679
63. Zhu B, Qian G, Xiao Y, Deng S, Wang M, Hu A (2011) J Polym Sci Polym Chem 49:5330
64. Wang Y, Hu A (2014) J Mater Chem C 2:6921
65. Zhu B, Sun S, Wang Y, Deng S, Qian G, Wang M, Hu A (2013) J Mater Chem C 1:580
66. Qian G, Zhu B, Wang Y, Deng S, Hu A (2012) Macromol Rapid Commun 33:1393
67. Xu Y, Jin S, Xu H, Nagai A, Jiang D (2013) Chem Soc Rev 42:8012
68. Chen L, Honsho Y, Seki S, Jiang D (2010) J Am Chem Soc 132:6742
69. Yang X, Yao SW, Yu M, Jiang JX (2014) Macromol Rapid Commun 35:834
70. Laybourn A, Dawson R, Clowes R, Hasell T, Cooper AI, Khimyak YZ, Adams DJ (2014) Polym Chem 5:6325
71. Bildirir H, Osken I, Ozturk T, Thomas A (2015) Chem Eur J 21:9306
72. Li B, Gong R, Wang W, Huang X, Zhang W, Li H, Hu C, Tan B (2011) Macromolecules 44:2410
73. Hu R, Lam JWY, Li M, Deng H, Li J, Tang BZ (2013) J Polym Sci Polym Chem 51:4752
74. Smith DW, Babb DA, Snelgrove RV, Townsend PH, Martin SJ (1998) J Am Chem Soc 120:9078
75. Shah HV, Brittain ST, Huang Q, Hwu SJ, Whitesides GM, Smith DW (1999) Chem Mater 11:2623
76. Perpall MW, Perera KPU, DiMaio J, Ballato J, Foulger SH, Smith DW (2003) Langmuir 19:7153
77. Zhang X-M, Ding X, Hu A, Han B-H (2015) Polym Chem 6:4734
78. Yang X, Li Z, Zhi J, Ma J, Hu A (2010) Langmuir 26:11244
79. Hu A, Li Z, Zhu X, Song D (2013) Chinese Sciencepaper Online 11:591
80. Li Z, Song D, Zhi J, Hu A (2011) J Phys Chem C 115:15829
81. Li Z, Zhu X, Chen S, Hu A (2013) Chem Asian J 8:560
82. Zhi J, Wang Y, Deng S, Hu A (2014) RSC Adv 4:40296
83. Wang Y, Xiong R, Dong L, Hu A (2014) J Mater Chem A 2:5212
84. Zhang Y, Wang YF, Hu AG (2015) RSC Adv 5:70297
85. Zhi J, Deng S, Zhang Y, Wang Y, Hu A (2013) J Mater Chem A 1:3171
86. Zhi J, Deng S, Wang Y, Hu A (2015) J Phys Chem C 119:8530
87. Zhi J, Song D, Li Z, Lei X, Hu A (2011) Chem Commun 47:10707
88. Deng S, Zhi J, Zhang X, Wu Q, Ding Y, Hu A (2014) Angew Chem Int Ed 53:14144
89. Deng S, Zhao P, Dai Y, Huang B, Hu A (2015) Polymer 64:216

Index